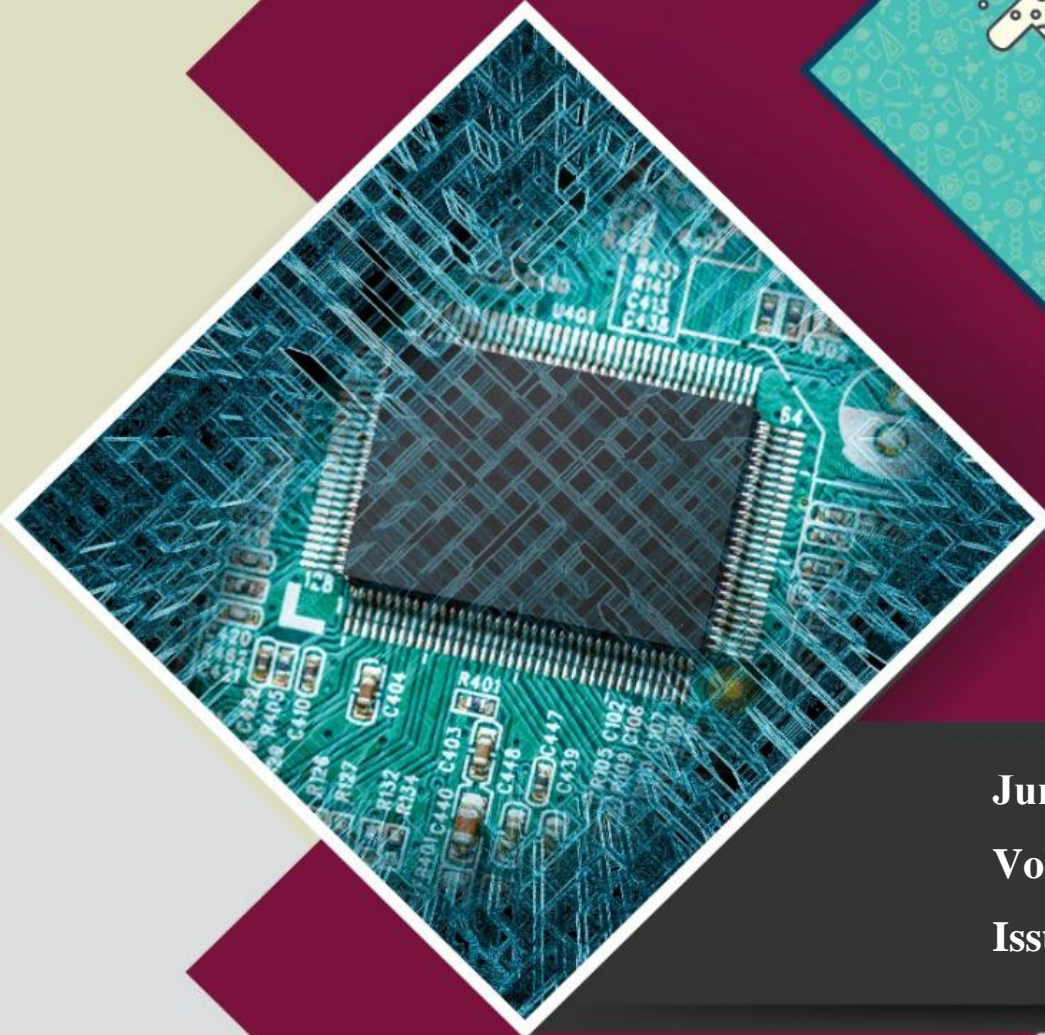


e-ISSN: 2822-2881



# FUJECE

Firat University Journal of Experimental and Computational Engineering



June : 2025

Volume : 4

Issue : 2



<https://dergipark.org.tr/tr/pub/fujece>

**Owner**

On Behalf of Firat University

**Rector**

 Prof. Dr. Fahrettin GÖKTAŞ (fgoktas@firat.edu.tr)

**Editor-in-Chief**

 Prof. Dr. Mehmet YILMAZ, Firat University, Türkiye (mehmetyilmaz@firat.edu.tr)

**Vice Editor-in-Chief**

 Prof. Dr. Ebru AKPINAR, Firat University, Türkiye (ebruakpinar@firat.edu.tr)

 Prof. Dr. Ragıp İNCE, Firat University, Türkiye (rince@firat.edu.tr)

 Prof. Dr. Mete Onur KAMAN, Firat University, Türkiye (mkaman@firat.edu.tr)


 Assoc. Prof. Dr. Erkut YALÇIN, Firat University, Türkiye (erkutyalcin@firat.edu.tr)


**Editorial Advisory Board**


 Prof. Dr. Yakup DEMİR, Firat University, Türkiye (ydemir@firat.edu.tr)

 Prof. Dr. Levent TAŞCI, Firat University, Türkiye (ltasci@firat.edu.tr)

 Prof. Dr. Abdussamet ARSLAN, Gazi University, Türkiye (aarslan@gazi.edu.tr)


 Prof. Dr. Ahmet ŞAŞMAZ, Firat University, Türkiye (asasmaz@firat.edu.tr)

 Prof. Dr. Abdulkadir Cuneyt AYDIN, Atatürk University, Türkiye (acaydin@atauni.edu.tr)

 Prof. Dr. Fatih CETİŞLİ, Pamukkale University, Türkiye (fcetisli@pau.edu.tr)

 Prof. Dr. Bilal ALATAŞ, Firat University, Türkiye (balatas@firat.edu.tr)


 Prof. Dr. Erhan AKIN, Firat University, Türkiye (eakin@firat.edu.tr)

 Prof. Dr. Erkan KÖSE, Nuh Naci Yazgan University, Türkiye (ekose@nny.edu.tr)

 Prof. Dr. Filiz KAR, Firat University, Türkiye (fkar@firat.edu.tr)


 Prof. Dr. Hasan SOFUOĞLU, Karadeniz Technical University, Türkiye (sofuoglu@ktu.edu.tr)


 Prof. Dr. Özge Kaya HANAY, Firat University, Türkiye (ohanay@firat.edu.tr)

 Prof. Dr. Yusuf AYVAZ, Yıldız Technical University, Türkiye (yayvaz@yildiz.edu.tr)


 Prof. Dr. M. Şaban TANYILDIZI, Firat University, Türkiye (mtanyildizi@firat.edu.tr)

 Doç. Dr. Tacettin GEÇKİL, İnönü University, Türkiye(tacettin.geckil@inonu.edu.tr)

 Doç. Dr. José NORAMBUENA-CONTRERAS, Bio Bio University, Chile (j.norambuena@swansea.ac.uk)

 Res. Assist. Dr. Ulaş Baran BALOĞLU, University of Bristol, England (ubbaloglu@gmail.com)


### Editorial Board


 Prof. Dr. Mehmet YILMAZ (Editor-in-Chief) Civil Engineering (mehmetyilmaz@firat.edu.tr)


 Prof. Dr. Ebru AKPINAR (Vice Editor-in-Chief) Mechanical Engineering  
(ebruakpinar@firat.edu.tr)


 Prof. Dr. Ragıp İNCE (Vice Editor-in-Chief) Civil Engineering (rince@firat.edu.tr)


 Prof. Dr. Mete Onur KAMAN (Vice Editor-in-Chief) Mechanical Engineering (mkaman@firat.edu.tr)


 Assoc. Prof. Dr. Erkut YALÇIN (Vice Editor-in-Chief) Civil Engineering (erkutyalcin@firat.edu.tr)

 Prof. Dr. Ali TOPAL Civil Engineering(ali.topal@deu.edu.tr)


 Prof. Dr. Ali YAZICI Software Engineering(ali.yazici@atilim.edu.tr)

 Prof. Dr. Ayşe Vildan BEŞE Chemical Engineering(avesis.atauni.edu.tr/vbese)


 Prof. Dr. Bilge Hilal CADIRCI EFELİ Bioengineering(bilgehilal.cadirci@gop.edu.tr)


 Prof. Dr. Kadir TURAN Mechanical Engineering(kturan@dicle.edu.tr)


 Prof. Dr. H. Soner ALTUNDOĞAN Bioengineering (saltundogan@firat.edu.tr)


 Prof. Dr. Mehmet Deniz TURAN Metallurgy and Materials Engineering  
(mdturan@firat.edu.tr)


 Prof. Dr. Mustafa YANALAK Geodesy and Photog. Engineering  
(yanalak@itu.edu.tr)

 Prof. Dr. Nuno MENDES Mechanical Engineering  
(nunomendes@civil.uminho.pt)

 Prof. Dr. Rashid NADİROV Chemical (nadir.rashid@gmail.com)


 Prof. Dr. Serdar Ethem HAMAMCI Electrical-Electronics  
Engineering(serdar.hamamci@inonu.edu.tr)

 Prof. Dr. Selçuk ALEMDAĞ Geological  
Engineering(selcuk@gumushane.edu.tr)

 Prof. Dr. Mehmet KARAKÖSE Computer Engineering (mkarakose@firat.edu.tr)


 Prof. Dr. Alvaro Garcia HERNANDEZ

Civil Engineering

 Prof. Dr. Ömür GÖKKUŞ

Environmental

Engineering(omurgokkus@cumhuriyet.edu.tr)

 Assoc. Prof. Dr. Fatih DEMİR

Software Engineering (fatihdemir@firat.edu.tr)

 Lecturer Batuhan SELVİ (Language Editor)


English Language

Teaching(batuhan.selvi@bozok.edu.tr)


 Mustafa Gani GENÇER (Language Editor)

English Language Teaching

(mg.gncr@hotmail.com)

 Res. Assist. Dr. Özge Erdoğan YAMAÇ (Secretariat)

Civil Engineering (ozgeerdogan@firat.edu.tr)


 Res. Assist. Beyza Furtana YALÇIN  
(Pub.Coordinators)

Civil Engineering (beyzafurtana@munzur.edu.tr)

Social Studies Education

Ahmet BAL (Layout Editor) Firat University (a\_bal@firat.edu.tr)

#### Composition

 Ahmet BAL

#### Correspondence Address

Firat University Faculty of Engineering Journal of Experimental and Computational Engineering Publishing

Coordinatorship

23119 Elazığ/TÜRKİYE

E-mail: fujeece@firat.edu.tr

Web page: <http://fujeece.firat.edu.tr/>

Firat University Journal of Experimental and Computational Engineering a peer-reviewed journal.



## CONTENTS

Experimental and Numerical Applications to Increase Thermal Performance of a Photovoltaic Solar Panel (Research Article) Fotovoltaik Bir Güneş Panelinin Termal Performansını Arttırmak için Deneysel ve Sayısal Uygulamalar (Araştırma Makalesi) <b>Murat ÇATALKAYA</b>	226
Innovative Approach to Adjustable Color Temperature in LED Luminaires (Research Article) Ayarlanabilir Renk Sıcaklığına Sahip LED Armatürlerde Yenilikçi Yaklaşım (Araştırma Makalesi) <b>Burak TAŞCI, Yavuz EROL</b>	245
Investigation of Adhesion and Stripping Properties of Asphalt Modified with Bio-oil (Research Article) Biyo-yağ ile Modifiyeli Asfaltın Yapışma ve Soyulma Özelliklerinin İncelenmesi (Araştırma Makalesi) <b>Öznur KARADAĞ, Mehmet SALTAN</b>	262
Rheological Analysis of The Aging Behavior of Short-Term Aged Pure And SBS-Modified Asphalt Binders (Research Article) Kısa Dönem Yaşlandırılmış Saf ve SBS Modifiyeli Asfalt Bağlayıcıların Yaşlanma Davranışlarının Reolojik Araştırması (Araştırma Makalesi) <b>Ahmet Münir ÖZDEMİR</b>	276
Transfer Learning Based Damage Detection in Public Areas (Research Article) Kamusal Alanlarda Transfer Öğrenme Tabanlı Hasar Tespiti (Araştırma Makalesi) <b>Tuğçe KELEŞ, Süha TEMUR, Furkan KILINÇ, Mehmet V. GÜN, Şengül DOĞAN, Türker TUNCER</b>	290
Carbon Tax-Aware Optimal Energy Management for Grid-Integrated Parking Facilities with Electric and Fuel Cell Vehicles Supported by PV Generation (Research Article) Şebeke Entegreli Elektrikli Araç ve Hidrojenli Araçları İçeren Otoparklar İçin Karbon Vergisi Odaklı Optimal Enerji Yönetimi (Araştırma Makalesi) <b>Merve LORDOĞLU, Benu PRENCUVA, Eda Nur TAŞ, Ayşe Kübra ERENOĞLU TATAR</b>	307
Barrier Number Estimation with Machine Learning for Intrusion Detection in Wireless Sensor Networks (Research Article) Kablosuz Sensör Ağlarında Saldırı Tespiti İçin Makine Öğrenimiyle Bariyer Sayısı Tahmini (Araştırma Makalesi) <b>Nisanur ÇAKAN, Duygu KAYA</b>	322
Assessment of Biogas Potential in Batman and Its Economic Comparison with Alternative Energy Sources (Research Article) Batman'daki Biyogaz Potansiyelinin Değerlendirilmesi ve Alternatif Enerji Kaynakları ile Ekonomik Karşılaştırması (Araştırma Makalesi) <b>Süleyman ATILGAN, Umut ERCAN, Muzaffer ALIM</b>	337
Performance of Transformer-Based Methods on Restaurant Reviews Analysis (Research Article) Transformer Tabanlı Yöntemlerin Restoran Yorumlarının Analizi Üzerindeki Başarımı (Araştırma Makalesi) <b>Mücahit KARADUMAN, Muhammed B. BAYDEMİR, Muhammed YILDIRIM</b>	351
Analysis of Brushless DC Motor Sounds with Machine Learning Methods Using Wavelet Transform Based Features (Research Article) Dalgacık Dönüşümü Tabanlı Özellikler Kullanarak Fırçasız DC Motor Seslerinin Makine Öğrenmesi Yöntemleri ile Analizi (Araştırma Makalesi) <b>Bilal TEKİN, Turgay KAYA</b>	363
Flood Discharge Estimation in Ungauged Basins Using Synthetic Unit Hydrographs and GIS (Research Article) Akım Gözlemi Olmayan Havzalarda Sentetik Birim Hidrograf Yöntemleri ve CBS Kullanılarak Taşkın Debilerinin Tahmini (Araştırma Makalesi) <b>Erdal KESGİN</b>	375
Classification of Cervical Vertebral Maturation Stages and Bone Age Assessment Using Transfer Learning-Based Deep-Learning Approaches (Research Article)	

Transfer Öğrenme Tabanlı Derin Öğrenme Yaklaşımlarıyla Servikal Vertebra Matürasyon Safhalarının Sınıflandırılması ve Kemik Yaşı Değerlendirilmesi (Araştırma Makalesi)

**Mazhar KAYAOĞLU, Abdülkadir ŞENGÜR, Sabahattin BOR, Seda KOTAN**

**393**

Thermodynamic Performance Evaluation of a Two-Stage Cascade Refrigeration System Using Parametric Analysis and Support Vector Machine Algorithm (Research Article)

Parametrik Analiz ve Destek Vektör Makinesi Algoritması Kullanılarak İki Kademeli Kaskad Soğutma Sisteminin Termodinamik Performans Değerlendirmesi (Araştırma Makalesi)

**Oğuzhan PEKTEZEL**

**406**

A Building Information Modeling Based Automated Rule-Checking Application for Zoning Regulation Compliance: The Case of Türkiye (Research Article)

İmar Mevzuatına Uygunluk Denetimi için Yapı Bilgi Modellemesi Tabanlı Otomatik Kural Kontrolü Uygulaması: Türkiye Örneği (Araştırma Makalesi)

**Cengiz YILMAZ, Hüseyin Atilla DİKBAŞ**

**424**

Machine Learning Approaches in Medical Data Processing: A Proposal for an Intelligent Stroke Diagnosis System (Research Article)

Medikal Veri İşlemede Makine Öğrenme Yaklaşımları: Felç için Akıllı Teşhis Sistemi Önerisi (Araştırma Makalesi)

**Azra Şilan PERİ, Nida KATI, Ferhat UÇAR**

**446**



## Fotovoltaik Bir Güneş Panelinin Termal Performansını Arttırmak için Deneyisel ve Sayısal Uygulamalar

Murat ÇATALKAYA<sup>1\*</sup>  

<sup>1</sup>Teknik Bilimler Meslek Yüksek Okulu, Kahramanmaraş Sütçü İmam Üniversitesi, Kahramanmaraş, Türkiye.

<sup>1</sup>[muratacalkaya@ksu.edu.tr](mailto:muratacalkaya@ksu.edu.tr)

Geliş Tarihi: 16.07.2024  
Kabul Tarihi: 30.01.2025

Düzeltilme Tarihi: 7.10.2024

doi: <https://doi.org/10.62520/fujece.1517038>  
Araştırma Makalesi

Alıntı: M. Çatalkaya, “Fotovoltaik bir güneş panelinin termal performansını arttırmak için deneyisel ve sayısal uygulamalar”, Fırat Üni. Deny. ve Hes. Müh. Derg., vol. 4, no 2, pp. 226-244, Haziran 2025.

### Öz

Son zamanlarda küresel ısınmanın etkileri, fosil yakıtlara alternatif olarak yenilenebilir enerji kaynaklarına olan ilgiyi artırmaktadır. Bu kaynaklar içerisinde güneş enerjisi, potansiyeli sebebiyle ayrı bir öneme sahiptir. Fotovoltaik (PV) paneller güneş enerjisini elektrik enerjisine dönüştürür. Fotovoltaik panellerle elektrik üretmenin en büyük sorunlarından biri, panel yüzeyine gelen enerjinin yaklaşık %80'inin ısıya dönüşmesidir. Bu dönüşüm sırasında PV panel yüzeyinde meydana gelen sıcaklık artışı panel verimliliğini olumsuz etkilemektedir. Dolayısıyla, panellerin verimli çalışabilmesi için soğutulması, çözülmesi gereken bir problem haline gelmektedir. Bu çalışmada; Kahramanmaraş iklim koşullarında monokristal PV panelin pasif soğutma üzerindeki etkilerini incelemek için sayısal analiz yöntemleri geliştirilmiştir. Öncelikle incelenecek olan fotovoltaik güneş panelinin performansı deneyisel olarak araştırılmıştır. Yapılan deneylerde ortalama panel yüzey sıcaklığı 43.54°C , güneş ışınımı ve panel gücü sırasıyla 785 W/m<sup>2</sup>, 36.32 W bulunmuştur. Daha sonra sayısal analiz için ANSYS-Fluent yazılımı kullanılmıştır. Yapılan hesaplamalı akışkanlar dinamiği (HAD) analizleri için en uygun çözüm ağı yapısını belirlemek üzere deneyisel veriler kullanılmış ve Ansys programında yüzey sıcaklığı için yapılan PV panelin HAD modeli 2.44% hatayla model oluşturulmuştur. HAD modeline deneyisel çalışma senaryolarında çeşitli kanat boyutları ve kanatlar arasında ki mesafenin PV panel yüzeyinde ki soğutma ya olan etkili incelenmiştir. HAD analizleri sonucunda kanat geometrisine nazaran, kanatlar arasında ki mesafede ki yaklaşık %40 lik (5mm) artışta kanat uç sıcaklığında yaklaşık 4°C bir azalma elde edilmiştir.

**Anahtar kelimeler:** Monokristal güneş paneli, Kanatçık, HAD, PV panel, Isı transferi

\*Yazışılan Yazar



## Experimental and Numerical Applications to Increase Thermal Performance of a Photovoltaic Solar Panel

Murat ÇATALKAYA <sup>1\*</sup>  

<sup>1</sup>Vocational School of Technical Sciences, Kahramanmaraş Sütçü İmam University, Kahramanmaraş, Turkey.

<sup>1</sup>[muratacatalkaya@ksu.edu.tr](mailto:muratacatalkaya@ksu.edu.tr)

Received: 16.07.2024

Accepted: 30.01.2025

Revision: 7.10.2024

doi: <https://doi.org/10.62520/fujece.1517038>

Research Article

Citation: M. Çatalkaya, "Experimental and numerical applications to increase thermal performance of a photovoltaic solar panel", *Firat Univ. Jour. of Exper. and Comp. Eng.*, vol. 4, no 2, pp. 226-244, June 2025.

### Abstract

Recently, the impact of global warming has intensified interest in renewable energy sources as alternatives to fossil fuels. Among these resources, solar energy stands out due to its potential. Photovoltaic (PV) panels play a crucial role in converting solar energy into electrical energy. However, one of the biggest challenges in generating electricity with PV panels is that approximately 80% of the energy from the panel surface is transformed into heat. This temperature increase on the PV panel surface negatively affects its efficiency, making it essential to find effective cooling solutions. In this study, we developed numerical analysis methods to investigate the effects of monocrystalline PV panels on passive cooling under the climatic conditions of Kahramanmaraş. First, we performed experimental investigations to assess the performance of the photovoltaic solar panels. The experiments revealed an average panel surface temperature of 43.54°C, with solar radiation and panel power measuring 785 W/m<sup>2</sup> and 36.32 W, respectively. We then employed ANSYS Fluent software for numerical analysis. The experimental data were utilized to determine the most suitable solution network structure for computational fluid dynamics (CFD) analyses, resulting in a CFD model of the PV panel with a surface temperature error of just 2.44%. The CFD model was used to examine how different fin sizes and distances between fins affected cooling on the PV panel surface. The CFD analysis indicated that increasing the distance between the fins by approximately 40% (5 mm) led to a reduction of about 4°C in fin tip temperature compared to the original fin geometry.

**Keywords:** Monocrystalline solar panel, Heatsink, CFD, PV panel, Heat transfer

---

\*Corresponding author



## 1. Introduction

Today, the increase in energy demand obtained from fossil fuels increases the interest in renewable energy sources as an alternative to fossil fuels. Among these sources, Solar energy, which stands out with its unlimited energy potential, has a significant place [1]. Solar energy is collected with the help of thermal panels or solar collectors and is used for many purposes. One of the common uses of solar energy is its direct conversion into electrical energy. Photovoltaic (PV) panels are used for this conversion. To use PV panels efficiently, it is necessary to determine their operating conditions well. The efficiency of PV panels depends on factors such as surface contamination, shining, the panel's position relative to the sun, cell type, and temperature [2]. PV panels absorb a significant portion of the energy from the sun. However, Only 15-20% of this energy, given out as heat, can be converted into electrical energy [3]. As the PV panel collects energy from the sun, the temperature on its surface increases. This negatively affects the panel's electricity production and reduces its efficiency. Therefore, for PV panels to become more efficient in electricity production, dissipating the heat on their surfaces becomes a problem that needs to be solved [4-5]. Various methods exist to solve the cooling problem of reducing the surface temperature of PV panels [6]. These are active cooling and passive cooling strategies. Active cooling converts a coolant into intermediate fluid using mechanical heat pipes or pumps [7]. In passive cooling, another cooling technique, heat is removed from the hot surface only by natural heat transfer without an active component [8-9]. Air-cooled fins are often preferred in the passive cooling method. The heat on the fins is evacuated from the system by passing to the air filtering through them. Thanks to these fins placed on the bottom surface of the PV panel, the heat transfer surfaces are increased, and the cooling capacity is increased [10]. It is essential to determine an effective cooling method for PV panels and to design them according to this method. In this context, experiments must be conducted after going through various experimental setups' design and manufacturing processes for the specified cooling systems. This requirement is a challenging process to overcome in terms of time and cost. These processes can be more efficient thanks to programs that perform computational fluid mechanics (CFD) analysis. Thanks to CFD programs, the behavior of systems is observed by analyzing them under various scenarios at the design stage before reaching the manufacturing stage [11].

The main goal of this research is to increase the efficiency of a monocrystalline PV panel under passive cooling by using a heatsink with specific parameters under Kahramanmaraş's climatic conditions. For this purpose, experimental studies were conducted in the ambient temperature range of 25-55 °C. Based on the data obtained from experimental studies, the panel's CFD model was created using the Ansys program. Fins of various sizes were applied to the CFD model, and temperature distributions were observed on the panel surface. With the help of CFD analyses supported by experimental parameters, the effects of the change between blade spacing, blade thickness, and blade height on PV panel surface cooling were examined.

## 2. Passive Cooling and Heatsink

Passive cooling methods, which operate without additional energy input, are simple yet effective in enhancing heat transfer through natural convection to cool PV panels. In passive cooling, the heat is effectively transferred from the heat source, such as a PV panel, to the outside air and then distributed to the environment. The three main categories of passive cooling techniques, namely passive air cooling, passive water cooling, and passive conductive cooling, are all simple to implement [12]. This study specifically focuses on the simplicity of passive air cooling and using a heatsink. Thermal fins, a simple and cost-effective solution for cooling PV panels, require minimal maintenance and consume no electricity. A heatsink, typically made of metal, is designed to significantly increase heat transfer from its source to the surroundings through natural or forced convection [13-15]. It is engineered to enhance heat dissipation and contact area with ambient air for efficient heat transfer. Natural convection, which occurs when cooling air moves across the fin array due to pressure or temperature differences, further enhances the simplicity of these techniques. Optimal heat transfer is achieved within a limited spacing range for high fins, whereas shallow fins benefit from a more extensive range [16-17]. To identify the most effective fin design, it is essential to conduct a heat transfer analysis for the simplest case. Figure 1 beautifully illustrates a surface adorned with a single fin, radiating heat into the surrounding air through unforced convection. Here,  $T_{\infty}$ -air signifies the air temperature, complemented by the air convective heat transfer coefficient [18].

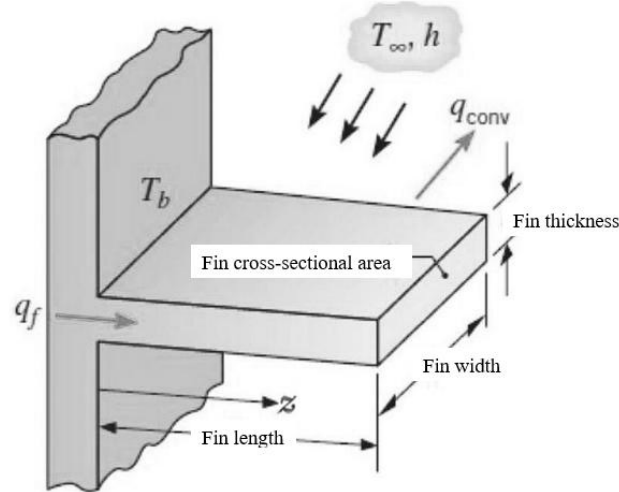


**Figure 1.** Surface with one fin [18]

Using the equations below, the total amount of heat to be transferred through the fins and its parameters can be calculated [18]. Equation 1 is expressed as the most general form of the total heat transfer relationship from the fin surface [19].

$$Q_T = Nq_f + \bar{h}A_b\Delta T \quad (1)$$

where  $A_b$  is non-finned surface (the base of the heat sink where there are no fins), Fourier's law is applied to the base of the fin to obtain  $q_f$ , and  $N$  is the total number of fins. Here,  $\bar{h}$  is the total convection heat transfer coefficient transferred from the fin surface and is calculated by Eq.2.

$$\bar{h} = \frac{\overline{N_{uH}}k_a}{H} \quad (2)$$

where  $N_{uH}$  is the Nusselt number and represents the dimensionless temperature gradient on the fin surface. The thermal conductivity of air at a given temperature is represented by  $k_a$ .  $H$  is the definitive characteristic length of the system.  $\overline{N_{uH}}$  is explicitly defined in terms of other Rayleigh and Prandtl numbers, as demonstrated in Eq. 3.

$$\overline{N_{uH}} = (Ra, Pr) \quad (3)$$

In Eq.3,  $Ra$  is Rayleigh and  $Pr$  is Prandtl number. Prandtl number as the ratio of momentum and thermal dissipations is defined. Rayleigh number is a dimensionless number that characterizes heat transfer in natural convection events. When the necessary simplifications are made, the heat transfer that will occur through a fin is obtained with the  $Ra$  number relation given in Eq. 4.

$$Ra = \frac{g\beta(T_b - T_\infty)H^3}{\nu^2} \cdot \frac{\nu}{\alpha} \quad (4)$$

At the junction between the heat sink and the PV panel, there is a resistance to heat transfer due to small air pockets between the surfaces. This resistance is reduced by using thermal interface materials (TIMs) to improve interface contact and reduce thermal resistance [18]. To provide effective passive cooling through the heatsink, materials with high thermal capacity and conductivity transfer thermal energy from the heat source and distribute heat efficiently to the environment. Aluminum alloys are commonly used for heatsinks

due to their favorable properties. Still, copper offers superior properties but requires unique manufacturing processes, such as milling, due to less forming properties or difficulty in machining operations. Typically, copper is also used by integrating it into the heatsink base, onto which aluminum fins are attached [20-21]. Heatsinks have emerged as a cornerstone in thermal management, celebrated for their versatile geometric designs. Among these, plate and pin shapes stand out as the most effective choices, balancing exceptional performance with cost efficiency and ease of production. The literature frequently highlights several fin types that excel in these applications, including the elegant Plate Fin, the robust Square Pin Fin, the efficient Round Pin Fin, and the innovative Stepped Round Pin Fin, all of which are beautifully illustrated in Figure 2.

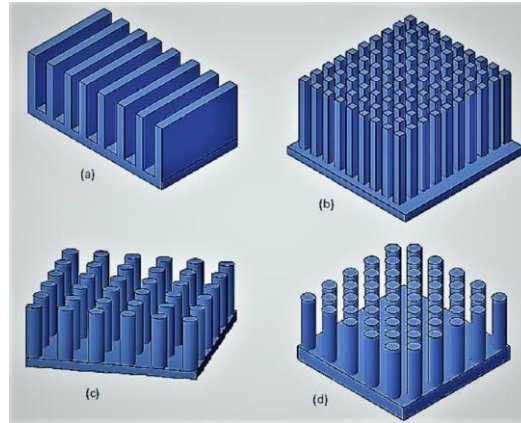


**Figure 2.** Various types of Heatsink; (a) Plate Fin (b) Square Pin Fin (c) Round Pin Fin (d) Stepped Round Pin Fin [22]

In a medium with limited thermal conductivity, as well as when heat is transferred to a large area, the distribution resistance must be taken into account, as it can lead to significant temperature gradients and uneven heat distribution [18].

It's important to note that uneven heat distribution, where some fins have lower temperatures than others, is a situation that needs to be avoided. Achieving even heat distribution is a key goal in the design and maintenance of PV panel systems, and this can be facilitated by strategies such as thickening the fin base.

Additionally, the effectiveness of a heat fin is important to note, which is greatly affected by the configuration of the PV panel system, including factors such as local climatic conditions, wind speed, and direction, solar panel height, orientation, fin geometry, etc. [21]. To achieve the cooling effect, increase the heat transfer from the back side of the PV panel [23]. Although increasing the thermal conductivity of the back sheet is one approach to achieve a cooling effect of up to 0.07°C, alternative methods need to be investigated [24]. Fourier's law of heat transfer is clear. Accordingly, assuming that the temperatures of the surroundings and the heat-radiating body are constant, the cooling effect can be increased by using a pump or fan to increase convection or by expanding the heat-radiation area to the surroundings [25]. This situation can be achieved using fins with additional rectangular or pin-shaped surfaces. It was carried out with the assumption that for every 1 °C increase in temperature on the PV panel, the electrical efficiency of the PV panel module decreases by 0.5% [26-27]. The effect of temperature on PV panel performance can also be explained as follows: PV panels start producing electricity when they receive radiation from the sun. While some of the radiation coming from the sun turns into electrical energy, some of it emerges as heat energy. This event causes the PV cells to heat up. As the PV cells heat up, the short circuit current (I) of the PV modules increases, while the open circuit voltage (V) decreases and thus the electrical efficiency decreases (Figure 3). Therefore, the cooling effect is significant for the PV panel.

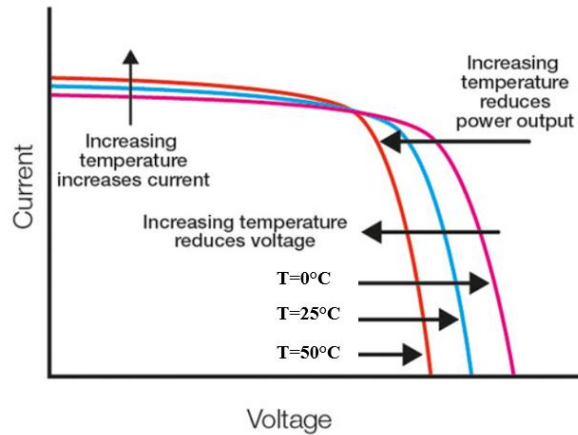


**Figure 3.** Effect of operating temperatures on PV panel performance [28-29]

### 3. Material and Methodology

To design an effective heatsink, modern approaches to design must be applied. These contemporary approaches require determining the temperature distribution characteristics of the designs and making designs considering these features. It is essential to conduct experimental studies to observe or evaluate the effectiveness of design results. However, experimental studies are methods that require both time and cost. In addition, situations such as lack of equipment and limited opportunities occur in experimental studies. For all these negative reasons, CFD simulation programs are used. By performing virtual modeling using experimental conditions in CFD simulations, high-quality solutions are obtained for the behavior of designs under flexible physical conditions [30]. Thus, it saves time and experimental expenses [31-32]. In this study, experimental studies were carried out under passive cooling conditions using monocrystalline panels to test the accuracy of CFD analyses and determine the PV panel's characteristic properties. Experimental study results: CFD simulations were used to numerically simulate the heat distribution on the panel and the cooling effect of the fins on the panel. Fin analysis in 9 different sizes was performed in the CFD environment. As a result of CFD studies, fin dimensions, adequate fin spacing, fin thickness, and distance between fins on the fin surface temperature distribution were determined.

#### 3.1 Material

##### 3.1.1. Solar panel module

The solar panel examined in this study is a monocrystalline module produced by Uretech company that can produce 50 W (watt peak) power. Table 1 shows the features of the solar panel module used in the study.

**Table 1.** Solar module features

Features	Values
Photovoltaic Panel	Mono-crystalline 159x39 mm
Number of Cells	36
Open-Circuit Voltage (VOC)	24.62 V
Short-Circuit Current (ISC)	2.57A
Maximum Power (PMPP)	50W
Operating Temperature Range	-20°C / 80°C
Dimensions	662x159x25mm

In Figure 4, the solar panel is designed in layers. Each layer used serves a different purpose. At the top, the panel used Ethylene Tetrafluoroethylene (ETFE) instead of tempered glass. ETFE was chosen due to its low



weight, higher transparency, and ability to make the laminated panel flexible. ETFE cells are free of dirt, etc. It serves the purpose of protection from external factors. Underneath the ETFE layer, it was used as a protective base on which a thin layer of Ethylene-Vinyl Acetate (EVA) was spread. EVA is a specially manufactured material used to bond the panel layers together. This bonding process is done using the lamination technique. The cells were placed between two EVA sheets, with dimensions of 159x39 mm and 36 cells. Under the EVA layer under the cells is a Polyethylene Terephthalate (PET) layer made of insulated plastic material. On the bottom layer of the panel, other layer series are fixed with a frame on a Carbon Fiber Composite Polymer (CFRP) plate. An aluminum frame was placed around the layers to hold all the layers together.

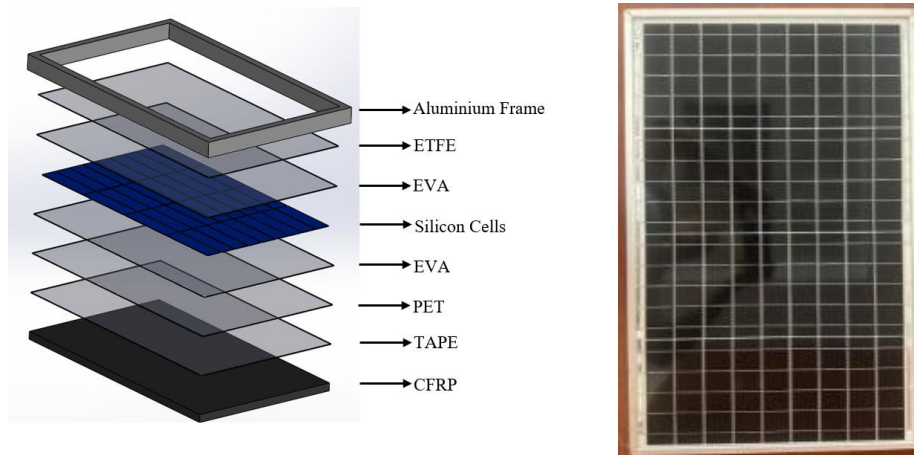


**Figure 4.** View of the layers of the monocrystalline PV Solar Panel used in the study

### 3.2. Method

The study covers two methods. The first of these is experimental studies to determine the characteristic features of the PV panel and to determine the accuracy of CFD analyses.

The second method is CFD analysis. ANSYS was used as the CFD program in numerical methods. Ansys models the system using fluid mechanics equations as well as heat and mass flow with finite element analysis.

#### 3.2.1 Experimental procedure

This study presents a thoughtfully designed experimental setup aimed at gathering insightful data and evaluating the performance of a solar panel. At the heart of the experiment is a high-quality monocrystalline photovoltaic (PV) panel. The panel's positive and negative terminals were expertly connected to a data acquisition socket via a robust cable, allowing for precise measurement of current and voltage. For this purpose, an ammeter was utilized to capture the DC current, while a voltmeter ensured accurate voltage readings.

In addition to the monocrystalline panel, the experimental design featured a 50 W polycrystalline PV panel, complemented by a multimeter to facilitate current and voltage measurements. To enrich the study even further, instruments were employed to monitor essential meteorological parameters, including temperature, air velocity, and solar radiation. This comprehensive approach not only underscores the rigor of the investigation but also enhances our understanding of solar panel performance under varying conditions. The panel in the experimental set is placed on the ground in such a way that it receives the sun's rays in the best way during the day. A dummy load of 2.5 ohms was included in the panel to obtain the current draw generated from the PV panel. The measurements required for the study were determined by manual readings every hour. To measure the power generated by the PV panel system, current-voltage values were obtained by

observing the multimeter display connected to the dummy load. Figure 5 shows the schematic of the experimental setup.

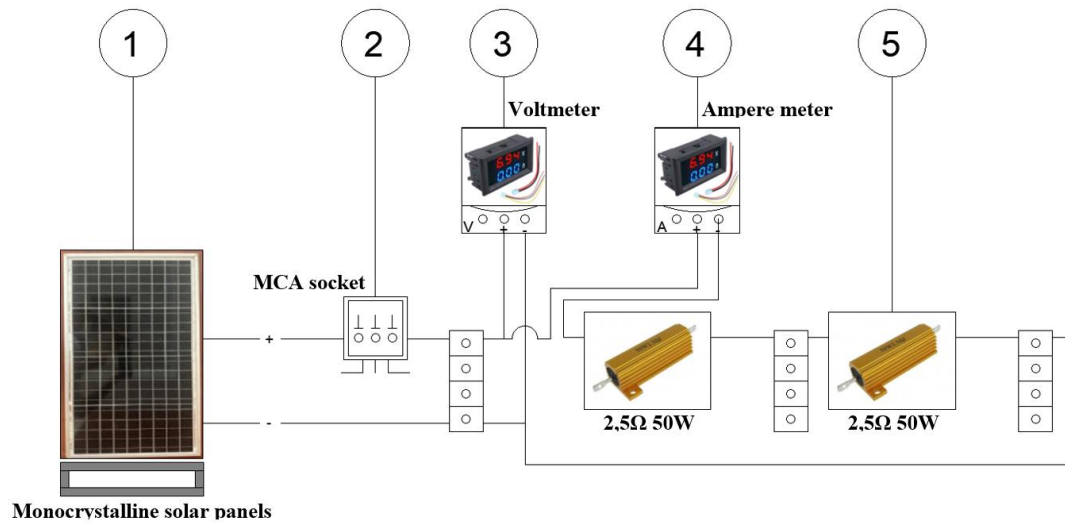


**Figure 5.** Schematic view of the experimental system.

This research used a monocrystalline PV solar panel measuring  $622 \times 393 \times 20$  mm. A precision Testo 875-2 irradiance meter was used to measure incident solar radiation. To measure the temperature and average temperature of the PV panel, it was monitored for a certain period using an infrared laser thermometer with a sensitivity of  $\pm 2^\circ\text{C}$ , model Uni-T UT306. The wind speed under the PV panel was measured using an anemometer with a Testo 405-V1 model sensitivity of  $\pm 0.1$  m/sec and a measurement range of  $0 \dots 10$  m/sec ( $0 \dots +50^\circ\text{C}$ ).

Furthermore, the comprehensive performance of the PV panel was measured by recording the instantaneous power, current and voltage values. This was done using a Wattmeter, Ammeter and Voltmeter, which are standard devices for such measurements. The devices used and the experimental process are shown in Figure 6.

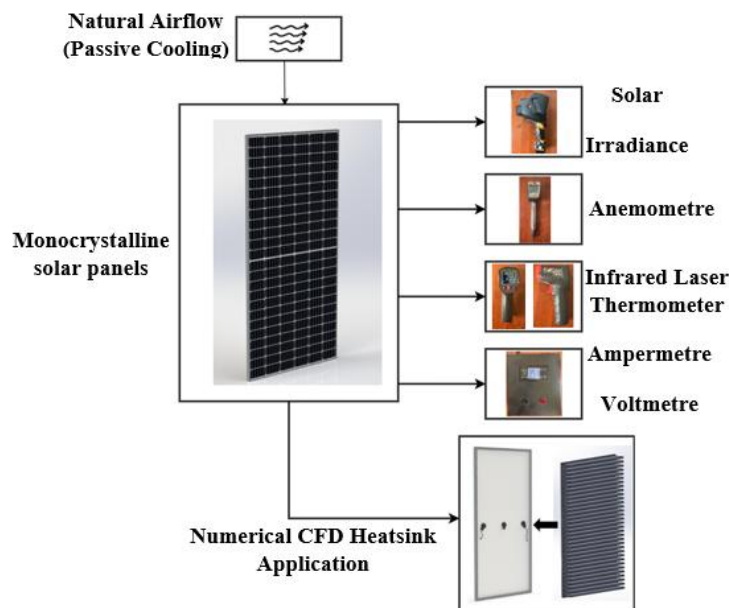


**Figure 6.** Experimental setup schematic configuration of PV panel

As shown in Figure 6, an infrared laser temperature meter was used to measure the surface temperature of the PV panel. An Anemometer was used to measure the speed of the air passing around the panel and a Solar Irradiance Meter was used to measure the radiation reaching the surface. In addition, a wattmeter was used to measure the amount of power that was generated by the panel during the experiment.

### 3.2.2 Numerical analysis procedure

In this section, numerical studies have been carried out to analyze the convective heat transfer of the PV panel and the heatsink to be placed on the bottom surface of the panel. Numerical studies were carried out in Ansys Fluent as steady-state CFD analysis. Since this analysis was performed to investigate thermal changes for conditions over a certain period of time, steady-state thermal analysis was chosen.

#### PV panel

In this study, geometry models were created in 6 layers, each 662x393 mm, using Ansys's Design Modeler Module. The cells in the PV panel are rectangular, with dimensions of 159x39 mm, and are modeled as 36 pieces. The appropriate material type and thickness of the layers used in the numerical study are given in Tables 2 and 3. In the analysis, the connected contacts that allow complete transfer of heat between layers were modeled by taking into account.

**Table 2.** Properties of the layers of the PV panel [33]

Layer	Material	Layer thickness(mm)
1	ETFE	0.28
2	EVA1	0.20
3	Silicon	0.15
4	EVA2	0.20
5	PET	0.20
6	Tape	0.13
7	CFRP	2.00

**Table 3.** Physical and thermal properties of the materials selected for the layers of the PV panel [33]

Material	Density (kg/m <sup>3</sup> )	Thermal conductivity (W/(m·K))	Specific heat (J/(kg·K))
ETFE	1730	0.24	1172
EVA	945	0.35	2090
Silicon	2330	148	700
PET	1350	0.275	1275
Tape	1012	0.19	2000
CFRP	2770	177	875

The intricate 3D models essential for performing CFD analyses of the PV panel utilized in the experiments are elegantly showcased in Figures 7 and 8. The thermal fin model is shown in Figure 7a. Figure 7b shows the geometry consisting of PV panels without thermal fins. Figure 8 shows the dimensions of the PVC panel used and the cells on the panel.

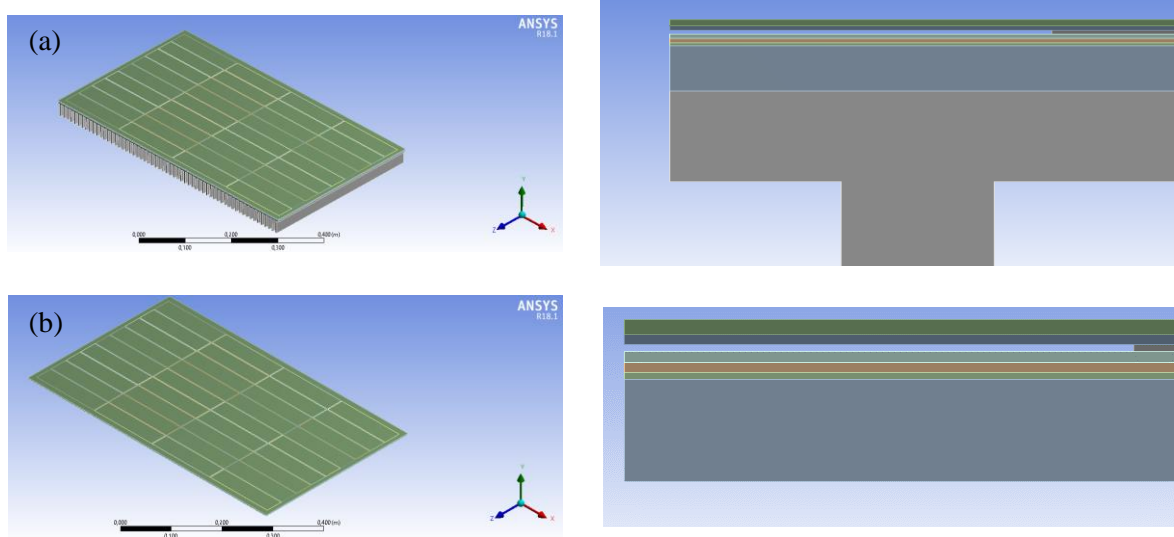


**Figure 7.** (a) PV panel with fin and (b) without thermal fins

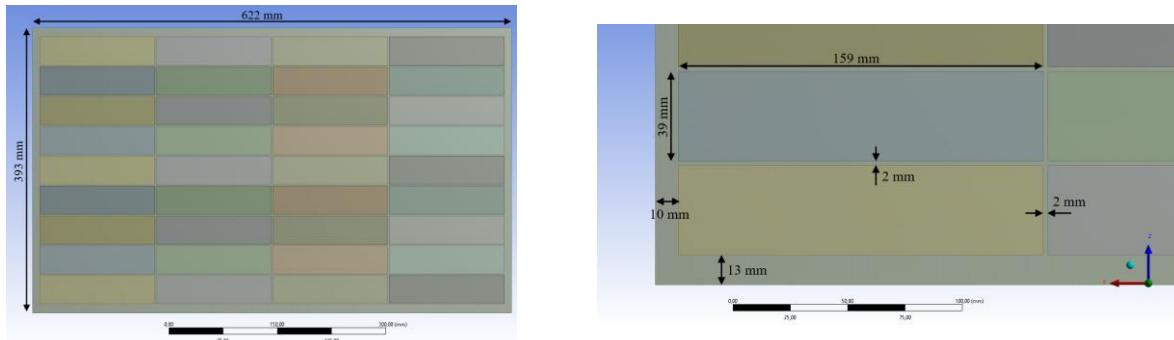


**Figure 8.** PV panel geometry

## Heatsink

In order to examine the effect of fin height, fin width and distance between fins on heat transfer, three different levels were determined for each parameter during design and other parameters were kept constant. In the finite element analyses, three different blade heights (30 mm - 40 mm - 50 mm), two different blade widths (4 mm - 7 mm) and two different distances between blades (7 mm -12 mm) were determined as variable parameters. Table 4 shows the experimental design set and dimensional values.

**Table 4.** Dimensions of fins

Model name	(mm)	b (mm)	w(mm)
HS3047	30.00	4.00	7.00
HS3077	30.00	7.00	7.00
HS30712	30.00	7.00	12.00
HS4047	40.00	4.00	7.00
HS4077	40.00	7.00	7.00
HS40712	40.00	7.00	12.00
HS5047	50.00	4.00	7.00
HS5077	50.00	7.00	7.00
HS50712	50.00	7.00	12.00



As seen in Table 4, the fin height is indicated by  $h$ , the finspan is indicated by  $b$  and the distance between fins is indicated by  $w$ . The geometries of the finlets are given in Figure 9. CFD analyzes of the fins were carried out only for the regions where the maximum temperature of the PV panel was achieved [18].

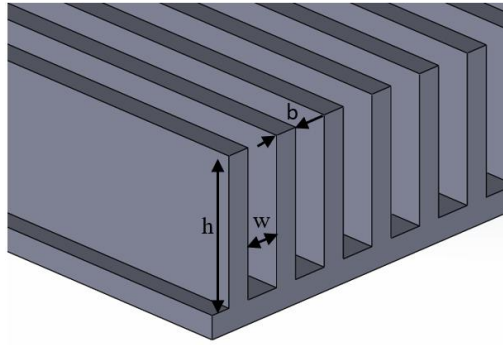


Figure 9. Fin geometry

### Mesh structure

For the numerical solution, the network model was created as a multizone. Network models were created in three different sizes: Model-1, Model-2, and Model-3, respectively, with the dimensions used in the network sensitivity study being 2.5 mm, 3.5 mm, and 4.5 mm. Network sizes are not uniform across the solution domain. In CFD simulations, the solutions' accuracy, rapid convergence, and stability largely depend on the network quality. Mesh quality is defined by many methods, the most common of which is the skewness value. Generally, skewness is a function of the angle between any two sides forming the cell. In CFD studies, the skewness value should be below a maximum of 0.95 and the orthogonal quality value should be greater than 0.15 [34]. Detailed information about the dimensions of the solution network structure is given in Table 5. Table 5 gives skewness and orthogonal quality values for 3 different models. It is clearly seen that the quality values for all three models are within acceptable limits. The image obtained after the mesh process is given in Figure 10.

Table 5. Mesh statistics

Model number	Number of elements	Maximum mesh size (mm)	Average skewness value	Maximum skewness value	Average orthogonal quality value
Model-1	581964	2.5	5.76e-002	0.63	0.96
Model-2	316271	3.5	8.74e-002	0.85	0.94
Model-3	141904	4.5	3.28e-002	0.58	0.98

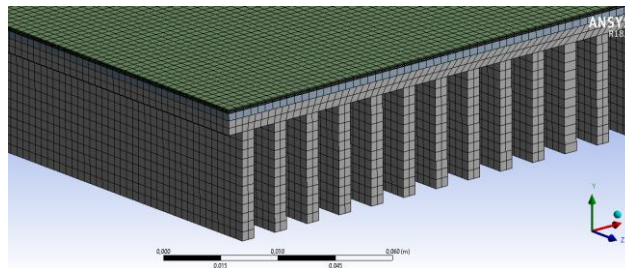


Figure 10. 3D MESH Model domain

### Boundary conditions

In this study, the boundary conditions used for the numerical CFD analysis of the PV Panel can be summarized as follows: The airflow is 3D, and analyses were performed at constant temperature. Air

temperature was obtained from experimental data for a specific day and time. Air distribution on the PV panel is the same everywhere. Side surfaces are entirely insulated. The radiation boundary condition for the upper surface is defined. k-ε was chosen as the turbulence model, and the turbulent viscosity ratio is 5% and 10%, respectively. The flow is assumed to be incompressible. The analyses were solved by considering steady-state conditions for specific hours during the day. The boundary condition in the outlet region is defined as the pressure outlet. The boundary conditions in the study were handled in accordance with the experimental conditions. The experimental studies were carried out in accordance with the PV panels used in the industry.

For the CFD analysis, we employed the powerful mesh-based ANSYS. This tool facilitated a comprehensive analysis of the numerical data by dividing the model into simpler regions [35]. The study involved solving the Navier-Stokes (N-S), energy, continuity, and turbulence equations numerically, under the specified boundary conditions, to simulate the heat transfer process between the air and the fin [36]. CFD solution equations used in numerical analysis are Equations. It is given in Equations 5-12.

N-S equations in x, y and z directions can be expressed in Eq.5-7.

$$\nabla(\rho \cdot \vec{U} \cdot u) = -\frac{\partial p}{\partial x} + \frac{\partial \tau_{xx}}{\partial x} + \frac{\partial \tau_{yx}}{\partial y} + \frac{\partial \tau_{zx}}{\partial z} \quad (5)$$

$$\nabla(\rho \cdot \vec{U} \cdot v) = -\frac{\partial p}{\partial y} + \frac{\partial \tau_{xy}}{\partial x} + \frac{\partial \tau_{yy}}{\partial y} + \frac{\partial \tau_{zy}}{\partial z} \quad (6)$$

$$\nabla(\rho \cdot \vec{U} \cdot w) = -\frac{\partial p}{\partial z} + \frac{\partial \tau_{xz}}{\partial x} + \frac{\partial \tau_{yz}}{\partial y} + \frac{\partial \tau_{zz}}{\partial z} \quad (7)$$

Here  $\rho$  is the density of the fluid, ( $u$ ,  $v$  and  $w$ ) are the velocity components in three directions,  $U$  is the air velocity,  $\tau$  is the viscous stress tensor and  $p$  is the pressure.

The energy equation in Eq.8 is;

$$\nabla(\rho \cdot h \cdot \vec{U}) = -p \nabla \vec{U} + \nabla(k \nabla T) + \delta + S_h \quad (8)$$

In Eq.8,  $h$  represents the total enthalpy,  $\delta$  denotes the dissipation term,  $k$  signifies the thermal conductivity,  $T$  stands for the temperature, and  $S_h$  indicates the thermal source term.

The continuity equation in Eq.9 is;

$$\nabla(\rho \cdot \vec{U}) = 0 \quad (9)$$

The turbulence solver realizable k-ε equations used in this study are given below in their general form [35-37].

Turbulence Kinetic Energy (k) equation in Eq.10;

$$\frac{\partial}{\partial x_j}(\rho k u_i) = \frac{\partial}{\partial x_i} \left[ \left( \mu + \frac{\mu_t}{\sigma_k} \right) \frac{\partial k}{\partial x_i} \right] + G_k + G_b - \rho \epsilon \quad (10)$$

Loss Rate (ε) equation in Eq.11;

$$\frac{\partial}{\partial x_i}(\rho \epsilon u_i) = \frac{\partial}{\partial x_j} \left[ \left( \mu + \frac{\mu_t}{\sigma_\epsilon} \right) \frac{\partial \epsilon}{\partial x_i} \right] + \rho C_1 - \rho C_2 \frac{\epsilon^2}{k + \sqrt{\nu \epsilon}} + C_{1\epsilon} \frac{\epsilon}{k} C_{3\epsilon} G_b \quad (11)$$

Turbulence viscosity equation in Eq.12;

$$C_1 = \max \left[ 0.43, \frac{\eta}{\eta + 5} \right], \rightarrow \eta = S \frac{k}{\epsilon}, \rightarrow S = \sqrt{2 S_{ij} S_{ij}} \quad (12)$$

The constant values used in the turbulence model of this study are as follows;

$$(C_{1\varepsilon} = 1.44), (C_2 = 1.9), (\sigma_k = 1.0)(\sigma_\varepsilon = 1.2)$$

## 4. Result and Discussion

### 4.1. Experimental result

Experiments with monocrystalline PV panels were carried out in Kahramanmaraş province, under passive cooling, in May, and solar radiation values varying according to hours are shown in Figure 11. Measurements were made between 9:00 and 17:00 local time, and the highest radiation values of 1010 W/m<sup>2</sup> were recorded at noon. In the calculations, the maximum radiation value falling on the PV panel was accepted as 1000 W/m<sup>2</sup>. The airspeed passing over the panel surface was recorded as 0.46 m/s during the experiments.

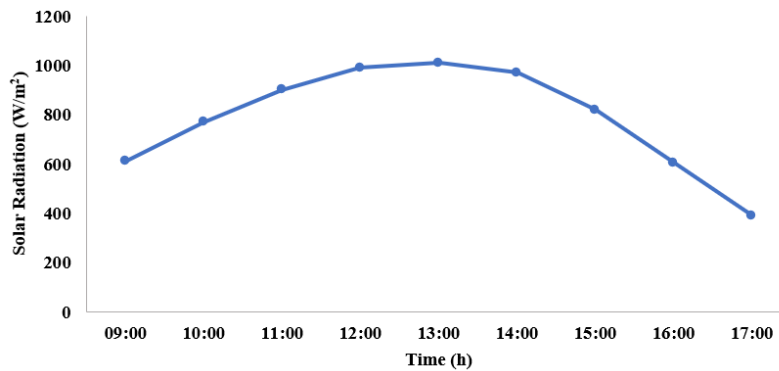


**Figure 11.** Kahramanmaraş solar radiation values varying according to hours in May

Figure 12 shows the variation graph of the surface temperatures of the PV panel under passive cooling throughout the day. As seen in the graph, the surface temperature of the panel reached a maximum of 50.856°C under passive cooling at around 13:00, when the temperature reached its highest level.

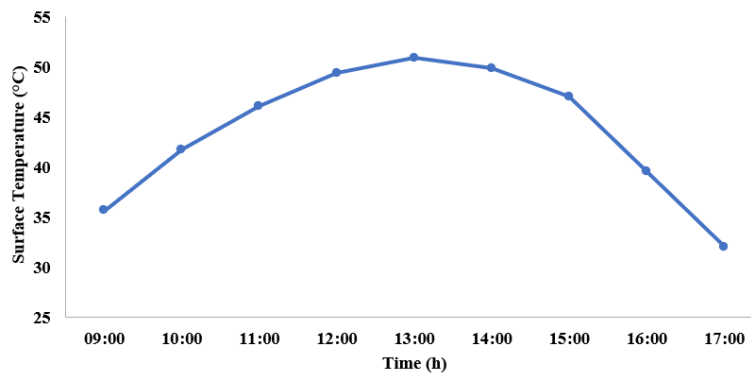


**Figure 12.** Change graph of surface temperatures of the PV panel under passive cooling throughout the day

Figure 13 shows the Current-Voltage and Power-Voltage characteristics of the PV Panel in a horizontal position under Passive air cooling, where the airspeed is 0.46 m/s. As seen in Figure 12, the current-voltage change at different operating temperatures can be seen. It is clearly seen that the voltage changes are inversely proportional to the increase in working surface temperature between 25°C and 55°C. For the PV panel used in the experimental system, the voltage drops approximately 0.3V for every 1°C temperature increase. As seen in Figure 12, it is clear that the PV panel used in the experiment reached maximum power at 25°C operating conditions. Power production varies inversely with the increase in temperature. In the experiments,

it is clearly seen that temperature is among the critical factors affecting the efficiency of monocrystalline PV panels.

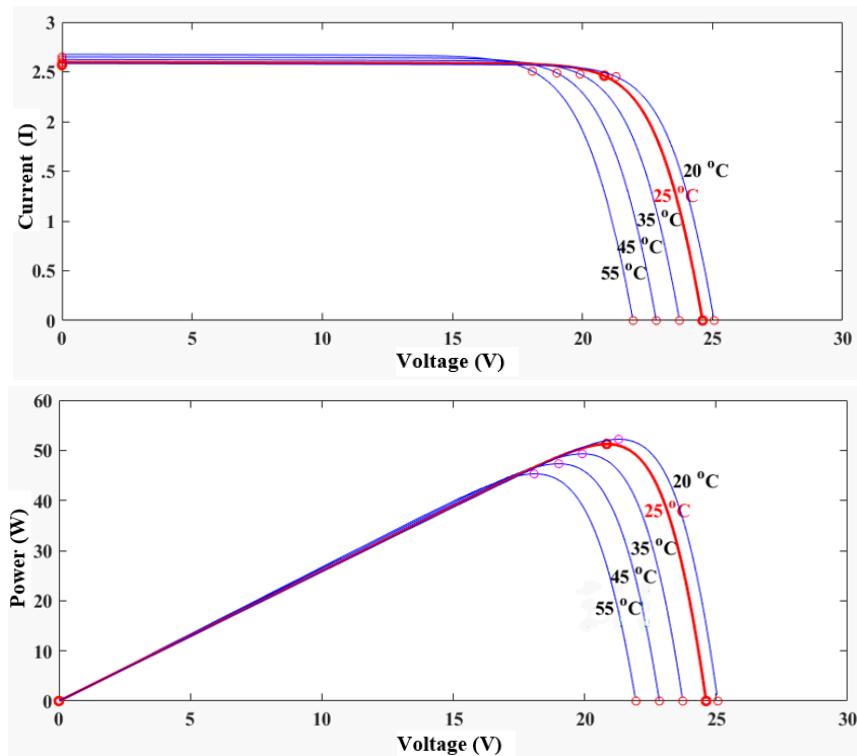


**Figure 13.** Current-Voltage and Power-Voltage characteristics of the PV Panel in horizontal position, under Passive air cooling where the air speed is 0.46 m/s

## 4.2 Numerical analysis result

This section includes the findings of thermal numerical studies to analyze the convective heat transfer of PV panels and a heatsink to be placed on the bottom surface of the panel. The study applied the network density test to select the optimum node and element sizes to obtain a reliable solution independent of the network size. A mesh density test was conducted for the PV panel to see the effect of the change in mesh size on the PV panel surface temperature at different times (Figure 14).

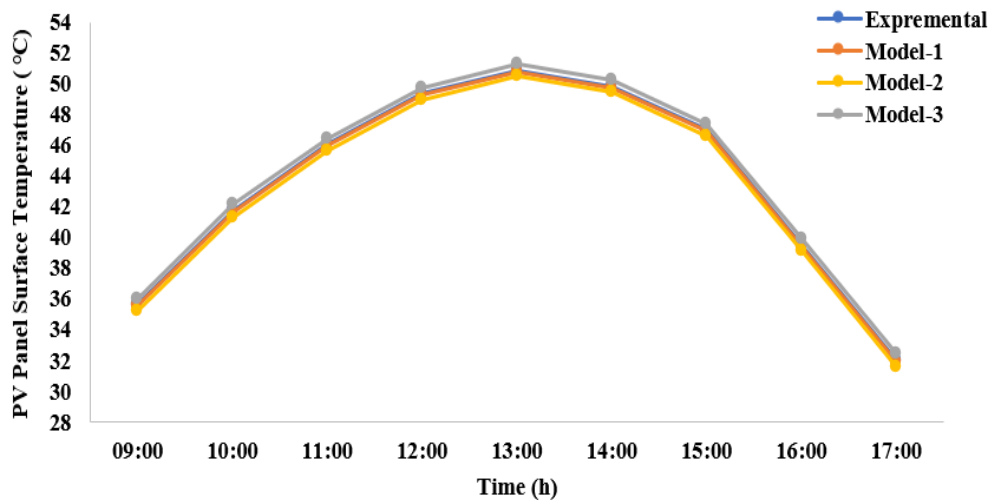
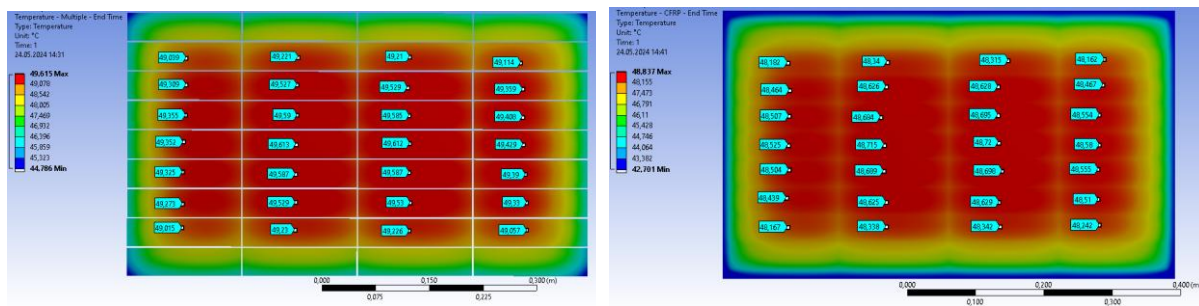


**Figure 14.** Graph showing the effect of mesh size on PV panel surface temperature at different times



In Figure 14, we observe a change in the mesh number from Model-1 fine size to Model-3 coarser size. This meticulous alteration affects the convergence of the PV Panel to the surface temperature. Despite this, all three models demonstrate a high degree of compatibility with the experimental results at specific time intervals. The error rate between the analysis in the mesh model created using Model-1 and the experimental data is less than 2.4%, a testament to the thoroughness of our simulation process.

Figure 15 (a) shows the temperature contours obtained to simulate the panel temperature under passive cooling at the desired boundary conditions of the PV panel for an air temperature of 32°C at 13:00. It is seen that the panel temperature varies around 49°C on the top and middle surface of the silicon cell layer responsible for electricity generation. The maximum cell temperature was obtained as 49.615°C. Experimentally, the max. The temperature was obtained as 50.856°C. Figure 15 (b) shows the temperature contours in the bottom CFRP layer as a result of simulating the panel temperature under passive cooling at the desired boundary conditions for the PV panel at 13:00. It is clearly seen that the temperature changes around 48°C on the upper and middle surface of the CFRP layer. Its maximum temperature was obtained as 48.837°C. Experimentally, the max. The temperature was obtained as 47.4°C.



(a)

(b)

**Figure 15.** (a) Temperature contours of the PV panel under passive cooling for 32°C air temperature at 13:00; (b) Temperature contours on the CFRP layer of the PV panel under passive cooling at 13:00

Numerical analysis studies of the fins were carried out based on the temperature distribution of the CFRP layer, which is the bottom layer of the PV panel. To obtain the temperature fields, CFD analyses of nine different heatsinks were simulated in the ANSYS FLUENT program (Figure 16). The CFD analysis calculates the average heat flux on the bottom region of the heatsink and the bottom surface of the PV panel, based on thermal analysis results. In addition to heat flux, the simulation also considers factors such as solar radiation and natural convection heat transfer to the fins. As illustrated in Figure 16, HS50712 features the longest blade length and the widest gap between the blades.

The fin model for HS50712 elegantly extends over a broader area, a testament to the influence of spreading resistance. In an intriguing comparison of temperature values at the tips of the finlets, the HS50712 model stands out with the lowest temperature, measured at a remarkable 300.2 K. Furthermore, the most striking temperature gradient between the base and tip is observed in the HS50712 fin model, showcasing its impressive thermal performance.

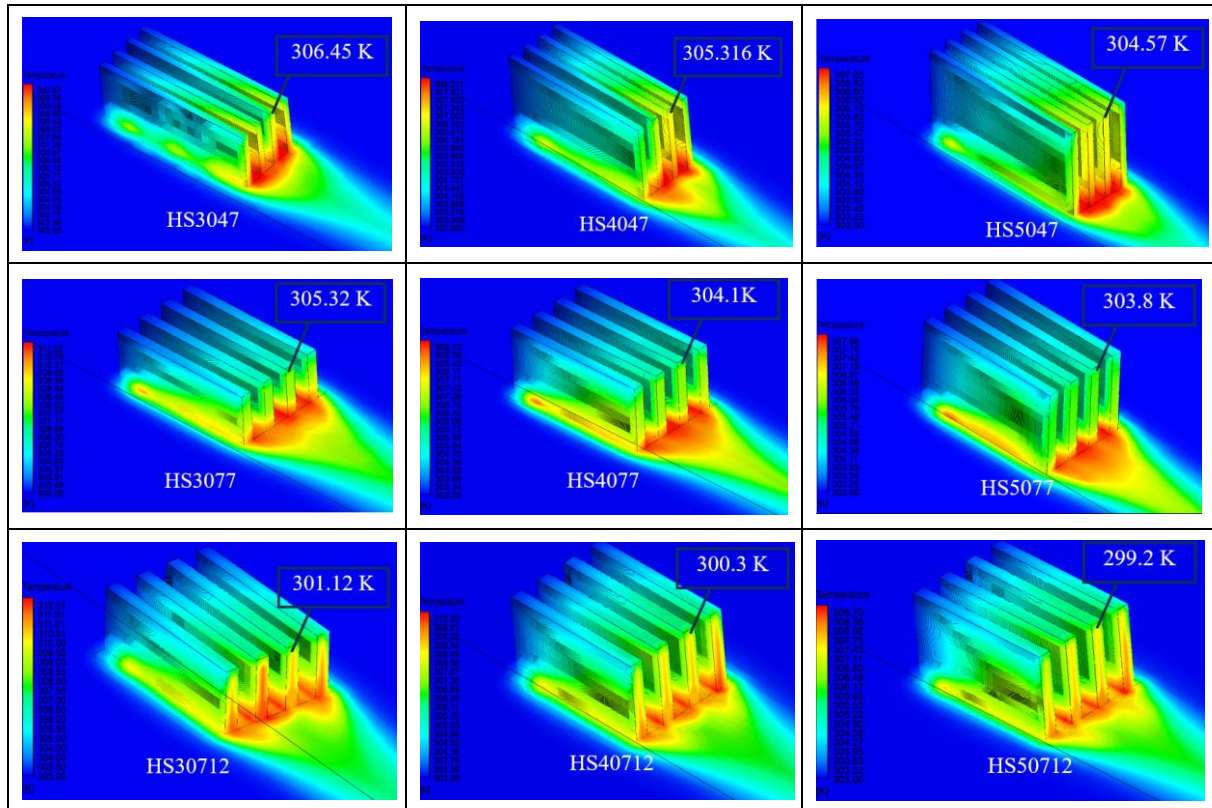


**Figure 16.** CFD analyzes nine different heatsinks to obtain temperature fields

In PV panels, 1°C change in surface temperature affects the panel efficiency by 0.5 [27]. As a result of the study, a cooling of 4°C is provided by optimizing the size of the fins placed on the bottom surface of the panel. In this case, an efficiency increase of 2% is achieved. Compared to similar studies in the literature, Amrizal et al. obtained a cooling of 1.25°C by changing the blade thickness and Reynolds number on the Pv panel [38]. Jing et al. obtained a 2°C decrease in surface temperature by changing the gaps between the blades [39].

## 5. Conclusion

In this study, experiments were carried out under Kahramanmaraş conditions using a monocrystalline PV solar panel, and the operating characteristics of the panel were determined. As a result of the experimental study, the panel efficiency used in the system examined was 1000 W/m<sup>2</sup>, while the thermal efficiency was obtained as 16.2%. This efficiency is clearly seen in the panel characteristic curves, where it decreases with increasing surface temperature of the panel surface. According to the data from the experiments, a 3D model of the PV panel was developed using ANSYS simulation software, and various CFD analyses were performed. The properties of the actual PV panel material, such as layer density, thermal conductivity, and specific heat capacity, created the CFD model of the panel. The PV panel model was simulated under the climate condition of Kahramanmaraş, where the ambient temperature at 13:00 was fixed at 32°C.

The experimental and simulation results in this study successfully converged, with a small error value of 2.4%. This convergence, a testament to the accuracy of the research process, was crucial in understanding and addressing the decrease in efficiency due to increasing surface temperature of the panel. To tackle this issue, CFD studies were conducted using the ANSYS program, ensuring the reliability of the findings.

In the CFD studies, heatsinks were applied to the PV panel to reduce the surface temperature under passive cooling. In the study, nine different heatsink sizes were used, and their thermal behavior was examined. The effect of the change in the size of the finlets was determined based on the temperature values at the fin tips. As a result of CFD analysis, it was observed that for the same fin width and distance between the fins, an

approximately 40% (10 mm) increase in fin height decreased the fin tip temperature by approximately 2°C. An increase of approximately 40% (3mm) in fin thickness showed a decrease of 1.16°C in tip temperature. With an increase of approximately 40% (5mm) in the distance between the fins, a decrease of approximately 4°C in fin tip temperature was achieved. As a result of the analysis, the lowest temperature value was obtained at 299.2K using the HS50712 fin type. In the future planning of this study, the most effective fin type for PV panel surface cooling will be produced as a result of numerical analysis, and surface temperatures and energy production performance will be investigated. The results will be compared with the numerical analysis results from this study.

## 6. Author Contribution Statement

In the study carried out, Author 1 contributed to the formation of the idea, making the design and literature review, evaluating the results obtained, obtaining the materials used and examining the results, spelling and checking the article in terms of content.

## 7. Ethics Committee Approval and Conflict of Interest

“There is no conflict of interest with any person/institution in the prepared article”

## 8. List of Abbreviations

$A_b$	: Cross section of the fin, $m^2$
CFD	: Computational fluids Dynamics
$g$	: Earth's gravity acceleration, $m/s^2$
$h$	: Air convective heat transfer coefficient,
$H$	: Characteristic length of the system, m
$k_a$	: Thermal conductivity of the air, W/m.K
$N$	: Total number of fins
$N_{uH}$	: Nusselt number
N-S	: Navier-Stokes
Pr	: Prandlt number
PV	: Photovoltaic
$q_f$	: energy transferred through the whole fin,
$Q_T$	: Total heat transfer, W
Ra	: Rayleigh's number
$T_\infty$	: Air temperature, K
$T_b$	: The temperature of the base of the fin, K
$\alpha$	: Thermal diffusivity of the fluid, $m^2/s$
$\beta$	: Thermal expansion coefficient, $K^{-1}$
$\Delta T$	: Temperature difference, K
$\nu$	: Kinetic viscosity, $m^2/s$
$\rho$	: Air density, $kg/m^3$

## 9. Ethical Statement Regarding the Use of Artificial Intelligence

No artificial intelligence-based tools or applications were used in the preparation of this study. The entire content of the study was produced by the author in accordance with scientific research methods and academic ethical principles.

## 10. References

- [1] A. Shukla, K. Kant, A. Sharma, and P. H. Biwale, "Cooling methodologies of photovoltaic module for enhancing electrical efficiency: A review," *Sol. Energy Mater. Sol. Cells*, vol. 160, pp. 275–286, Nov. 2016.
- [2] F. Ekinçi, A. Yavuzdeğer, H. Nazlıgül, B. Esenboğa, B. D. Mert, and T. Demirdelen, "Experimental investigation on solar PV panel dust cleaning with solution method," *Sol. Energy*, vol. 237, pp. 1–10, Apr. 2022.
- [3] R. Stropnik and U. Stritih, "Increasing the efficiency of PV panel with the use of PCM," *Renew. Energy*, vol. 97, pp. 671–679, Jun. 2016.
- [4] A. Yigit, N. Arslanoglu, and H. Gul, "Transient thermal modeling and performance analysis of photovoltaic panels," *Environ. Prog. Sustain. Energy*, vol. 42, no. 4, Nov. 2022.
- [5] E. Cuce, P. M. Cuce, and T. Bali, "An experimental analysis of illumination intensity and temperature dependency of photovoltaic cell parameters," *Appl. Energy*, vol. 111, pp. 374–382, Jun. 2013.
- [6] P. Dwivedi, K. Sudhakar, A. Soni, E. Solomin, and I. Kirpichnikova, "Advanced cooling techniques of P.V. modules: A state of art," *Case Stud. Therm. Eng.*, vol. 21, p. 100674, Jun. 2020.
- [7] G. Ömeroğlu, "Fotovoltaik - Termal (PV / T) Sistemin Sayısal (CFD) ve Deneysel Analizi," *Fırat Univ. Müh. Bilim. Derg.*, vol. 30, no. 1, pp. 161–167, Mar. 2018.
- [8] S. K. Marudapillai, B. K. Ramaraj, R. K. Kottala, and M. Lakshmanan, "Experimental study on thermal management and performance improvement of solar PV panel cooling using form stable phase change material," *Energy Sources Part A*, vol. 45, no. 1, pp. 160–177, Aug. 2020.
- [9] S. V. Hudişteanu et al., "Enhancement of PV panel power production by passive cooling using heat sinks with perforated fins," *Appl. Sci.*, vol. 11, no. 23, p. 11323, Nov. 2021.
- [10] W. Hammad et al., "Thermal management of grid-tied PV system: A novel active and passive cooling design-based approach," *IET Renew. Power Gener.*, vol. 15, no. 12, pp. 2715–2725, May 2021.
- [11] F. Al-Amri, F. Saeed, and M. A. Mujeebu, "Novel dual-function racking structure for passive cooling of solar PV panels – thermal performance analysis," *Renew. Energy*, vol. 198, pp. 100–113, Aug. 2022.
- [12] A. Q. Jakhrani, A. R. Jatoti, and S. H. Jakhrani, "Analysis and fabrication of an active cooling system for reducing photovoltaic module temperature," *Eng. Technol. Appl. Sci. Res.*, vol. 7, no. 5, pp. 1980–1986, Oct. 2017.
- [13] A. M. A. Soliman, H. Hassan, and S. Ookawara, "An experimental study of the performance of the solar cell with heat sink cooling system," *Energy Procedia*, vol. 162, pp. 127–135, Apr. 2019.
- [14] A. Monavari, J. Jamaati, and M. Bahiraei, "Thermohydraulic performance of a nanofluid in a microchannel heat sink: Use of different microchannels for change in process intensity," *J. Taiwan Inst. Chem. Eng.*, vol. 125, pp. 1–14, Jun. 2021.
- [15] M. Bahiraei et al., "Irreversibility characteristics of a modified microchannel heat sink operated with nanofluid considering different shapes of nanoparticles," *Int. J. Heat Mass Transf.*, vol. 151, p. 119359, Jan. 2020.
- [16] R. C. Adhikari, D. H. Wood, and M. Pahlevani, "Optimizing rectangular fins for natural convection cooling using CFD," *Therm. Sci. Eng. Prog.*, vol. 17, p. 100484, Mar. 2020.
- [17] R. M. Elavarasan et al., "An experimental investigation on coalescing the potentiality of PCM, fins and water to achieve sturdy cooling effect on PV panels," *Appl. Energy*, vol. 356, p. 122371, Nov. 2023.
- [18] M. Krstic et al., "Passive cooling of photovoltaic panel by aluminum heat sinks and numerical simulation," *Ain Shams Eng. J.*, vol. 15, no. 1, p. 102330, Jun. 2023.
- [19] T. L. Bergman, F. P. Incropera, D. P. DeWitt, and A. S. Lavine, *Fundamentals of Heat and Mass Transfer*. New York, NY, USA: Wiley, 2012.
- [20] C.-F. Yang et al., "Develop asymmetric, interference-free and excellent heat-dissipation CPU cooler," *Case Stud. Therm. Eng.*, vol. 60, p. 104730, Jun. 2024.
- [21] A. M. Elbreki et al., "Experimental and economic analysis of passive cooling PV module using fins and planar reflector," *Case Stud. Therm. Eng.*, vol. 23, p. 100801, Dec. 2020.



- [22] Z. Khattak and H. M. Ali, "Air cooled heat sink geometries subjected to forced flow: A critical review," *Int. J. Heat Mass Transf.*, vol. 130, pp. 141–161, Oct. 2018.
- [23] Y. Sheikh et al., "Enhancing PV solar panel efficiency through integration with a passive Multi-layered PCMs cooling system: A numerical study," *Int. J. Thermofluids*, vol. 23, p. 100748, Jul. 2024.
- [24] N. Soares et al., "Can movable PCM-filled TES units be used to improve the performance of PV panels? Overview and experimental case-study," *Energy Build.*, vol. 210, p. 109743, Dec. 2019.
- [25] Z. M. Alaas, "The effects of temperature on photovoltaic and different mitigation techniques: a review," *IEEE Access*, p. 1, Jan. 2024.
- [26] Q. Yang et al., "Enhancing concentrated photovoltaic power generation efficiency and stability through liquid air energy storage and cooling utilization," *Sol. Energy*, vol. 280, p. 112875, Aug. 2024.
- [27] S. Kumari et al., "Efficiency enhancement of photovoltaic panel by heat harvesting techniques," *Energy Sustain. Dev.*, vol. 73, pp. 303–314, Mar. 2023.
- [28] L. Assiya, D. Aziz, and H. Ahmed, "Comparative study of P&O and INC MPPT algorithms for DC-DC Converter Based PV System on MATLAB/SIMULINK," in *Proc. IEEE Int. Conf. Electron., Control, Optim. Comput. Sci. (ICECOCS)*, Dec. 2020, pp. 1–5.
- [29] S. A. Mohamed and M. A. E. Sattar, "A comparative study of P&O and INC maximum power point tracking techniques for grid-connected PV systems," *SN Appl. Sci.*, vol. 1, no. 2, Jan. 2019.
- [30] M. A. Mahmood, K. Ishfaq, and M. Khraisheh, "Inconel-718 processing windows by directed energy deposition: a framework combining computational fluid dynamics and machine learning models with experimental validation," *Int. J. Adv. Manuf. Technol.*, vol. 130, no. 7–8, pp. 3997–4011, Jan. 2024.
- [31] P. A. D. Cruz et al., "Computational Fluid Dynamics (CFD) analysis of the heat transfer and fluid flow of copper (II) oxide-water nanofluid in a shell and tube heat exchanger," *Digit. Chem. Eng.*, vol. 3, p. 100014, Feb. 2022.
- [32] X. Y. Zhang et al., "Experimental investigation and CFD modelling analysis of finned-tube PCM heat exchanger for space heating," *Appl. Therm. Eng.*, vol. 244, p. 122731, Feb. 2024.
- [33] A. Pavlovic et al., "Thermal behavior of Monocrystalline silicon Solar cells: A Numerical and Experimental Investigation on the Module Encapsulation Materials," *DOAJ*, Jul. 2021.
- [34] F. Ghafoorian et al., "Self-Starting improvement and performance enhancement in Darrieus VAWTs using auxiliary blades and deflectors," *Machines*, vol. 12, no. 11, p. 806, Nov. 2024.
- [35] H. İ. Yamaç, A. Koca, and T. Yılmaz, "Using computational fluid dynamics for wave generation and evaluation of results in numerical wave tank modelling," *Firat Univ. J. Exp. Comput. Eng.*, vol. 1, no. 1, pp. 31–42, Jan. 2022.
- [36] D. Kumar and B. Premachandran, "Effect of atmospheric wind on natural convection based solar air heaters," *Int. J. Therm. Sci.*, vol. 138, pp. 263–275, Jan. 2019.
- [37] T. T. Göksu, "Investigation of the effect of geometrical parameters and fluid properties of heat sinks on cooling by RSM method," *Firat Univ. J. Exp. Comput. Eng.*, vol. 3, no. 2, pp. 185–203, May 2024.
- [38] N. A. Nalis et al., "Effects of Fin Height, Fin Thickness and Reynolds number on heat transfer enhancement of Flat-Plate thermal Collector: a numerical analysis," *CFD Lett.*, vol. 15, no. 4, pp. 53–63, Feb. 2023.
- [39] J. Jiang et al., "Evaluating the impacts of fin structures and fin counts on photovoltaic panels integrated with phase change material," *Energy*, vol. 283, p. 129143, Sep. 2023.





## Ayarlanabilir Renk Sıcaklığına Sahip LED Armatürlerde Yenilikçi Yaklaşım

Burak TAŞCI<sup>1\*</sup> , Yavuz EROL<sup>2</sup>

<sup>1\*</sup>Teknik Meslek Yüksekokulu, Fırat Üniversitesi, Elazığ, Türkiye.

<sup>2</sup>Elektirik ve Elektronik Mühendisliği, Mühendislik Fakültesi, Fırat Üniversitesi, Elazığ, Türkiye.

<sup>1</sup>btasci@firat.edu.tr, <sup>2</sup>yerol@firat.edu.tr

Geliş Tarihi: 23.08.2024  
Kabul Tarihi: 18.01.2025

Düzeltilme Tarihi: 28.12.2024

doi: <https://doi.org/10.62520/fujece.1537662>  
Araştırma Makalesi

Alıntı: B. Taşcı ve Yavuz Erol, "Ayarlanabilir renk sıcaklığına sahip LED armatürlerde yenilikçi yaklaşım", Fırat Üni. Deny. ve Hes. Müh. Derg., vol. 4, no 2, pp. 245-261, Haziran 2025.

### Öz

Aydınlatma teknolojisi hızla gelişmektedir. Bu teknolojiler arasında, yüksek verimli ışık kaynakları olarak öne çıkan Işık Yayan Diyot (LED) sistemleri bulunmaktadır. LED'ler, çeşitli özellikler ve yapılarla üretilmektedir. Örneğin, RGB (Kırmızı Yeşil Mavi) LED'ler geniş bir renk yelpazesi üretebilmektedir. RGB LED'leri kullanarak, farklı renk sıcaklıklarına sahip beyaz ışık elde etmek de mümkündür. Renk sıcaklığı, gözlerimizin nesnelerin renklerini nasıl algıladığı üzerinde önemli bir rol oynar. Bir nesnenin gerçek renklerini, 6500K renk sıcaklığına sahip gün ışığı aydınlatması altında gözlemleyebiliriz. Aynı nesne, çeşitli renk sıcaklıklarına sahip aydınlatma altında farklı görünebilir. Sonuç olarak, tek bir aydınlatma armatüründe farklı renk sıcaklıklarını ayarlama ihtiyacı doğmuştur. Mevcut LED aydınlatma sistemleri, renk sıcaklığı ve parlaklığın hassas şekilde kontrol edilmesinde genellikle donanım entegrasyonu ve hesaplama verimliliği konularında sınırlamalar yaşamaktadır. Ayrıca, bu sistemler genellikle yüksek maliyetli sensörler gerektirmekte veya değişen çevresel koşullara uyum sağlayabilme esnekliğinden yoksun kalmaktadır. Bu eksiklikleri gidermek için önerilen sistem, PSoC teknolojisini AS7261 XYZ Kromatik Beyaz Renk Sensörü ile birleştirerek renk sıcaklığı ve parlaklık seviyelerini gerçek zamanlı olarak daha hassas ve maliyet etkin bir şekilde ayarlama imkanı sunmaktadır. Bu çalışmada, hem parlaklık hem de renk sıcaklığı açısından ayarlanabilir bir LED armatürü tasarımı, gömülü sistemler alanında giderek daha fazla önem kazanan PSoC (Programmable System on Chip) teknolojisi kullanılarak geliştirilmiştir. RGB LED'lerden oluşan armatürün renk sıcaklığına yönelik gerekli XYZ verileri, AS7261 XYZ Kromatik Beyaz Renk Sensörü'nden elde edilmiştir. Bu sensörden toplanan XYZ bilgileri, tasarlanan sistemin algoritmasında kullanılmıştır. RGB LED'lerin istenen renk sıcaklığı ve aydınlatma seviyesine göre çalıştığı parlaklık seviyeleri ayarlanarak sistem başarıyla uygulanmıştır. Bu yenilikçi yaklaşım, enerji verimli aydınlatma sistemleri, endüstriyel üretim süreçleri ve konut, ticari ve otomotiv ortamları için özelleştirilebilir aydınlatma çözümleri gibi pratik uygulamalara sahiptir ve yaygın endüstriyel benimseme potansiyelini vurgulamaktadır.

**Anahtar kelimeler:** CCT ayarlanabilir LED armatür, CCT kontrol, Gömülü PSoC sistemi

\* Yazışılan yazar



## Innovative Approach to Adjustable Color Temperature in LED Luminaires

Burak TAŞCI<sup>1\*</sup> , Yavuz EROL<sup>2</sup> 

<sup>1\*</sup>Vocational School of Technical Sciences Firat University, Elazığ, Türkiye.

<sup>2</sup>Electrical and Electronic Engineering, Faculty of Engineering, Firat University, Elazığ, Türkiye.

<sup>1</sup>btasci@firat.edu.tr, <sup>2</sup>yerol@firat.edu.tr

Received: 23.08.2024

Accepted: 18.01.2025

Revision: 28.12.2024

doi: <https://doi.org/10.62520/fujece.1537662>

Research Article

Citation: B. Taşçı and Y. Erol, "Innovative approach to adjustable color temperature in LED luminaires", Firat Univ. Jour. of Exper. and Comp. Eng., vol. 4, no 2, pp. 245-261, June 2025.

### Abstract

The field of lighting technology is rapidly evolving. Among these technologies, Light Emitting Diode (LED) systems stand out as highly efficient light sources. LEDs are manufactured with various characteristics and structures. For instance, RGB (Red Green Blue) LEDs are capable of producing a wide spectrum of colors. By using RGB LEDs, it is also possible to achieve white light with different color temperatures. Color temperature plays a crucial role in how our eyes perceive the colors of objects. We can observe the true colors of an object under daylight illumination with a color temperature of 6500K. The same object may appear differently under lighting with various color temperatures. Consequently, there has arisen a need to adjust different color temperatures within a single lighting fixture. Existing LED lighting systems often struggle with achieving precise control over color temperature and brightness due to limitations in hardware integration and computational efficiency. Additionally, these systems may require costly sensors or lack the flexibility to adapt to varying environmental conditions. To address these gaps, the proposed system integrates PSoC technology with an AS7261 XYZ Chromatic White Color Sensor, enabling real-time adjustments of color temperature and brightness with enhanced precision and cost-effectiveness. In this study, a design of an adjustable LED luminaire in terms of both brightness and color temperature has been developed using PSoC (Programmable System on Chip) technology, which is gaining significant traction and importance in the field of embedded systems. The necessary XYZ data for the color temperature of the luminaire, which consists of RGB LEDs, were obtained from the AS7261 XYZ Chromatic White Color Sensor. The XYZ information gathered from this sensor was utilized in the algorithm of the designed system. By adjusting the brightness levels at which the RGB LEDs operate according to the desired color temperature and illumination level, the system was successfully implemented. This innovative approach has practical applications in energy-efficient lighting systems, industrial production processes, and customizable illumination solutions for residential, commercial, and automotive environments, highlighting its potential for widespread industrial adoption.

**Keywords:** CCT tunable LED luminaire, CCT control, Embedded PSoC system

---

\*Corresponding author

## 1. Introduction

Electromagnetic waves consist of electric and magnetic fields moving perpendicular to each other in a coordinated manner. The portion of electromagnetic waves that can be perceived by the human eye is called "visible light." The smallest wavelength of visible light is 380 nm (violet) and the largest wavelength is 780 nm (red). Our eyes can only see wavelengths between 380–720 nm and cannot perceive all electromagnetic waves. Objects appear colored based on the absorption and reflection of light rays with wavelengths in the visible range. Color can be physically defined as a measure of which wavelengths a specific light ray contains and in what proportions, and light is necessary for the observation of color [1]. The temperature of a light source that has the same color coordinates as the radiation color of a black body at a specific temperature is called 'Color Temperature.' This relates not to the heat output of the light source but to the color of the light output. The CIE (Commission internationale de l'éclairage) also recommends expressing the closeness of temperatures to ideal distributions in Kelvin (K). At this point, the CCT (Correlated Color Temperature) magnitude is defined as a measure of how closely the emission of visual artificial light sources resembles the theoretical black body radiation at a specific temperature [2]. In this study, the PSoC embedded system was used to adjust the brightness of the designed luminaire, obtain the XYZ information from the AS7261 XYZ Chromatic White Color Sensor according to the changing brightness, and ensure the operation of the luminaire according to the developed algorithm. PSoC technology, which is rapidly gaining popularity today, holds an important place in embedded systems due to its significant features such as allowing the simultaneous use of analog and digital blocks and its ease of use. The PSoC family consists of devices that feature a controlled mixed-signal array on a single chip. These devices are designed to integrate many traditional microprocessor-based system components into a programmable, low-cost single chip. The PSoC device includes configurable analog and digital circuit elements as well as programmable interconnects. This structure offers configurations that the user can adjust as desired, thus meeting the requirements of many applications. In addition to these features, it includes a fast CPU, flash program memory, SRAM data memory, and configurable inputs and outputs [3].

Figure 1 shows the PSoC CY8CKIT-059 kit used in the study. This kit uses the CY8C5888LTI-LP097 68-pin PSoC 5LP chip, which has an M3 cortex. The CY8C5888LTI-LP097 chip features an 80MHz CPU (Central Processing Unit) speed, 256kb flash, 64kb sram, 2kb eeprom, 1x20-bit delta sigma adc, 2x12-bit sar adc, 4 dacs, 4 comparators, 4 sc/ct analog blocks, 4 opamps, 24 udbs, 4 16-bit timer/pwm, and a total of 48 input/output pins.

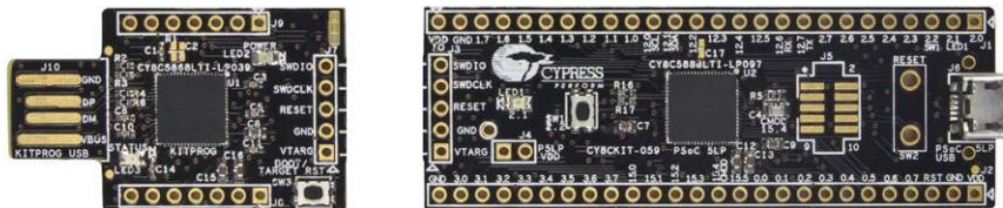


Figure 1. PSoC CY8CKIT-059 Kit [4]

Fedasyuk et al. [5] attempted to solve the problem of developing magnetic tracking sensors for high-precision object localization within the concepts of the Internet of Things and virtual reality using PSoC 5LP. Alakananda and Venugopal [6] tested the operation and performance of a quadcopter. In their study, the PSOC 6 was used, featuring a dual-core processor, which allows for simultaneous data sampling and processing. PSOC 6 was chosen due to its power efficiency, which enhances battery life or flight time. Kim et al. [7] proposed an LED matrix headlight system that reduces communication burden by using bilinear interpolation shift and masking operations, allowing fine adjustments in brightness and color with minimal data transfer. Liu et al. [8] demonstrated an energy-efficient embedded system for electrical engineering automation, integrating fuzzy logic with a PID control algorithm to optimize energy consumption. Their findings, implemented in a tunnel lighting project, revealed a significant energy savings rate of up to 51% per day, showcasing the potential of embedded

systems in enhancing energy efficiency. Satvaya et al. [9], developed an outdoor luminaire based on LEDs that can wirelessly control illuminance, CCT, color rendering index (CRI), and spectral power using a microcontroller and pulse width modulation (PWM) technique. The system, controlled via a smartphone, demonstrated a wide range of color temperature options, enhanced spectral power, improved CRI, and the ability to create a calming nocturnal lighting ambiance. Barbadekar and Patil [10] proposed a PSoC-based smart antenna system, which offers features such as reliability, reconfigurability, automatic steering, and low cost. Ghoroury et al.[11] designed a color temperature adjustable white LED based on a newly developed monolithic color-tunable LED structure, capable of producing white light in the range of 2700 K to 6500 K. Kumar et al.[12] proposed a stand-alone, cost-effective, and innovative design for comprehensive online analysis of arc welding processes using PSoC embedded systems. Rafał Kociszewski [13] demonstrated the practical application of a PI controller using the PSoC embedded system. Tasci and Erol [14] designed a multi-channel wireless communication system using a PSoC and an RF transceiver module. Wojtkowski and Kociszewski [15] utilized SPDM (Stochastic Pulse Density Modulation) in their PSoC-based LED application to minimize harmonic effects. Lin et al. [16] developed a photometric optimization model for color temperature (CCT) tunable white LED clusters under the constraint of color rendering index (CRI), including downconversion energy loss. Lovasoa et al. [17] experimentally analyzed white LEDs with a wavelength of 445 nm. Using different module configurations, they examined the variations in different photometric parameters according to varying supply voltages. Nandhini et al. [18] implemented a color detection application for a wireless robotic arm using PSoC, utilizing LabVIEW graphical language for virtual instrument programming. Komiyama et al.[19] developed a prototype to demonstrate wireless visible light communication using RGB LEDs, with PSoC used to control the parallel signal communication provided by the RGB LEDs. He and Zeng [20] designed a simulation program capable of predicting not only the spectral power distribution, chromaticity coordinates, CCT, and color rendering index (CRI) but also the drive currents, luminous flux, input power, and luminous efficacy of white light LEDs. Chang et al. [21] developed a mixed light control module with RGB LEDs by integrating a photodiode with PSoC. In this study, the sensor was used to examine the ambient temperature and feedback voltage levels of the RGB photodiodes. Yang et al. [22] presented a reflection-based color measurement using a tricolor LED. The color of the tested sample was determined by measuring the three reflective intensities of different colors. A modulation/demodulation technique was used to distinguish the three reflected intensities. The three reflected signals could be processed by a computer to provide an (x, y) coordinate on the CIE chromaticity diagram. Since the three-terminal measurements provide insufficient predictions for an entire spectral reflection, a calibration procedure was successfully developed to correct the predicted results, which significantly differed from the values measured by a well-calibrated device. Speier and Salsbury [23] reviewed efficient white light LED systems with adjustable color temperatures (CT) ranging from 3000 K to 6500 K. Cho et al.[24] examine the historical development, technological advancements, and future potential of white light-emitting diodes (LEDs). The study focuses on the evolution of blue LED chips, device architecture, and the role of phosphors in generating white light. It highlights the commercial success of the blue LED and phosphor combination due to its energy efficiency and durability. While noting the limitations in color rendering capabilities, the authors report remarkable performance metrics, such as a luminous efficacy reaching up to 303 lm/W. The study also discusses the future potential of smart LED applications.

## **2. Color Space**

Due to the vast diversity of colors, there arose a need to group and standardize these colors, leading to the concept of color space. Color spaces are mathematical models used to define colors. They are designed to represent all colors and are typically constructed in three dimensions. This is because, according to Grassmann's first law, which forms the basis of colorimetry, three independent variables are needed to determine a color. The positions of colors within the color space are determined by these variables. Each color space has its own standards for color generation. While constructing color spaces,

it should be possible to transform from one color space to another using linear or non-linear methods[25].

Different devices for color display and processing use different color spaces. For instance, televisions, computer monitors, and scanners use the RGB color space, while printers and plotters use the CMY(K) color space. Color spaces are generally divided into two groups: device-dependent and device-independent color spaces. In device-dependent color spaces, colors are produced based on the characteristics of the device, meaning they are entirely dependent on the device's technical specifications. Device-independent color spaces, on the other hand, are developed by the CIE (Commission Internationale de L'Eclairage) and are used for color measurement in colorimetry, ensuring consistent color measurement across all colors. In these color spaces developed by the CIE, definitions and standards related to color (such as the standard observer and standard illuminant) are utilized [26]. Figure 2 presents the Planckian locus and the CIE 1931 chromaticity diagram, which determine the colors and color temperature of light sources.

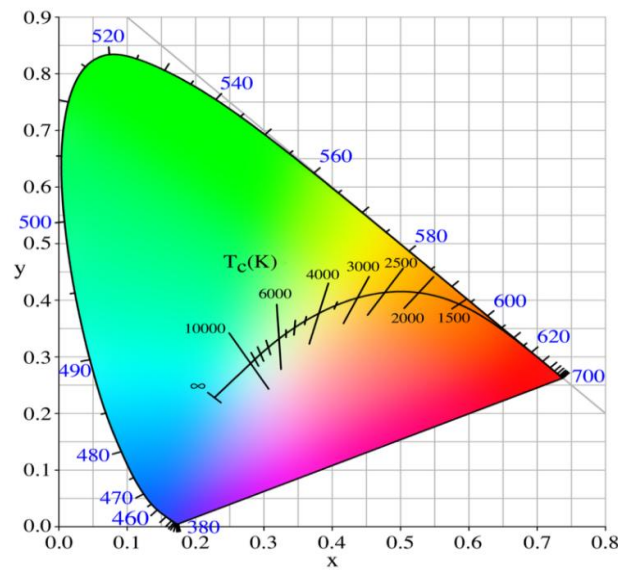


**Figure 2.** Planckian locus 1931 chromatic diagram in CIE 1931

The X, Y, and Z values are the sum of the signals sent to the brain by the nerves that perceive the three primary colors (red, green, blue). Each of these three signals, in relation to the total amount of stimulus, defines the color. While the brain combines these three magnitudes, it uses ratios to achieve the overall perception of color. The sum of the X, Y, and Z values equals the total visual perception of the color[27]. The proportion of red perception within this total is given by Equation 1, the proportion of green perception by Equation 2, and the proportion of blue perception by Equation 3. The calculated x, y, and z values are in the range of 0-1 and their total must be 1.

$$x = \frac{\sum_{i=1}^S X_i}{\sum_{i=1}^S X_i + Y_i + Z_i} \quad (1)$$

$$y = \frac{\sum_{i=1}^S Y_i}{\sum_{i=1}^S X_i + Y_i + Z_i} \quad (2)$$

$$z = \frac{\sum_{i=1}^S Z_i}{\sum_{i=1}^S X_i + Y_i + Z_i} \quad (3)$$

Using Equations 1 and 2, the coordinates of the color on the chromaticity diagram can be determined. According to the tristimulus theory of color perception, color can be represented by three parameters. In 1931, the CIE introduced the three primary colors, denoted as X, Y, and Z, which are calculated using Equations 4, 5, and 6. Here,  $r(\lambda)$  represents the spectral reflectance;  $P(\lambda)$  represents the spectral power



distribution of the illuminant; and  $x(\lambda)$ ,  $y$ , and  $x(\lambda)$ ,  $y(\lambda)$ ,  $z(\lambda)$  are the CIE color matching functions. The CIE color matching functions are shown in Figure 3.

$$x = \int r(\lambda)P(\lambda)\bar{x}(\lambda)d\lambda \quad (4)$$

$$y = \int r(\lambda)P(\lambda)\bar{y}(\lambda)d\lambda \quad (5)$$

$$z = \int r(\lambda)P(\lambda)\bar{z}(\lambda)d\lambda \quad (6)$$

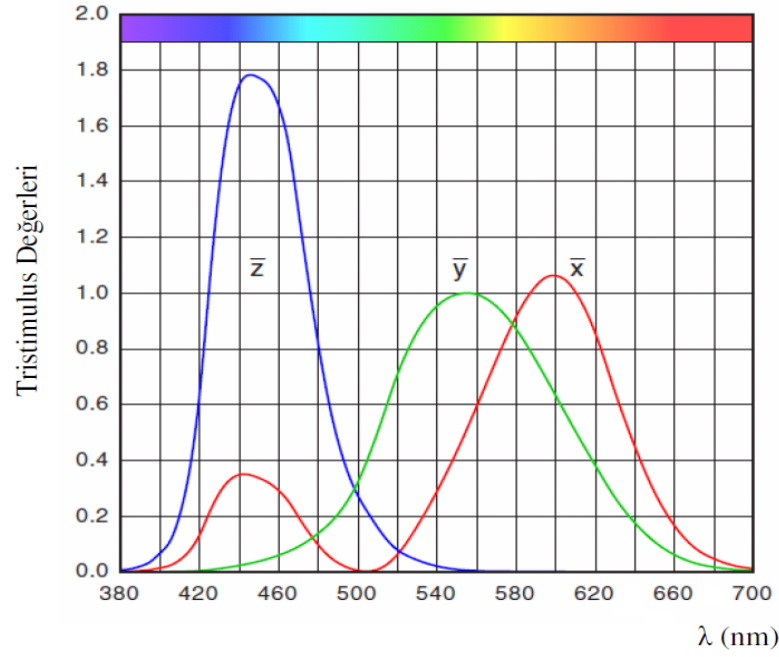


Figure 3. XYZ color matching functions [24]

### 3. Measurement Procedures With As7261 Spectral Sensor

In this study, the XYZ values were measured to ensure that the designed LED RGB luminaire operates at the desired color temperature and illumination level. The measurement of XYZ values was carried out using the AS7261 XYZ Chromatic White Color Sensor, as shown in Figure 4.

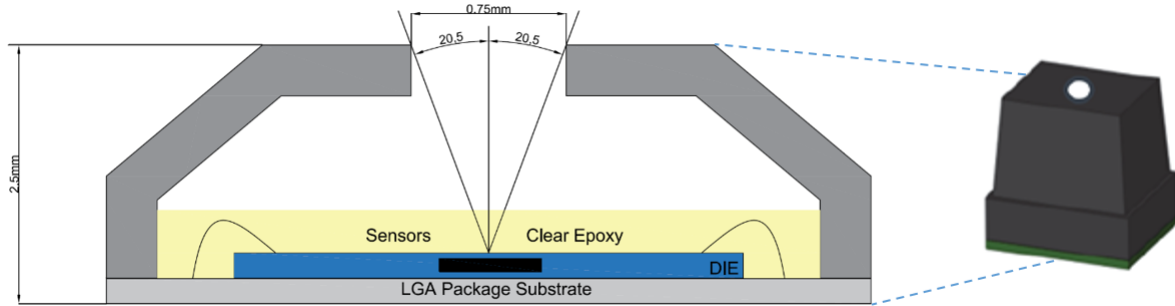


Figure 4. AS7261 XYZ Chromatic White Color Sensor

The AS7261 is a chromatic white color sensor that provides direct XYZ color coordinates consistent with the CIE 1931 2° Standard Observer color coordinates. The AS7261 controls the light entering the



sensor array by integrating Gaussian filters through nano optic deposited interference filter technology into standard CMOS silicon. Control and spectral data access are provided via I<sup>2</sup>C or a serial UART [28]. The field of view of the AS7261 sensor's LGA package is shown in Figure 5.



**Figure 5.** AS7261 LGA Package Field of View [24]

To examine how the brightness of the RGB LED luminaire changes according to the XYZ information, the experimental setup shown in Figure 6 was established. The brightness level of the RGB LED luminaire was adjusted in the range of 0-255 using the PWM blocks of the PSoC 5LP. The brightness level of the luminaire was controlled with the help of an LED driver connected to the output pins of the PSoC 5LP. Changes in brightness levels were measured using the AS7261 sensor, which was connected to another PSoC 5LP kit via I<sup>2</sup>C. The measured values were read as XYZ values from the computer connected to the PSoC via UART.

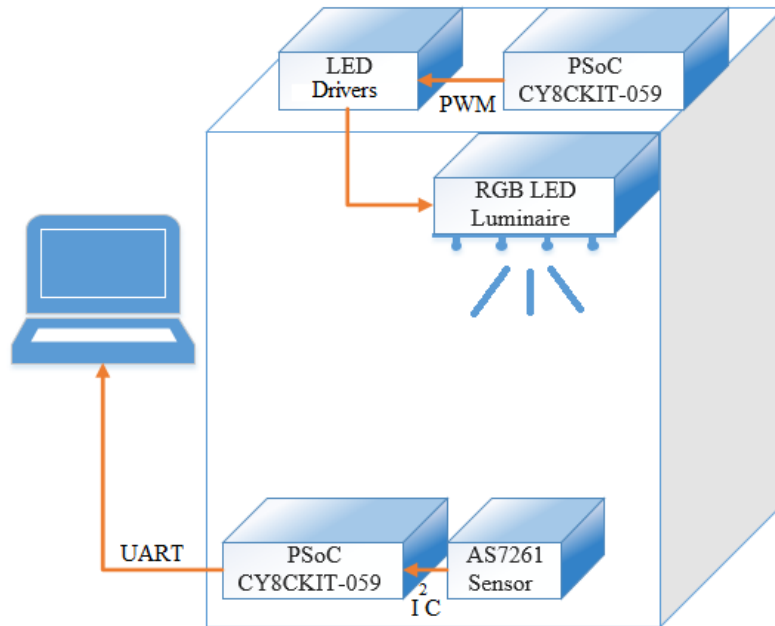


**Figure 6.** Experimental setup set up to read XYZ values

In the experimental setup, the PWM values for the red, green, and blue LEDs were individually varied within the range of 0-255. The XYZ values were recorded for each LED's PWM variation. These recorded values, obtained from experimental studies, are point values. There is no continuous function definition among the data. In such cases, the data are given as pairs of points  $(x_1, y_1), \dots, (x_n, y_n)$ . It is desired to find a function  $f(x)$  such that  $f(x_j) \approx y_j$  for  $j = 1, \dots, n$ . In other words, it is necessary to perform curve fitting to determine another function that is closest to the given point-by-point function values or to replace practically difficult-to-use functions with ones that can facilitate calculations.

For the obtained XYZ values, graphs were plotted using Matlab's curve fitting application. Curve fitting was applied to the plotted graphs. Initially, curve fitting was performed for the XYZ values of each color, resulting in a total of 9 fittings. However, upon further examination, it was observed that the differences in the fitted curve values were significant. Therefore, the curve fitting process was repeated by dividing the XYZ values of each color into three segments. As a result, 9 second-degree equations were obtained for each color, totaling 27 equations.

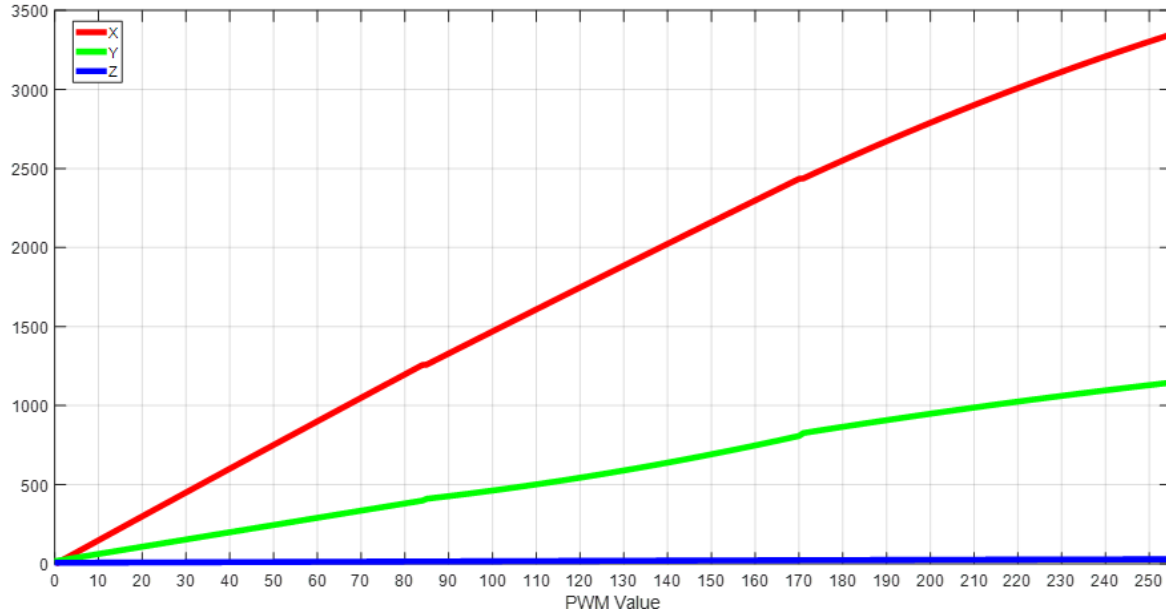


**Figure 7.** Red XYZ PWM exchange

The variation of the XYZ values for the red LED according to the PWM values varied in the range of 0-255 is shown in Figure 7. Nine fitted equations, numbered in the order in Figure 7, are given in equations 7-15.

$$-1.607*((R-42.5)/24.39)^2 + 366.2*((R-42.5)/24.39)+638.3 \quad (7)$$

$$-0.2844*((R-42.5)/24.39)^2 + 111.4*((R-42.5)/24.39)+210.1 \quad (8)$$

$$-0.009132*((R-42.5)/24.39)^2 + 2.476*((R-42.5)/24.39)+9.569 \quad (9)$$

$$-1.466*((R-127.5)/24.97)^2 + 345.1*((R-127.5)/24.97)+1851 \quad (10)$$

$$10.85*((R-127.5)/24.97)^2 + 116.7*((R-127.5)/24.97)+577.8 \quad (11)$$

$$-0.01346*((R-127.5)/24.97)^2 + 2.331*((R-127.5)/24.97)+17.83 \quad (12)$$

$$-14.33*((R-213)/24.68)^2 + 267.4*((R-213)/24.68)+2934 \quad (13)$$

$$-4.51*((R-213)/24.68)^2 + 93.77*((R-213)/24.68)+999 \quad (14)$$

$$-0.1109*((R-213)/24.68)^2 + 1.808*((R-213)/24.68)+25.09 \quad (15)$$

Equations 7, 8, and 9 represent the XYZ values for PWM ranges from 0 to 84. Specifically, Equation 7 calculates the X value, Equation 8 calculates the Y value, and Equation 9 calculates the Z value. For the PWM range of 85 to 170, Equations 10, 11, and 12 are used, where Equation 10 determines the X value, Equation 11 determines the Y value, and Equation 12 determines the Z value. Finally, for PWM values ranging from 171 to 255, Equations 13, 14, and 15 are employed. Equation 13 calculates the X value, Equation 14 calculates the Y value, and Equation 15 calculates the Z value. These equations are crucial

for determining the appropriate PWM values to achieve the desired color temperature and brightness in the LED luminaire.

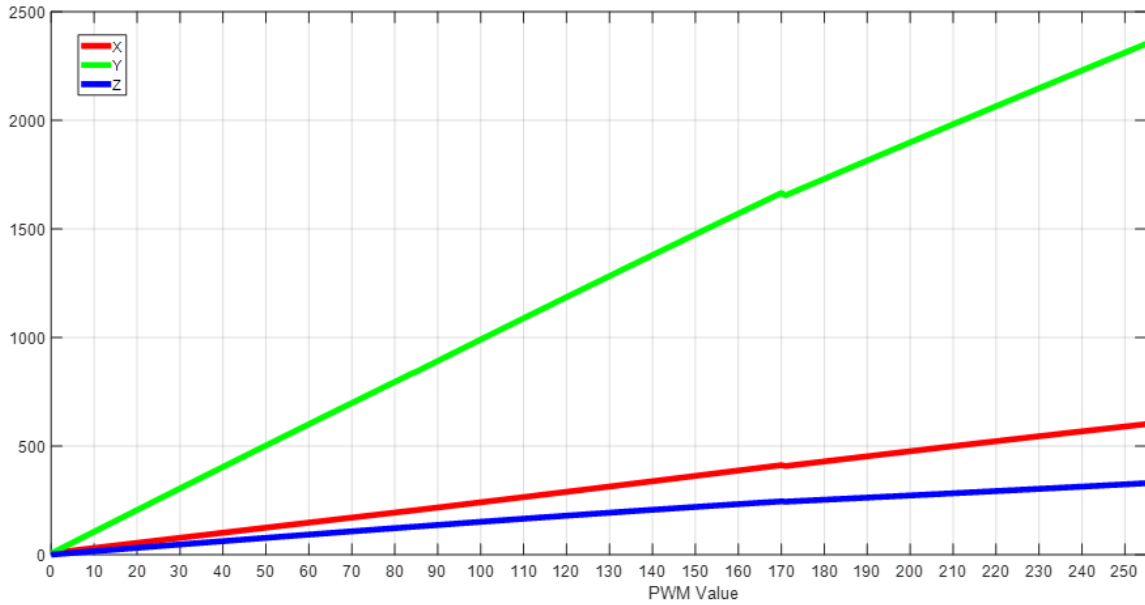


**Figure 8.** Green XYZ PWM variation

The variation of the XYZ values for the green LED according to the PWM values varied in the range of 0-255 is shown in Figure 8. Nine fitted equations, numbered in the order in Figure 8, are given in equations 16-24.

$$-0.21*((G-42.5)/24.39)^2 + 56.86*((G-42.5)/24.39) + 107 \quad (16)$$

$$-1.339*((G-42.5)/24.39)^2 + 240.6*((G-42.5)/24.39) + 428.9 \quad (17)$$

$$-0.3941*((G-42.5)/24.39)^2 + 37.07*((G-42.5)/24.39) + 66.22 \quad (18)$$

$$0.3643*((G-127.5)/24.97)^2 + 60.81*((G-127.5)/24.97) + 307.8 \quad (19)$$

$$-1.77*((G-127.5)/24.97)^2 + 241.7*((G-127.5)/24.97) + 1259 \quad (20)$$

$$-0.869*((G-127.5)/24.97)^2 + 34.07*((G-127.5)/24.97) + 190 \quad (21)$$

$$-0.6235*((G-213)/24.68)^2 + 56.83*((G-213)/24.68) + 506.6 \quad (22)$$

$$-1.166*((G-213)/24.68)^2 + 205.1*((G-213)/24.68) + 2007 \quad (23)$$

$$0.3105*((G-213)/24.68)^2 + 24.95*((G-213)/24.68) + 285.9 \quad (24)$$

For the PWM range of 0 to 84, Equations 16, 17, and 18 are used, where Equation 16 calculates the X value, Equation 17 calculates the Y value, and Equation 18 calculates the Z value. In the PWM range of 85 to 170, Equations 19, 20, and 21 are employed, with Equation 19 determining the X value, Equation 20 determining the Y value, and Equation 21 determining the Z value. For the PWM range of 171 to 255, Equations 22, 23, and 24 are used, where Equation 22 calculates the X value, Equation 23 calculates the Y value, and Equation 24 calculates the Z value. These equations are essential for adjusting the PWM values to achieve the desired color temperature and brightness for the Green LED in the luminaire.

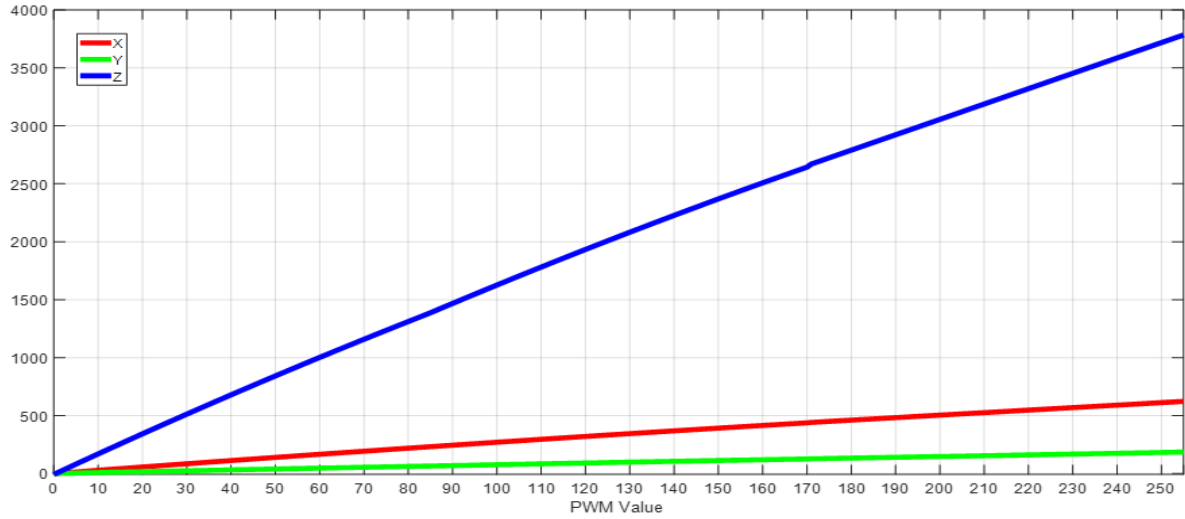


**Figure 9.** Blue XYZ PWM variation

The variation of the XYZ values for the blue LED according to the PWM values varied in the range of 0-255 is shown in Figure 9. Nine fitted equations, numbered in the order in Figure 9, are given in equations 25-33.

$$-1.081*((B-42.5)/24.39)^2 + 66.64*((B-42.5)/24.39) + 118.8 \quad (25)$$

$$-0.2957*((B-42.5)/24.39)^2 + 18.51*((B-42.5)/24.39) + 33.52 \quad (26)$$

$$-10*((B-42.5)/24.39)^2 + 400*((B-42.5)/24.39) + 720 \quad (27)$$

$$-1.311*((B-127.5)/24.97)^2 + 60.5*((B-127.5)/24.97) + 338.3 \quad (28)$$

$$-0.4176*((B-127.5)/24.97)^2 + 17.98*((B-127.5)/24.97) + 96.44 \quad (29)$$

$$-10.21*((B-127.5)/24.97)^2 + 369.1*((B-127.5)/24.97) + 2045 \quad (30)$$

$$-0.07585*((B-213)/24.68)^2 + 53.26*((B-213)/24.68) + 532.1 \quad (31)$$

$$0.2312*((B-213)/24.68)^2 + 17.03*((B-213)/24.68) + 155.8 \quad (32)$$

$$-0.1808*((B-213)/24.68)^2 + 327.2*((B-213)/24.68) + 3228 \quad (33)$$

For the PWM range of 0 to 84, Equations 25, 26, and 27 are used, where Equation 25 calculates the X value, Equation 26 calculates the Y value, and Equation 27 calculates the Z value. In the PWM range of 85 to 170, Equations 28, 29, and 30 are employed, with Equation 28 determining the X value, Equation 29 determining the Y value, and Equation 30 determining the Z value. For the PWM range of 171 to 255, Equations 31, 32, and 33 are used, where Equation 31 calculates the X value, Equation 32 calculates the Y value, and Equation 33 calculates the Z value. These equations are essential for adjusting the PWM values to achieve the desired color temperature and brightness for the Blue LED in the luminaire.

#### 4. Obtaining PWM Ratios

Color temperature can be determined using the x and y coordinate information obtained from Equations 1 and 2. In this study, the x and y coordinate information for color temperature values of 3000K, 4000K, and 5000K were taken from Figure 10. For example, for 5000K, x = 0.346 and y = 0.362. The calculation of the CCT value from these x and y coordinates is performed using Equations 34 and 35.

$$n = (x - 0.3320) / 0.1858 - y \quad (34)$$

$$CCT = 449n^3 + 3525n^2 + 6823.2n + 5520.33 \quad (35)$$

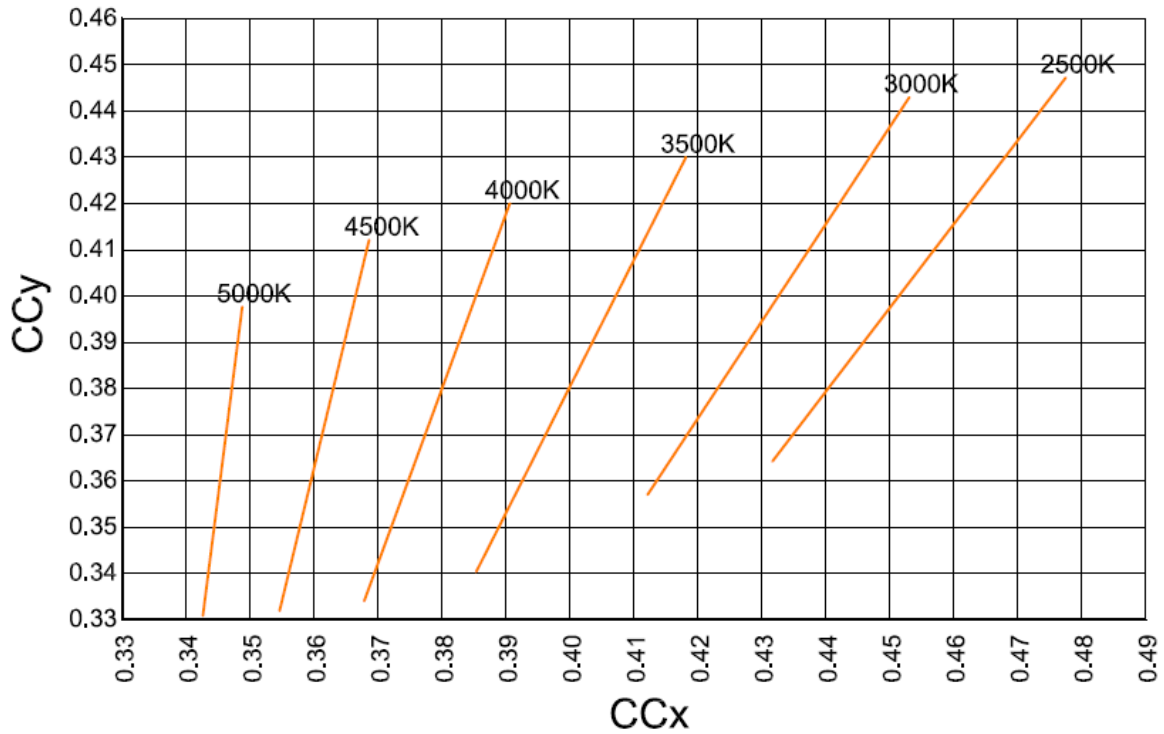


**Figure 10.** CCT change according to xy coordinates

For the brightness level, the Y data from the AS7261 XYZ Chromatic White Color Sensor is used. Accordingly, the target X and Z values are calculated using Equations 36 and 37.

$$X=x*(Y/y) \quad (36)$$

$$Z=(Y/y)*(1-x-y) \quad (37)$$

After calculating the X, Y, Z, x, and y values for the target color temperature and brightness level, the PWM values need to be determined. Using the equations obtained from curve fitting in the previous section, we determine the appropriate PWM values.

For an RGB LED, a separate PWM value needs to be determined for each color. The intersection point of the xy coordinates of the determined PWM values for the RGB LEDs provides the desired color temperature and brightness level.

For example, let's select 5000K and a brightness level of Y = 3000. From Figure 10, x = 0.346 and y = 0.362 are found. Substituting these values into Equations 9 and 10, we find X = 2867.4 and Z = 2419.8. To achieve the desired XYZ values, the appropriate PWM curves need to be determined.

$$X_R = -1.466*((R-127.5)/24.97)^2 + 345.1*((R-127.5)/24.97) + 1851 \quad (38)$$

$$Y_R = 10.85*((R-127.5)/24.97)^2 + 116.7*((R-127.5)/24.97) + 577.8 \quad (39)$$

$$Z_R = -0.01346*((R-127.5)/24.97)^2 + 2.331*((R-127.5)/24.97) + 17.83 \quad (40)$$

$$X_G = -0.6235*((G-213)/24.68)^2 + 56.83*((G-213)/24.68) + 506.6 \quad (41)$$

$$Y_G = -1.166*((G-213)/24.68)^2 + 205.1*((G-213)/24.68) + 2007 \quad (42)$$

$$Z_G = 0.3105*((G-213)/24.68)^2 + 24.95*((G-213)/24.68) + 285.9 \quad (43)$$

$$X_B = -0.07585*((B-213)/24.68)^2 + 53.26*((B-213)/24.68) + 532.1 \quad (44)$$

$$Y_B = 0.2312*((B-213)/24.68)^2 + 17.03*((B-213)/24.68) + 155.8 \quad (45)$$

$$Z_B = -0.1808*((B-213)/24.68)^2 + 327.2*((B-213)/24.68) + 3228 \quad (46)$$

Using the equations, the PWM values are determined according to the targeted values. The obtained PWM values are substituted into Equations 47, 48 and 49 to verify their accuracy.

$$X_T = X_R + X_G + X_B \quad (47)$$

$$Y_T = Y_R + Y_G + Y_B \quad (48)$$

$$Z_T = Z_R + Z_G + Z_B \quad (49)$$

For the PWM values,  $R = 133$ ,  $G = 248$ , and  $B = 128$  are found. When these values are substituted into Equations 11, 12, and 13,  $X = 2852.4$ ,  $Y = 2996.35$ , and  $Z = 2392.64$  are calculated. Substituting these values into Equations 7 and 8 yields a CCT value of 5000.2 K. Figure 11 shows the xy coordinates of the RGB LEDs for 5000K.

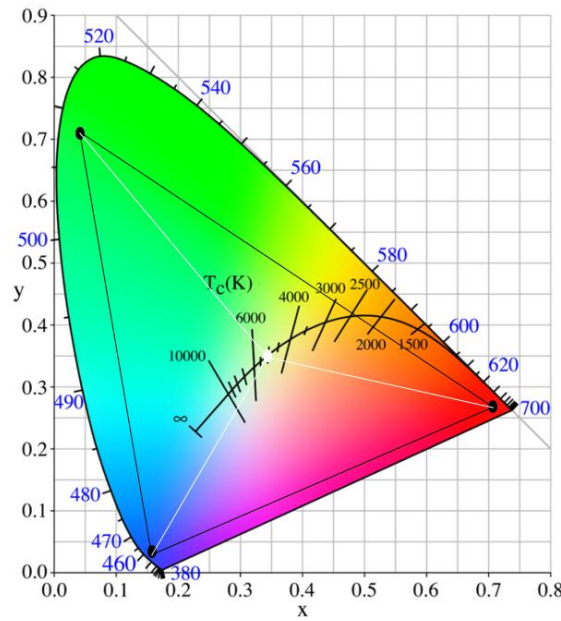


**Figure 11.** Representation of RGB LEDs in xy coordinates for 5000K

LEDs are preferred due to their low voltage operation, high efficiency, and long lifespan. To adjust the light intensity of an LED, an LED driver is required. LED drivers convert the AC or DC voltage at their input into a current and/or voltage suitable for the LED's operation. The selection of the driver is just as important as the selection of the LED in LED luminaires. If the correct LED driver is not chosen, the lifespan of the LEDs will be shortened. There are two main types of drivers on the market based on the driving methods for LEDs: constant voltage and constant current drivers. Constant voltage LED drivers are generally used with decorative lighting strips or bar LEDs, while constant current LED drivers are preferred in general lighting applications such as street lights and projectors. Constant current LED



drivers drive the LEDs at desired currents such as 350, 500, 700, 1000, and 1400mA, with variable output voltages determined by the voltage drop across the LED [29].

Various ready-made driver circuits are available on the market for driving LEDs at constant current. In this PSoC-based study, the constant current C series product from ACG Electronics, shown in Figure 11, was used as the LED driver.



**Figure 12.** C series constant current LED driver circuit

Adjusting the brightness of an LED with a PWM signal is based on the principle of changing the average current of the LED. The average value of the PWM signal is given in Equations 50-52.

$$I_{\text{ort}} = \frac{1}{T} \int_0^T I(t) dt \quad (50)$$

$$I_{\text{ort}} = \frac{1}{T} \left[ \int_0^{T_{\text{on}}} I_{\text{max}}(t) dt + \int_{T_{\text{on}}}^T I_{\text{min}}(t) dt \right] \quad (51)$$

$$I_{\text{ort}} = d \cdot I_{\text{max}} \quad (52)$$

Since the minimum value of the signal is 0V, the average value is equal to the product of the duty cycle and the maximum value of the signal.

## 5. Programming The Designed System

In the designed system, the color temperature and brightness level at which the RGB LED luminaire will operate are selected using a touch LCD screen. The touch LCD screen is connected to the PSoC 5LP via UART. The values selected from the touch screen are transmitted to the PSoC. Based on the experiments conducted, the PSoC sends the obtained PWM values to the LED driver, as shown in Figure

13. By operating the RGB LEDs with different PWM values, the desired illumination levels are achieved.

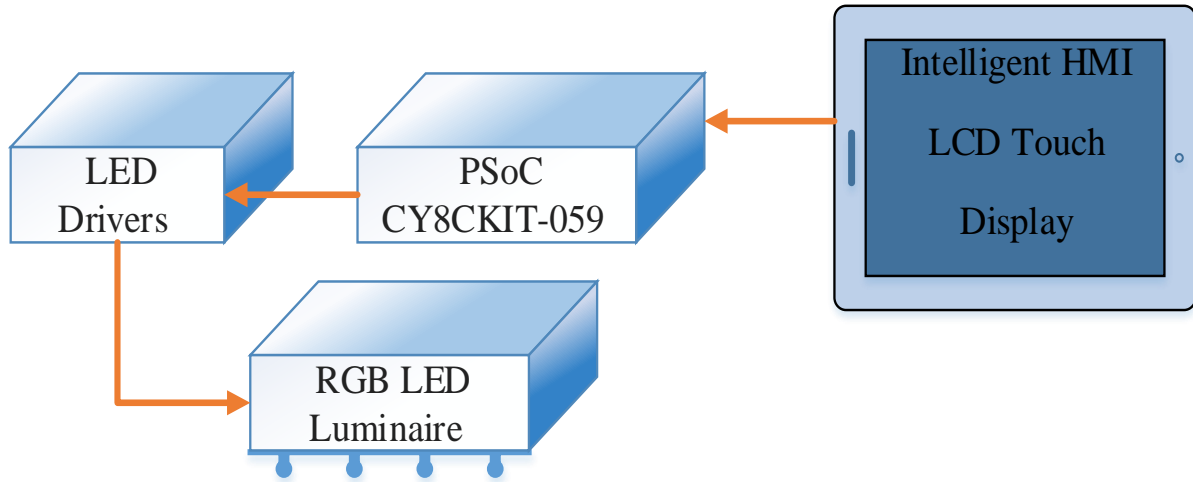


**Figure 13.** Block Diagram

In LED technology, manufacturers document a lifespan of up to 50,000-60,000 hours through testing. However, these tests are conducted under specific temperature conditions. Therefore, using a heat sink in luminaire design is very important. In this study, a heat sink was used to minimize the system's heating. The overall appearance of the designed system is shown in Figure 14.



**Figure 14.** General view of the system

The designed RGB LED luminaire is made using 50x50 RGB LEDs. The circuit of the LED luminaire consists of 12 parallel groups. Each group contains 3 series-connected RGB LEDs.

## **6. Conclusion**

In this innovative project, which integrates the AS7261 XYZ Chromatic White Color Sensor and the PSoC microcontroller, a design has been developed that can be particularly utilized by LED luminaire manufacturers. This study allows for the design of luminaires during the production phase based on precise data obtained from the AS7261 XYZ Chromatic White Color Sensor. The significant advantage of this system is that it eliminates the need to use a sensor in the design of every luminaire, thereby offering a cost-effective solution. This approach ensures accurate color and brightness control while reducing the overall production costs, making it a viable option for mass production of LED luminaires. The implementation of the PSoC microcontroller for managing the PWM signals provides precise control over the RGB LEDs, enabling the attainment of the desired color temperature and brightness levels. The flexibility and programmability of the PSoC platform allow for easy adjustments and scalability in production, accommodating various design requirements and preferences. Moreover, by utilizing a heat sink in the luminaire design, the system's longevity and performance are enhanced, ensuring that the LEDs operate within optimal temperature ranges. This contributes to the durability and reliability of the luminaires, meeting the high standards expected in modern lighting solutions. This project not only demonstrates the practical application of advanced sensor technology and embedded systems in lighting design but also provides a framework for future developments in the field. Future studies could explore the thermal effects of prolonged operation to optimize the system's performance and longevity. Additionally, addressing scalability challenges and investigating adaptability to diverse luminaire designs can expand the system's applicability. Future research could also explore ways to enhance the scalability of the system for industrial-scale applications and improve its adaptability to various luminaire designs. Additionally, integrating advanced control systems, such as IoT frameworks, could further expand the system's functionality and practical applications. The methodologies and findings presented can serve as a reference for further research and innovation, promoting the development of more efficient and versatile lighting systems. Overall, the integration of the AS7261 sensor with the PSoC microcontroller presents a robust and efficient approach to LED luminaire design, paving the way for enhanced performance, cost savings, and increased adaptability in the lighting industry.

## **7. Author Contribution Statement**

All authors contributed equally to this study.

## **8. Ethics Committee Approval and Conflict of Interest**

“There is no need for an ethics committee approval in the prepared article”

“There is no conflict of interest with any person/institution in the prepared article”

## **9. Ethical Statement Regarding the Use of Artificial Intelligence**

During the preparation of this manuscript, the writing assistance tool ‘Grammarly’ was used solely for limited linguistic editing; all scientific content, analyses, and conclusions remain entirely the responsibility of the authors.

## 10. References

- [1] R. McDonald, *The Measurement of Colour, Colour Physics for Industry*. SDC Publication, England, 1997.
- [2] A. K. Türkoğlu and Y. Çalkın, "Siyah Cisim Renk Sıcaklığı," in *V. Ulusal Aydınlatma Sempozyumu Bildiriler Kitapçığı*, pp. 44–47, 2009.
- [3] R. Ashby, *Designer's Guide to the Cypress PSoC*. Elsevier, 2005.
- [4] C. Semiconductor, "CY8CKIT-059 PSoC® 5LP Prototyping Kit Guide," Document, 2015.
- [5] D. Fedasyuk, R. Holyaka, and T. Marusenкова, "Signal chain of programmable system on chip for magnetic tracking sensors," in *Proc. 2020 IEEE 15th Int. Conf. Adv. Trends Radioelectron., Telecommun. Comput. Eng. (TCSET)*, pp. 46–49, 2020.
- [6] B. Alakananda and N. Venugopal, "Development of a programmable system on chip (PSoC) based quadcopter," in *Proc. 2020 4th Int. Conf. Trends Electron. Informatics (ICOEI)*, pp. 93–98, 2020.
- [7] S.-Y. Kim and S.-W. Lee, "A controller system for LED matrix headlights with adjustable brightness and color," *IEIE Trans. Smart Process. Comput.*, vol. 12, no. 3, pp. 275–282, 2023.
- [8] Y. Liu, "Application of embedded systems in electrical engineering automation and energy-saving design," *Appl. Math. Nonlinear Sci.*, vol. 9, no. 1, 2023.
- [9] P. Satvaya and S. Mazumdar, "Performance analysis of a variable flux and CCT-based outdoor LED luminaire," *J. Opt.*, vol. 52, no. 3, pp. 1305–1317, 2023.
- [10] A. B. Barbadekar and P. M. Patil, "A novel method of smart communication using PSoC for wireless push system," in *Proc. 2020 Int. Conf. Emerg. Smart Comput. Informatics (ESCI)*, pp. 184–187, 2020.
- [11] H. S. El-Ghoroury et al., "Color temperature tunable white light based on monolithic color-tunable light emitting diodes," *Opt. Express*, vol. 28, no. 2, pp. 1206–1215, 2020.
- [12] V. Kumar, S. K. Albert, and N. Chandrasekhar, "Development of programmable system on chip-based weld monitoring system for quality analysis of arc welding process," *Int. J. Comput. Integr. Manuf.*, vol. 33, no. 9, pp. 925–935, 2020.
- [13] R. Kociszewski, "Implementation of PI controller in reconfigurable PSoC microcontroller to control the speed of mobile robot drives," in *Proc. 2020 Int. Conf. Mechatron. Syst. Mater. (MSM)*, pp. 1–6, 2020.
- [14] B. Tasci and Y. Erol, "PSoC based embedded RF link design," in *Proc. 2020 13th Int. Conf. Commun. (COMM)*, pp. 381–385, 2020.
- [15] W. Wojtkowski and R. Kociszewski, "Stochastic pulse density modulation for a power LED driver," *Photonics Lett. Pol.*, vol. 12, no. 2, pp. 64–66, 2020.
- [16] D. Lin, P. Zhong, and G. He, "Color temperature tunable white LED cluster with color rendering index above 98," *IEEE Photon. Technol. Lett.*, vol. 29, no. 12, pp. 1050–1053, 2017.
- [17] R. Lovasoa et al., "Lens impact investigation on photometric parameters of some LED luminaires for exterior lighting," in *Proc. 2016 Int. Conf. Appl. Theor. Electr. (ICATE)*, pp. 1–6, 2016.
- [18] J. Nandhini, K. Shabatini, and S. Karthikeyan, "Wireless colour sensing arm robot," in *Proc. 2015 Int. Conf. Robot., Autom., Control Embedded Syst. (RACE)*, pp. 1–6, 2015.
- [19] T. Komiyama et al., "Study of visible light communication system using RGB LED lights," in *Proc. SICE Annu. Conf. 2011*, pp. 1926–1928, 2011.
- [20] G. He and L. Zheng, "Color temperature tunable white-light light-emitting diode clusters with high color rendering index," *Appl. Opt.*, vol. 49, no. 24, pp. 4670–4676, 2010.
- [21] Y. N. Chang, C. C. Hung, S. C. Tung, and S.-Y. Chan, "Auto mixed light for RGB LED backlight module," in *Proc. 2009 IEEE Int. Symp. Ind. Electron.*, pp. 864–869, 2009.
- [22] P. Yang, J. Chen, and Y. Chuang, "Improvement on reflective color measurement using a tri-color LED by multi-point calibration," *Opt. Commun.*, vol. 272, no. 2, pp. 320–324, 2007.
- [23] I. Speier and M. Salisbury, "Color temperature tunable white light LED system," in *Proc. SPIE Int. Conf. Solid State Light.*, vol. 6337, pp. 301–312, 2006.
- [24] J. Cho, J. H. Park, J. K. Kim, and E. F. Schubert, "White light-emitting diodes: history, progress, and future," *Laser Photon. Rev.*, vol. 11, no. 2, p. 1600147, 2017.
- [25] İ. Yılmaz, "Renk uzayları ve dönüşüm algoritmaları," M.S. thesis, Selçuk Üniv., Fen Bilimleri Enst., Jeodezi ve Fotogrametri ABD, 2002.
- [26] H. R. Kang, *Color Technology for Electronic Imaging Devices*. SPIE Press, 1997.

- [27] İ. Yılmaz, M. Güllü, T. Baybura, and A. O. Erdoğan, "Renk Uzayları ve Renk Dönüşüm Programı (RDP)," *Afyon Kocatepe Üniv. Fen Müh. Bilim. Derg.*, vol. 2, no. 2, pp. 19–35, Dec. 2002. [Online]. Available: <https://dergipark.org.tr/tr/pub/akufemubid/issue/1594/19803>
- [28] OSRAM, "AS7261 XYZ Chromatic White Color Sensor Datasheet". [Online]. Available: <https://ams-osram.com/products/sensors/ambient-light-color-spectral-proximity-sensors/ams-as7261-spectral-sensing-engine> [Accessed: Jul. 23, 2024].
- [29] M. Sezer, "Kablosuz haberleşmeli fotovoltaiik modüllü LED aydınlatma sistemi," M.S. thesis, Selçuk Üniv., Fen Bilimleri Enst., Elektrik-Elektronik Müh. ABD, 2018.



## Biyo-yag ile Modifiyeli Asfaltın Yapışma ve Soyulma Özelliklerinin İncelenmesi

Öznur KARADAĞ<sup>1\*</sup> , Mehmet SALTAN<sup>2</sup> 

<sup>1,2</sup>İnşaat Mühendisliği Bölümü, Mühendislik ve Doğa Bilimleri Fakültesi, Süleyman Demirel Üniversitesi, Isparta, Türkiye.

<sup>1</sup>oznurkaradag92@gmail.com, <sup>2</sup>mehmetsaltan@sdu.edu.tr

Geliş Tarihi: 24.09.2024  
Kabul Tarihi: 23.01.2025

Düzeltilme Tarihi: 6.11.2024

doi: <https://doi.org/10.62520/fujece.1555398>  
Araştırma Makalesi

Alıntı: Ö. Karadağ ve M. Saltan, "Biyo-yag ile modifiyeli asfaltın yapışma ve soyulma özelliklerinin incelenmesi", Fırat Üni. Deny. ve Hes. Müh. Derg., vol. 4, no 2, pp. 262-275, Haziran 2025.

### Öz

Plastik malzemeler düşük maliyetleri ve kolay taşınabilmeleri nedeniyle yaygın olarak kullanılmaktadır. Bunun sonucunda çevrede plastik atık miktarı sürekli artmaktadır. Özellikle COVID-19 pandemide paketleme işlemlerinde kullanılan polietilen, polipropilen, polistiren, polietilen tereftalat ve naylon gibi atık plastik malzemeler artmıştır. Bu atık plastik malzemeleri geri dönüştürmek veya yeniden kullanımı sağlamak için depolama, yakma ve gömme gibi yöntemler uygulanmaktadır. Fakat hem atık plastik malzemelerin geri dönüşümünü sağlamak hem de çevre kirliliğini azaltmak amacıyla piroliz yöntemi tercih edilmektedir. Bu çalışmada piroliz yöntemiyle granüler halde atık geri dönüştürülmüş polipropilen oksijensiz ortamda, 500°C sıcaklıkta 45 dakika süresince yakılarak biyo-yag elde edilmiştir. 50/70 asfalt ile %1, 2 ve 3 oranlarında biyo-yag sıcaklık kontrollü yüksek devirli karıştırıcı yardımıyla 160°C sıcaklıkta, 3000 rpm karıştırma hızında 30 dakika süresince homojen şekilde modifiye edilmiştir. 50/70 asfalt ve biyo-yag ile modifiyeli asfalt kullanılarak hazırlanan gevşek asfalt karışımların su ve nem etkisi altında adezyonunu değerlendirmek için Vialit, Nicholson ve Kaliforniya soyulma testleri gerçekleştirilmiştir. Vialit deneyi sonucuna göre, 50/70 asfalta ilave edilen biyo-yag miktarı arttıkça modifiyeli asfaltın agregalarla daha iyi bağlanma performansı göstermiştir. Nicholson soyulma testinde %1 biyo-yag ile modifiyeli asfalt nem hassasiyetine karşı daha iyi direnç gösterirken, Kaliforniya soyulma testinde ise sıcaklık ve laboratuvar ortamında simule edilen yağmur suyu hareketine karşı farklı oranlarda biyo-yag ile modifiyeli asfalt daha az direnç göstermiştir. Deneysel sonuçlar istatistiksel yöntem kullanılarak analiz edilmiştir.

**Anahtar kelimeler:** Biyo-yag, Piroliz yöntemi, Asfalt modifikasyonu, Gevşek asfalt karışım yapışma ve soyulma testleri

\*Yazışılan yazar

İntihal Kontrol: Evet – Turnitin

Şikayet: [fujece@firat.edu.tr](mailto:fujece@firat.edu.tr)

Telif Hakkı ve Lisans: Dergide yayın yapan yazarlar, CC BY-NC 4.0 kapsamında lisanslanan çalışmalarının telif hakkını saklı tutar





## Investigation of Adhesion and Stripping Properties of Asphalt Modified with Bio-oil

Öznur KARADAĞ<sup>1\*</sup> , Mehmet SALTAN<sup>2</sup> 

<sup>1,2</sup>Civil Engineering Department, Faculty of Engineering and Natural Sciences, Süleyman Demirel University, Isparta, Türkiye.

<sup>1</sup>oznurkaradag92@gmail.com, <sup>2</sup>mehmetsaltan@sdu.edu.tr

Received: 24.09.2024

Revision: 6.11.2024

doi: <https://doi.org/10.62520/fujece.1555398>

Accepted: 23.01.2025

Research Article

Citation: Ö. Karadağ and M. Saltan, "Investigation of Adhesion and Stripping Properties of Asphalt Modified with Bio-oil", *Firat Univ. Jour. of Exper. and Comp. Eng.*, vol. 4, no 2, pp. 262-275, June 2025.

### Abstract

Plastic materials are widely used due to their low cost and ease of transportation. As a result, plastic waste is continuously increasing in the environment. Especially, waste plastic materials such as polyethylene, polypropylene, polystyrene, polyethylene terephthalate and nylon used in packaging processes increased during COVID-19 pandemic. Methods such as storage, burning and burying are used to recycle or reuse these waste plastic materials. However, the pyrolysis method is preferred in order to both recycle waste plastic materials and reduce environmental pollution. In this study, bio-oil was obtained by burning waste recycled polypropylene in granular form for 45 minutes at 500°C in an oxygen-free environment with the pyrolysis method. Bio-oil at 1, 2 and 3% ratios and 50/70 asphalt were homogeneously modified for 30 minutes, at 3000 rpm and 160°C with the help of temperature-controlled mixer. Vialit, Nicholson and California Stripping tests were carried out to evaluate adhesion of loose asphalt mixtures containing 50/70 asphalt and modified asphalt under influence of water and humidity. According to the results of the vialit test, as ratio of bio-oil, added to 50/70 asphalt increased, modified asphalt showed better bonding performance with aggregates. In Nicholson stripping test, asphalt modified with bio-oil at ratio of 1% showed better resistance to moisture susceptibility, while in California stripping test, asphalt modified with bio-oil at different ratios showed less resistance to temperature and rainwater movement, simulated in laboratory conditions. The experimental results were analyzed using statistical methods.

**Keywords:** Bio-Oil, Pyrolysis method, Asphalt modification, Loose asphalt mixture, Adhesion and stripping tests

---

\*Corresponding author

## 1. Introduction

Although plastic materials, consisted of elements such as hydrogen, carbon, nitrogen and chloride, do not decompose in nature a long time due to molecular bonds. However, they are indispensable parts of our daily lives because they are cheap and easy to produce [1]. Accordingly, both the consumption of plastic materials and the generation of waste plastic materials increased recently. Waste plastic materials are generally divided into two groups post-industrial and post-consumer. Post-industrial waste materials are clean, consistent, good quality and generally have define components. Waste plastic materials collected from consumers are quite dirty and contain different types of foreign materials such as organic waste, wood, glass and metal [2]. Especially, waste plastics materials such as polyethylene, polypropylene, polystyrene, polyethylene terephthalate and nylon used for packaging purposes emerged during the COVID-19 pandemic [3]. Nowadays, different waste plastic materials are thrown into landfills and the environment. Waste plastic materials thrown into landfills are mixed with municipal solid waste and this situation causes environmental, air and water pollution. In addition to these methods, it is known that waste plastic materials are burned. When plastic materials such as polystyrene and poly vinyl chloride are burned, it can cause breathing, vomiting and complications in the people and especially children around. Therefore, people should not be exposed to smoke that occurred during the burning of toxic plastics such as polystyrene. Methane gas, dioxins, furans, mercury and polychlorinated biphenyls, released during the burning of waste plastic materials damages the ozone layer and causes global warming [4-8]. The pyrolysis method is a mechanical recycling method used to reduce the negative effects of waste plastic materials on both human health and environmental pollution. Mechanical recycling of waste plastic materials is the obtaining of second raw materials without significantly changing the chemical structure of the materials. The pyrolysis method is heated biomass in an oxygen-free environment, and they break down into simpler hydrocarbons. Biomass is classified as woody (stem, branch, chips of different trees), agricultural, aquatic biomass (microalgae, plants and microbes found in water), human, animal and industrial wastes. When different biomass is burned in the absence of oxygen, bio-oil, bio-char and non-condensed gas ( $\text{CO}$ ,  $\text{CO}_2$ ,  $\text{CH}_4$ , and  $\text{H}_2$ ) are obtained. The properties of the materials obtained from the pyrolysis method are affected by the reaction conditions (temperature, residence time, particle size, components of the biomass). The amounts of cellulose, hemicellulose, lignin, volatiles, fixed carbon and ash, found in biomass affect yields of products obtained from the pyrolysis method [9-13].

Asphalt, the primary material in pavement, becomes harmful material at temperature between 160-220°C. Toxic gases emitted into the atmosphere during the production of asphalt mixtures cause adverse effects on both environmental pollution and human health. Thus, researchers are searching for alternative asphalt that are environmentally friendly, economical and efficient [14-15]. Also, deteriorations on pavement occur due to heavy traffic load and environmental conditions such as, humidity, temperature, UV radiation. Modifying asphalt with polymers is one of the most suitable and popular methods to create alternative asphalt, to increase the field performance and life of the pavement. Polymers, recycled from waste plastic materials in asphalt and asphalt mixtures are used to reduce environmental pollution of waste plastic materials, increase the quality of asphalt and reduce the cost of the mixture. In order to both reduce environmental pollution of waste plastic materials and improve the properties of asphalt, use of bio-oil and bio-char obtained from the pyrolysis of waste plastic materials is preferred. In the pyrolysis method, polymers such as polyethylene, polystyrene, polyvinyl chloride and polypropylene, used in the production of goods and materials preferred in our daily lives, are used [16-20]. Bio-asphalt is obtained by modifying the asphalt with bio-oil obtained from the pyrolysis of different polymers. The use of bio-oil in asphalt mixtures positively affects the rheological properties, rutting performance and fatigue life of asphalt mixtures. Additionally, an increase in the viscosity values of asphalt modified with bio-oil at high temperatures is observed [21]. Mills-Beale et al. (2014) [22] obtained bio-binder from swine manure with thermochemical liquefaction process in the absence of oxygen. They stated that bio-modified asphalt exhibited better rutting resistance at high temperatures. In the study carried out by Pratama and Saptoadi (2024) [23], waste polyethylene (PE), polypropylene (PP), polystyrene (PS), polyethylene terephthalate (PET) as biomass was used in the pyrolysis method. The highest amount of waste plastic pyrolytic oil (WPPO) was obtained from the pyrolysis of the mixture of 50% PE, 40% PP and 10% PS. According to the obtained results, it was stated that WPPO could be an alternative fuel for diesel fuel blending. In the study carried out by Fasial et al. (2024) [24], they used high-density polyethylene (HDPE), PP and PS as biomass in certain ratios (1:1:1) in the pyrolysis method. They investigated the effects

of temperature (460-540°C), residence time (30-150 min) and particle size (5-45 mm) parameters on yield of bio-oil obtained from the pyrolysis method. It was stated that the yield of bio-oil obtained from biomass decreased when particle size was less than 20 mm or more than 30 mm. It was explained that the optimum particle size of the biomass used in the pyrolysis method should be approximately 25 mm.

Polypropylene is used in suitcases, bags, shaving cream and toothpaste tubes, sterile health supplies, flowerpots, office folders, buckets, carpets, furniture, storage boxes, cosmetic box lids, household and industrial packaging. Thus, waste plastic materials contain 60-70% wt. PE+PP and 30-40% wt. PET [25-27]. In this study, waste recycled polypropylene in granular form was supplied by the Plastic Recycling Company located in Gaziantep province. Polypropylene-based-oil (PPB) material from the pyrolysis of waste recycled polypropylene in granular form for the first time in the literature was obtained. 50/70 asphalt was modified with bio-oil at ratios of 1, 2, and 3% to increase performance between 50/70 asphalt modified with bio-oil and aggregates. Bio-oil (1-3 %) was blended with 50/70 asphalt at 160°C and 3000 rpm for 30 minutes using a temperature-controlled mixer. The Vialit test was carried out to investigate the adhesion properties of asphalt modified with bio-oil at ratios of 1, 2, and 3%. The Nicholson test was carried out to determine resistance to moisture susceptibility of loose asphalt mixtures prepared with modified asphalt. In addition, the California stripping test was conducted to examine effect of movement of rainwater, simulated in laboratory conditions and temperature on loose asphalt mixtures prepared using modified asphalt.

## 2. Materials

In this study, 50/70 asphalt, limestone aggregate and bio-oil (PPB) obtained from pyrolysis of waste recycled polypropylene in granular form was used.

### 2.1. 50/70 asphalt

Softening point is performed to determine the temperature that begins to flow of asphalt and maximum temperature before rutting deformation of asphalt mixtures begins to increase. It is stated that asphalt, has a high softening point will not flow during process and will be low temperature sensitivity [28-29]. In this study, softening point test was carried out according to TS EN 1427 standard to evaluate high temperature performance of asphalt modified with bio-oil. Generally, stiffness asphalt shows lower fatigue resistance and therefore penetration test is performed to determine stiffness of asphalt [28]. In order to determine the stiffness of modified asphalt, penetration test was carried out in comparison with TS EN 1426 standard. Rotational viscometer test carried out according to ASTM D 4402 standard in order to determine the viscosity of asphalt at high temperatures, exposed to asphalt mixtures during production and application. In addition, rolling thin film oven test (RTFOT), pressure aging vessel (PAV), dynamic shear rheometer (DSR) and bending beam rheometer (BBR) were performed to determine performance properties of asphalt (Table 1).

**Table 1.** Physical and performance properties of 50/70 asphalt

Test	50/70 Asphalt		Standard
Penetration (25°C)	54		TS EN 1426
Softening Point (°C)	49.3		TS EN 1427
Ductility (5 cm/min)	>100		TS EN 13589
Rotational Viscometer (cP)	135°C 470	165°C 123	ASTM D 4402
Specific Gravity (gr/cm <sup>3</sup> )	1.021		TS EN 12607-1
DSR (64°C)	1555.65		
G*/sinδ (Pa)	88.23		
Phase Angle (°)			
BBR (-18°C)			TS EN 14771
Stiffness (MPa)	232.7498		
m-value	0.273		

## 2.2. Bio-oil obtained from waste plastic material

Polymers as additive material to increase performance of asphalt and improve properties of asphalt mixtures are used. Use of waste polymer materials in asphalt and asphalt mixtures both can reduce environmental pollution of waste materials and the problem of disposal in landfills. In these studies, carried out by Abdulkhabeer et al. (2021) [30] and Moubark et al. (2017) [31], waste polypropylene (WPP) and polypropylene which are the most popular polymer with good plastic properties was used to improve mechanical properties of asphalt and asphalt mixtures, respectively. According to obtained results, asphalt modified with polymers were increased the physical properties of asphalt mixtures containing modified asphalt. In this study, waste recycled polypropylene in granular form (Figure 1) obtained from the recycling collection and separation textile factory in Gaziantep province was provided. The pyrolysis method was used to recycle this waste plastic material. Bio-oil (PPB), bio-char and gas were obtained by burning waste recycled polypropylene in granular form with nitrogen gas in an oxygen-free environment.



**Figure 1.** Appearance of materials used in this study

## 3. Methods

In the study, pyrolysis method, Vialit, Nicholson and California tests were carried out.

### 3.1. Pyrolysis method

The pyrolysis method is heated biomass in an oxygen-free environment, and they break down into simpler hydrocarbons. Biomass is classified as woody (stem, branch, chips of different trees), agricultural, aquatic biomass (microalgae, plants and microbes found in water), human, animal and industrial wastes. When different biomass is burned in the absence of oxygen, bio-oil, bio-char and non-condensed gas ( $\text{CO}$ ,  $\text{CO}_2$ ,  $\text{CH}_4$ , and  $\text{H}_2$ ) are obtained. Properties of materials obtained from the pyrolysis method are affected by biomass composition, reaction conditions (temperature, residence time, particle size), presence of catalyst (catalytic and thermal pyrolysis), residence time [9, 32]. Within scope of the study, after waste recycled polypropylene in granular form in the reactor of the pyrolysis device was placed, the reactor is placed in temperature oven at  $500^\circ\text{C}$  (Figure 2). During the pyrolysis method, nitrogen gas is introduced to remove oxygen from the reactor. Thus, when the studies in the literature are taken into consideration [17, 33, 34], waste recycled polypropylene in granular form was burned with nitrogen gas for 45 minutes with a ratio of  $15^\circ\text{C}/\text{min}$  when the device reached a temperature of  $500^\circ\text{C}$ .



**Figure 2.** The pyrolysis device

### **3.2. Modification parameters of asphalt and bio-oil**

The mixing of asphalt and different plastic materials is carried out in two ways: dry and wet mixing methods. Dry mixing method is addition of asphalt at a determined ratios after adding plastic waste materials to the aggregates. In this method, the use of hard plastics, have high melting points such as PET and HDPE is commonly preferred. Since thermal behavior of asphalt modified with different polymers enhanced, the wet mixing method is used for polymer asphalt modification. Polymers have low melting temperatures such as low-density polyethylene (LDPE), PP and ethylene-vinyl acetate copolymer (EVA) are preferred in the wet mixing method. The parameters (temperature, mixing time, ratio of modifier) used in modification of asphalt with different waste plastic materials depend on only on properties of asphalt and waste plastic materials but also on specific requirements of the asphalt [35-37]. Considering the studies, conducted by Shirzad et al. (2024) [38], Dalhat and Wahhap (2017) [1], bio-oil (1-3%) was blended with 50/70 asphalt at 160°C and 3000 rpm for 30 minutes using a temperature-controlled mixer.

### **3.3. Adhesion and stripping tests**

Different factors such as aggregate properties (porosity, texture, mineralogy, chemical composition, and size), design, construction, traffic and temperature affect the adhesion of the chip seal and asphalt pavement. It is determined that the most important factors affecting adhesion between aggregate and asphalt in the chip seal are chemical composition and size of aggregates [39-41]. In addition to these factors, due to the water and traffic density on asphalt pavements, deterioration on asphalt pavements is observed as a result of the decrease in adhesion between asphalt and aggregates. The Vialit test according to the Highway Technical Specification (2013) was carried out to investigate the effect of 50/70 asphalt and asphalt modified with PPB (1-3%) and aggregates under the influence of water.

One of the most important parameters, affected performance of asphalt mixtures is resistance to moisture susceptibility. Resistance to moisture susceptibility of asphalt mixtures depends on the type of aggregate source (calcium carbonate, dolomite, granite), the chemical and physical properties of the asphalt, traffic level, environment conditions and different additives added to aggregate and asphalt. For example, asphalt modified with waste plastic modifiers have better resistance to moisture susceptibility than neat asphalt [42-43]. Therefore, Nicholson and California stripping (Figure 3) tests were carried out to investigate adhesion between 50/70 asphalt and asphalt modified with PPB (1-3%) and aggregates under the influence of water and humidity.





**Figure 3.** California stripping test device

### 3.4. Statistical analysis

Statistical analysis is preferred to examine statistically significant differences between obtained results. Kruskal-Wallis H and Mann-Whitney U tests are used as an alternative when the data does not show normally distribution. Kruskal-Wallis H Test for Oneway Analysis of Variance (ANOVA) by ranks is the nonparametric equivalent of the parametric Oneway Analysis of Variance (ANOVA). The Kruskal-Wallis H Test is preferred in cases where the statistically significant differences between three or more groups is determined, and the data is not provide with normal distribution [44-46]. In the study, the significant of changes in the values by adhesion and stripping tests according to different PPB ratios (1-3%) were examined by Kruskal-Wallis Test and Mann-Whitney tests.

## 4. Results

In this section, the results of adhesion and stripping tests, performed on loose asphalt mixtures prepared with 50/70 asphalt and asphalt modified with PPB (1-3%) are given.

### 4.1. Results of vialit test

100 limestone aggregates spread on 50/70 asphalt and asphalt modified asphalt with PPB (1-3%), distributed homogeneously on the flat steel plate used in the vialit test, were conditioned in a water bath at 40°C temperature for 24 hours. After a 500±5 g steel ball is thrown over the conditioned the flat steel plate, the number of aggregates falling from the plates is given in Figure 4. According to the obtained results, while the number of aggregates falling from 50/70 asphalt and asphalt modified with PPB at ratio of 1% was equal, the number of aggregates falling from asphalt modified with PPB at ratio of 2% decrease. Similar to the results of the study conducted by Saltan et al. (2020) [47], as the ratio of PPB added to 50/70 asphalt increases, the adhesion of asphalt modified with PPB to aggregates increases. Considering the adhesion properties of asphalt modified with PPB to aggregates, in the study conducted by Karadağ (2023) [48], the use of this material as tack coat on the interface between binder and wearing courses was investigated.

In the study carried out by Bagampadde et al. (2013) [49], they determined that a secondary network formed as a result of the interaction of polymers with the molecules in the asphalt during the modification of 50/70 asphalt. In this study, it is thought that the second network formed during the modification of PPB with 50/70 asphalt positively affects the adhesion between the asphalt modified with PPB and the aggregates. Thus, it is thought that as the PPB ratio, added to 50/70 asphalt increases, adhesion between aggregates and modified



asphalt increased. Use of asphalt modified with PPB in the chip sea, widely used in countries such as Turkey, Australia and South Africa is recommended. The use of modified asphalt will provide better performance, especially in the chip seal, exposed to heavy traffic and different temperature conditions. Moreover, the use of asphalt modified with waste material in the chip seal results is reduced consumption of natural resources.

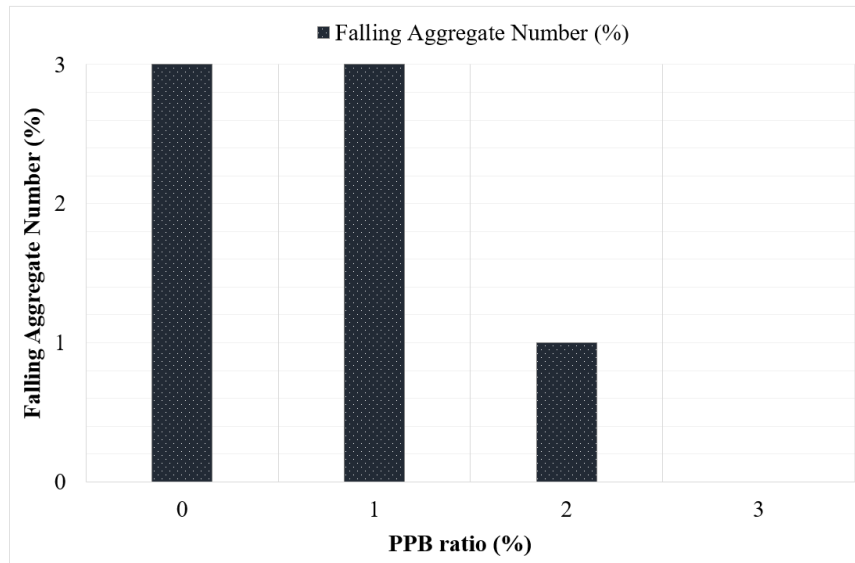


Figure 4. Results of Vialit test

#### 4.2. Results of nicholson stripping test

Stripping occurs in the pavement due to different factors such as the decrease in bonding between aggregate and asphalt, traffic, construction practices, properties of aggregate and asphalt [50-51]. In order to reduce the stripping, occurred in the pavement, the stripping resistance of modified asphalt under influence of water and humidity was investigated. Aggregates remaining without stripping for loose asphalt mixtures containing both 50/70 asphalt and asphalt modified with PPB (1-3%) is given in Figure 5. It is seen that the percentage of aggregate remaining without stripping in all loose asphalt mixtures under influence of water and humidity provided specification limit value determined as 60%. The loose asphalt mixture containing asphalt modified with PPB at the ratio of 1% showed better resistance to the effects of water and humidity. Modified asphalt from the aggregates was stripped due to the increase of polar constituents on surface of modified asphalt and water penetrating into interface of loose asphalt mixtures prepared with asphalt modified with PPB (1-3%) during the conditioning of the Nicholson stripping test [52]. Similar to the results of the study conducted by Liu et al. (2014) [53], it was determined that moisture susceptibility of loose asphalt mixtures containing asphalt modified with PPB, has a low softening point was low.

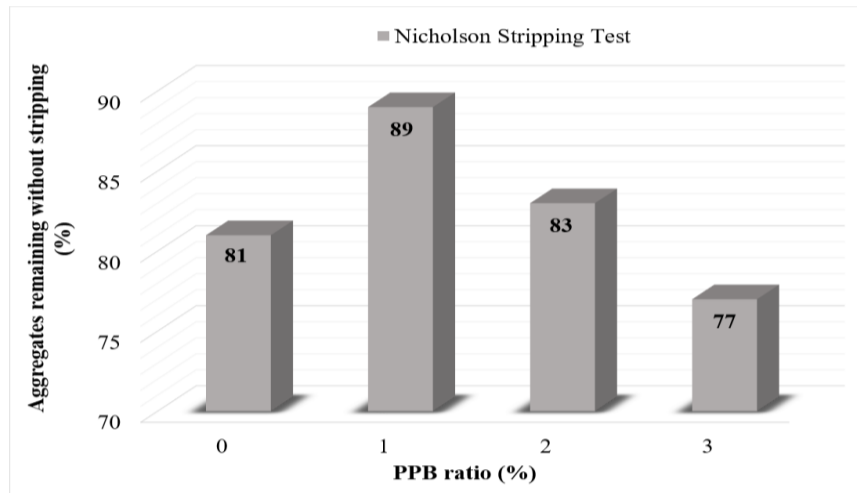


Figure 5. Results of Nicholson test

#### 4.3. Results of california stripping test

Depending on the seasonal conditions (high temperature, rain, freeze-thaw, salty) which the pavement is exposed, the adhesion between asphalt and aggregates decreases due to water infiltration [54]. Thus, the California Stripping test was conducted to examine the effect of rain on loose asphalt mixtures prepared in the laboratory. In the California Stripping test, it is observed that stripping percentage of asphalt modified with PPB (1-3%) increased according to 50/70 asphalt (Figure 6). The loose asphalt mixture containing asphalt modified with PPB at the ratio of 2% showed the best performance. The loose asphalt mixtures containing asphalt modified with bio-oil according to 50/70 asphalt showed less resistance to water movement.

When the results of stripping tests were examined, loose asphalt mixtures prepared by using asphalt modified with PPB (1-3%) showed better stripping resistance. Since the loose asphalt mixtures were conditioned under water and moisture conditions in the Nicholson stripping test, asphalt modified with PPB at ratios of 2 and 3% which were softer than asphalt modified with PPB at ratio of 1% showed less stripping resistance. Asphalt modified with PPB (1-3%) showed lower stripping resistance than 50/70 asphalt under temperature conditions in the California stripping test due to the decrease in adhesive bond between aggregate and modified asphalt with increasing temperature [55]. Asphalt modified with PPB at ratio of 2% is considered to be the optimum ratio for stripping resistance while asphalt modified with PPB at ratio of 1% is found to be insufficient for stripping resistance, under temperature conditions. According to the obtained results, factors such as water, humidity and temperature affect adhesion and stripping performance between modified asphalt and aggregate. Considering adhesion performance of asphalt modified with bio-oil, use of asphalt modified with PPB at ratio of 3% is recommended. Considering stripping performance of modified asphalt, the use of asphalt modified with PPB at ratio of 1% should be preferred.

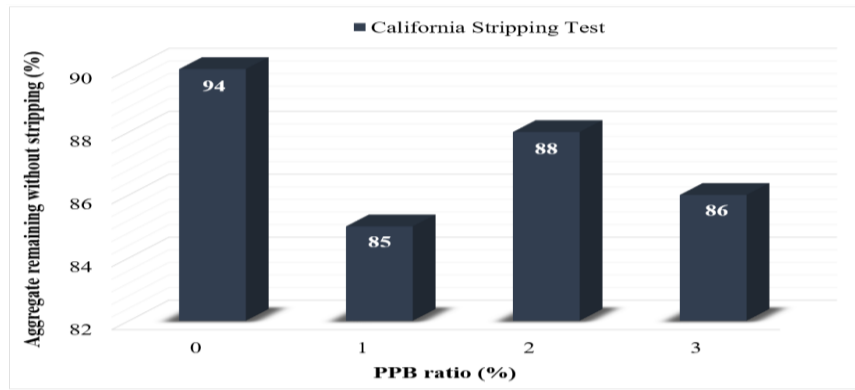


Figure 6. Results of California test

#### 4.4. Results of statistical analysis

Kruskal-Wallis test was performed to investigate whether there was statistically significant differences between adhesion and stripping performances of loose asphalt mixtures prepared with asphalt modified with PPB (1-3%). The obtained values from these tests were interpreted for different PPB ratios which p-value is less than 0.05 meaning level. The Mann-Whitney U test was performed to understand the significance between group variables. It is observed that adhesion performance of loose asphalt mixtures prepared with asphalt modified with PPB at ratio of 3% (p-value <0.05) is statistically higher than asphalt mixtures containing PPB at ratios of 0-1% (Table 2). The difference in Vialit values was statistically insignificant when the additive ratio is 1% or 2%. It was concluded that the additive ratio of PPB should be at least 3% in order to affect adhesion performance of the 50/70 asphalt. In the adhesion test, loose asphalt mixture prepared by using asphalt modified with PPB at ratio of 3% showed 100% adhesion performance, which proved to be consistent with the statistical analysis result.

Table 2. Results of statistical analysis

Group Variables	Dependent Variables	Kruskal-Wallis Test p-values
3% - 2%	Adhesion performance	0.281
3% - 1%		0.027*
3% - 0%		0.014*
2% - 1%		0.256
2% - 0%		0.169
1% - 0%		0.811
3% - 0%	Nicholson stripping performance	0.454
2% - 0%		0.100
1% - 0%		0.007*
3% - 2%		0.369
3% - 1%		0.052
2% - 1%		0.295
1% - 0%	California stripping performance	0.653
2% - 0%		0.061
3% - 0%		0.002*
2% - 1%		0.155
3% - 1%		0.009*
3% - 2%		0.231
* Meaningful at 0.05 significance level		

According to the statistical analysis results, loose asphalt mixtures prepared by using asphalt modified with PPB at ratio of 1% showed statistically better resistance to stripping than asphalt mixtures containing PPB at ratios of 0, 2, and 3%. It is observed that increase in the PPB ratio which is added to 50/70 asphalt is not statistically significant in stripping resistance of loose asphalt mixtures. The best stripping resistance of loose

asphalt mixtures prepared by using asphalt modified with PPB at ratio of 1% in the Nicholson stripping test is consistent with the statistical analysis result.

In the statistical analysis of California stripping test, loose asphalt mixtures prepared by using 50/70 asphalt are statistically better resistance to stripping than asphalt mixtures containing PPB. PPB additive which is added to 50/70 asphalt is not statistically effective on stripping resistance performance of loose asphalt mixtures to temperature and water movement. The high stripping resistance to water movement of loose asphalt mixtures prepared by using 50/70 asphalt in the California stripping test is consistent with the statistical analysis result.

## **5. Conclusions**

Plastic materials (polypropylene, polystyrene, polyethylene terephthalate and nylon), widely used in packaging during COVID-19 pandemic, caused an increase in waste plastic materials in our environment. In our study, bio-oil from waste recycled polypropylene in granular form with the pyrolysis method in order to reduce environmental pollution caused by these waste plastic materials and to improve properties of asphalt was obtained. Vialit, Nicholson and California Stripping tests were carried out to investigate adhesion of loose asphalt mixture containing asphalt modified with bio-oil under the influence of water and humidity. According to the Vialit test result, as the ratio of bio-oil added to 50/70 asphalt increased, the bonding property of modified asphalt with aggregates increased. In Nicholson Stripping test result, the loose asphalt mixture containing asphalt modified with PPB at the ratio of 1% showed better resistance to the effects of water and humidity. However, the loose asphalt mixtures containing asphalt modified with bio-oil according to 50/70 asphalt showed less resistance to rainwater movement, simulated in laboratory conditions and temperature in California Stripping test. Moreover, the obtained results are consistent with the statistical analysis method. Considering the adhesion performance of modified asphalt, use of asphalt modified with PPB at ratio of 3% is recommended. Considering stripping performance of modified asphalt, the use of asphalt modified with PPB at ratio of 1% should be preferred. This study demonstrated that bio-oil derived from recycled polypropylene enhances the adhesion properties of 50/70 asphalt while reducing environmental waste.

## **6. Author Contribution Statement**

In the study, Author 1 contributed to, making design, the analysis of results and provision of materials. Author 2 contributed to, forming idea, examination of results and checking spelling and checking article in terms of content.

## **7. Ethics Committee Approval and Conflict of Interest**

“There is no conflict of interest with any person/institution in the prepared article”

## **8. Ethical Statement Regarding the Use of Artificial Intelligence**

No artificial intelligence-based tools or applications were used in the preparation of this study. The entire content of the study was produced by the authors in accordance with scientific research methods and academic ethical principles.

## 9. References

- [1] M. A. Dalhat and H. I. Al-Abdul Wahhab, "Performance of recycled plastic waste modified asphalt binder in Saudi Arabia," *Int. J. Pavement Eng.*, vol. 18, no. 4, pp. 349–357, Sep. 2015.
- [2] M. S. Qureshi et al., "Pyrolysis of plastic waste: opportunities and challenges," *J. Anal. Appl. Pyrolysis*, vol. 152, p. 104804, Nov. 2020.
- [3] S. Dharmaraj et al., "Pyrolysis: an effective technique for degradation of COVID-19 medical wastes," *Chemosphere*, vol. 275, p. 130092, Jul. 2021.
- [4] U. Gaur, M. Musaiib, and W. Akram, "Waste cooking oil and waste plastic used in bitumen modification," *JETIR*, vol. 8, no. 7, pp. 83–88, Jul. 2021.
- [5] G. Wu, J. Li, and Z. Xu, "Triboelectrostatic separation for granular plastic waste recycling: a review," *Waste Manag.*, vol. 33, no. 3, pp. 585–597, Mar. 2013.
- [6] B. B. Uzoejinwa et al., "Co-pyrolysis of biomass and waste plastics as a thermochemical conversion technology for high-grade biofuel production: recent progress and future directions elsewhere worldwide," *Energy Convers. Manag.*, vol. 163, pp. 468–492, May 2018.
- [7] R. Verma et al., "Toxic pollutants from plastic waste – a review," *Procedia Environ. Sci.*, vol. 35, pp. 701–708, 2016.
- [8] M. T. Rahman, A. Mohajerani, and F. Giustozzi, "Recycling of waste materials for asphalt concrete and bitumen: a review," *Materials*, vol. 13, no. 7, p. 1495, Mar. 2020.
- [9] W. U. Eze et al., "Plastics waste management: a review of pyrolysis technology," *Clean Technol. Recycl.*, vol. 1, pp. 50–69, Jul. 2021.
- [10] M. Tripathi, J. N. Sahu, and P. Ganesan, "Effect of process parameters on production of biochar from biomass waste through pyrolysis: a review," *Renew. Sustain. Energy Rev.*, vol. 55, pp. 467–481, Nov. 2015.
- [11] F. Abnisa et al., "Utilization of oil palm tree residues to produce bio-oil and bio-char via pyrolysis," *Energy Convers. Manag.*, vol. 76, pp. 1073–1082, Dec. 2013.
- [12] J. Akhtar and N. S. Amin, "A review on operating parameters for optimum liquid oil yield in biomass pyrolysis," *Renew. Sustain. Energy Rev.*, vol. 16, no. 7, pp. 5101–5109, Sep. 2012.
- [13] J. Park et al., "Slow pyrolysis of rice straw: analysis of products properties, carbon and energy yields," *Bioresour. Technol.*, vol. 155, pp. 63–70, Mar. 2014.
- [14] M. T. Rahman et al., "Impact of bitumen binder: scope of bio-based binder for construction of flexible pavement," *J. Teknol.*, vol. 70, no. 7, 2014.
- [15] M. M. A. Aziz et al., "An overview on alternative binders for flexible pavement," *Constr. Build. Mater.*, vol. 84, pp. 315–319, Jun. 2015.
- [16] S. H. Pangestika et al., "Utilization of plastic waste to improve properties of road material: a review," *MESI*, vol. 3, no. 3, pp. 119–135, 2023.
- [17] S. Kavuştu, "Co-pyrolysis of polystyrene and polyolefin plastic wastes," M.S. thesis, Ankara Univ., Inst. of Natural and Applied Sci., Ankara, 2013.
- [18] S. Haider, I. Hafeez, and R. Ullah, "Sustainable use of waste plastic modifiers to strengthen the adhesion properties of asphalt mixtures," *Constr. Build. Mater.*, vol. 235, p. 117496, Feb. 2020.
- [19] S. Saadeh and P. Katawal, "Performance testing of hot mix asphalt modified with recycled waste plastic," *Mineta Transp. Inst. Publ.*, 2021.
- [20] P. Singh, A. Tophel, and A. K. Swamy, "Properties of asphalt binder and asphalt concrete containing waste polyethylene," *J. Pet. Technol.*, vol. 35, no. 5, pp. 495–500, 2017.
- [21] R. Mamat et al., "A review of performance asphalt mixtures using bio-binder as alternative binder," *J. Teknol.*, vol. 77, no. 23, 2015.
- [22] J. Mills-Beale et al., "Aging influence on rheology properties of petroleum-based asphalt modified with biobinder," *J. Mater. Civ. Eng.*, vol. 26, no. 2, Oct. 2012.
- [23] N. N. Pratama and H. Saptoadi, "Characteristics of waste plastics pyrolytic oil and its applications as alternative fuel on four cylinder diesel engines," *Int. J. Renew. Energy Dev.*, vol. 3, pp. 13–20, 2014.
- [24] F. Faisal et al., "Optimisation of process parameters to maximise the oil yield from pyrolysis of mixed waste plastics," *Sustainability*, vol. 16, no. 7, p. 2619, 2024.

- [25] S. D. A. Sharuddin et al., "A review on pyrolysis of plastic wastes," *Energy Convers. Manag.*, vol. 115, pp. 308–326, May 2016.
- [26] P. Das and P. Tiwari, "Valorization of packaging plastic waste by slow pyrolysis," *Resour. Conserv. Recycl.*, vol. 128, pp. 69–77, Jan. 2018.
- [27] S. Bezergianni et al., "Alternative diesel from waste plastics," *Energies*, vol. 10, no. 11, p. 1750, 2017.
- [28] L. M. B. Costa et al., "Incorporation of waste plastic in asphalt binders to improve their performance in the pavement," *Int. J. Pavement Res. Technol.*, vol. 6, no. 4, pp. 457–464, 2013.
- [29] M. N. Razali et al., "Modification of bitumen using polyacrylic wig waste," *AIP Conf. Proc.*, vol. 1930, no. 1, 2018.
- [30] W. N. Abdulkhabeer, M. Y. Fattah, and M. M. Hilal, "Characteristics of asphalt binder and mixture modified with waste polypropylene," *Eng. Sci. Technol.*, vol. 39, no. 8, pp. 1224–1230, 2021.
- [31] S. Moubark, F. Khodary, and A. Othman, "Evaluation of mechanical properties for polypropylene modified asphalt concrete mixtures," *Int. J. Sci. Res. Manag.*, vol. 5, no. 12, pp. 7797–7801, 2017.
- [32] T. Maqsood et al., "Pyrolysis of plastic species: a review of resources and products," *J. Anal. Appl. Pyrolysis*, vol. 159, p. 105295, 2021.
- [33] M. M. Akmaz, "Investigation of Engineering Properties of hot mix asphalt modified with solid product obtained from co-pyrolysis of different waste plastics," Ph.D. dissertation, Konya Tech. Univ., Dept. Civil Eng., Konya, 2020.
- [34] Y. Bow and L. S. Pujiastuti, "Pyrolysis of polypropylene plastic waste into liquid fuel," *IOP Conf. Ser.: Earth Environ. Sci.*, vol. 347, no. 1, p. 012128, 2019.
- [35] F. Xu, Y. Zhao, and K. Li, "Using waste plastics as asphalt modifier: a review," *Materials*, vol. 15, no. 1, p. 110, 2021.
- [36] G. White and F. Hall, "Laboratory comparison of wet-mixing and dry-mixing of recycled waste plastic for binder and asphalt modification," in *Proc. 100th Annu. Meet. Transp. Res. Board*, Washington, DC, USA, 2021.
- [37] S. H. Pangestika et al., "Utilization of plastic waste to improve properties of road material: a review," *MESI*, vol. 3, no. 3, 2023.
- [38] S. Shirzard and H. Zouzias, "Enhancing the performance of wood-based bio-asphalt: strategies and innovations," *Clean Technol. Environ. Policy*, pp. 1–21, 2024.
- [39] C. Güner et al., "Effects of construction-related factors on chip seal performance," *Constr. Build. Mater.*, vol. 35, pp. 605–613, 2012.
- [40] F. Rahman et al., "Aggregate retention in chip seal," *Transp. Res. Rec.*, vol. 2267, pp. 56–64, 2012.
- [41] M. Shamsaei, A. Carter, and M. Vaillancourt, "Using construction and demolition waste materials to develop chip seals for pavements," *Infrastructures*, vol. 8, no. 5, p. 95, 2023.
- [42] S. Haider et al., "A pure case study on moisture sensitivity assessment using tests on both loose and compacted asphalt mixture," *Constr. Build. Mater.*, vol. 239, p. 117817, 2020.
- [43] C. Görekem and B. Sengoz, "Predicting stripping and moisture induced damage of asphalt concrete prepared with polymer modified bitumen and hydrated lime," *Constr. Build. Mater.*, vol. 23, no. 6, pp. 2227–2236, 2009.
- [44] S. Guo, S. Zhang, and A. Zhang, "Privacy-preserving Kruskal-Wallis test," *Comput. Methods Programs Biomed.*, vol. 112, pp. 135–145, 2013.
- [45] T. W. Macfarland and J. M. Yates, "Kruskal-Wallis H-test for one-way analysis of variance (ANOVA) by ranks," in *Introduction to Nonparametric Statistics for the Biological Sciences Using R*, pp. 177–211, 2016.
- [46] O. Munoz-Caceres et al., "Mechanical performance of sustainable asphalt mixtures manufactured with copper slag and high percentages of reclaimed asphalt pavement," *Constr. Build. Mater.*, vol. 304, p. 124653, 2021.
- [47] M. Saltan, G. Kaçaroğlu, and Ö. Karadağ, "Hot mixture performances of bituminous binders modified with soybean oil," *Adv. Struct. Eng.*, vol. 9, no. 1, pp. 427–443.
- [48] Ö. Karadağ, "Examination of materials that can be used in tack coat applied on highways," Ph.D. dissertation, Süleyman Demirel Univ., Dept. Civil Eng., Isparta, 2023.
- [49] U. Bagampadde, D. Kaddu, and B. M. Kiggundu, "Evaluation of rheology and moisture susceptibility of asphalt mixtures modified with low density polyethylene," *Int. J. Pavement Res. Technol.*, vol. 6, no. 3, pp. 217–224, 2013.



- [50] U. Bagampadde, U. Isacson, and B. M. Kiggundu, "Classical and contemporary aspects of stripping in bituminous mixes," *Road Mater. Pavement Des.*, vol. 5, no. 1, pp. 7–43, 2003.
- [51] M. Nazirizad, A. Kavussi, and A. Abdi, "Evaluation of the effects of anti-stripping agents on the performance of asphalt mixtures," *Constr. Build. Mater.*, vol. 84, pp. 348–353, 2015.
- [52] A. M. Hung, A. Goodwin, and E. H. Fini, "Effects of water exposure on bitumen surface microstructure," *Constr. Build. Mater.*, vol. 135, pp. 682–688, 2017.
- [53] Y. Liu et al., "Examination of moisture sensitivity of aggregate-bitumen bonding strength using loose asphalt mixture and physico-chemical surface energy property tests," *Int. J. Pavement Eng.*, vol. 15, no. 7, pp. 657–670, 2014.
- [54] Y. Luo et al., "The deterioration and performance improvement of long-term mechanical properties of warm-mix asphalt mixtures under special environmental conditions," *Constr. Build. Mater.*, vol. 135, pp. 622–631, 2017.
- [55] L. G. Cucalon et al., "Physicochemical characterization of binder-aggregate adhesion varying with temperature and moisture," *J. Transp. Eng. B: Pavements*, vol. 143, no. 3, p. 04017007, 2017.



## Kısa Dönem Yaşlandırılmış Saf ve SBS Modifiyeli Asfalt Bağlayıcıların Yaşlanma Davranışlarının Reolojik Araştırması

Ahmet Münir ÖZDEMİR<sup>1\*</sup>

<sup>1</sup>İnşaat Mühendisliği Bölümü, Mühendislik ve Doğa Bilimleri Fakültesi, Bursa Teknik Üniversitesi, Bursa, Türkiye.  
<sup>1</sup>[ahmet.ozdemir@btu.edu.tr](mailto:ahmet.ozdemir@btu.edu.tr)

Geliş Tarihi: 15.10.2024  
Kabul Tarihi: 23.01.2025

Düzeltilme Tarihi: 24.12.2024

doi: <https://doi.org/10.62520/fujece.1568166>  
Araştırma Makalesi

Alıntı: A. M. Özdemir, "Kısa dönem yaşlandırılmış saf ve SBS modifiyeli asfalt bağlayıcıların yaşlanma davranışlarının reolojik araştırması", Fırat Üni. Deny. ve Hes. Müh. Derg., vol. 4, no 2, pp. 276-289, Haziran 2025.

### Öz

Esnek üstyapılar bitümlü bağlayıcı ve uygun gradasyonda agreganın karışımından elde edilmekte ve bitümün performansı kaplamanın nihai performansı üzerinde belirleyici faktör olmaktadır. Bitüm, üretilmesinden uygulanmasına kadar geçen sürede kısa dönemli yaşlanmaya maruz kalır ve bu yaşlanma servis ömrü boyunca meydana gelecek yaşlanmanın büyük kısmını oluşturur. Bu sebeple kısa dönemli yaşlanma davranışı oldukça önemlidir. Bu çalışmada çeşitli analitik yaklaşımlar ile 70/100 saf bitüm ve Stiren-Butadien-Stiren (SBS) modifiyeli bitümün yaşlanma davranışları reolojik olarak incelenmiştir. Bitüm numuneleri üzerinde Dinamik Kayma Reometresi (DSR) cihazı ile farklı frekans (0.01-10 Hz) ve sıcaklık (40, 50, 60, 70°C) aralıklarında Frekans Tarama testi uygulanmıştır. Deneysel veriler işlenerek bağlayıcıların kompleks modül ve kompleks viskozite ana eğrileri elde edilmiş, eğriler reolojik analizlere tabi tutulmuştur. Sonuçlar, SBS modifikasyonu ile yaşlanma esnasında elastik özelliklerin korunma kabiliyetinin artırılarak yaşlanma direncinin iyileştirildiğini göstermiştir. Ayrıca, ana eğriler reolojik modellere yüksek doğrulukta uygulanmıştır.

**Anahtar kelimeler:** Bitüm, SBS, Reolojik model, DSR, Frekans taraması

\*Yazışılan Yazar

İntihal Kontrol: Evet – Turnitin

Şikayet: [fujece@firat.edu.tr](mailto:fujece@firat.edu.tr)

Telif Hakkı ve Lisans: Dergide yayın yapan yazarlar, CC BY-NC 4.0 kapsamında lisanslanan çalışmalarının telif hakkını saklı tutar.



## Rheological Analysis of The Aging Behavior of Short-Term Aged Pure And SBS Modified Asphalt Binders

Ahmet Münir ÖZDEMİR<sup>1\*</sup> 

<sup>1</sup>Civil Engineering, Engineering and Natural Sciences, Bursa Technical University, Bursa, Türkiye.

<sup>1</sup>[ahmet.ozdemir@btu.edu.tr](mailto:ahmet.ozdemir@btu.edu.tr)

Received: 15.10.2024

Accepted: 23.01.2025

Revision: 24.12.2024

doi: <https://doi.org/10.62520/fujece.1568166>

Research Article

Citation: A.M. Özdemir, "Rheological analysis of the aging behavior of short-term aged pure and SBS-modified asphalt binders", *Firat Univ. Jour. of Exper. and Comp. Eng.*, vol. 4, no 2, pp. 276-289, June 2025.

### Abstract

Flexible pavements consist of a bituminous binder and certain graded aggregate. The performance of the bitumen determines the overall pavement performance. Bitumen undergoes short-term aging from production to application, accounting for most of its total aging during service life. This study rheologically investigates the short-term aging behavior of 70/100 pure bitumen and SBS-modified bitumen. Frequency Sweep test was performed on bitumen samples with Dynamic Shear Rheometer (DSR) device at different frequency (0.01-10 Hz) and temperature (40, 50, 60, 70°C) ranges. The complex modulus and complex viscosity master curves of the binders were obtained by processing the experimental data and the curves were subjected to rheological model analysis. The study showed that SBS modification enhanced aging resistance by preserving elastic properties. Moreover, the master curves were applied to rheological models with high accuracy.

**Keywords:** Bitumen, SBS, Rheological model, DSR, Frequency sweep

---

\*Corresponding Author

## **1. Introduction**

Bitumen is a thermoplastic material obtained by refining petroleum [1]. After complex processes such as volatilization, oxidation and condensation, bitumen becomes harder and more brittle, which leads to various structural problems [2-3]. This whole process is called aging of bitumen. The aging process is analyzed in two parts as short-term and long-term aging [4-5]. Both types of aging significantly change the physical and chemical properties of bitumen, but in different time periods and conditions [6]. Considering the entire aging process of bitumen, the greatest aging occurs in the short term. For this reason, the measures to be taken in the short-term aging process are critical.

Short-term aging occurs during the production and application of bitumen [7]. During hot mix asphalt production, binder is mixed with hot aggregate and exposed to high temperatures. This process usually takes place between 140°C and 160°C. The high temperature starts to change the chemical structure of the bitumen [8]. Under the influence of heat, the more volatile components of bitumen evaporate, oxidation of larger molecules becomes easier and hardening begins. Oxidation is one of the main causes of short-term aging [9]. During heating, the surface of the bitumen comes into contact with oxygen in the air and oxidative reactions begin. These reactions result in the oxidation of aromatic and unsaturated components, especially in bitumen. During transportation and paving of the bitumen mixture from the production plant to the construction site, the bitumen still remains at high temperatures. At this stage, oxidation and loss of volatile components continues [10]. Since the surface layer of the bitumen is in contact with more oxygen, short-term aging may be more pronounced on this surface. After the mixture is laid, compaction is performed. During this process, the temperature of the asphalt mixture is still high. During compaction, both oxidation continues and some components in the mix condense and cause hardening [7-12]. Short-term aging is simulated in the laboratory using the Rolling Film Thin Oven Test (RTFOT) and the aging resistance of different bitumens can be determined after this test method [13-14].

Various additives are used to improve the aging resistance of bitumen, and the effects of polymer additives are generally investigated. Zhang et al. emphasized that aging of modified bitumen has significant effects on pavement properties and investigated the effect of polymer modification on aging by a series of experiments in the laboratory. The results showed that the stress relaxation property of bitumen decreases with aging and tends to behave with higher viscosity due to the decrease in phase angle values. Polymer additive was found to help bitumen to show good elastic properties under short-term aging conditions [15]. Liu et al. stated in their study that SBS, which is the most common polymer additive, may cause various disadvantages due to its high viscosity. Within the scope of the study, the effect of SBS in combination with polyphosphoric acid (PPA) on the aging performance of bitumen was investigated. The results showed that some physical properties such as complex modulus of SBS changed when PPA was added and some properties such as zero shear viscosity, relaxation stress were not affected independently of RTFO short-term aging. It was concluded that PPA would improve the short-term aging resistance [16]. Another common additive is crumb rubber (CR) derived from waste vehicle tires. CR provides significant performance gains to bitumen. While obtaining a CR modified asphalt pavement, various negative effects can occur due to the increase in construction temperatures. Jin et al. subjected CR modified bitumen to RTFOT at different aging temperatures. The experimental results show that the appropriate RTFOT temperature is related not only to the viscosity of the CR modified binders but also to the mix gradation. Binders with higher viscosity require elevated RTFOT temperatures between 173 °C and 193 °C to simulate short-term aging, especially for mixtures with higher air voids. Furthermore, swelling of CR in bitumen has been associated with improved aging performance [17]. In another study, the aging behavior of bitumen with SBS and CR was investigated. As a result of the study, it was determined that CR would increase the aging resistance by preventing polymer degradation in SBS modified bitumen [18].

In this study, 70/100 pure bitumen and bitumen containing 2% SBS were subjected to short-term aging (RTFOT) and their aging performances were investigated. In addition to experimental data, various rheological models and mathematical analyses were used to deepen the evaluation of aging effects. Within the scope of the study, bitumen samples were subjected to frequency sweep testing with a dynamic shear rheometer (DSR) device. The effects of different temperatures and loading rates on unaged and aged binders were investigated and the modification effect was determined. The frequency sweep test was performed at

10 different frequencies (0.01-10 Hz) and 4 different temperatures (40, 50, 60, 70°C) and master curves were obtained using the complex modulus values obtained from the experiment.

## 2. Materials and Method

In this section, the bituminous binder, additives and analysis methods used in the study are discussed. In addition, the experimental preparation process and modified bitumen preparation process are given. The experimental and theoretical approaches preferred in the study are explained in accordance with the purpose of the study.

### 2.1. Materials

In this study, 70/100 penetration grade pure bitumen obtained from TÜPRAŞ Batman refinery was used. Styrene-butadiene-styrene (SBS) was used as additive. The properties of pure bitumen and SBS are given in Table 1.

**Table 1.** Properties of 70/100 bitumen and SBS

Bitumen			SBS	
Property	Unit	Value	Property	Value
Penetration	dmm	86.5	Molecular structure	Linear
Softening Point	°C	51.4	Styrene/butadiene ratio	31/69
Flash Point	°C	230	Density (gr/cm <sup>3</sup> )	0.94
Density	gr/cm <sup>3</sup>	1.034	Oil content	N/A
			Melting index (kgw/cm <sup>2</sup> )	<1
			Stiffness	70

## 2.2. Method

Within the scope of the study, the differences in the mechanistic and rheological behavior of pure and SBS modified bitumen after short-term aging were analyzed. The experimental flowchart is given in Figure 1.

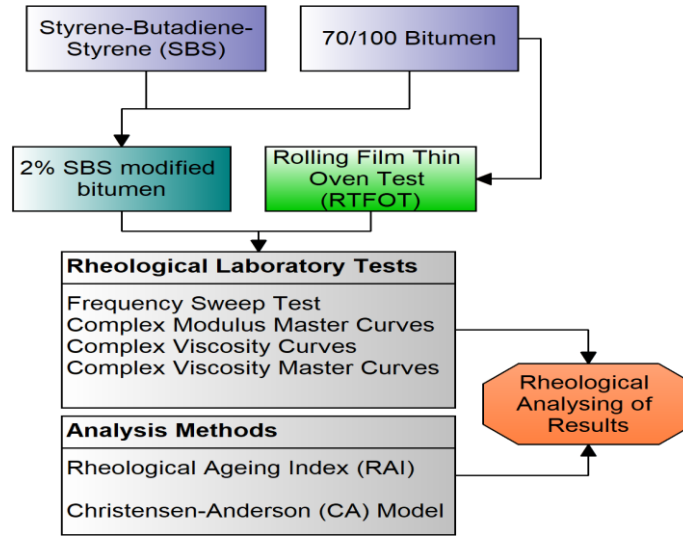


Figure 1. Flowchart of the experimental procedure

### 2.2.1. Preparation of SBS modified bitumens

Modified bitumen was obtained by adding 2 wt% SBS additive to bituminous binder with 70/100 penetration degree liquefied at appropriate temperature. The modification process was carried out at 180°C, 1000 rpm speed for 1 hour.

### 2.2.2. Rolling film thin oven test (RTFOT)

The RTFOT test is conducted in accordance with TS EN 12607-1 [19] and is designed to replicate the aging process that occurs from the time of production to the stages of paving and compaction. This testing methodology is applicable to both unmodified and modified binders, focusing on the thermal and oxidative aging associated with short-term aging. In the course of the test, an bitumen film is created and subjected to airflow at a temperature of 163°C for a duration of 85 minutes. This process accelerates the oxidation of the bitumen, resulting in an increase in the binder's viscosity and a notable alteration in its hardness. The implications of short-term aging are critical, as they influence the initial performance characteristics of the bitumen, particularly regarding workability, adhesion, and resistance to cracking within the mixture. The RTFOT test for modified bitumens is an essential instrument for assessing the impact of additives, thereby facilitating the evaluation of the binders' resistance to aging. RTFOT test device was given in Figure 2.



Figure 2. RTFOT device and test samples



### 2.2.3. Frequency sweep test and master curve construction

The frequency sweep test is performed with the Dynamic Shear Rheometer (DSR) device and the behavior of bitumen under oscillation loading at different frequencies is examined. This loading at different frequencies characterizes the viscoelastic properties of bitumen. Different frequencies within the scope of the experiment represent different loading speeds and it has been determined that a loading frequency of 10 Hz corresponds to a speed of 60-65 km/h [20]. Oscillatory tests were performed on pure and SBS modified bitumen at four different temperatures (40°C, 50°C, 60°C and 70°C) and ten different frequencies (0.01-10 Hz). The DSR device and test specimens are shown in Figure 3.



**Figure 3.** DSR device and test samples

As a result of the experiment, important rheological parameters such as elastic modulus ( $G'$ ), viscous modulus ( $G''$ ), complex modulus ( $G^*$ ), phase angle ( $\delta$ ), complex viscosity are obtained for different frequency values of binders at each temperature. The  $G^*$  values obtained after the experiment are converted into a “master curve” at a certain reference temperature value in order to examine the rheological behavior of bitumen in a wide frequency range by adhering to the Time-Temperature Superposition Principle (TTSP). The obtained master curves were subjected to rheological analysis according to the Christensen-Anderson (CA) Model. In this model, presented in Equation 1, the rheological behavior is described in terms of  $G^*$  values as a function of the frequency applied to the bituminous binder. Although the model was originally intended to characterize pure bitumen, it has recently been used to describe the behavior of modified bitumen. Numerous studies have been conducted with the CA model [21-23]. After CA Model analysis, glass modulus ( $G_g$ ), crossover frequency ( $\omega_c$ ) and rheological index ( $R$ ) values are obtained for pure and modified binders. As a result of the studies, it was determined that the  $G_g$  value can be accepted as  $1 \times 10^9$  for all bituminous binders.

$\omega_c$  represents the frequency at which the viscous and elastic modulus values are the same. It is also the point where the viscous asymptote and the glassy asymptote overlap.  $\omega_c$  characterizes the overall hardness of the bitumen.  $R$  is defined as the difference between the complex modulus at  $\omega_c$  and the intercept asymptotes. It is also called shape factor. An increase in  $R$  indicates a decrease in the viscous properties and an improvement in the elastic properties of the binder at intermediate loading times and temperatures and gives the idea that it will show wider relaxation spectra.

$$|G^*| = G_g \left[ 1 + \left( \frac{\omega_c}{\omega} \right)^{\frac{\log 2}{R}} \right]^{\frac{-R}{\log 2}} \quad (1)$$

#### 2.2.4. Rheological ageing index (rai)

Complex modulus values obtained at different temperatures and loading rates (frequency) show that the mechanistic behavior of bitumen changes significantly with temperature and frequency. In previous studies, the area between the master curves of bitumen before and after aging was found to be an important indicator of aging, and the rheological aging index (RAI) was introduced to evaluate aging over a wide frequency range [24-25].

### 3. Results and Discussions

The TTSP master curves of the  $G^*$  values of pure and 2% SBS modified bitumen before and after short-term aging process (RTFOT) are given in Figure 4.

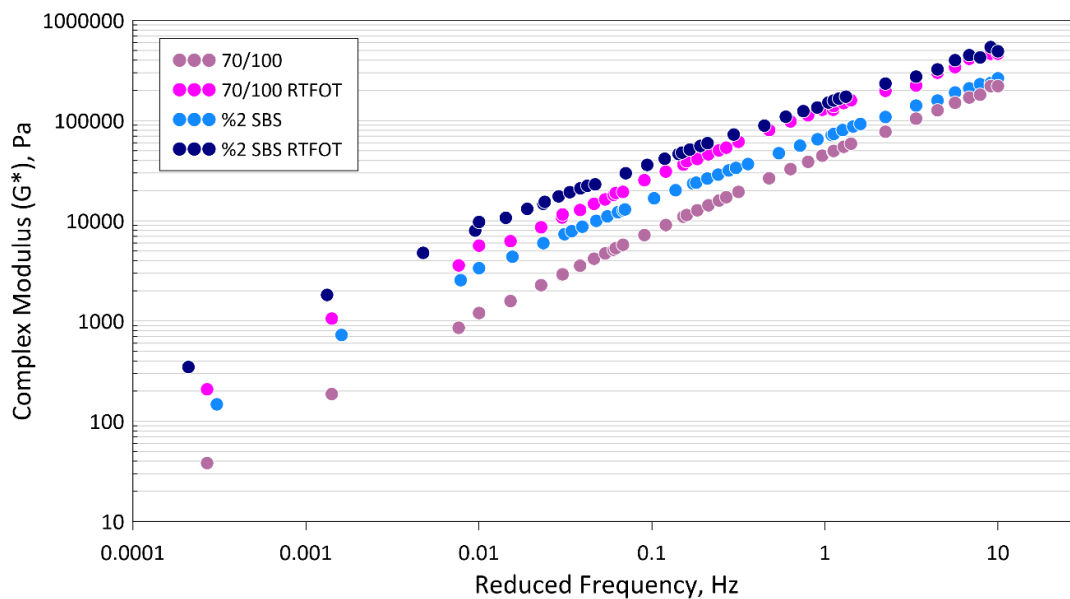


**Figure 4.** Master curves of pure and 2% SBS modified bitumens

When creating complex shear modulus ( $G^*$ ) master curves, a reference temperature is selected and other isothermal curves are shifted to this temperature value. Asphalt pavements are usually subjected to loading at moderate temperatures (20°C–60°C). A reference temperature is usually chosen within this range because the rheological properties of the bitumen are particularly important. For the master curve given in Figure 4, the reference temperature is 40°C [26]. The complex modulus values increased with increasing frequency, i.e. loading rate. When low frequency (long-term loading rate) is applied, the shear strength of the binders decreases. This is associated with the viscoelastic behavior of the material. Among the unaged bitumen, the lowest  $G^*$  values were observed in 70/100 bitumen, while  $G^*$  values increased with the addition of 2% SBS. After RTFOT,  $G^*$  values of all binders were higher than their pure state. The short-term aging process constitutes the major part of the total aging process and the bituminous binder is subjected to intense oxidation during this process. The material hardens due to the removal of volatile components from the bitumen, the functional groups formed in the bitumen due to oxidation and the increase in the proportion of components with high molecular weights. The desired phenomenon when obtaining the master curve is that the curve is smooth and continuous. When Figure 4 is examined, it is seen that the curve is smooth and continuous for each binder type, indicating the applicability of TTSP and that the binders are “thermo-rheologically simple”.

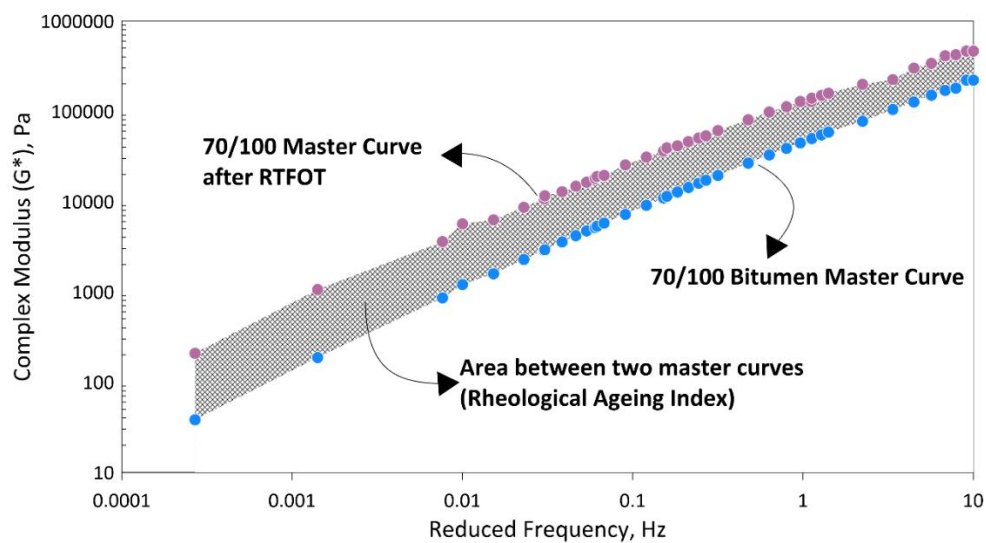
The master curves were analyzed using the Christensen-Anderson (CA) Model to conduct detailed rheological evaluations. The curves were fit according to Equation 1 and the model parameters were obtained and given in Table 2.

**Table 2.** CA Model paramaters

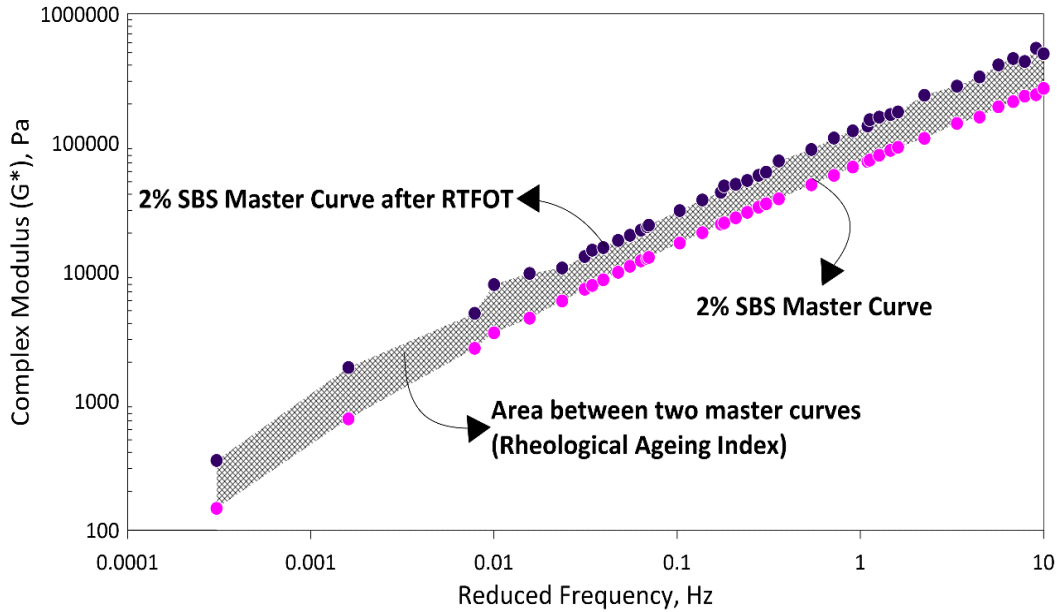
Sample Name	Parameter	Value	R <sup>2</sup>
70/100	Gg	1.00E+09	0.99
	$\omega_c$	1974.085	
	R	2.30379	
70/100 RTFOT	Gg	1.00E+09	0.99
	$\omega_c$	183.9779	
	R	2.62321	
2% SBS	Gg	1.00E+09	0.99
	$\omega_c$	72.98642	
	R	3.0771	
2% SBS RTFOT	Gg	1.00E+09	0.99
	$\omega_c$	24.1748	
	R	3.12519	

Table 2 confirmed that the CA Model successfully fits both aged and unaged bitumen master curves ( $R^2 > 0.99$ ). As mentioned in the methodology section, the Gg value was fixed at  $10^9$  and R and  $\omega_c$  values were left free. It was observed that both pure and 2% SBS binder presented higher R values with the aging effect after RTFOT. The R-value of pure bitumen increased by about 14% after RTFOT, while that of modified bitumen was 1.63%. The R-value is related to the total amount of colloidal matter in the bitumen and is therefore reported to be proportional to the asphaltene content [27-28]. With aging, maltenes with lower molecular weights degrade and some of their components, especially aromatic components, are converted into asphaltenes. As the maltene ratio decreases and the asphaltene ratio increases, R values also increase. The  $\omega_c$  value refers to the frequency value at which the storage and viscous modulus are equal and is interpreted as the point at which the material switches from elastic to viscous behavior. Since bitumen hardens, it starts to exhibit viscous behavior at low frequencies and therefore  $\omega_c$  decreases. When Table 2 is analyzed, the lowest  $\omega_c$  value is observed in 2% SBS RTFOT binder, while the highest  $\omega_c$  value is observed in 70/100 pure bitumen. The  $\omega_c$  values of both binders decreased with the effect of aging.

Figures 5 and 6 show the calculation of the RAI value representing the aging of 70/100 and 2% SBS modified bitumen.



**Figure 5.** RAI calculation of 70/100 bitumen



**Figure 6.** RAI calculation of 2% SBS modified bitumen

The area between the master curve obtained from the frequency sweep test performed on the bitumen sample after aging with RTFOT and the master curve of the unaged sample is associated with aging. It is practically the difference of the areas under both curves. The RAI values of 70/100 and 2% SBS modified bitumen are given in Table 3.

**Table 3.** RAI values of binder samples

Sample Name	Unaged	RTFOT-aged	RAI
70/100	$1.21 \times 10^6$	$3.03 \times 10^6$	$1.82 \times 10^6$
2% SBS	$1.64 \times 10^6$	$3.37 \times 10^6$	$1.72 \times 10^6$

The RAI value is effective for determining the rheological behavior characteristics of pure and modified bitumen over a wide frequency range. When Table 3 is analyzed, the area under the curve values increased with the increase in  $G^*$  values with aging. As a result of SBS modification, RAI values were lower than those of the pure binder. The decrease in the area under the master curve indicates a bitumen that is more resistant to aging and reveals the modification effect. Higher RAI values indicate lower aging resistance [25-29]. The results in Table 3 show that SBS additive increases the aging resistance of pure bitumen over a wide frequency range. The complex viscosity values obtained from the frequency scan test of 70/100 % pure and 2% SBS modified bitumen are given in Figure 7.

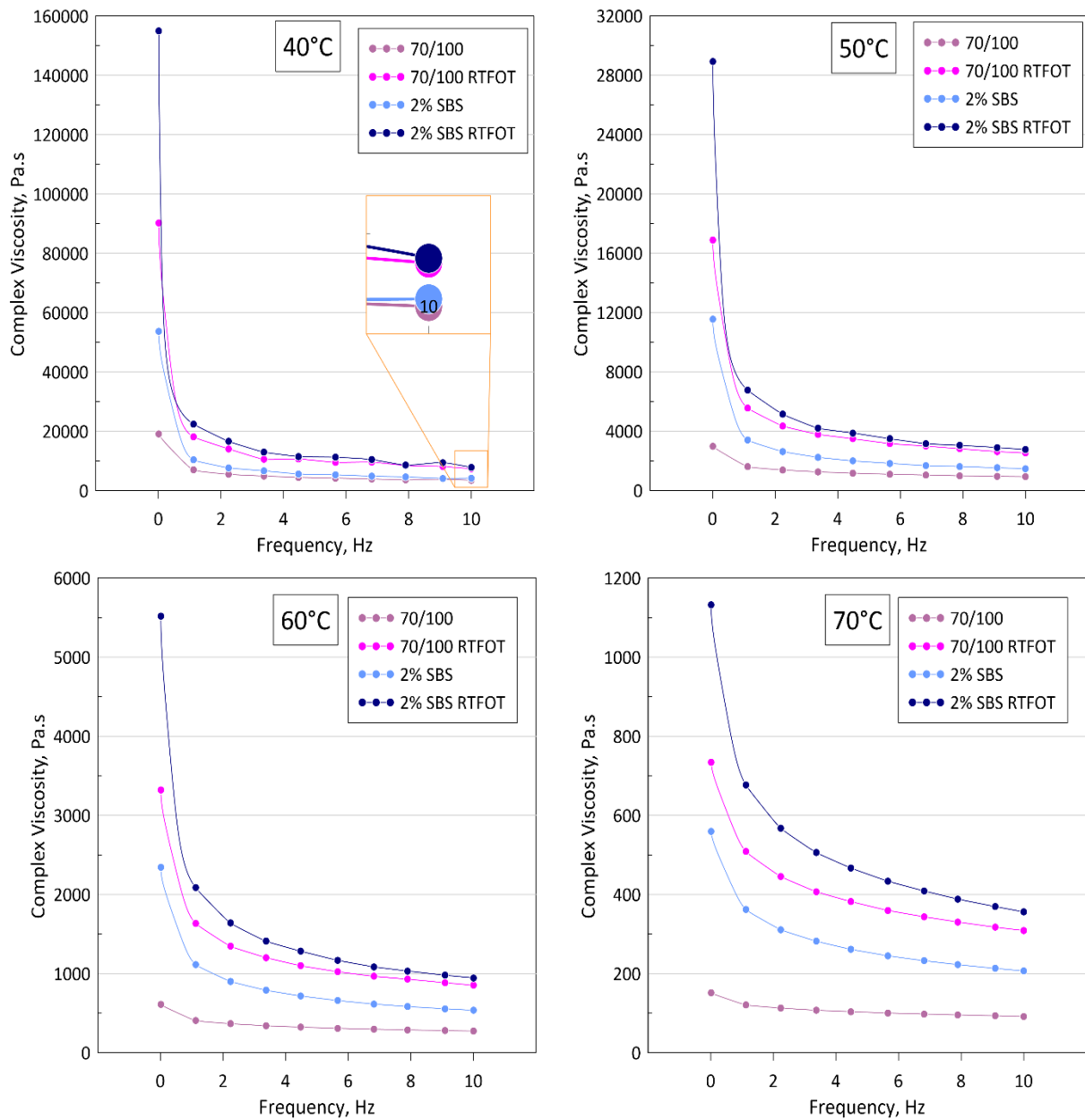


**Figure 7.** Complex viscosity values of pure and modified bitumen before and after RTFOT

Complex viscosity tends to decrease with increasing temperature. This is associated with bitumen becoming more fluid at higher temperatures. Tests conducted between 40°C and 70°C show that the viscosity decreases as the temperature increases and the bitumen deforms more easily. However, thanks to the SBS modification, this reduction is more limited compared to pure bitumen, because the elastic nature of SBS allows the material to better maintain its shape in the face of temperature. At low frequencies, bitumen exhibits a more viscous and fluid behavior, while at high frequencies elastic properties become dominant. At low frequencies, such as 0.01 Hz, the complex viscosity is higher, while at 10 Hz these values decrease. SBS-modified bitumen better compensates for these frequency differences and increases the elastic behavior, showing better resistance especially at low frequencies. It was observed that the viscosity values of the bitumen increased significantly after RTFOT.

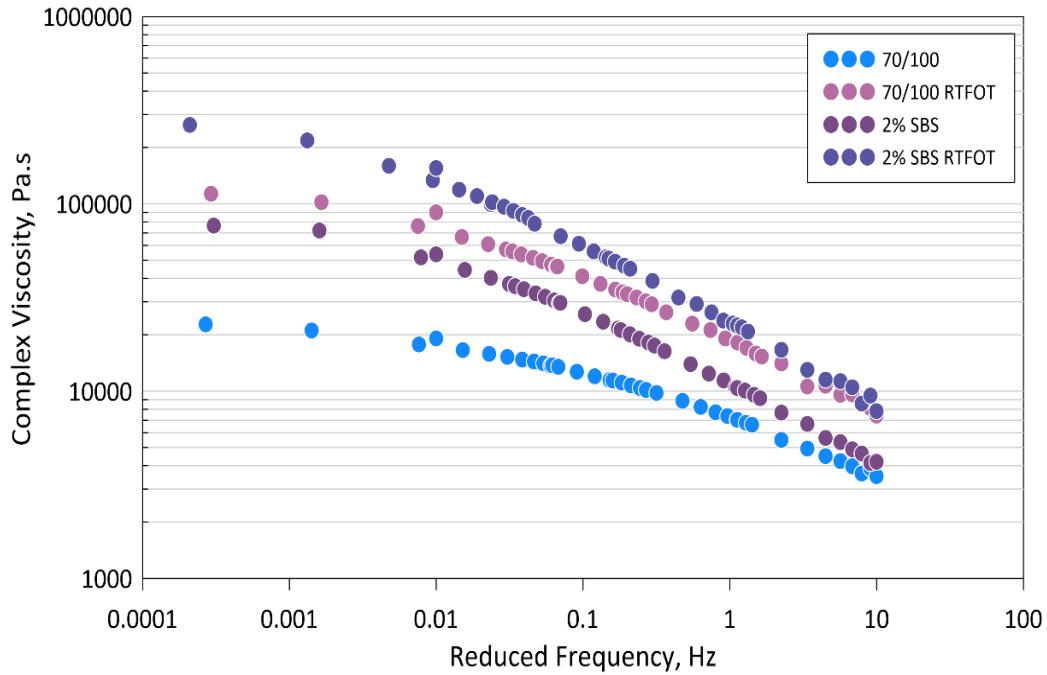


**Figure 8.** Complex viscosity master curves

In order to observe the rheological behavior at different frequency and temperature values in a single curve, complex viscosity master curves were obtained just like  $G^*$  values and presented in Figure 8. When Figure 8 is examined, the differences between the bitumens are more pronounced at low frequencies, while the curves get closer to each other as the frequency increases. The highest complex viscosity value was observed in the 2% SBS-RTFOT binder, while the lowest viscosity values were determined in the 70/100 binder. Figure 8 shows that TTSP can be successfully applied to complex viscosity curves.

#### 4. Conclusions

This study examined the short-term aging effects on 70/100 pure and 2% SBS-modified bitumen using RTFOT and frequency sweep tests with a DSR device. The frequency scan test was performed at ten different frequencies (0.01-10 Hz) and 4 different temperatures (40, 50, 60, 70°C). The results obtained from the study are compiled below:

- When the TTSP  $G^*$  master curves obtained from the test data were analyzed, the results showed that  $G$  values significantly increased with aging and SBS modified bitumen presented higher  $G^*$  values compared to pure bitumen. The master curves are very smooth and continuous.
- The master curves were analyzed using the Christensen-Anderson (CA) Model to conduct detailed rheological evaluations over a wider frequency range. CA Model results showed that rheological index ( $R$ ) values increased with aging, while  $\omega c$  values decreased. These effects deepened with the additive and showed that the additive increased the ability of the binder to maintain its elastic properties after aging.
- The Rheological Aging Index (RAI) results showed that the SBS modification increased the aging resistance of 70/100 bitumen. The area under the main curve was found to increase significantly after short-term aging for both binders.
- According to the complex viscosity values, the viscosity values decreased with increasing temperature and were limited by the use of additives. The modification effect, which was more pronounced at low frequencies, lost its effect slightly as the frequency increased. Viscosity values increased significantly with aging.



- Complex viscosity master curves provided the opportunity to analyze the viscosity behavior in a wide frequency range and showed that complex viscosity master curves can be successfully obtained with TTSP.

In this study, 2% SBS additive was selected because it is a widely used concentration in practice and is considered the threshold at which modification effects begin to manifest. This concentration provides an effective balance between performance enhancement and economic feasibility. However, it is acknowledged that the performance of SBS-modified binders can vary with different molecular structures or concentrations, and future research should explore these aspects to broaden the scope of the findings.

## **5. Author Contribution Statement**

In the realized study, Author 1 undertook the idea, design, literature review, experimental study and writing of the article.

## **6. Ethics Committee Approval and Conflict of Interest**

“Ethics committee permission is not required for the prepared article”

“There is no conflict of interest with any person/institution in the prepared article.”

## **7. Ethical Statement Regarding the Use of Artificial Intelligence**

No artificial intelligence-based tools or applications were used in the preparation of this study. The entire content of the study was produced by the authors in accordance with scientific research methods and academic ethical principles.

## 8. References

- [1] R. Hunter, A. Self, and J. Read, *The Shell Bitumen Handbook*, 6th ed. London, U.K.: ICE Publishing, 2015.
- [2] R. Rahbar-Rastegar, R. Zhang, J. E. Sias, and E. V. Dave, "Evaluation of laboratory ageing procedures on cracking performance of asphalt mixtures," *Road Mater. Pavement Des.*, vol. 20, no. sup2, pp. S647–S662, 2019.
- [3] B. V. Kok and M. Yilmaz, "The effects of using lime and styrene–butadiene–styrene on moisture sensitivity resistance of hot mix asphalt," *Constr. Build. Mater.*, vol. 23, no. 5, pp. 1999–2006, 2009.
- [4] D. Zhang, B. Birgisson, X. Luo, and I. Onifade, "A new short-term aging model for asphalt binders based on rheological activation energy," *Mater. Struct.*, vol. 52, no. 4, p. 68, 2019.
- [5] P. Radziszewski et al., "Ageing evaluation of foamed polymer modified bitumen with bio-flux additive," *Materials*, vol. 16, no. 6, p. 2167, 2023.
- [6] Y. R. Kim, *Modeling of Asphalt Concrete*, 1st ed. New York, NY, USA: McGraw-Hill Education, 2009.
- [7] T. Zhen et al., "Multiscale evaluation of asphalt aging behaviour: A review," *Sustainability*, vol. 15, no. 4, p. 2953, 2023.
- [8] D. N. Little, D. H. Allen, and A. Bhasin, *Modeling and Design of Flexible Pavements and Materials*, Springer, 2017.
- [9] N. Dehouche, M. Kaci, and K. A. Mokhtar, "Influence of thermo-oxidative aging on chemical composition and physical properties of polymer modified bitumens," *Constr. Build. Mater.*, vol. 26, no. 1, pp. 350–356, 2012.
- [10] F. Wang et al., "Correlation of asphalt performance indicators and aging degrees: A review," *Constr. Build. Mater.*, vol. 250, p. 118824, 2020.
- [11] O. Sirin, D. K. Paul, and E. Kassem, "State of the art study on aging of asphalt mixtures and use of antioxidant additives," *Adv. Civ. Eng.*, vol. 2018, p. 1, 2018.
- [12] N. C. L. Madeira, V. Lacerda, and W. Romão, "Characterization of asphalt aging by analytical techniques: A review on progress and perspectives," *Energy Fuels*, vol. 36, no. 11, pp. 5531–5549, 2022.
- [13] S.-J. Lee, S. N. Amirkhanian, K. Shatanawi, and K. W. Kim, "Short-term aging characterization of asphalt binders using gel permeation chromatography and selected Superpave binder tests," *Constr. Build. Mater.*, vol. 22, no. 11, pp. 2220–2227, 2008.
- [14] S.-J. Lee, S. N. Amirkhanian, and K. W. Kim, "Laboratory evaluation of the effects of short-term oven aging on asphalt binders in asphalt mixtures using HP-GPC," *Constr. Build. Mater.*, vol. 23, no. 9, pp. 3087–3093, 2009.
- [15] H. Zhang et al., "Effect of long-term laboratory aging on rheological properties and cracking resistance of polymer-modified asphalt binders at intermediate and low temperature range," *Constr. Build. Mater.*, vol. 226, pp. 767–777, 2019.
- [16] X. Liu, T. Li, and H. Zhang, "Short-term aging resistance investigations of polymers and polyphosphoric acid modified asphalt binders under RTFOT aging process," *Constr. Build. Mater.*, vol. 191, pp. 787–794, 2018.
- [17] T. Jin et al., "Laboratory short-term aging of crumb rubber modified asphalt: RTFOT temperature optimization and performance investigation," *J. Clean. Prod.*, vol. 434, p. 140327, 2024.
- [18] S. Wang and W. Huang, "Investigation of aging behavior of terminal blend rubberized asphalt with SBS polymer," *Constr. Build. Mater.*, vol. 267, p. 120870, 2021.
- [19] EN 12607-1: Bitumen and Bituminous Binders – Determination of the Resistance to Hardening under Influence of Heat and Air – Part 1: RTFOT Method, CEN, 2014.
- [20] J. Xie and Z. Guo, "Researching on fatigue model of asphalt mixtures," *J. Highway Transp. Res. Dev.*, vol. 2, no. 2, pp. 25–29, 2007.
- [21] D. W. Christensen, D. A. Anderson, and G. M. Rowe, "Relaxation spectra of asphalt binders and the Christensen–Anderson rheological model," *Road Mater. Pavement Des.*, vol. 18, no. sup1, pp. 382–403, 2017.
- [22] F. Liu, Z. Zhou, and X. Zhang, "Linking chemical to rheological properties of asphalt binder with oxidative aging effect," *Road Mater. Pavement Des.*, vol. 22, no. 9, pp. 2014–2028, 2021.

- [23] K. Zhao and Y. Wang, "Influences of aging conditions on the rheological properties of asphalt binders," *Int. J. Pavement Eng.*, vol. 21, no. 5, pp. 653–665, 2020.
- [24] M. C. Cavalli et al., "Effect of ageing on the mechanical and chemical properties of binder from RAP treated with bio-based rejuvenators," *Compos. B Eng.*, vol. 141, pp. 174–181, 2018.
- [25] P. L. D. et al., "Impact of asphalt aging temperature on chemo-mechanics," *RSC Adv.*, vol. 9, no. 21, pp. 11602–11613, 2019.
- [26] M. Akpolat, B. V. Kök, and E. Aydoğmuş, "Research on the rheological properties of asphalt binder modified by fume silica and crumb rubber compound," *Period. Polytech. Civ. Eng.*, 2022.
- [27] D. Lesueur et al., "Relationships between the structure and the mechanical properties of paving grade asphalt cement," *Asphalt Paving Technol.*, vol. 66, 1997.
- [28] D. Lesueur et al., "Impact of the asphalt binder rheological behavior on the value of the  $\Delta T_c$  parameter," *Constr. Build. Mater.*, vol. 293, p. 123464, 2021.
- [29] D. Kaya Özdemir, "Temperature susceptibility and rheological aging characteristics of the bitumen having different penetration grades," *Black Sea J. Eng. Sci.*, vol. 4, no. 4, pp. 209–213, 2021.



## Kamusal Alanlarda Transfer Öğrenme Tabanlı Hasar Tespiti

Tuğçe KELEŞ<sup>1\*</sup>, Suha TEMUR<sup>2</sup>, Furkan KILINÇ<sup>3</sup>, Mehmet Veysel GÜN<sup>4</sup>,  
Şengül DOĞAN<sup>5</sup>, Türker TUNCER<sup>6</sup>

<sup>1,2,3,4,5,6</sup>Adli Bilişim Mühendisliği Bölümü, Teknoloji Fakültesi, Fırat Üniversitesi, Elazığ, Türkiye.

<sup>1</sup>tkeles@firat.edu.tr, <sup>2</sup>shatmr2304@gmail.com, <sup>3</sup>fkilinc732@gmail.com, <sup>4</sup>mvgun@firat.edu.tr, <sup>5</sup>sdogan@firat.edu.tr,  
<sup>6</sup>turkertuncer@firat.edu.tr

Geliş Tarihi: 11.11.2024  
Kabul Tarihi: 27.04.2025

Düzeltilme Tarihi: 23.12.2024

doi: <https://doi.org/10.62520/fujece.1583372>  
Araştırma Makalesi

Alıntı: T. Keleş, S. Temur, F. Kılınç, M. V. Gün, Ş. Doğan ve T. Tuncer'' Kamusal alanlarda transfer öğrenme tabanlı hasar tespiti'', Fırat Üni. Deny. ve Hes. Müh. Derg., vol. 4, no 2, pp. 290-306, Haziran 2025.

### Öz

Kentlerde hızla artan nüfus ve yoğun kentleşme süreci, kamusal alanların etkin yönetimini ve bu alanlardaki altyapının sürdürülebilirliğini önemli hale getirmiştir. Bu süreç, kent yönetimlerini kamusal alanlardaki hasarların hızlı ve doğru bir şekilde tespiti için yenilikçi çözümler aramaya itmiştir. Geleneksel hasar tespit yöntemleri yavaş ve maliyetli olup, büyük kentlerin dinamik yapısı karşısında yetersiz kalmaktadır. Bu durum kentsel güvenliği ve yaşam kalitesini olumsuz etkilemektedir. Bu noktada, derin öğrenme ve yapay zeka teknolojilerinin hasar tespit süreçlerini otomatik hale getirerek bu soruna bir çözüm sunduğu görülmektedir. Bu çalışmada, kentlerdeki kamusal alanlardaki hasarların otomatik olarak tespiti için yapay zeka tabanlı bir sistem geliştirilmiştir. Düşük kaynak gereksinimi ve elde ettiği yüksek başarı oranı ile MobileNetv2 modeli kullanılmıştır. Veri kümesinin sınırlı olması nedeniyle meydana gelebilecek aşırı uyum sorununu önlemek için veri artırma yöntemleri uygulanmıştır. Model, doğruluk, hassasiyet, geri çağırma ve F1 skoru açısından sırasıyla %83,33, %84,20, %83,30 ve %83,70 başarı elde etmiştir. Bu sonuçlar sayesinde modelin farklı hasar tiplerini iyi bir oranda tespit ettiği görülmektedir. Bu çalışmanın sonuçları, günümüzün hızla kentleşen dünyasında yenilikçi bir çözüm sunmaktadır. Bu çözüm altyapı unsurlarında meydana gelen hasarları hızlı ve etkili bir şekilde tespit ederek şehir yönetimlerine etkili bir yol haritası sunacaktır. Bu durum, hızlı kentleşmenin getirdiği sorunların çözülmesine olanak tanır. Bu kapsamda gerçekleştirilen çalışma hem teorik hem de pratik açıdan önemli bir değer taşımaktadır.

**Anahtar kelimeler:** Yapay zeka, Kamusal alanlar, Hasar tespiti

\*Yazışılan Yazar

İntihal Kontrol: Evet – Turnitin

Şikayet: [fujece@firat.edu.tr](mailto:fujece@firat.edu.tr)

Telif Hakkı ve Lisans: Dergide yayın yapan yazarlar, CC BY-NC 4.0 kapsamında lisanslanan çalışmalarının telif hakkını saklı tutar.



## Transfer Learning Based Damage Detection in Public Areas

Tugce KELES<sup>1\*</sup> , Suha TEMUR<sup>2</sup> , Furkan KILINC<sup>3</sup> , Mehmet Veysel GUN<sup>4</sup> ,  
Sengul DOGAN<sup>5</sup> , Turker TUNCER<sup>6</sup> 

<sup>1,2,3,4,5,6</sup>Department of Digital Forensic Engineering, Faculty of Technology, Firat University, Elazig, Türkiye.

<sup>1</sup>tkeles@firat.edu.tr, <sup>2</sup>shatmr2304@gmail.com, <sup>3</sup>fkilinc732@gmail.com, <sup>4</sup>mvgun@firat.edu.tr,

<sup>5</sup>sdogan@firat.edu.tr, <sup>6</sup>turkertuncer@firat.edu.tr

Received: 11.11.2024

Accepted: 27.04.2025

Revision: 23.12.2024

doi: <https://doi.org/10.62520/fujece.1583372>

Research Article

Citation: T. Keleş, S. Temur, F. Kılınç, M. V. Gün, Ş. Doğan and T. Tuncer, "Transfer learning based damage detection in public areas", *Firat Univ. Jour. of Exper. and Comp. Eng.*, vol. 4, no 2, pp. 290-306, June 2025.

### Abstract

The rapidly increasing population and dense urbanization process in cities have made the effective management of public spaces and the sustainability of the infrastructure in these areas important. This process has led city administrations to seek innovative solutions for rapid and accurate detection of damage in public spaces. Traditional damage detection methods are slow and costly, and are insufficient in the face of the dynamic structure of large cities. This situation negatively affects urban security and quality of life. At this point, it is seen that deep learning and artificial intelligence technologies offer a solution to this problem by automating damage detection processes. In this study, an artificial intelligence-based system has been developed for automatic detection of damage in urban public spaces. The MobileNetv2 model was used with its low resource requirement and high success rate. Data augmentation methods were applied to prevent the overfitting problem that may occur due to the limited dataset. The model achieved 83.33%, 84.20%, 83.30% and 83.70% success in terms of accuracy, precision, recall and F1 score, respectively. These findings demonstrate that, the model detects different damage types at a good rate. The results of this study provide an innovative solution in today's rapidly urbanizing world. This solution will provide an effective roadmap to city administrations by quickly and effectively detecting damage to infrastructure elements. This facilitates addressing challenges caused by rapid urbanization. The study carried out in this context has significant value both theoretically and practically.

**Keywords:** Artificial intelligence, Public areas, Damage detection

\*Corresponding author

## **1. Introduction**

Today, urban growth and urban population density are rapidly increasing. This poses a threat to the infrastructure of cities. As a result, problems such as sustainability and the effective management of infrastructure have become increasingly important. Public areas, which are at the center of society, have an important place in social life. Damage, wear and tear of infrastructure components such as roads, benches, sidewalks, street lights and parking areas cause problems [1]. These problems can create visual, functional or security problems [2]. For example, damage to roads causes traffic accidents, while damage to other infrastructure elements directly affects people's quality of life. Failure to intervene quickly in problems in infrastructure elements increases the cost of repair. Delayed repairs also cause further deterioration of infrastructure elements. As a result, larger problems occur and economic losses occur. This also reveals the need for city administrations to use resources primarily in infrastructure repair. Today, the detection of these damages is based on intensive manpower labor. Manual inspections and controls in large cities are very time-consuming and costly. However, these inspections can be prone to error. Such reasons can make it difficult to detect damages accurately and quickly. Traditional methods may be inadequate due to the dynamically changing structure of large and developing cities [3]. In light of these limitations, AI-based methods have emerged as promising alternatives. Today, with the continuous development of technology, advances are also being made in the field of artificial intelligence and image processing. As a result of these developments, studies can be conducted in different disciplines. This study also offers an important opportunity for the damage detection process in public areas [4]. Deep learning methods can reach high accuracy rates in image analysis using convolutional neural networks (CNN) [5]. In this way, processes become faster and more reliable, and high costs can be reduced [6]. City administrations can prioritize necessary repairs by taking this process into account. This can provide an effective roadmap for more effective and efficient use of resources.

The motivation of this study is to address infrastructure problems in public areas and to offer an innovative approach to traditional solutions. The aim of the study is to develop a system that can automatically detect damages in infrastructure in social settlement areas. The developed system aims to accelerate the detection of damages and achieve high accuracy by using deep learning models. In addition, a large and constantly changing dataset will be created by encouraging citizen participation. In this way, not only dataset diversity but also individuals are active in solving problems. This will be the first step in creating livable cities and sustainability. The performance of deep learning models will be evaluated at regular intervals using the dataset, which will be constantly updated with the participation of citizens. Another aim of this project is to increase city security, improve the quality of life of individuals and make resource management more efficient. The study also aims to eliminate the deficiencies in the literature. When the studies in the literature are examined, most damage detection studies usually focus on a single category. However, most datasets are static and inadequate to reflect different regions and conditions. Unlike previous studies, this study was conducted on more than one class. In addition, the fact that the dataset will be updated regularly is one of the unique aspects of the project. This system, which aims to ensure the security and order of public spaces in cities, has the potential to offer significant innovations both theoretically and practically.

### **1.1.Literature review**

In the literature, studies on detecting various types of damage in public spaces in cities are limited, with most existing research primarily focusing on crack detection. Studies on crack detection employ advanced image processing and artificial intelligence techniques to identify specific types of damage and to facilitate the classification of these types. However, these studies typically concentrate on a single class of damage, neglecting a broader spectrum of damage categories. Some of the studies conducted in the literature are reviewed as follows.

Shim et al. [7] sought to detect road damage by using super-resolution and semi-supervised learning techniques with generative adversarial network (GAN). The researchers aimed to improve the quality of road damage images and increase damage detection performance in cases where there is a limited number of labeled images. To improve image quality, super-resolution generative adversarial network (SRGAN) is



applied and combined with semi-supervised learning method. As a result of the proposed method, an F1 score of 79.22% was obtained. Bibi et al. [8] developed a system that identifies road defects using Edge AI. The study aimed to help vehicles recognize road hazards and defects, such as potholes, bumps and cracks. The dataset, created using images collected from various online sources and open datasets, was trained on ResNet-18 and VGG-11 models. While ResNet-18 provided 100% accuracy for bumps and cracks, VGG-11 achieved accuracy rates of over 99% for cracks and potholes. The study focused on only four damage types. Kyslytsyna et al. [9] proposed a method called ICGA to detect road surface cracks. This model, which was developed to eliminate the difficulties that cGANs experience in shape detection despite their high accuracy, consists of two stages. This model, which removes non-road elements as noise in the first stage and only detects cracks in the second stage, reached an accuracy rate of 88.03% in the Llamas dataset containing 100,000 labeled photographs. Ye et al. [10] proposed a detection network architecture that uses deep learning-based dilated convolution for detecting concrete cracks. They also employed a watershed algorithm to segment the detected cracks. In the proposed STCNet I architecture, the number of parameters is lower and the computation speed is higher compared to traditional networks. While the VGG16 architecture achieved an accuracy of 99.29% and the ResNet50 architecture reached 96.67% accuracy, the STCNet I architecture obtained an accuracy rate of 99.33%. Zou et al. [11] proposed a fully automated method called CrackTree for detecting cracks from road images. To test this method, they collected 206 pavement images containing different types of cracks. Initially, they devised a geodesic shadow removal algorithm to eliminate road shadows while retaining the cracks. Subsequently, they generated a crack probability map through tensor voting, enhancing the connectivity of crack segments by ensuring proximity and curve continuity. Lastly, by selecting crack seed samples from the probability map and representing these seeds with a graph model, they extracted minimum spanning trees from the graph and conducted iterative pruning of tree edges to accurately identify the targeted cracks. The proposed CrackTree method achieved an average F-measure of 85%. Fan et al. [12] designed a new network called U-HDN for crack detection. This network is designed to add multi-scale features to a U-net based encoder-decoder architecture. Using the multiple expansion modulus (MDM), crack information was obtained through expanded convolutions with different expansion rates. Additionally, a hierarchical feature learning module is developed to extract multi-scale features. U-HDN outperformed other methods with an F1 score of 92.4%. Mandal et al. [13] proposed an automatic sidewalk problem analysis system using YOLO v2 deep learning. In their study, a dataset was created containing road images of 9,053 different types of cracks, obtained from a smartphone mounted on a vehicle. During the training phase, 7,240 images captured by mobile cameras were used, and 1,813 road images were employed in the testing phase. The model attained an F1 score of 87,80% for detection without predicting the crack class and 73.94% for classification including the crack class. Zhang et al. [14] introduced a deep learning method for crack detection. In their study, a dataset of 500 images with a resolution of 3264 by 2448 pixels, collected using a smartphone, was utilized. A supervised deep convolutional neural network was utilized to classify each image patch within the collected dataset. The proposed ConvNet-based method achieved an F1 score of 89.65%.

## **1.2. Literature gap**

When the studies conducted in the literature are examined, it is seen that the number of studies on damage detection in public areas is limited. However, the studies conducted have focused on a single or small number of damage types. These studies generally examine cracks on the road surface. Damage detection studies focusing on different infrastructure elements in public areas are insufficient. This shows that the existing studies focus on narrow-scope problems. Comprehensive studies addressing different types of damage in public area infrastructures are quite limited. This is seen as an important gap in the literature. Methods that allow for detailed examination of various damage types are needed. In addition, when the existing studies are analyzed, it is seen that the datasets used contain a limited number of classes. This is one of the reasons that restricts the studies conducted in this field. The datasets used in this field have a static structure. For this reason, the studies conducted are not sustainable. In this study, a dynamic dataset was created in order to eliminate the deficiency in this field. The created dataset will be continuously updated depending on time and region. In this way, it is possible for different damage types to emerge and the number of classes to increase. When the studies are examined, it is seen that a comprehensive and dynamic approach is needed to identify different types of damage in public spaces and to help the decision-making mechanisms of city

administrations. The aim of this study is to eliminate these deficiencies and offer an innovative solution by presenting a flexible and applicable method in different regions.

### **1.3. Novelities**

- When the studies conducted in the literature are examined, it is seen that the studies conducted in the field of damage detection generally have a small number of classes. In contrast to prior research, this study expands the number of damage classes. A comprehensive dataset including 12 different damage types has been created to be used in the study. The created dataset is more comprehensive than the existing datasets in terms of the number of classes. In this respect, it is aimed to make a significant contribution to the literature.
- It is aimed to continuously update the created dataset. In this way, the dataset will be renewed and expanded depending on different regions and different times.
- In the study, unlike the studies with a small number of classes in the literature, a multi-class damage detection process has been carried out. In this way, different damage types have been separated from each other and detailed examination has been carried out.
- The developed method has a flexible architecture. It is possible to add different classes and different damage types to the dataset. This increases the applicability of the system in different cities and regions.
- The developed system has an architecture suitable for working on mobile devices. In this way, it can be used in real-time applications with future studies.

### **1.4. Contributions**

- In this study, unlike the limited datasets in the literature, the most comprehensive dataset has been created to our knowledge. The created dataset has 12 classes. With this diversity, it is possible for the proposed model to detect different damage types.
- The dataset will continue to be updated continuously. In this way, different damage types from different regions will be added.
- The proposed system performs the damage detection process quickly and accurately. In this way, resources can be used more efficiently. This will allow for increased public safety.
- Unlike single-class studies in the literature, an innovative solution has been presented with multi-class examination.
- The proposed system is compatible with mobile devices. This provides a significant advantage for real-time applications in future studies.

## **2. Material and Method**

### **2.1. Material**

The first step of this study is the data collection phase. In this phase, images of specific objects from different cities and regions were collected. Then, these images were labeled as damaged and intact. As a result of the data collection process, a comprehensive dataset was created. The data collection process is shown in Figure 1.

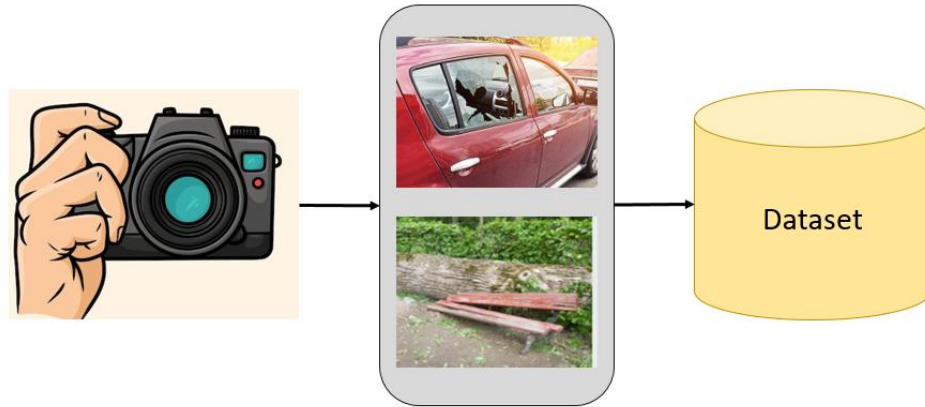


**Figure 1.** Data collection phase

First, the objects focused on in the study were determined. These objects include roads, benches, trash cans, pavement stones, street lamps and windows. Then, damaged and intact labels were defined for each infrastructure element based on certain standards. Images collected from different regions with different mobile phones were classified as damaged and intact. Sample images of each class in the obtained dataset are shown in Figure 2.



**Figure 2.** Classes and sample images in the dataset.

Data augmentation was performed to prevent negative situations such as overfitting that may occur due to the limited number of images in the obtained dataset. Data augmentation is a method used in machine learning and deep learning models to increase the number of data. The purpose of this method is to increase the dataset with various methods and thus increase the performance of the model [15]. In the data augmentation process applied in this study, images were rotated by 90, 180 and 270 degrees. For each image in the original dataset, three different variations were created that allowed the model to be trained with

variations obtained from different angles. As a result, it was aimed to reduce the overfitting tendency of the model and to achieve high performance.

The resulting dataset consists of 12 classes, 6 damaged/broken classes and 6 healthy classes. Each class contains a minimum of 701 and a maximum of 3,436 images, and the total dataset consists of 23,508 images, as presented in Table 1.

**Table 1.** Dataset Details

No	Name	Quantity	
		Without augmentation	With augmentation
1	Damaged Sidewalk	442	1768
2	Damaged Road	859	3436
3	Damaged Lamp	254	1019
4	Broken Bench	309	1236
5	Broken Window	680	2720
6	Broken Trash Bin	175	701
7	Intact Sidewalk	703	2812
8	Intact Road	554	2216
9	Intact Lamp	816	3264
10	Intact Bench	265	1060
11	Intact Window	222	888
12	Intact Trash Bin	597	2388

## 2.2. Method

The method used in the study consists of data preparation, comparison of traditional CNN architectures, feature selection and classification steps. This process is shown step by step in Figure 3;

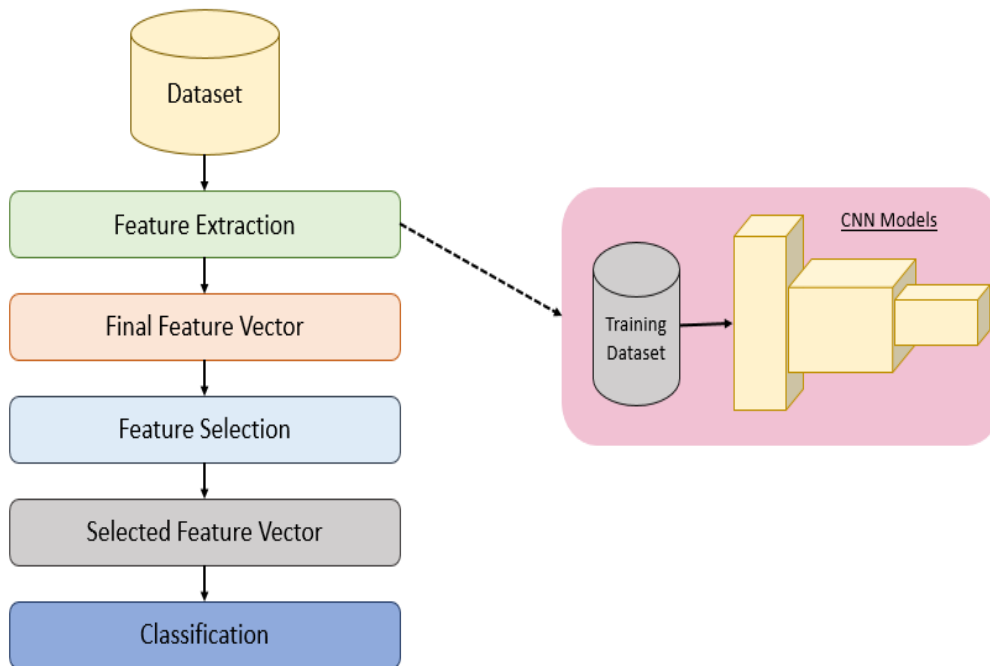


**Figure 3.** Steps of the method used in the study

In the development process of machine learning models, CNN architectures have been actively used. In this process, the first step included organizing the dataset into test and training folders. Then, CNN architectures widely used in the literature such as ResNet50 [16], MobileNetV2 [17], GoogleNet [18], AlexNet [19], InceptionResNetV2 [20], DenseNet201 [21], InceptionV3 [22], DarkNet-53 [23] were examined and the accuracy rates of each architecture were compared. The accuracy rates obtained by the compared CNN architectures [24] are shown in Figure 4. The obtained results revealed that MobileNetV2 performed well with an accuracy rate of 83.3%

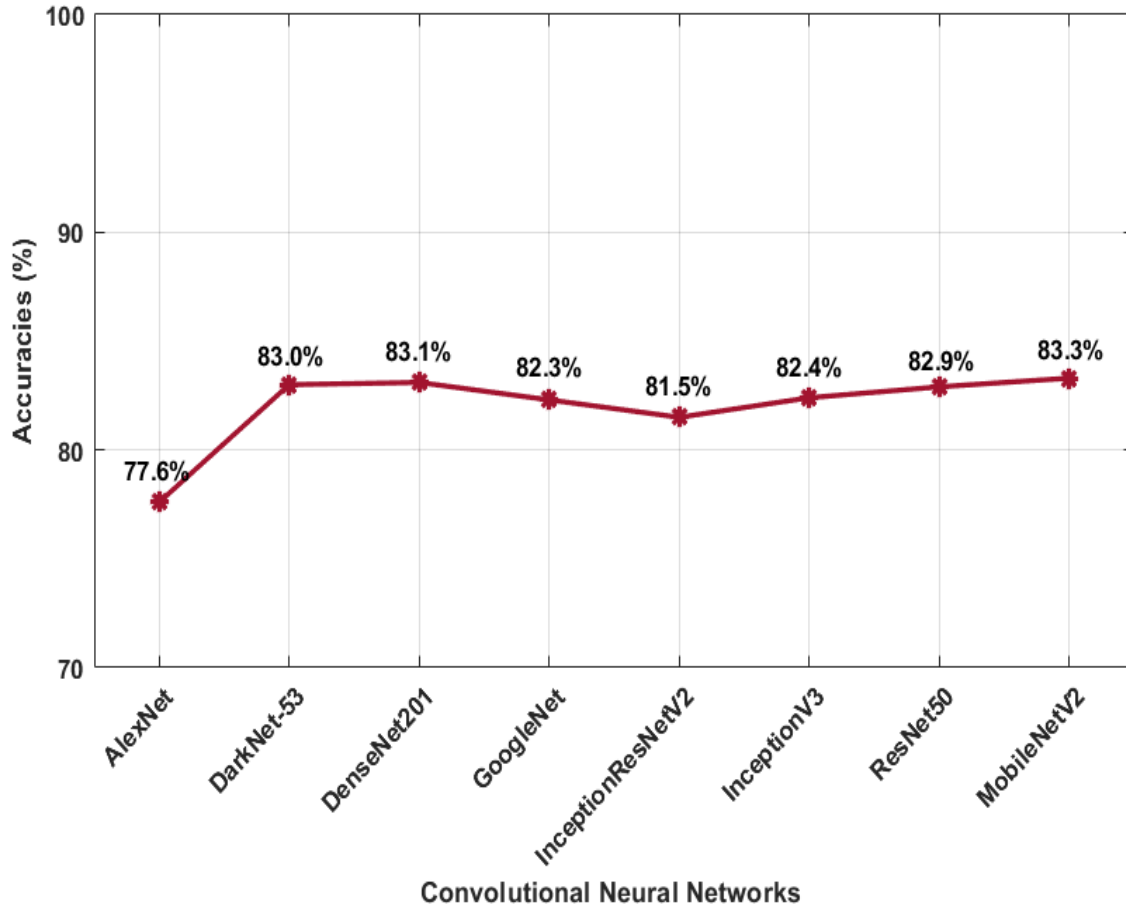


**Figure 4.** Comparison of accuracy rates of different neural networks

In addition, MobileNetV2 [17], uses depth-discrete convolutions and invert residual blocks. This design reduces model parameters and computational cost without sacrificing accuracy. It prevents gradient loss with residual connections and enables complex feature recognition.

MobileNetV2 [17] a lightweight deep learning model, is designed for mobile devices and embedded systems. The model, which performs object detection and segmentation tasks, has less computational and memory usage in image classification. It was introduced by Google as an improved version of MobileNetV1. It has 3.4 million parameters and 154 layers. Its performance has been increased with improved layer structures such as inverse residual blocks and linear bottleneck layers. The architecture of the model is shown in Figure 5.



**Figure 5.** MobileNetV2 architecture

MobileNetV2 provides efficient switching between bottleneck layers without information loss through inverse residual connections. It also avoids the distortion caused by nonlinear processing of low-dimensional features by using linear bottleneck layers. This also increases computational efficiency. As in MobileNetV2, it uses depth-based separable convolutions, which increases computational efficiency and helps reduce computational cost. In the convolution process of the model, the initial step is depth-directed convolution, followed by 1x1 point convolution. The MobileNetV2 architectural structure is shown in Figure 6.

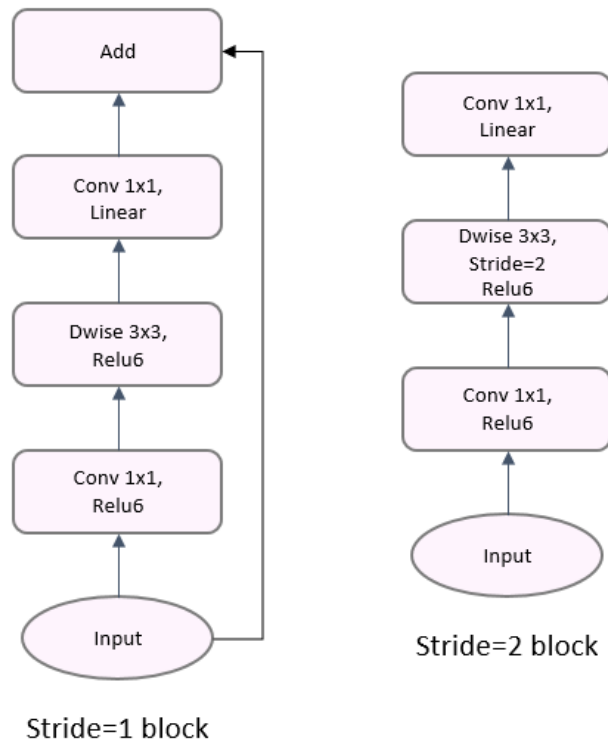


**Figure 6.** MobileNetV2 architecture 2



This structure of the architecture increases efficiency and reduces computational cost. Thanks to the expansion layer, the number of channels is increased and it processes more data. In this way, the input channels of the model are expanded and it processes more information and produces more output channels. This increases the computational power and performance of the model. Although this number of parameters is quite low compared to other CNN models, the model offers high accuracy. The 4.24 million parameters used in MobileNetV1 have been reduced to 3.47 million in MobileNetV2, further improving accuracy. Compared to MobileNetV1, MobileNetV2 has a more efficient architecture and innovations such as inverse residual connections and linear bottlenecks. It also provides efficiency in memory usage. It provides high accuracy in applications such as image classification and object detection on mobile devices.

After developing the model, feature selection step was applied to improve the result of the obtained features. Neighborhood component analysis (NCA) [25] and Chi2 algorithms [26] were used to select the best features.

While NCA performed dimensionality reduction to improve classification accuracy, Chi2 testing measured the contribution of each feature to classification and identified the most important ones. This two-stage feature selection process improved the overall performance of the model and resulted in more accurate classification results [27]. Following the feature selection phase, classification was performed with the selected features. Support Vector Machines (SVM) were preferred at this stage. SVM is an effective classification method for distinguishing between classes in high-dimensional datasets [28]. In this study, the SVM model successfully classified damaged road and pavement images. As a result of the classification, the data was divided into categories such as "Damaged Pavement," "Damaged Road" and "Intact Trash Can" and damage detection was divided into groups based on these categories.

### 3. Results

In this study, it is aimed to perform damage detection of infrastructure elements in public areas. For this purpose, the performances of different convolutional Neural Networks architectures are examined and compared. The examined models include AlexNet, Darknet53, DenseNet201, GoogLeNet, InceptionResNetV2, InceptionV3, MobileNetV2 and ResNet50 architectures. As seen in Table 2, the accuracy rates obtained from the examined models are listed below.

**Table 2.** Comparison of results from different neural networks

CNN Models	Accuracies (%)
AlexNet	77.6%
Darknet53	83.0%
DenseNet201	83.1%
GoogLeNet	82.3%
InceptionResNetV2	81.5%
InceptionV3	82.4%
MobileNetV2	83.3%
ResNet50	82.9%

Within the scope of the project, various classification models were tested and their accuracy rates were calculated. Table 3 presents the accuracy rates of the tested classifiers.

**Table 3.** Comparison of Accuracy Rates of Different Models

Classifiers Names	Accuracy (%)
Fine Tree	57.0
Boosted Trees	64.0
Bagged Trees	72.8
Linear Discriminant	76.6
SVM Kernel	81.5
Medium Gaussian SVM	80.0
Quadratic SVM	82.5
Cubic SVM	83.3

MobileNetV2 model was used together with Cubic SVM, reaching the highest accuracy rate of 83.33% and demonstrating high performance.

A confusion matrix was also created to further evaluate the success of the classification model. This matrix, shown in Figure 7, reveals how accurately the model predicts each class and the cases of misclassification.

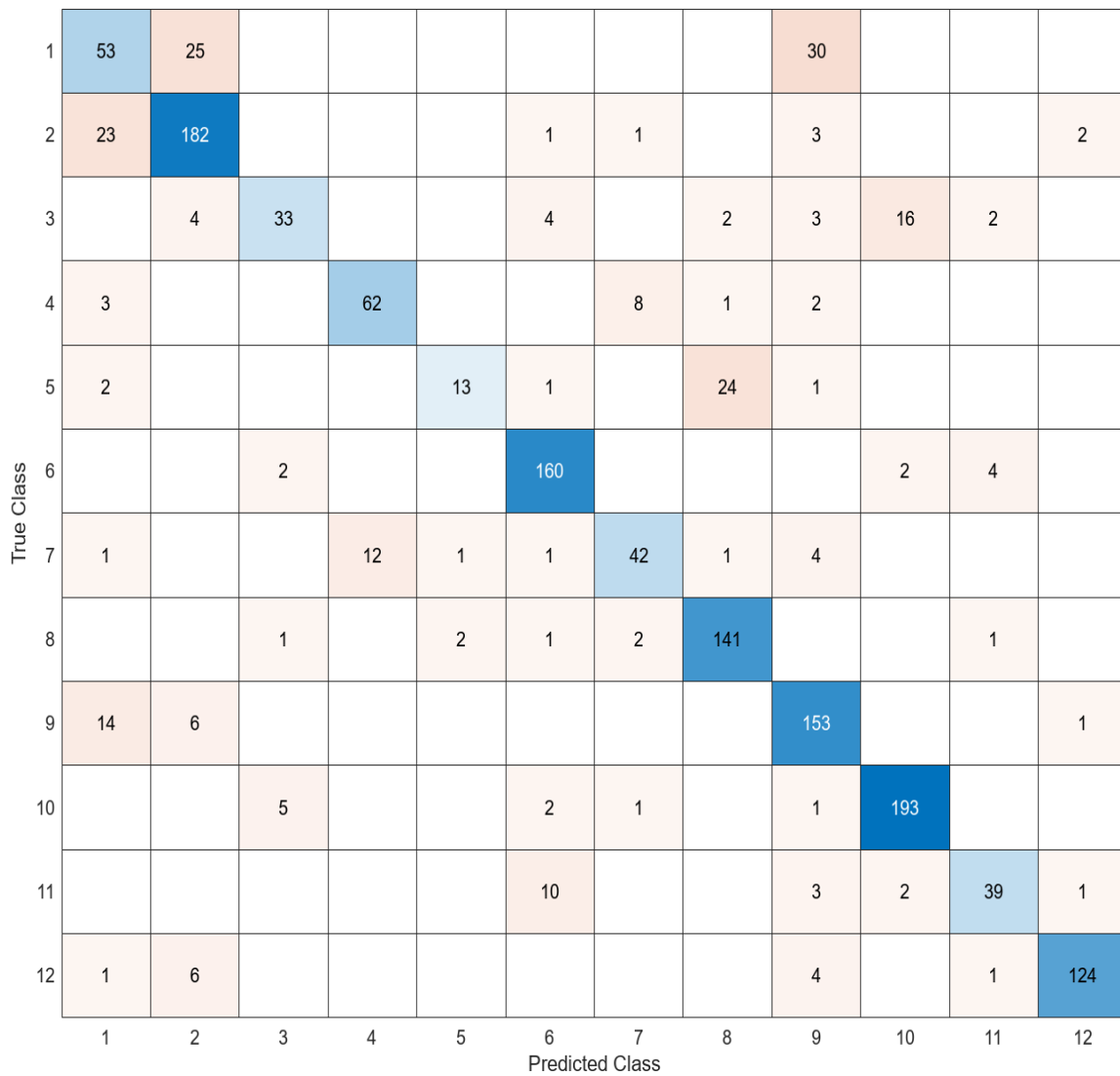


**Figure 7.** Confusion Matrix

For an overall evaluation of this performance, the average accuracy, precision, recall and F1 score for all classes were calculated and the results are presented in Table 4 [29]:

Accuracy: Accuracy is the ratio of all correct predictions to the total predictions and is calculated as in Equation 1:

$$\frac{TP + TN}{TP + TN + FP + FN} \quad (1)$$

Precision: Precision shows how many of the classes the model positively predicts are correct. It is calculated as in Equation 2:

$$\frac{TP}{TP + FP} \quad (2)$$

Recall: Recall indicates how accurately the model detects classes that are actually positive. It is calculated as in Equation 3:

$$\frac{TP}{TP + FN} \quad (3)$$

F1 Score: F1 Score is the harmonic average of Precision and Recall and provides a balanced evaluation. It is calculated as in Equation 4:

$$2 * \frac{Pre * Rec}{Pre + Rec} \quad (4)$$

**Table 4.** Overall Evaluation of the Proposed Model

Metric	Value (%)
Accuracy	83.33
Precision	84.20
Recall	83.30
F1 Score	83.70

This MobileNetV2 based method applied in the study achieved 83.33%, 84.20%, 83.30% and 83.70% accuracy rates in accuracy, precision, recall and F1 score, respectively. High accuracy rate was achieved in the detection of damage types with the classification step performed after feature selection. The proposed method is not dependent on the dataset used in this study and can be applied in different scenarios. Another advantage of the method is that it can obtain effective results even with limited resources such as mobile devices. The obtained results provide an important resource for the automatic detection of damaged infrastructure objects in public areas.

#### 4. Discussion

The dataset used in this study covers more classes compared to the datasets found in the literature. The created dataset includes 12 different classes that include both damaged and intact states of objects such as benches, street lamps, trash cans, sidewalks and roads in public areas. Unlike most literature studies, a multi-class classification task was performed rather than a single class. MobileNetV2 architecture was preferred to process this classification structure, and in the discussion section, the performance of this architecture on multiple classes, the accuracy of the model, its comparison with other studies in the literature, its advantages and limitations will be examined.

In Figure 8, the accuracy rates of the models obtained using various classification algorithms are presented comparatively. This analysis details the performance of classifiers such as Fine Tree, Boosted Trees, Bagged Trees, Linear Discriminant, SVM Kernel, Medium Gaussian SVM, Quadratic SVM and Cubic SVM. The results reveal that the models differ significantly in terms of accuracy. While the Fine Tree algorithm achieved the lowest accuracy rate with 57%, the highest accuracy rate was provided by Cubic SVM with 83.3%. These results reveal which model performs best under the given conditions, allowing for a comparison of the effectiveness of different classifiers on the dataset.

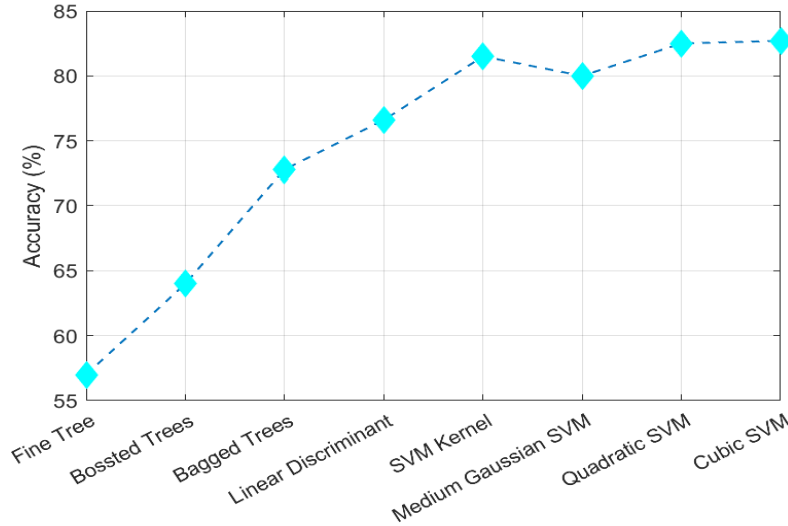


**Figure 8.** Comparison of Accuracy Rates of Different Models

The findings of other studies in the literature are summarized to help better understand the current knowledge in the literature. A comparative analysis was made with the results of this study. The findings obtained are shown in Table 5.

**Table 5.** Literature review

Study	Method	Dataset	Results (%)
Xu et al. [30]	Transformer-based deep neural network	Stone331, CrackLS315, CrackTree260, CrackWH100	Avr. precision: 93.04%, Recall: 92.85%
Hu et al. [31]	YOLOv5l	3001 images	Accuracy: 88.1%
Huyan et al. [32]	CrackU-net	3000 images	Accuracy: 99.01%
Chen et al. [33]	Customized-CNN	2000 images	Accuracy: 90%
Liu et al. [34]	YOLOv3 and U-Net	27,966 images	Precision: 91.95%, Recall: 89.31%, F1 score: 90.58%
Djenouri et al. [35]	IGCNN-RCD	CrackTree, CrackForest ALE	Precision: Over 70%
Ahmedi et al. [36]	Machine Learning Model	400 images	%93,86
Haciefendioglu et al. [37]	Faster R-CNN	323 images	Sunny day and a cloudy day: 100% Foggy day: 50%
Nguyen et al. [38]	Customized-CNN	2StagesCrack	F1 score: 90.00%
Our study	MobileNetV2	Our dataset	Accuracy: 83.33%

Beyond technical accuracy, the model's practical utility is enhanced by enabling citizen participation. The accuracy rate achieved by the model can be beneficial not only in theory but also in real-world applications. Damage detection in public areas is carried out by municipal teams. This process is time-consuming and costly. In addition, the scope of the study can be expanded with the participation of citizens. Thanks to the participation of citizens, the infrastructure of cities can be continuously monitored and city administrations will be faster and more effective. Citizens can report infrastructure problems through mobile phones or mobile applications. In this way, city administrations can carry out repairs faster, which prevents greater economic losses. For example, citizens can report broken roads or broken banks to the municipality through mobile applications. The image uploaded to the application is classified by the developed system and can accelerate the repair process by directing municipal teams to this area. In addition, critical infrastructure problems such as roads and bridges after natural disasters can be reported and rescue and repair processes can be accelerated. By encouraging the participation of citizens, data diversity will increase thanks to the data obtained from different regions and conditions. In addition, citizens will become more sensitive and will directly contribute to infrastructure improvement. As a result of all this, the decision-making mechanism of city administrations will be assisted and resources will be used more effectively.

#### **4.1. Advantages**

1. Designed for mobile devices, MobileNetv2 has significant advantages for limited capacity applications.
2. In this study, data augmentation was applied to increase the performance of the model.
3. This study was carried out on 12 different classes.
4. Thanks to the optimization of the model, it allows it to be used in real-time applications in future studies.
5. The dataset created with the contribution and feedback of citizens can be improved up-to-date.

#### **4.2. Limitations**

1. The images in the dataset used in the study are concentrated in certain regions. And have a small number of damage types. This can make it difficult to apply the model to different regions and different damage types.
2. The images in the dataset consist of images taken by citizens from their mobile phones. This introduces variability in image quality and angle, which may affect model performance.
3. MobilNetv2, which is optimized for mobile devices, may experience difficulties in applications as the dataset grows.

#### **5. Conclusion**

In this study, MobileNetV2 model was used to detect different types of damages in infrastructure objects located in public areas in cities. The dataset used in the study is limited. Therefore, a data augmentation technique was applied by rotating the images at different angles in order to achieve better model accuracy. In this way, a high success rate was achieved in the damage detection task. The model achieved 83.33%, 84.20%, 83.30% and 83.70% accuracy rates in accuracy, precision, recall, and F1 score, respectively. The results obtained from the study show that the model detects different types of damage with good accuracy and is adaptable to different scenarios. Another advantage of the proposed method is its strong performance on resource-constrained platforms such as mobile devices. Thus, it increases the possibility of deployment in practical urban applications. One of the important factors in increasing the performance of the model is the application of the feature selection stage together with data augmentation. Overfitting was prevented with these techniques. This study aims to automate the maintenance of social centers in cities by increasing the performance of the model. As a result of the findings, it is demonstrated that different types of damage can be detected quickly and reliably. This enables city administrations to use resources efficiently and follow an efficient path in repair interventions. In addition, it helps improve the quality of life of the society and contribute to sustainability by encouraging the participation of citizens.

## **6. Future Directions**

The findings of this method based on the Mobilenetv2 model have been explained in detail in the previous sections. However, suggestions for the diversity and development of future studies are as follows:

- The dataset used in the study is currently limited. In future studies, the dataset can be expanded by adding different damage types from different regions to increase the applicability of the model to different scenarios.
- Higher resolution images can be added so that the model can detect smaller and more complex damage types.
- To be proposed as a practical tool for municipal decision-making, the model's performance should be tested in current real-time applications.
- In future studies, applications can be implemented with different deep learning architectures and a comparison can be made with the performance of the MobileNetV2 model.
- The diversity of the dataset can be increased with different techniques such as cropping and brightness adjustments during the data augmentation process.
- Studies can be conducted on integrating the model into infrastructure repair processes to provide auxiliary support to decision-making mechanisms in cities.
- Mobile applications can be developed to encourage citizens to use it. By adding a feedback mechanism to these applications, the system's performance can be continuously improved through model updates.

## **7. Author Contribution Statement**

Author 1 contributed to Conceptualization, Methodology, Software, Investigation, Resources, Data Collection, Writing - Original Draft, Writing - Review & Editing. Author 2 was responsible for Investigation, Dataset Collection. Author 3 participated in Investigation, Dataset Collection. Author 4 contributed to Software, Methodology, Visualization. Author 5 was responsible for Validation, Formal Analysis, Investigation, Writing - Original Draft, Writing - Review & Editing, Supervision, Project Administration. Author 6 contributed to Validation, Formal Analysis, Investigation, Writing - Original Draft, Writing - Review & Editing, Supervision, Project Administration.

## **8. Ethics Committee Approval and Conflict of Interest Statement**

There is no need to obtain ethics committee permission for the prepared article. There is no conflict of interest with any person/institution in the prepared article.

## **9. Ethical Statement Regarding the Use of Artificial Intelligence**

No artificial intelligence-based tools or applications were used in the preparation of this study. The entire content of the study was produced by the authors in accordance with scientific research methods and academic ethical principles.



## 10. References

- [1] C. A. Vogt, K. L. Andereck, and K. Pham, "Designing for quality of life and sustainability," *Ann. Tour. Res.*, vol. 83, p. 102963, 2020.
- [2] S. M. Low, *Why Public Space Matters*. Oxford, U.K.: Oxford Univ. Press, 2023.
- [3] M. Reba and K. C. Seto, "A systematic review and assessment of algorithms to detect, characterize, and monitor urban land change," *Remote Sens. Environ.*, vol. 242, p. 111739, 2020.
- [4] H. S. Munawar et al., "Image-based crack detection methods: A review," *Infrastructures*, vol. 6, no. 8, p. 115, 2021.
- [5] Z. Li et al., "A survey of convolutional neural networks: analysis, applications, and prospects," *IEEE Trans. Neural Netw. Learn. Syst.*, vol. 33, no. 12, pp. 6999–7019, 2021.
- [6] V. Pham, C. Pham, and T. Dang, "Road damage detection and classification with detectron2 and faster R-CNN," in *Proc. IEEE Int. Conf. Big Data (Big Data)*, 2020, pp. 5592–5601.
- [7] S. Shim et al., "Road damage detection using super-resolution and semi-supervised learning with generative adversarial network," *Autom. Constr.*, vol. 135, p. 104139, 2022.
- [8] R. Bibi et al., "Edge AI-based automated detection and classification of road anomalies in VANET using deep learning," *Comput. Intell. Neurosci.*, vol. 2021, no. 1, p. 6262194, 2021.
- [9] A. Kyslytsyna et al., "Road surface crack detection method based on conditional generative adversarial networks," *Sensors*, vol. 21, no. 21, p. 7405, 2021.
- [10] W. Ye et al., "Deep learning-based fast detection of apparent concrete crack in slab tracks with dilated convolution," *Constr. Build. Mater.*, vol. 329, p. 127157, 2022.
- [11] Q. Zou et al., "CrackTree: Automatic crack detection from pavement images," *Pattern Recognit. Lett.*, vol. 33, no. 3, pp. 227–238, 2012.
- [12] Z. Fan et al., "Automatic crack detection on road pavements using encoder-decoder architecture," *Materials*, vol. 13, no. 13, p. 2960, 2020.
- [13] V. Mandal, L. Uong, and Y. Adu-Gyamfi, "Automated road crack detection using deep convolutional neural networks," in *Proc. IEEE Int. Conf. Big Data*, 2018, pp. 5212–5215.
- [14] L. Zhang, F. Yang, Y. D. Zhang, and Y. J. Zhu, "Road crack detection using deep convolutional neural network," in *Proc. IEEE Int. Conf. Image Process. (ICIP)*, 2016, pp. 3708–3712.
- [15] L. Perez and J. Wang, "The effectiveness of data augmentation in image classification using deep learning," *arXiv preprint, arXiv:1712.04621*, 2017.
- [16] K. He, X. Zhang, S. Ren, and J. Sun, "Deep residual learning for image recognition," in *Proc. IEEE Conf. Comput. Vis. Pattern Recognit.*, 2016, pp. 770–778.
- [17] M. Sandler et al., "MobileNetV2: Inverted residuals and linear bottlenecks," in *Proc. IEEE Conf. Comput. Vis. Pattern Recognit.*, 2018, pp. 4510–4520.
- [18] C. Szegedy et al., "Going deeper with convolutions," in *Proc. IEEE Conf. Comput. Vis. Pattern Recognit.*, 2015, pp. 1–9.
- [19] A. Krizhevsky, I. Sutskever, and G. E. Hinton, "ImageNet classification with deep convolutional neural networks," in *Adv. Neural Inf. Process. Syst.*, vol. 25, 2012.
- [20] C. Szegedy, S. Ioffe, V. Vanhoucke, and A. Alemi, "Inception-v4, Inception-ResNet and the impact of residual connections on learning," in *Proc. AAAI Conf. Artif. Intell.*, vol. 31, no. 1, 2017.
- [21] G. Huang, Z. Liu, L. Van Der Maaten, and K. Q. Weinberger, "Densely connected convolutional networks," in *Proc. IEEE Conf. Comput. Vis. Pattern Recognit.*, 2017, pp. 4700–4708.
- [22] C. Szegedy, V. Vanhoucke, S. Ioffe, J. Shlens, and Z. Wojna, "Rethinking the Inception architecture for computer vision," in *Proc. IEEE Conf. Comput. Vis. Pattern Recognit.*, 2016, pp. 2818–2826.
- [23] A. Farhadi and J. Redmon, "YOLOv3: An incremental improvement," in *Comput. Vis. Pattern Recognit.*, vol. 1804, Springer, pp. 1–6, 2018.
- [24] A. Khan, A. Sohail, U. Zahoor, and A. S. Qureshi, "A survey of the recent architectures of deep convolutional neural networks," *Artif. Intell. Rev.*, vol. 53, pp. 5455–5516, 2020.
- [25] J. Goldberger, G. E. Hinton, S. Roweis, and R. R. Salakhutdinov, "Neighbourhood components analysis," in *Adv. Neural Inf. Process. Syst.*, vol. 17, 2004.
- [26] Y. Zhai et al., "A chi-square statistics based feature selection method in text classification," in *Proc. IEEE Int. Conf. Softw. Eng. Service Sci. (ICSESS)*, 2018, pp. 160–163.

- [27] R. Aggarwal and S. Kumar, "Classification model for meticulous presaging of heart disease through NCA using machine learning," *Evol. Intell.*, vol. 16, no. 5, pp. 1689–1698, 2023.
- [28] T. Evgeniou and M. Pontil, "Support vector machines: Theory and applications," in *Adv. Course Artif. Intell.*, Springer, pp. 249–257, 1999.
- [29] M. Hossin and M. N. Sulaiman, "A review on evaluation metrics for data classification evaluations," *Int. J. Data Mining Knowl. Manag. Process.*, vol. 5, no. 2, p. 1, 2015.
- [30] Z. Xu et al., "Pavement crack detection from CCD images with a locally enhanced transformer network," *Int. J. Appl. Earth Obs. Geoinf.*, vol. 110, p. 102825, 2022.
- [31] G. X. Hu et al., "Pavement crack detection method based on deep learning models," *Wireless Commun. Mobile Comput.*, vol. 2021, no. 1, p. 5573590, 2021.
- [32] J. Huyan et al., "CrackU-net: A novel deep convolutional neural network for pixelwise pavement crack detection," *Struct. Control Health Monit.*, vol. 27, no. 8, p. e2551, 2020.
- [33] T. Chen et al., "Pavement crack detection and recognition using the architecture of SegNet," *J. Ind. Inf. Integr.*, vol. 18, p. 100144, 2020.
- [34] J. Liu et al., "Automated pavement crack detection and segmentation based on two-step convolutional neural network," *Comput.-Aided Civ. Infrastruct. Eng.*, vol. 35, no. 11, pp. 1291–1305, 2020.
- [35] Y. Djenouri et al., "Intelligent graph convolutional neural network for road crack detection," *IEEE Trans. Intell. Transp. Syst.*, vol. 24, no. 8, pp. 8475–8482, 2022.
- [36] A. Ahmadi, S. Khalesi, and A. Golroo, "An integrated machine learning model for automatic road crack detection and classification in urban areas," *Int. J. Pavement Eng.*, vol. 23, no. 10, pp. 3536–3552, 2022.
- [37] K. Hacıfendioğlu and H. B. Başağa, "Concrete road crack detection using deep learning-based faster R-CNN method," *Iran. J. Sci. Technol. Trans. Civ. Eng.*, vol. 46, no. 2, pp. 1621–1633, 2022.
- [38] N. H. T. Nguyen et al., "Two-stage convolutional neural network for road crack detection and segmentation," *Expert Syst. Appl.*, vol. 186, p. 115718, 2021.



## Şebeke Entegreli Elektrikli Araç ve Hidrojenli Araçları İçeren Otoparklar İçin Karbon Vergisi Odaklı Optimal Enerji Yönetimi

Merve LORDOĞLU<sup>1</sup>, Benu PRENCUVA<sup>2</sup>, Eda Nur TAŞ<sup>3</sup>,  
Ayşe Kübra Erenoğlu TATAR<sup>4,5</sup>

<sup>1,2,3,4</sup>Elektrik Mühendisliği Bölümü, Elektrik-Elektronik Mühendisliği Fakültesi, Yıldız Teknik Üniversitesi, İstanbul, Türkiye.

<sup>5</sup>Temiz Enerji Teknolojileri Enstitüsü, Yıldız Teknik Üniversitesi, İstanbul, Türkiye.

<sup>1</sup>merve.lordoglu@std.yildiz.edu.tr, <sup>2</sup>benu.prencuva@yildiz.edu.tr, <sup>3</sup>edanur.tas@yildiz.edu.tr, <sup>4</sup>erenayse@yildiz.edu.tr

Geliş Tarihi: 4.05.2025  
Kabul Tarihi: 19.6.2025

Düzeltilme Tarihi: 13.6.2025

doi: <https://doi.org/10.62520/fujece.1691050>  
Araştırma Makalesi

Alıntı: M. Lordoğlu, B. Prencuva, E. N. Taş ve A. K. E. Tatar, “Şebeke entegreli elektrikli araç ve hidrojenli araçları içeren otoparklar için karbon vergisi odaklı optimal enerji yönetimi”, Fırat Üni. Deny. ve Hes. Müh. Derg., vol. 4, no 2, pp. 307-321, Haziran 2025.

### Öz

Bu çalışma, fotovoltaiik (PV) üretimi, elektrikli araçlar (EV) ve yakıt hücreli elektrikli araçlar (FCEV) içeren şebeke bağlantılı bir otoparkın optimal enerji yönetimini ele almaktadır. Otopark, EV’lerin şarj taleplerine cevap verecek şekilde donatılmış olup park alanındaki elektrolizör aracılığıyla FCEV’ler için hidrojen üretimi sağlanmaktadır. Hem EV şarj gücü hem de elektrolizör talebi, PV sisteminden, enerji depolama sisteminden (ESS) veya elektrik şebekesinden esnek bir şekilde karşılanabilmektedir. Çalışmanın temel amacı, karbon vergisinin etkisini de dikkate alarak toplam işletme maliyetlerini en aza indirmektir. Karbon vergisinin dahil edilmesiyle birlikte, önerilen optimizasyon çerçevesi araç şarjı ve hidrojen üretimi süreçlerinde emisyonların azaltılmasını doğal olarak hedeflemektedir. Optimizasyon problemi, Karmaşık Tamsayılı Doğrusal Programlama (MILP) modeli olarak formüle edilmiş ve GAMS programı kullanılarak uygulanmıştır. Çözüm, CPLEX çözücüsü ile elde edilmiştir. Elde edilen sonuçlar, PV enerji üretimi, şebeke elektriği kullanımı, EV şarj zamanlamaları ve hidrojen üretiminin optimal şekilde eşgüdümüyle önerilen yöntemin maliyetleri düşürmede ve emisyonları azaltmada etkili olduğunu doğrulamaktadır. Sonuçlara göre karbon emisyonundan ve karbon vergisinden %21.63 kar edilmiştir.

**Anahtar kelimeler:** Karbon vergisi, Şarj istasyonları, Enerji yönetimi, Hidrojenli araçlar, Optimizasyon.

\*Yazışılan Yazar





İntihal Kontrol: Evet – Turnitin

Şikayet: [fujece@firat.edu.tr](mailto:fujece@firat.edu.tr)

Telif Hakkı ve Lisans: Dergide yayın yapan yazarlar, CC BY-NC 4.0 kapsamında lisanslanan çalışmalarının telif hakkını saklı tutar.



## Carbon Tax-Aware Optimal Energy Management for Grid-Integrated Parking Facilities with Electric and Fuel Cell Vehicles Supported by PV Generation

Merve LORDOĞLU<sup>1</sup> , Benu PRENCUVA<sup>2</sup> , Eda Nur TAŞ<sup>3</sup> ,  
Ayşe Kübra Erenoğlu TATAR<sup>4,5\*</sup> 

<sup>1,2,3,4</sup>Department of Electrical Engineering, Electrical and Electronics Engineering Faculty, Yıldız Technical University, İstanbul, Türkiye.

<sup>5</sup>Clean Energy Technologies Institute, Yıldız Technical University, İstanbul, Türkiye.

<sup>1</sup>merve.lordoglu@std.yildiz.edu.tr, <sup>2</sup>benu.prencuva@yildiz.edu.tr, <sup>3</sup>edanur.tas@yildiz.edu.tr, <sup>4</sup>erenayse@yildiz.edu.tr

Received: 4.5.2025

Accepted: 19.6.2025

Revision: 13.6.2025

doi: <https://doi.org/10.62520/fujece.1691050>

Research Article

Citation: M. Lordoğlu, B. Prencuva, E. N. Taş ve A. K. E. Tatar, “Carbon tax-aware optimal energy management for grid-integrated parking facilities with electric and fuel cell vehicles supported by pv generation”, *Firat Univ. Jour. of Exper. and Comp. Eng.*, vol. 4, no 2, pp. 307-321, June 2025.

### Abstract

This study addresses the optimal energy management of a grid-connected parking lot integrating photovoltaic (PV) generation, fuel cell electric vehicles (FCEVs) and EVs. The parking area is equipped to meet the charging demands of EVs, and hydrogen is produced for FCEVs via an electrolyzer located within the parking area. Both EV charging power and electrolyzer demand can be met flexibly from the PV system, energy storage system (ESS) or the electrical grid. The objective is to minimize total operational costs while incorporating the impact of carbon taxation. Due to the inclusion of carbon taxes, the proposed optimization framework inherently aims to reduce emissions during vehicle charging and hydrogen production processes. To address the problem, a mixed-integer linear programming-based optimization model is constructed and executed within the GAMS platform. The solution is obtained with the CPLEX solver. Results confirm that the proposed methodology effectively achieves cost reduction and emission mitigation by optimally coordinating PV energy generation, grid electricity usage, EV charging schedules, and hydrogen production. According to the results, a 21.63% saving was achieved in carbon emissions and carbon tax.

**Keywords:** Carbon tax, Charging stations, Energy management, Hydrogen vehicles, Optimization

\*Corresponding author

## Nomenclature

### Sets

$t$	Time horizon set
$m$	Electric vehicle fleet set
$e$	Fuel-cell vehicle set
$d$	Set of hydrogen requirements for hydrogen vehicles

### Parameters

$t^{tot}$	Total time [h]
$CE^{ESS}$	Energy conversion efficiency of ESS during charging
$DE^{ESS}$	Discharge conversion efficiency
$CR^{ESS}$	Charge power limit of ESS
$DR^{ESS}$	Discharge power limit of ESS
$SoE^{ESS,init}$	Initial energy level stored in the ESS [kWh]
$SoE^{ESS,max}$	Upper limit of energy capacity for the ESS [kWh]
$SoE^{ESS,min}$	Minimum state of energy for ESS [kWh]
$\beta_t^{sell,gr}$	Electricity selling price to the grid during period $t$ [₺]
$F^{tax}$	Carbon emission tax rate [₺/kg]
$n^{H_2,st/P_{init}}$	Initial hydrogen quantity in the tank [kg]
$n^{H_2,cap/P}$	Maximum hydrogen tank capacity [kg]
$n^{H_2,st/P_{min}}$	Minimum hydrogen storage level [kg]
$P_t^{PV}$	PV power output during period $t$ [kW]
$\beta_t^{buy,gr}$	Electricity purchase price from the grid during period $t$ [₺]
$SoE_m^{EV,max}$	Maximum state of energy for EVs [kWh]
$CR_m^{EV}$	Charging rate of EVs [kW]
$CE_m^{EV}$	Charging efficiency of EVs
$SoE_m^{EV,init}$	Initial state of energy for EVs [kWh]
$SoE_m^{EV,dem}$	Minimum required energy level for EVs [kWh]
$T_m^{d,EV}$	Departure time of EVs from the parking area
$C_t^{gr}$	Carbon emissions coefficient of the grid during period $t$ [kg/kWh]
$D_{t,d}^{H_2}$	Hydrogen demand of hydrogen vehicles over time period $t$ [kg]
$T_m^{a,EV}$	Arrival time of EVs from the parking area.

### Variables

$P_t^{gr}$	Net power exchange with the grid during period period $t$ [kW]
$P_t^{gr,buy,ESS}$	Power imported from the grid for ess charging at time $t$ [kW]
$P_t^{gr,sell,ESS}$	Power exported to the grid from ESS at time $t$ [kW]
$P_t^{PV,use,gr}$	Amount of power produced in PV and sold to the grid during period $t$ [kW]
$P_t^{PV,use,ESS}$	Amount of power produced in the PV and given to the ESS [kW]
$P_t^{ESS,chg}$	Power supplied to the ESS for charging at time $t$ [kW]
$P_t^{ESS,disch}$	Power extracted from the ESS through discharging at time $t$ [kW]
$SoE_t^{ESS}$	State of energy for ESS in period $t$ [kWh]
$P_{m,t}^{EV,fr,gr}$	Power drawn from the grid for EVs during time interval $t$ [kW]
$P_{m,t}^{EV,fr,PV}$	Power drawn from PV for EVs during time interval $t$ [kW]
$P_{m,t}^{EV,fr,ESS}$	Power drawn from ESS for EVs during time interval $t$ [kW]
$SoE_{m,t}^{EV}$	State of energy for EVs in period $t$ [kWh]
$P_{m,t}^{EV,chg}$	Power required to charge EVs during time interval $t$ [kW]

$u_t^{ESS}$	Binary variables for ESS
$cost^{min}$	Minimum total cost [₺]
$P_t^{elk}$	Electrical power consumed by the electrolyzer during period $t$ [kW]
$N_t^{elk,H_2}$	The amount of pressure caused by hydrogen gas in the hydrogen tank in period $t$ [kg]
$P_t^{H_2}$	Hydrogen tank pressure in time $t$ [bar]
$cost_t^{crb}$	Total cost of carbon emissions [₺]
$C_t^{tax}$	Carbon emission coefficient of the grid at time $t$ [kWh/kg]
$P_t^{gr,sell}$	Electrical power sold by the grid during the time period $t$ [kW]
$P_t^{ESS,elk}$	Power supplied by the ESS to the electrolyzer over the time interval $t$ [kW]
$P_t^{PV,elk}$	Electricity generated by the PV system and directed to the electrolyzer at time $t$ [kW]
$P_t^{gr,elk}$	Grid-supplied electricity used by the electrolyzer during time interval $t$ [kW]
$P_t^{elk,capacity}$	Maximum capacity of electrolyzer [kW]

## 1. Introduction

### 1.1. Research motivation and related works

The transportation sector plays a major role in global greenhouse gas emissions, contributing approximately one-third of energy-related CO<sub>2</sub> emissions in nations like the United States [1]. The health risks and climate threats associated with CO<sub>2</sub> emissions have led policymakers to implement various strategies that promote the adoption of environmentally friendly vehicles and discourage the use of conventional fossil-fuel cars through financial mechanisms such as carbon taxation [2]. The urgency to reduce carbon emissions in transportation has been widely recognized in global frameworks such as the Paris Agreement and COP26, both of which promote electric vehicles (EVs) as a central solution for achieving carbon neutrality by 2040 [3]. However, according to estimates by the International Energy Agency, transportation-related emissions could increase by 50% globally by 2050 if no effective mitigation measures are implemented [4]. In parallel, the deployment of distributed energy resources—such as photovoltaic (PV) systems and battery energy storage systems (ESSs)—has gained significant momentum, driven by rapid technological advancements and growing environmental awareness [5].

Recent solar energy and electromobility advancements have opened up new opportunities, particularly for integrated solutions and applications. When energy storage systems are incorporated into PV-based charging infrastructures, they enable effective and efficient management of supply-demand balance while stabilizing the system by absorbing excess solar production [6-7]. These systems contribute to a higher share of renewables in the energy sector while allowing EVs to be charged during peak times with solar energy that was stored earlier. This helps to reduce the strain on the grid and provides an effective way to minimize grid dependency. Thanks to this mutually beneficial relationship between the PV sector and electromobility, sudden fluctuations in electricity prices can be mitigated, helping to avoid scenarios of negative pricing [8-10].

In recent years, the alignment of carbon pricing and energy market mechanisms with carbon markets has become a frequently discussed topic in power system planning, leading to active policies in many countries. For instance, China officially launched its national carbon trading market in 2021 [11] to regulate emissions and establish emission limits. In Türkiye, efforts toward carbon pricing have been ongoing since 2013 and are in line with the 2053 Net Zero Emissions and Green Development targets. By 2020, the Emissions Trading System was identified as the most appropriate pricing mechanism [12]. Academic research, a key driver in shaping these policies, has shown that integrating energy and carbon markets leads to more sustainable and economically efficient operations.



This has led to a growing body of literature focusing on the optimal management of charging and refueling operations at stations serving electric and hydrogen vehicles in a way that reduces carbon emissions, further enriching our understanding of these complex systems. For example, the study in [13] investigated how EV owners could benefit from bidirectional charging, with a particular focus on how these advantages change depending on electricity prices, grid tariffs, and support mechanisms for energy pricing. A cost minimization problem was formulated to analyze the benefits of discharging EV batteries to the grid. However, there is no evaluation based on carbon taxation, and hydrogen-powered vehicles have not been considered in that analysis.

A multi-period distribution system expansion model was proposed in [14], where uncertainties in demand growth, renewable generation, EV load, and energy prices were addressed using a CVaR-based approach to minimize investment, operational, and carbon-related risks. The model enabled optimal planning of DERs, EV charging stations, and storage systems under carbon tax and budget constraints. Gong et al. proposed [15] a coordinated planning approach for low-carbon distributed energy stations by modeling the spatial-temporal charging behaviors of four EV types using Monte Carlo simulations and integrating PV and power-to-gas systems under a stepped carbon trading mechanism. In [16], the problem of selecting the optimal power level for a single EV charging station, considering carbon tax and computational energy constraints, was formulated as a cost and delay minimization task. A Multi-Agent Deep Deterministic Policy Gradient algorithm was employed to address dynamic user behaviors, resulting in reduced charging costs, CO<sub>2</sub> emissions, and load imbalance across stations. In [17], a mixed-integer linear programming model (MILP) was proposed for a charging network operator managing geographically distributed EV charging stations, where electricity market costs, carbon taxes, and reserve market incentives are jointly considered to maximize operational profit. However, the studies did not consider fuel cell electric vehicles (FCEVs) [14-17], or the integration of DERs [16-17] which limits its applicability in comprehensive low-carbon transportation and energy management systems.

The study in [18] introduced a carbon footprint evaluation method that accounts for spatial and temporal variations in electricity generation. By incorporating a carbon integration mechanism aligned with green electricity trading, the Authors enabled the identification of low-carbon charging routes, encouraging environmentally sustainable EV usage and supporting the transition to carbon-neutral mobility. In [19], Zhang et al. developed an optimization framework for managing the operation of integrated photovoltaic-storage-charging stations by simultaneously considering electricity and carbon market dynamics. The study utilized game-theoretic modeling to represent the strategic interaction between charging station operators and EV users, with the objective of maximizing overall revenue, reducing load variability, and improving user satisfaction. A ladder-based carbon trading scheme was incorporated into the model, and a genetic algorithm was applied to derive optimal solutions. In [20], the authors explored the integration of decentralized EVs into the carbon trading framework, with the goal of mitigating peak-valley load disparities and promoting coordinated charging behavior. To this end, a two-level Stackelberg game model was formulated: the upper-level problem sought to optimize the revenue of a centralized EV aggregator, while the lower-level model aimed to minimize the charging expenses of individual EV users. Li et al. [21] proposed an optimal scheduling strategy for a coupled electric-hydrogen energy system involving both EVs and hydrogen-powered vehicles. Their model incorporated Vehicle-to-Grid (V2G) operations along with carbon market participation, enabling dynamic coordination between energy exchange and environmental policy constraints. The model addressed renewable energy uncertainties using Latin hypercube sampling and scenario reduction. While the scenario-based modeling approach enhances theoretical robustness, its computational intensity might hinder real-time or large-scale practical deployment.

Another study by the author, presented in [22], proposed a real-time optimization model for managing a multi-energy system integrating combined heat and power units, heat pumps, renewable sources, and hydrogen-based technologies to meet the electricity, heating, cooling, and transportation demands. While it successfully reduced grid dependency through local renewable use and optimized hydrogen logistics, it did not consider participation in carbon markets, which limits its applicability in carbon-constrained policy environments.



As illustrated in Figure 1, the electricity required for both vehicle charging and hydrogen production is supplied from three sources: the grid, PV generation, and the ESS. A time-based constraint ensures that EVs are charged within their designated arrival and departure time slots.

For hydrogen FCEVs, the electrolyzer produces hydrogen using electricity drawn from the available sources. The model also accounts for the time-varying carbon emission factor of the grid and evaluates the financial impact of carbon taxation. The overall objective is to minimize the total electricity-related costs.

## 2.1. Input

In the proposed model, the vehicle parking area has a capacity of 50 EVs. A total of 25 AC charging ports are available. The parameters related to EVs are provided in Table 1.

**Table 1.** Specifications of EV

Charging Efficiency	Battery Capacity [kWh]	AC Charging Rate [kW]
0.96	50	7.2

The capacity of the PV system installed at the parking facility was selected considering both the expected daily energy demand of the EVs and the hydrogen production requirements of the electrolyzer. The power generation of the PV system located in the parking area is presented in Figure 2.

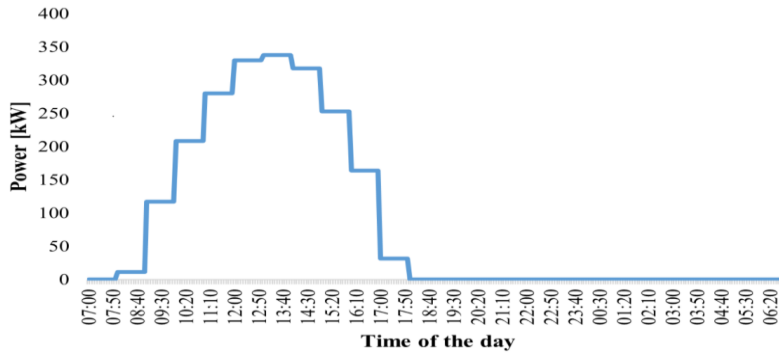


**Figure 2.** Power generation of PV

The parking area is also equipped with an ESS, and its parameters are given in Table 2.

**Table 2.** Specifications of ESS

Charging/Discharging Efficiency	Charging/Discharging Rate [kW]	Battery Capacity [kWh]
0.95	25	100

An electrolyzer and a hydrogen tank are installed to support the charging operations of FCEVs. The capacity of the electrolyzer was set at 510 kW to meet the hydrogen demand of the FCEVs.

Moreover, the grid electricity selling price is illustrated in Figure 3. The price of electricity sold to the grid is 0.32 TL.

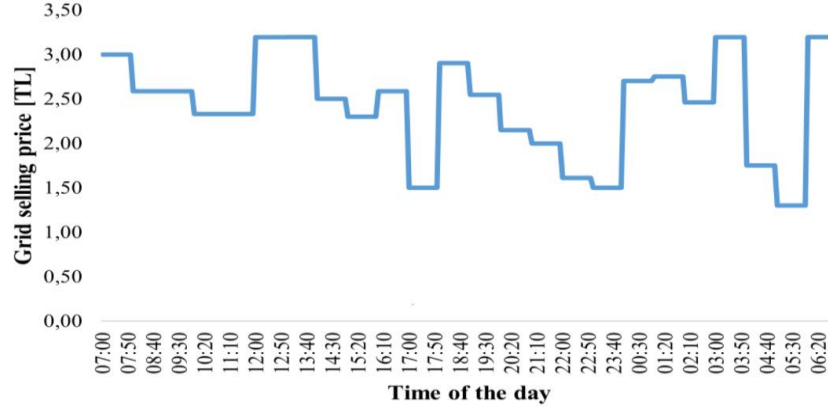


**Figure 3.** Energy selling price of grid

The carbon tax corresponding to the energy production in 5-minute intervals over a day is presented in Figure 4 according to open access data.

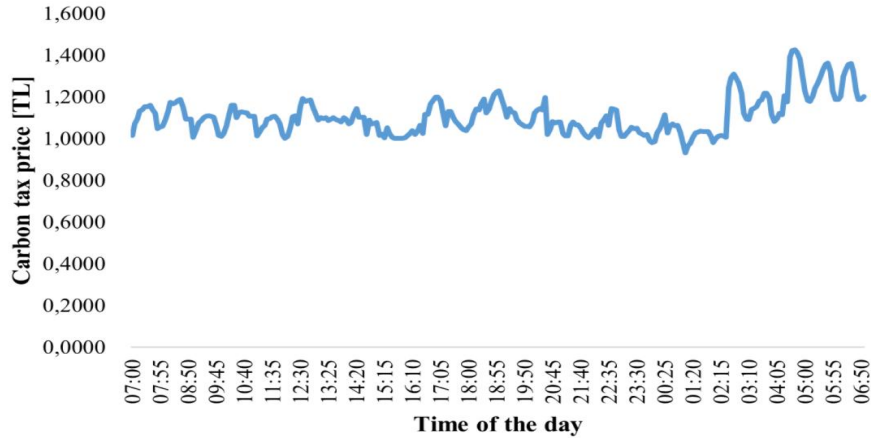


**Figure 4.** Time-dependent carbon tax pricing profile applied to grid electricity during the simulation period

## 2.2. Mathematical model of proposed scheme

$$cost^{min} = \sum_t \left( \sum_m (P_{m,t}^{EV,fr,gr} + P_t^{gr,buy,ESS} + P_t^{gr,elk}) \cdot DT \cdot \beta_t^{buy,gr} \right) + \sum_t cost_t^{crb} - \sum_t (P_t^{PV,use,gr} + P_t^{gr,sell,ESS}) \cdot DT \cdot \beta_t^{sell,gr} \quad (1)$$

The primary objective is to minimize the overall electricity expenditure, accounting for both the carbon tax imposed on grid-supplied electricity and the revenue generated from feeding electricity back into the grid. This objective is mathematically expressed in Equation (1).

$$P_t^{gr,sell} = P_t^{gr,sell,ESS} + P_t^{PV,use,gr} \quad (2)$$

$$P_t^{PV} = P_t^{PV,use,gr} + P_t^{PV,use,ESS} + \sum_m (P_{m,t}^{EV,fr,PV}) + P_t^{PV,elk} \quad (3)$$

$$P_t^{gr} = P_t^{gr,buy,ESS} + \sum_m (P_{m,t}^{EV,fr,gr}) + P_t^{gr,elk} \quad (4)$$

$$cost_t^{crb} = P_t^{gr} \cdot C_t^{gr} \cdot F^{tax} \quad (5)$$

As expressed in Equation (2), the total electricity fed into the grid at time  $t$  is determined by the combined contribution of energy discharged from the ESS and that generated by the PV system during the same interval. Equations (3) and (4) describe how the available electricity at time  $t$  is allocated, with respect to its origin—either from the PV system or the grid. In turn, Equation (5) quantifies the carbon tax by considering the amount of grid-supplied electricity consumed at time  $t$ , along with the associated emission factor for that period.

$$P_{m,t}^{EV,fr,gr} + P_{m,t}^{EV,fr,PV} + P_{m,t}^{EV,fr,ESS} = P_{m,t}^{EV,chg} \quad (6)$$

$$P_{m,t}^{EV,chg} \leq CR_m^{EV}, \forall t, T_m^{a,EV} < t \leq T_m^{d,EV} \quad (7)$$

$$P_{m,t}^{EV,chg} = 0, t < T_m^{a,EV}, t > T_m^{d,EV} \quad (8)$$

$$SoE_{m,t}^{EV} = 0, t < T_m^{a,EV}, t > T_m^{d,EV} \quad (9)$$

$$SoE_{m,t}^{EV} = SoE_m^{EV,init}, \text{ if } t = T_m^{a,EV} \quad (10)$$

$$SoE_{m,t}^{EV} = SoE_{m,(t-1)}^{EV} + CE_m^{EV} \cdot P_{m,t}^{EV,chg} \cdot DT, \forall t, T_m^{a,EV} < t \leq T_m^{d,EV} \quad (11)$$

$$SoE_{m,t}^{EV} = SoE_m^{EV,dem}, \text{ if } t = T_m^{d,EV} \quad (12)$$

$$SoE_{m,t}^{EV} \leq SoE_m^{EV,max} \quad (13)$$

Equation (6) represents the total power used to charge the EVs at time  $t$ , injected from the grid, ESS, and PV system. Equations (7) and (8) ensure that the EV is only charged during its stay at the station, while Equations (9) to (13) calculate the battery's State of Energy (SoE), enforce the required SoE at the time of departure, and set the upper bounds.

$$P_t^{PV,use,ESS} + P_t^{gr,buy,ESS} = P_t^{ESS,chg} \quad (14)$$

$$\sum_m (P_{m,t}^{EV,fr,ESS}) + P_t^{gr,sell,ESS} + P_t^{ESS,elk} = P_t^{ESS,disch} \quad (15)$$

$$P_t^{ESS,chg} \leq CR^{ESS} \cdot u_t^{ESS} \quad (16)$$

$$P_t^{ESS,disch} \leq DR^{ESS} \cdot (1 - u_t^{ESS}) \quad (17)$$

$$SoE_t^{ESS} = SoE^{ESS,init}, \text{ if } t = 1 \quad (18)$$

$$SoE_t^{ESS} = SoE_{t-1}^{ESS} + CE^{ESS} \cdot P_t^{ESS,chg} \cdot DT - \frac{P_t^{ESS,disch} \cdot DT}{DE^{ESS}}, \text{ if } t > 1 \quad (19)$$

$$SoE_t^{ESS} \leq SoE^{ESS,max} \quad (20)$$

$$SoE_t^{ESS} \geq SoE^{ESS,min} \quad (21)$$

Equations (14) and (15) define the sources of ESS charging and the distribution of discharged power for each station. Equations (16) and (17) together ensure that the station's ESS cannot charge and discharge simultaneously at time  $t$ . Equations (18) and (19) calculate the ESS's SoE, while Equations (20) and (21) ensure that the SoE stays within capacity limits.

$$P_t^{elk} = P_t^{gr,elk} + P_t^{PV,elk} + P_t^{ESS,elk} \quad (22)$$

$$P_t^{elk} \leq P_t^{elk,capacity} \quad (23)$$

$$P_t^{elk} \geq 0 \quad (24)$$

$$N_t^{elk,H_2} = \frac{0.9 \times P_t^{elk}}{240} \times 3.6 \times DT \quad (25)$$

$$P_t^{H_2} = P_{t-1}^{H_2} + K \times \frac{N_t^{elk,H_2} - D_{t,d}^{H_2}}{2}, \text{ if } t > 1 \quad (26)$$

Equations (22) and (23) constrain the power consumed for electrolysis within the electrolyzer's capacity limits. Equation (24) determines the total power input to the electrolyzer at time  $t$ . Equation (25) calculates the total molar amount produced by the electrolyzer. Equation (26) calculates the hydrogen tank pressure at time  $t$  based on the amount of hydrogen produced at time  $t$  and the tank pressure at time  $(t - 1)$ .

### 3. Test and Results

In the proposed model, PV and ESS are integrated into EV parking lot operating under a carbon taxation scheme, with the aim of minimizing its operational costs. The system also includes hydrogen-powered vehicles, for which an electrolyzer is incorporated to supply the necessary hydrogen fuel. A detailed cost analysis is conducted for the entire system, explicitly incorporating the effects of carbon taxation. The formulated optimization problem is solved using the MILP method within the GAMS environment. All time references in this paper are provided using the 24-hour clock format for consistency and clarity.

As a result of the simulations, the graph illustrating the power balance in the ESS is presented in Fig. 5. As shown in Figure 5, the ESS is charged from the grid during the hours of 17:00–18:00 and later at night, when the grid selling prices are low. The energy drawn from the grid during these low-price periods is then utilized for operating the electrolyzer and charging EVs. As also observed from the graph, the ESS is predominantly charged from the grid, as the PV generation is mainly reserved for operating the electrolyzer and charging the EVs.

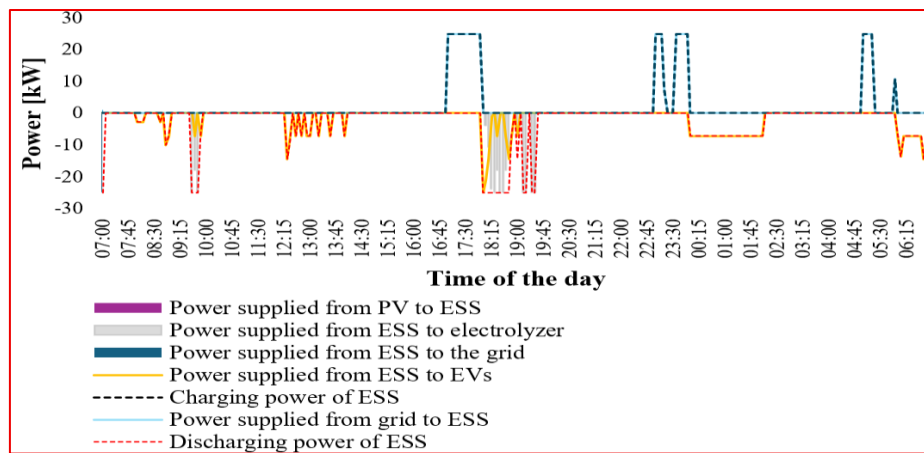


Figure 5. General power balance of the system over time

As shown in Figure 6, the charging profile of EVs indicates that during periods of PV generation, the vehicles are primarily charged using PV power. Furthermore, during certain hours when PV generation is insufficient due to increased demand from the electrolyzer, the ESS also contributes to vehicle charging. In hours without PV generation, the EVs are supplied by both the grid and the ESS. Notably, during periods of high grid prices—such as between 00:00 and 02:05—the ESS supplies the vehicles, whereas before 00:00, when the grid price is lower, the vehicles are charged directly from the grid.

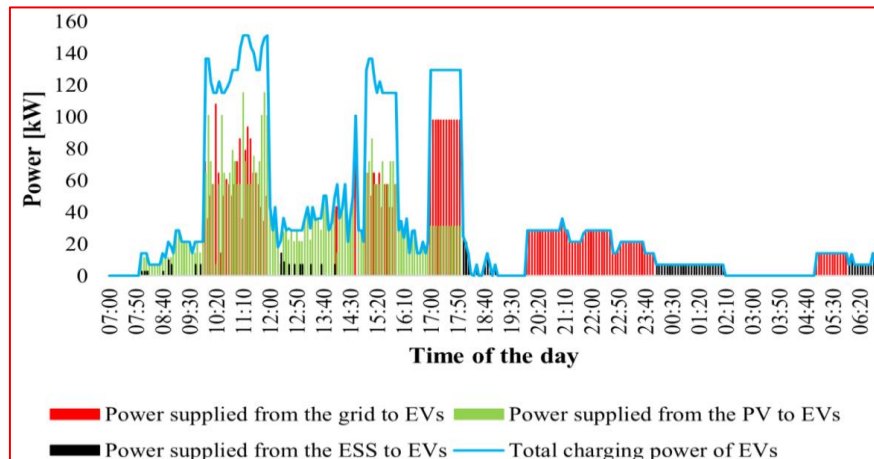
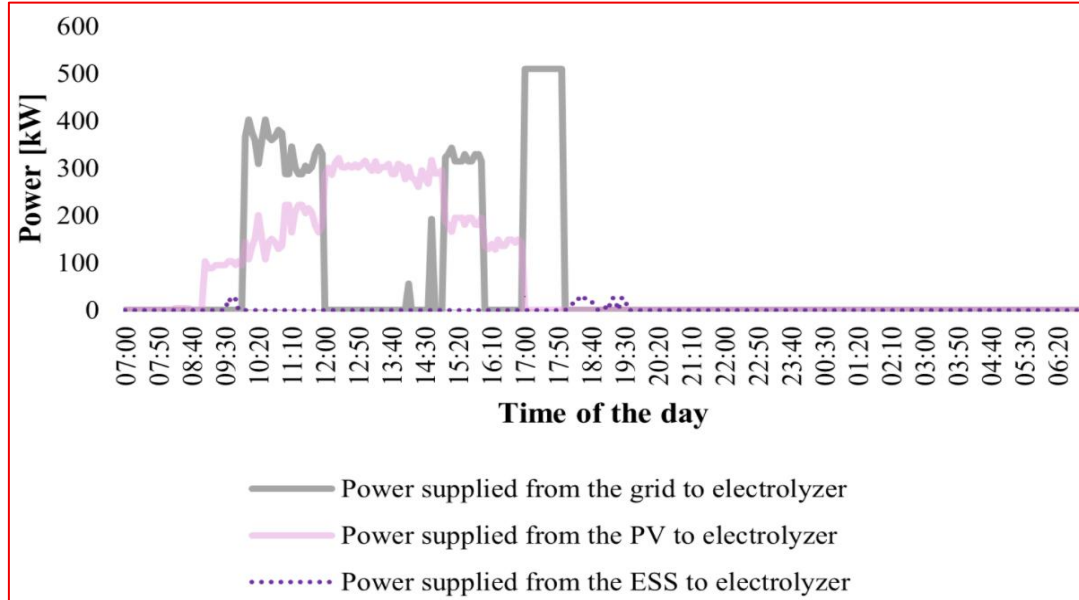


Figure 6. Battery charging and discharging status over time



As illustrated in Figure 7, the power profile of the electrolyzer shows that the majority of its energy demand is met by PV and the grid. Due to the limited capacity of the battery, the contribution from the ESS remains relatively low. During the peak hydrogen demand period between 09:35 and 09:45, when PV generation is insufficient, the remaining energy required by the electrolyzer is supplemented by both the battery and the grid.



**Figure 7.** Electrolyzer power balance over time

The load profile of the PV system is shown in Figure 8. The graph indicates that the PV generation is used entirely for powering the electrolyzer and charging EVs. There is no energy sold to the battery or the grid. This is mainly because there is a constant energy demand, and selling electricity to the grid offers low returns. As a result, feeding energy into the grid and then meeting the loads later from the grid would be more costly.

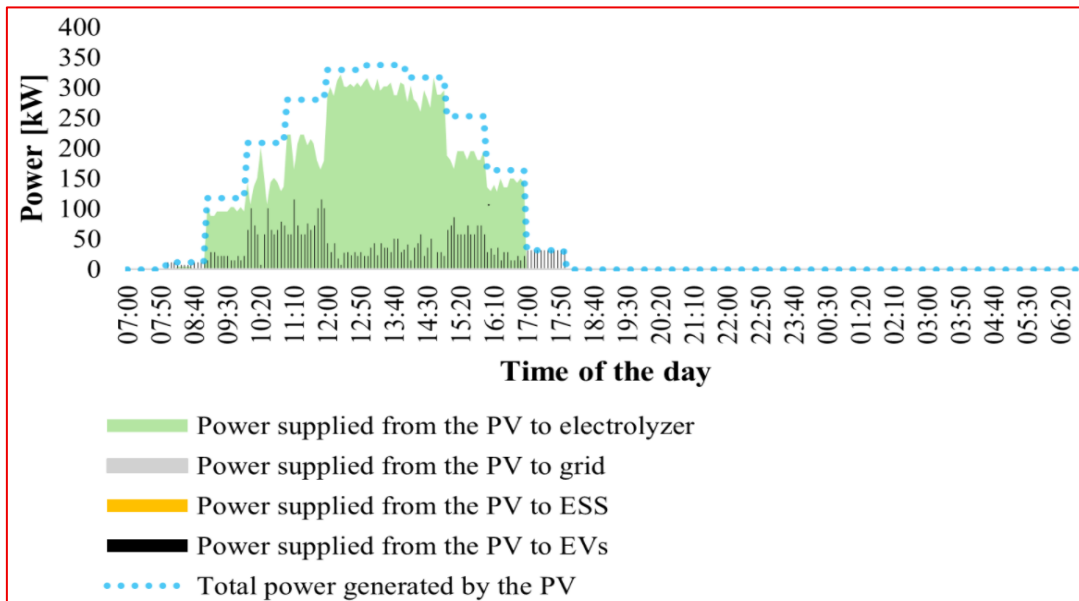


**Figure 8.** PV system power balance over time

The graph showing the power imported from and exported to the grid is presented in Figure 9. As seen, the only instance of energy being sold to the grid occurs at 07:00, when there is no power demand from the electrolyzer or EVs, and the ESS discharges to the grid. No further grid export is observed after this point. During other time intervals, particularly when PV generation is available, less energy is drawn from the grid. Additionally, the ESS is charged from the grid between 22:45 and 23:45, when carbon emissions—and therefore the carbon tax—are relatively low. Grid electricity prices also influence this behavior. In hours with no demand from hydrogen FCEVs or EVs, no grid transactions (neither purchase nor sale) are carried out due to the combined effects of high electricity prices and carbon taxation.

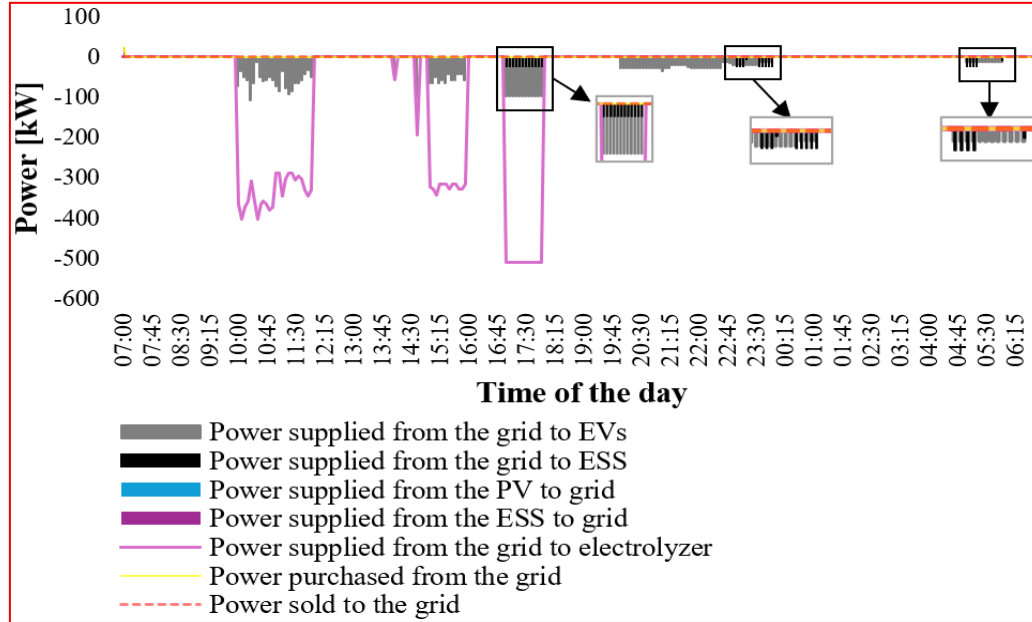


**Figure 9.** Power balance of the grid over time

#### 4. Conclusion

In this study, a comprehensive cost-minimization model for a grid-connected parking facility serving both EVs and FCEVs was proposed and analyzed. The system integrates PV generation, an ESS, and an electrolyzer for on-site hydrogen production, all under a carbon taxation framework. The model was formulated as a MILP problem, ensuring accurate representation of operational constraints, energy flows, and carbon tax considerations.

The optimization model was implemented using the GAMS platform and solved via the CPLEX solver. The solution process for the defined scenario, which included a one-day horizon with 5-minute intervals (resulting in 288 time steps), was completed within approximately 22 seconds on a standard workstation (Intel i7 processor, 16 GB RAM). This confirms the computational efficiency of the proposed framework, making it suitable for practical planning purposes.

Simulation results demonstrated the tangible economic and environmental benefits of the proposed model:

- 21.63% reduction in carbon tax costs was achieved compared to a non-optimized baseline scenario, emphasizing the model's effectiveness in lowering emissions through coordinated energy management.
- The PV system supplied 51.58% of the electrolyzer's total energy demand, minimizing grid dependency during high-carbon periods.
- The ESS played a critical role by charging predominantly during low-price, low-emission periods (e.g., between 17:00–18:00) and discharging during high-price periods, supporting both cost savings and carbon reduction.

- The system avoided unnecessary electricity export to the grid, as internal consumption of PV energy was prioritized, which prevented additional costs associated with repurchasing electricity at higher rates.

Furthermore, the model enabled dynamic allocation of power between EV charging and hydrogen production, adapting to time-varying PV output, grid prices, and carbon emission factors. This flexibility allowed the system to maintain continuous energy supply for critical services while reducing operational costs.

In summary, the proposed model not only provided significant cost savings and emission reductions but also demonstrated operational strategies that can contribute to net-zero carbon targets in multi-energy parking facilities. Future studies may enhance the model by incorporating dynamic electricity markets, carbon trading mechanisms, and other regulatory frameworks to further explore its economic and environmental benefits.

## **5. Acknowledgements**

No funding was received from any institution for this study.

## **6. Author Contribution Statement**

In the conducted work, Author 1 contributed to the formation of the idea, the design, and the analyses; Author 2 contributed to the evaluation of the obtained results and the development of the concept; Author 3 contributed to the interpretation of the results and the writing process; and Author 4 contributed to the literature review, the writing, the development of the modeling, and the interpretation of the results.

## **7. Ethics Committee Approval and Conflict of Interest**

"There is no need for an ethics committee approval for the prepared manuscript."

"There is no conflict of interest with any individual or institution in the prepared manuscript."

## **8. Ethical Statement Regarding the Use of Artificial Intelligence**

No artificial intelligence-based tools or applications were used in the preparation of this study. The entire content of the study was produced by the authors in accordance with scientific research methods and academic ethical principles.

## 9. References

- [1] U.S. Energy Information Administration, "How Much Carbon Dioxide Is Produced from US Gasoline and Diesel Fuel Consumption?," 2018.
- [2] S. Sibdari and Y. Asayesh, "Eco-drive or tax strive? Assessing consumer vehicle selection behavior under carbon taxation," *\*J. Clean. Prod.\**, vol. 479, p. 143869, 2024.
- [3] European Commission, "Questions and Answers on COP26," Dec. 2021. [Online]. Available: [[https://ec.europa.eu/info/events/cop26-2021-11-01\\_en](https://ec.europa.eu/info/events/cop26-2021-11-01_en)]([https://ec.europa.eu/info/events/cop26-2021-11-01\\_en](https://ec.europa.eu/info/events/cop26-2021-11-01_en)). [Accessed: Apr. 14, 2025].
- [4] International Energy Agency, *\*Global EV Outlook 2024: Moving Towards Increased Affordability\**, 2024.
- [5] International Renewable Energy Agency, "Renewable Energy and Climate Change," Dec. 2020.
- [6] P. Nunes and T. Farias, "Synergies between electric vehicles and solar electricity penetrations in Portugal," *\*World Electric Vehicle J.\**, vol. 6, pp. 1151–1158, 2013.
- [7] H. Tidey and S. Lyden, "Coordination of electric vehicle battery charging with photovoltaic generation," in *\*2017 Australasian Universities Power Engineering Conference (AUPEC)\**, pp. 1–6, 2017.
- [8] L. Held et al., "The influence of electric vehicle charging on low voltage grids with characteristics typical for Germany," *\*World Electr. Veh. J.\**, vol. 10, p. 88, 2019.
- [9] A. Foley et al., "Impacts of electric vehicle charging under electricity market operations," *\*Applied Energy\**, vol. 101, pp. 93–102, 2013.
- [10] P. Nunes and T. Farias, "Synergies between electric vehicles and solar electricity penetrations in Portugal," *\*World Electric Vehicle J.\**, vol. 6, pp. 1151–1158, 2013.
- [11] Z. Weng et al., "Effect of China's carbon market on the promotion of green technological innovation," *\*J. Clean. Prod.\**, vol. 373, 2022, Art. no. 133820.
- [12] Türkiye Karbon Piyasası Geliştirme Projesi. [Online]. Available: [<https://iklim.gov.tr/turkiye-karbon-piyasasi-gelistirme-projesi-acilisi-t.c.-cevre-sehircilik-ve-iklim-degisikligi-bakani-mehmet-ozhaseki-tarafindan-gerceklestirildi-haber-4258>](<https://iklim.gov.tr/turkiye-karbon-piyasasi-gelistirme-projesi-acilisi-t.c.-cevre-sehircilik-ve-iklim-degisikligi-bakani-mehmet-ozhaseki-tarafindan-gerceklestirildi-haber-4258>). [Accessed: Apr. 14, 2025].
- [13] A. Bjørndal et al., "Electricity tariffs and temporal trading opportunities from bidirectional charging of electric vehicles," *\*Energy Policy\**, vol. 203, Art. 114614, 2025.
- [14] T. D. de Lima et al., "A Risk-Based Planning Approach for Sustainable Distribution Systems Considering EV Charging Stations and Carbon Taxes," *\*IEEE Trans. Sustainable Energy\**, vol. 14, no. 4, pp. 2294-2307, Oct. 2023.
- [15] H. Gong et al., "An optimal coordinated planning strategy for distributed energy station based on characteristics of electric vehicle charging behavior under carbon trading mechanism," *\*Int. J. Electr. Power Energy Syst.\**, vol. 147, Art. 108884, 2023.
- [16] L. Peng et al., "Charging Scheduling with Computation Energy Consumption and Carbon Tax in Vehicle Networks," in *\*2024 IEEE 100th Vehicular Technology Conference (VTC2024-Fall)\**, Washington, DC, USA, 2024, pp. 1-5.
- [17] C. Li et al., "Optimal Charging Network Operation to Provide Responsive Reserve Considering Electricity and Carbon Markets," in *\*2022 IEEE 6th Conference on Energy Internet and Energy System Integration (EI2)\**, Chengdu, China, 2022, pp. 2684-2689.
- [18] G. Qing et al., "Carbon footprint evaluation for electric vehicles considering green electricity trading," *\*Renew. Energy\**, vol. 237, Part A, Art. 121510, 2024.
- [19] M. Zhang et al., "Game theoretic operation optimization of photovoltaic storage charging station considering uncertainty and carbon trading," *\*J. Energy Storage\**, vol. 102, Part A, Art. 114111, 2024.
- [20] H. Wang et al., "Research on the pricing strategy of park electric vehicle agent considering carbon trading," *\*Appl. Energy\**, vol. 340, Art. 121017, 2023.
- [21] R. Li et al., "Cooperative economic dispatch of EV-HV coupled electric-hydrogen integrated energy system considering V2G response and carbon trading," *\*Renewable Energy\**, vol. 227, Art. 120488, 2024.

- [22] A. K. Erenoğlu, "Real-time optimization for integrated R2 charging and refueling stations in a multi-carrier energy system considering hydrogen chain management," *\*Int. J. Hydrogen Energy\**, vol. 85, pp. 310-326, 2024.
- [23] P. Yadav et al., "Fuel demand, carbon tax and electric vehicle adoption in India's road transport," *\*Transportation Res. Part D: Transport and Environment\**, vol. 119, Art. 104010, 2024.
- [24] X. Huang et al., "Electric vehicle charging station diffusion: An agent-based evolutionary game model in complex networks," *\*Energy\**, vol. 257, Art. 124700, 2022.
- [25] W. Qiao et al., "A Carbon-Tax-Based Pricing Scheme for Vehicle Scheduling in Coupled Power-Traffic Networks," *\*IEEE Trans. Transportation Electrification\**, vol. 10, no. 2, pp. 4029-4041, Jun. 2024.



## Kablosuz Sensör Ağlarında Saldırı Tespiti İçin Makine Öğrenimiyle Bariyer Sayısı Tahmini

Nisanur ÇAKAN<sup>1\*</sup> , Duygu KAYA<sup>2</sup> 

<sup>1</sup>Elektrik-Elektronik Mühendisliği Bölümü, Mühendislik Fakültesi, Fırat Üniversitesi, Elazığ, Türkiye.

<sup>2</sup>Elektrik-Elektronik Mühendisliği Bölümü, Mühendislik Fakültesi, Fırat Üniversitesi, Elazığ, Türkiye.

<sup>1</sup>nisanurcakan219@gmail.com, <sup>2</sup>dgur@firat.edu.tr

Geliş Tarihi: 7.01.2025

Kabul Tarihi: 18.04.2025

Düzeltilme Tarihi: 17.04.2025

doi: <https://doi.org/10.62520/fujece.1615097>

Araştırma Makalesi

Alıntı: N. Çakan ve D. Kaya, "Kablosuz sensör ağlarında saldırı tespiti için makine öğrenimiyle bariyer sayısı tahmini", Fırat Üni. Deny. ve Hes. Müh. Derg., vol. 4, no 2, pp. 322-336, Haziran 2025.

### Öz

Kablosuz sensör ağlarında saldırı tespiti, ağ güvenliğinin sağlanması için çok önemlidir. Bu çalışma, KSA'larda etkin izinsiz giriş tespiti için gereken bariyer sayısını tahmin etme sorununa odaklanmaktadır. Amaç, KSA'lardaki güvenlik optimizasyonunu geliştirmek için doğru tahminler yapmaktır. Bu amaçla, alan boyutu, algılama aralığı, iletim aralığı ve sensör düğüm sayısı gibi parametreleri içeren bir veri seti üzerinde çeşitli regresyon modelleri (Doğrusal Regresyon, Ridge ve Lasso Regresyon, Rastgele Orman, Destek Vektör ve Gradient Boosting ) uygulandı. Modellerin performansları R<sup>2</sup>, RMSE, MAE ve MSE gibi metriklerle değerlendirildi ve 5 kat çapraz doğrulama ile doğrulandı. Sonuçlar, Doğrusal Regresyon modelinin, en düşük hata değerleri (RMSE 0.0181, MAE 0.0136 ve MSE 0.0003) ile en iyi performansı elde ettiğini ve bunu yakından Ridge Regresyonunun takip ettiğini göstermektedir. Bu bulgular, basit doğrusal modellerin bariyer gereksinimlerini doğru bir şekilde tahmin etmedeki etkinliğini vurgulayarak, kablosuz sensör ağı güvenlik altyapısının optimizasyonuna katkıda bulunmaktadır.

**Anahtar kelimeler:** Kablosuz sensör ağları, Saldırı tespiti, Makine öğrenimi, Regresyon modelleri, Bariyer tahmini

\*Yazışılan Yazar

İntihal Kontrol: Evet – Turnitin

Şikayet: [fujece@firat.edu.tr](mailto:fujece@firat.edu.tr)

Telif Hakkı ve Lisans: Dergide yayın yapan yazarlar, CC BY-NC 4.0 kapsamında lisanslanan çalışmalarının telif hakkını saklı tutar.





## Barrier Number Estimation with Machine Learning for Intrusion Detection in Wireless Sensor Networks

Nisanur ÇAKAN<sup>1\*</sup> , Duygu KAYA<sup>2</sup> 

<sup>1</sup>Department of Electrical and Electronics Engineering, Faculty of Engineering, Firat University, Elazig, Türkiye.

<sup>2</sup>Department of Electrical and Electronics Engineering, Faculty of Engineering, Firat University Elazig, Türkiye.

<sup>1</sup>nisanurcakan219@gmail.com, <sup>2</sup>dgur@firat.edu.tr

Received: 7.01.2025  
Accepted: 18.04.2025

Revision: 17.04.2025

doi: <https://doi.org/10.62520/fujece.1615097>  
Research Article

Citation: N. Çakan and D. Kaya, "Barrier number estimation with machine learning for intrusion detection in wireless sensor networks", *Firat Univ. Jour. of Exper. and Comp. Eng.*, vol. 4, no 2, pp. 322-336, June 2025.

### Abstract

Intrusion detection in wireless sensor networks is crucial for ensuring network security. This study focuses on the problem of estimating the number of barriers necessary for effective intrusion detection in WSNs. The aim is to make accurate predictions to improve security optimization in WSNs. To this end, various regression models (Linear Regression, Ridge and Lasso Regression, Random Forest, Support Vector and Gradient Boosting) were applied on a dataset including parameters such as field size, sensing range, transmission range, and the number of sensor nodes. The performance of the models was evaluated with metrics such as R<sup>2</sup>, RMSE, MAE, and MSE, and validated with 5-fold cross-validation. The results show that the Linear Regression model achieved the best performance with the lowest error values (RMSE 0.0181, MAE 0.0136, and MSE 0.0003), followed closely by Ridge Regression. These findings highlight the effectiveness of simple linear models in accurately predicting barrier requirements, supporting the optimization of WSN security systems

**Keywords:** Wireless sensor networks, Intrusion detection, Machine learning, Regression models, Barrier prediction

---

\*Corresponding author

## 1. Introduction

The widespread adoption of Micro-Electro-Mechanical Systems technology, which has significantly advanced the development of smart sensors, has contributed to a surge in global interest in wireless sensor networks. These sensors, in addition to their small size, limited processing power and programming capabilities, are more economical than traditional sensors. These sensor nodes possess the ability to sense, measure, and acquire environmental data. They can also make local decisions before transmitting the sensed information to end-users [1].

Sensors detect environmental variations and transmit the acquired data to the base station, utilizing either direct communication paths or intermediary nodes within the established communication architecture. The base station serves as an interface between the sensor network and the user. The number of sensor networks can vary depending on the requirements and needs of the environment, proving the scalability of the system. Especially when there is a need to collect data from areas that people cannot access or where access is not possible for security reasons, the importance of sensor networks becomes more evident [2].

A wide range of sensors, including thermal, seismic, magnetic, and visual sensors, can be integrated into sensor networks to monitor environmental changes such as humidity, temperature, pressure, sound, light, and motion. Usage areas of these networks include military, environmental, healthcare, household, and commercial applications. They are employed in military operations to access up-to-date equipment information on battlefields, monitor enemy movements, and assess battle damage. In environmental contexts, they help track animal movements, enable chemical and biological detection, and assist in identifying forest fires and floods. When it comes to healthcare, these networks are valuable for monitoring patients and supporting medical observation systems [3].

In home applications, it is integrated into devices such as vacuum cleaners and microwave ovens, while in commercial applications it is used in the ventilation and heating systems of buildings or in areas such as detecting vehicle theft [4].

Additionally, detecting unauthorized entries in border areas and identifying unauthorized access in restricted areas and infrastructures is one of the important areas of use of WSNs. For example, as seen in Figure 1, a WSN can be deployed to create sensor barriers to block any possible intrusion paths [5].

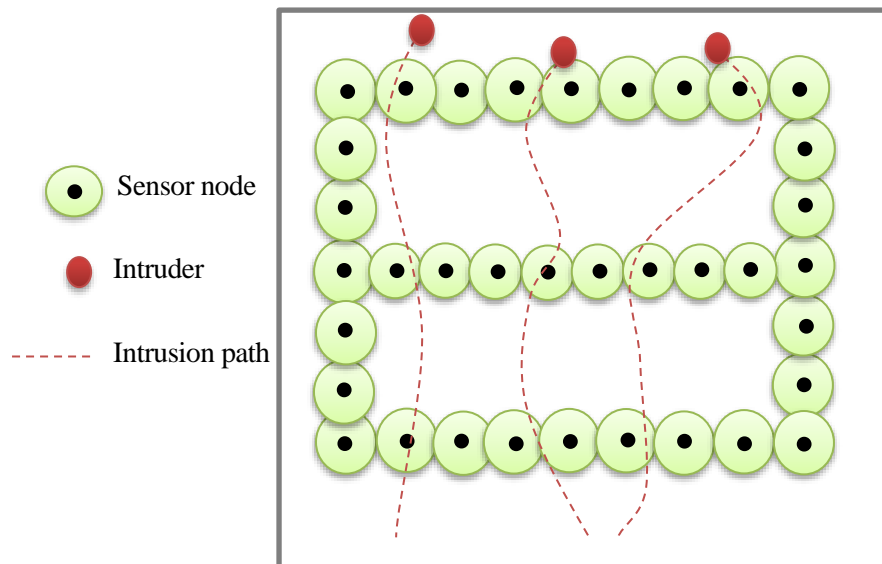


**Figure 1.** Illustration of 3-barrier coverage for each intrusion path

Wireless sensor networks are vulnerable to many attacks due to factors such as resource constraints, communication environment and infrastructure, and vulnerable areas where sensors are placed. In addition, it is necessary to develop special security solutions for these networks due to their different infrastructure from traditional networks and physical resource constraints [6].

Some of the studies found in the literature on this subject are as follows:

In the study in [7], the AR-MAC (Attack Resistant MAC) protocol was designed to detect different types of DoS attackers and provide appropriate solutions for each type of attacker. Thanks to this new protocol, wireless sensor networks have been made more secure against DoS attacks at the media access layer and the lifespan of the nodes has been increased without the need for any additional hardware.

In the study in [6], an intrusion detection system was proposed to ensure WSN security. To ensure effective security, a hybrid model has been developed that combines anomaly and misuse-based detection methods used in intrusion detection systems. In order for the system to classify normal and attack traffic, data mining algorithms such as BayesNet, J48, JRip, PART and RandomForest were used and the performance values of these algorithms were compared.

[8], Various algorithms have been developed to build intrusion detection systems in WSN based on different classifications of routing protocols in terms of energy efficiency. This article discusses routing protocol classification according to network structure, focusing on a critical parameter such as energy consumption in WSNs, and provides a comprehensive overview of IDS research.

The paper in [9] focuses on the development of a theoretical framework for barrier formation in wireless sensor networks. A key contribution is the definition of k-barrier coverage for a specified belt region and the development of efficient algorithms for evaluating this coverage metric. Methods are presented to quickly determine whether a region is within the scope of the k-barrier after the placement of sensors. Moreover, the design focuses on an optimal placement pattern that guarantees k-barrier coverage, provided that the sensors are deployed in a specific manner. Lastly, the paper addresses the challenge of achieving high-probability barrier coverage in scenarios where sensor deployment is random.

In the study in [10], a dense feedforward neural network based deep learning architecture is proposed for the accurate estimation of the k-barrier number in order to quickly detect and prevent intrusions.

In the study in [11], investigates the k-barrier coverage area formation problem in sensor networks. A novel weighted barrier graph model is proposed, demonstrating a relationship between the minimum number of mobile sensors needed to achieve k-barrier coverage and the problem of finding k vertex-disjoint paths with minimum total length on the WBG. However, it is shown that these two problems are not equivalent.

In [12], this article introduces an IDS model that facilitates unsupervised learning through the implementation of Conditional Generative Adversarial Networks . To enhance result comparison and visualization, the model incorporates the Extreme Gradient Boosting classifier. The proposed model aims to achieve superior accuracy and efficiency in attack detection by leveraging the power of deep learning algorithms.

In the study in [13], investigated key research on the security issues affecting wireless sensor networks, identified the obstacles and requirements, and presented open research areas in the field.

The work in [14], offers a valuable overview of wireless sensor network infrastructure and the security vulnerabilities it encounters. It also explores the potential of employing machine learning algorithms to mitigate the security costs associated with wireless sensor networks across diverse applications. The paper also examines challenges in threat detection and proposes machine learning-based solutions to enhance sensor capabilities in identifying threats, attacks, risks, and malicious nodes, leveraging the algorithms' learning and self-improvement potential.

In [15], barrier coverage is a critical method for enhancing security in wireless sensor networks. This work presents a technique based on geometric mathematical models to achieve barrier coverage with the fewest sensors. Additionally, it aims to create a fault-tolerant network by detecting faulty sensors and assigning appropriate sensors in their place. Simulation results show the effectiveness of the proposed algorithms.

In [16], recently, the development of lightweight and effective security protocols for wireless sensor networks has been the subject of numerous studies. In this study, prominent protocols were examined and classified according to the security issues addressed.

In [17], the security of a WSN depends on ensuring the security of all layers. In this study, first all layers are discussed separately, and then inter-layer approaches are discussed to combat some complex attacks. Integrating a secure routing protocol and key management architecture will definitely provide a stronger security measure.

One of the most effective methods of ensuring security in wireless sensor networks is to create barriers to monitor entry points into the network. These barriers are designed to detect and block potential attacks based on a specific sensor distribution and characteristics. However, determining the number of these barriers correctly is critical for both efficient use of network resources and optimizing the security level of the system [11]. A machine learning approach is proposed in this article to predict the necessary number of barriers for effective intrusion detection in wireless sensor networks. The proposed method seeks to determine the optimal number of barriers, considering features such as area size, detection range, transmission range, and the number of sensor nodes. The remainder of this article is organized as follows: The next section examines the dataset used in the study and talks about the applied machine learning methods. The next section contains the findings and results.

## 2. Materials and Methods

The dataset, sourced from study [5], is a synthetically produced dataset created through Monte Carlo simulations. It is tailored to examine the interplay of various parameters impacting the effectiveness of an intrusion detection system. The dataset features four input variables representing area, detection range, transmission range, and sensor node quantity, and a single output variable indicating the necessary number of barriers. The dataset used in this study is intended to estimate the number of barriers required for intrusion detection and prevention in wireless sensor networks. Dataset parameters are given in Table 1.

**Table 1.** Dataset parameters

Parameters
Area
Sensing Range
Transmission Range
Number of Sensor Nodes
Number of Barriers

First of all, when the data set is examined, it is seen that all variables are continuous and there are no missing values. Table 2 below shows the basic statistical properties of the variables in the data set.

**Table 2.** Statistical properties of the dataset

	count	mean	std	min	lower quartile	median	upper quartile	max
Area	182.00	24375.00	15197.25	5000.00	9375.00	21875.00	39375.00	50000.00
Sensing Range	182.00	27.50	7.52	15.00	21.00	27.50	34.00	40.00
Transmission Range	182.00	55.00	15.00	30.00	42.00	55.00	68.00	80.00
Number of Sensor nodes	182.00	250.00	90.25	100.00	172.00	250.00	328.00	400.00
Number of Barriers	182.00	94.07	65.17	12.00	42.00	80.00	128.75	320.00

In this process, we first took the raw dataset and prepared it for modeling. During data preprocessing, we standardized the variables and applied logarithmic transformation and scaling operations to optimize them for analysis. Next, we split the data into training and testing sets using an 80-20 ratio. We applied various machine learning regression methods, including Linear Regression, Ridge, Lasso, Random Forest, Support Vector Regression, and Gradient Boosting, on the training set. To evaluate the generalization ability of each model, we used 5-fold cross-validation and calculated their respective error metrics. Finally, we selected the model that achieved the lowest error and highest performance as the best regression method for the study. This entire process aimed to identify the most suitable prediction model through accurate data processing and analysis. The scheme of these processing processes is shown in Figure 2.

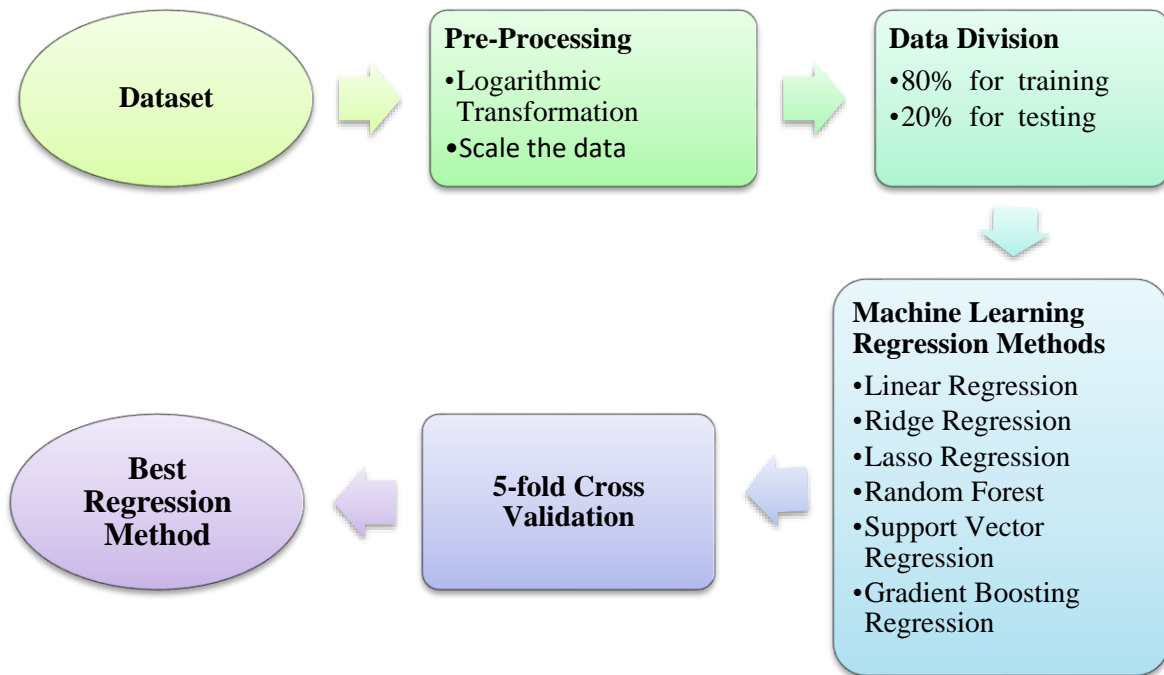


**Figure 2.** Flow diagramı of the work process

## 2.1. Logarithmic transformation

Logarithmic transformations are divided into two groups: full logarithmic transformations and semi-logarithmic transformations. In full logarithmic transformation, the logarithm of both variables, The outcome

variable (Y) and the factors that influence it (X), is taken. In semi-logarithmic transformation, the logarithm of only one of the variables X or Y is taken; The other variable is included in the model as is [18].

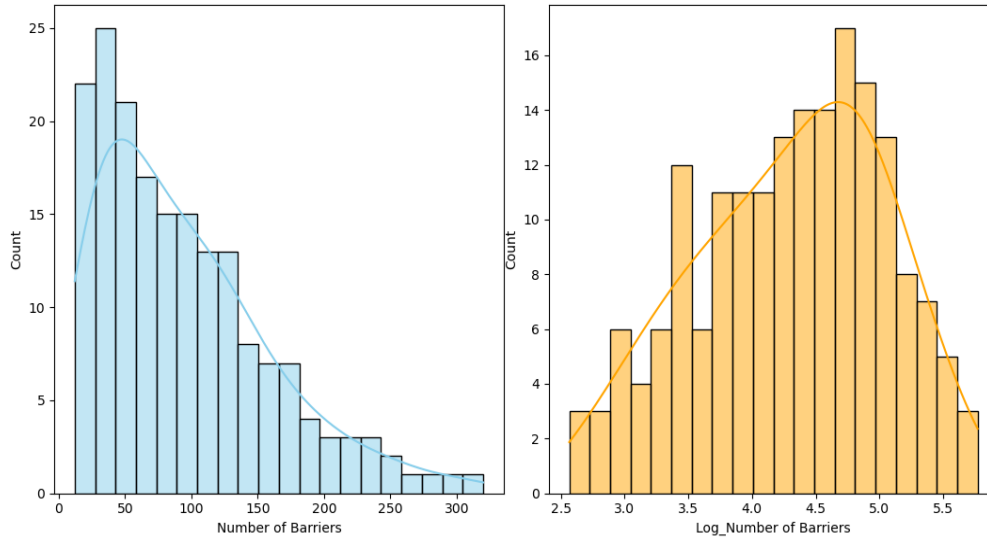


**Figure 3.** Distribution of number of barriers variable before and after logarithmic transformation

As shown in Figure 3, the logarithmic transformation affected the distribution of the "Number of Barriers" variable in the dataset. In the left panel, the original distribution of the data is shown and it is seen that it has a right-skewed structure. This type of skewness can cause problems, especially in statistical analyzes such as regression, because these analyzes generally perform better based on data closer to a normal distribution. The right panel shows the distribution obtained after logarithmic transformation. Thanks to this transformation, the distorted structure of the data has been significantly reduced and a more symmetrical structure has been gained. Logarithmic transformation balanced the distribution by minimizing the influence of outliers.

## 2.2. Linear regression

In a study, multiple linear regression analysis is used when there are more than one variable that will affect a single variable to be predicted and the relationship between these variables is linear. In other words, it's a statistical approach that models how a dependent variable is influenced by several independent variables. This model allows examining the impact of multiple variables on the outcome simultaneously [19].

$$Y = \beta_0 + \beta_1 X_{1i} + \beta_2 X_{2i} + \dots + \beta_n X_{ni} + \varepsilon_i \quad (1)$$

In this equation, Y is the dependent variable,  $\beta_0$  is the intercept,  $\beta_1, \beta_2, \beta_n$  are the coefficients of the independent variables  $X_{1i}, X_{2i}, X_{ni}$  and  $\varepsilon_i$  is the error term.

## 2.3. Ridge regression

The linear regression method aims to create a line equation that best fits the data. However, When the predictor count exceeds the observation count, the model cannot calculate any values. This may lead to overfitting and poor predictive performance, especially when the model encounters unseen data. Additionally, if there are multiple correlations among the data in linear regression, the method may create various problems. Ridge regression allows to overcome such problems. In the Ridge regression model, a small deviation value is added to the linear regression model to fit the data. Adding this bias results in the variance being significantly reduced [20].

$$\tilde{X}_i = \beta_0 + \beta_1 X_i + \lambda(\beta_1^2) \quad (2)$$



Here;  $\tilde{X}_i$ : is the estimated value.  $\beta_0$ : is the y-intercept.  $\beta_1$ : is the slope of the line.  $\lambda$ : is the penalty intensity multiplier.  $\lambda(\beta_1^2)$ : the ridge penalty.

L2 regularization, the penalty coefficient in Ridge regression, is a fundamental approach used to address the problem of overfitting. By adding this coefficient to the model's cost function, it enhances the model's generalizability. L2 regularization is equal to the sum of the squared values of the model's variables. It constrains the model's high coefficient values, pushing them towards zero, but not exactly zero [21].

## 2.4. Lasso regression

Lasso Regression is another method developed to improve the linear regression model. Lasso Regression is one of the methods developed to improve the linear regression model. With an increasing number of variables in multiple linear regression, the model becomes more susceptible to overfitting. This may cause forecast results to deviate from actual results. Additionally, increasing non-zero coefficients may make the interpretation of the model difficult. The aim of Lasso Regression is to increase prediction accuracy by reducing these problems. To address this, a penalty term, coefficient  $\lambda$ , is included in the model.  $\lambda$  is a parameter that aims to reduce the overall squared err. The choice of the  $\lambda$  parameter is of great importance for the model to work correctly. If  $\lambda$  is chosen too high, the coefficients may drop to zero and the model may lose meaning. If  $\lambda$  is selected as zero, classical regression analysis is performed. Consequently, the optimal value of  $\lambda$  is typically found through cross-validation [22].

$$\tilde{X}_i = \beta_0 + \beta_1 X_i + \lambda |\beta_1| \quad (3)$$

Here,  $\beta_0$  is the intercept,  $\beta_1$  is the coefficient for predictor  $X_i$  and  $\lambda$  is the regularization parameter. L1 regularization, the coefficient in Lasso regression, is the sum of the absolute values of the model's parameters. By incorporating L1 into the model's cost function, it enhances the model's generalization capability. It achieves this by zeroing out unnecessary variables. Consequently, the model focuses solely on the most significant variables and adopts a simpler structure [23].

## 2.5. Random forest

The random forest algorithm is an ensemble learning technique that seeks to enhance performance by combining multiple models. This algorithm consists of an ensemble of multiple decision trees. One of the advantages of the random forest algorithm is that it can work with both continuous and discrete variables. Additionally, it can be used effectively on small or large data sets. It generally gives higher accuracy compared to other algorithms [24].

## 2.6. Support vector regression

In contrast to conventional supervised learning approaches, SVR leverages the concept of structural risk minimization. This framework seeks to minimize not only the training error but also the potential for generalization error. As a result of this approach, SVR exhibits strong generalization capabilities on unseen test examples, capitalizing on the learned input-output mapping during the training phase [25].

## 2.7. Gradient boosting regression

In addition to traditional regression methods and robust regression techniques, Gradient Boosting algorithms are a powerful method that has an important place in data analysis and prediction processes. These algorithms aim to create a strong prediction model by combining weak predictors. Each weak predictor focuses on correcting the model's previous errors, improving the overall prediction performance. It has been stated that this method, first introduced by Breiman, can be evaluated as an optimization method with an appropriate loss function. Later, Friedman developed a more advanced version of this algorithm. The algorithm utilizes a sequential model training approach to construct a robust classifier [26].

## 2.8. Model evaluation methods

The  $R^2$  value indicates how well the experimental data fits a linear curve, and it is preferable for the value to be close to 1 [27].

$$\text{Adjusted } R^2 = 1 - (1 - R^2) * \frac{n-1}{n-p-1} \quad (4)$$

Model accuracy increases as the MSE value approaches zero. MAE measures how close the predictions are to the true values, and a low MAE indicates that the model's predictions are usually accurate. RMSE evaluates the deviation of the model's estimates from the true values. The smaller this value, the better the model's predictions align with the actual values [28].

$$RMSE = \sqrt{\frac{1}{n} \sum_{i=1}^n (y_i - \hat{y}_i)^2} \quad (5)$$

$$MSE = \frac{1}{n} \sum_{i=1}^n (y_i - \hat{y}_i)^2 \quad (6)$$

$$MAE = \frac{1}{n} \sum_{i=1}^n |y_i - \hat{y}_i| \quad (7)$$

## 2.9. K-Fold cross validation

K-fold cross-validation involves dividing the dataset into k mutually exclusive folds. In each iteration, one fold serves as the validation set, and the remaining k-1 folds are combined to form the training set. The model's performance is evaluated on each validation set, and the average performance across all folds is used as an estimate of the model's true performance [29]. The accuracy of the models in this study was evaluated using a 5-fold CV procedure. The scheme is given in figure 4.

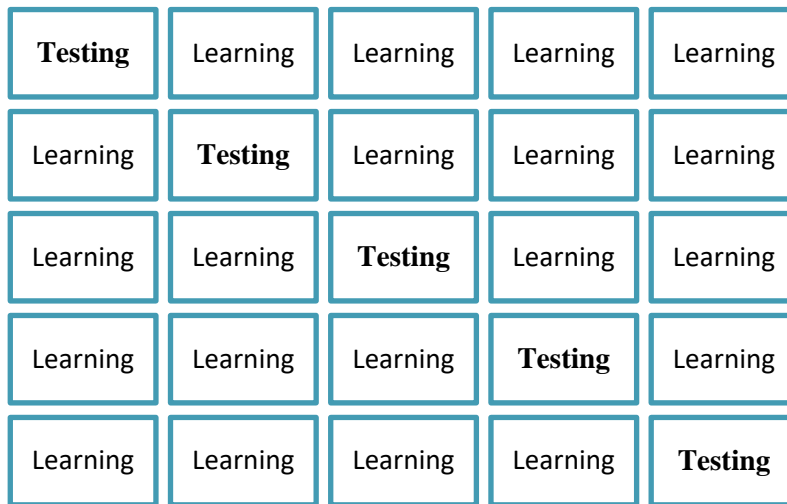


Figure 4. 5- fold cross validation diagram

## 3. Experimental Results

In this section, the 5-fold cross-validation results of the regression methods used in the study are presented. The analysis was conducted in PyCharm. Table 3 displays the outcomes. Linear Regression exhibited the best performance by achieving.

**Table 3.** Model outcomes

Regression Methods	$R^2$	RMSE	MAE	MSE
<b>Linear Regression</b>	<b>0.99</b>	<b>0.0181</b>	<b>0.0136</b>	<b>0.0003</b>
Ridge Regression	0.99	0.0194	0.0146	0.0004
Lasso Regression	0.96	0.1433	0.1170	0.0208
Random Forest	0.98	0.0785	0.0624	0.0065
Support Vector Regression	0.99	0.0727	0.0567	0.0055
Gradient Boosting Regression	0.99	0.0551	0.0450	0.0032

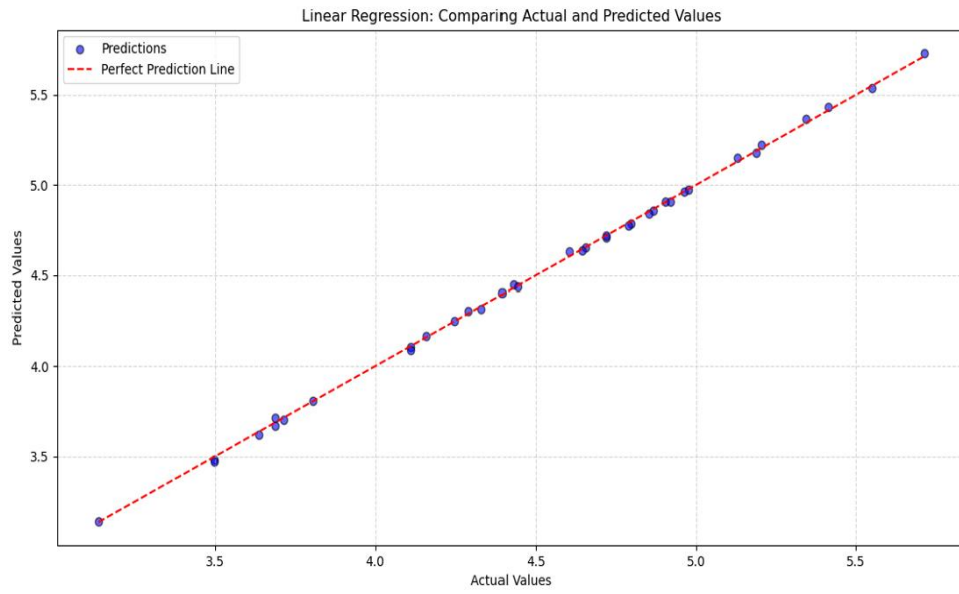


**Figure 5.** Linear regression scatter graph

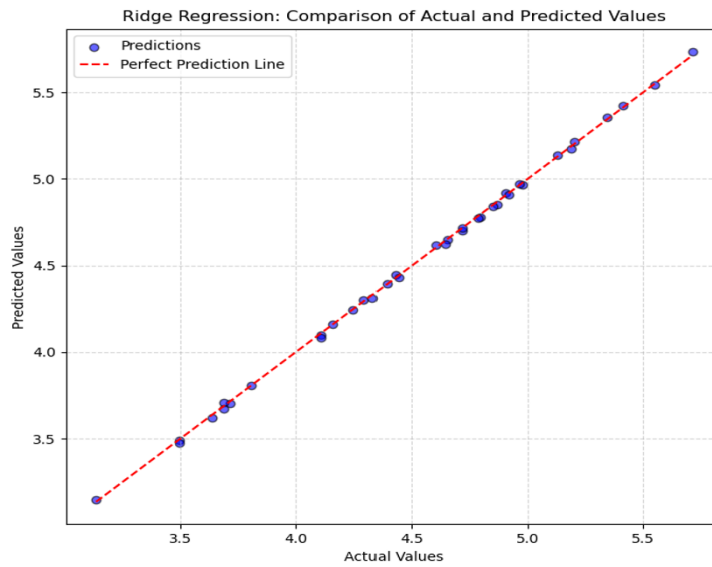


**Figure 6.** Ridge regression distribution graph

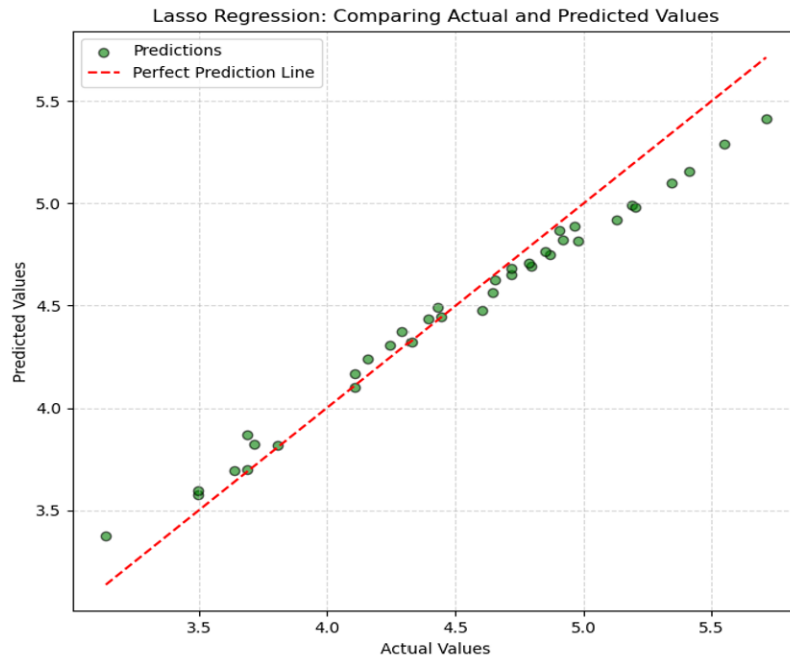


**Figure 7.** Lasso regression scatter distribution graph

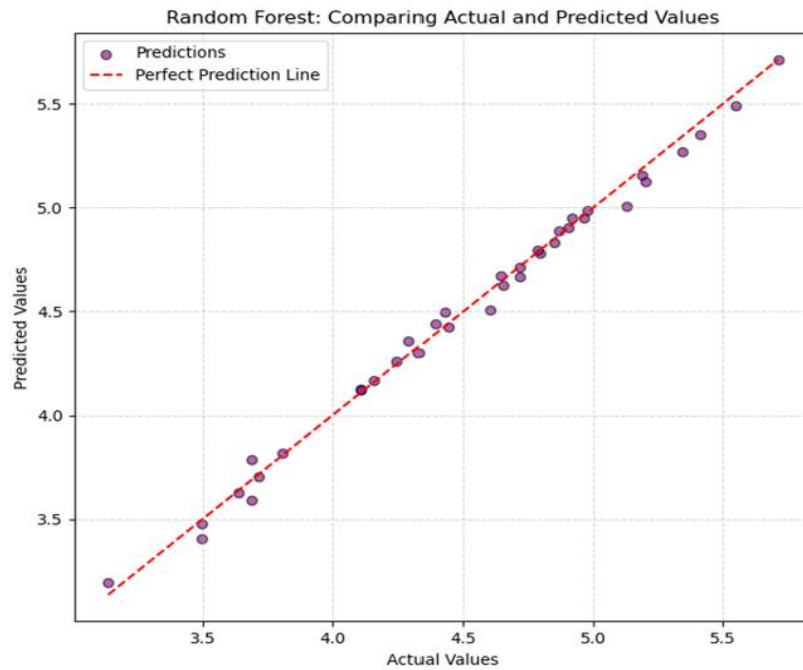


**Figure 8.** Random forest regression distribution graph

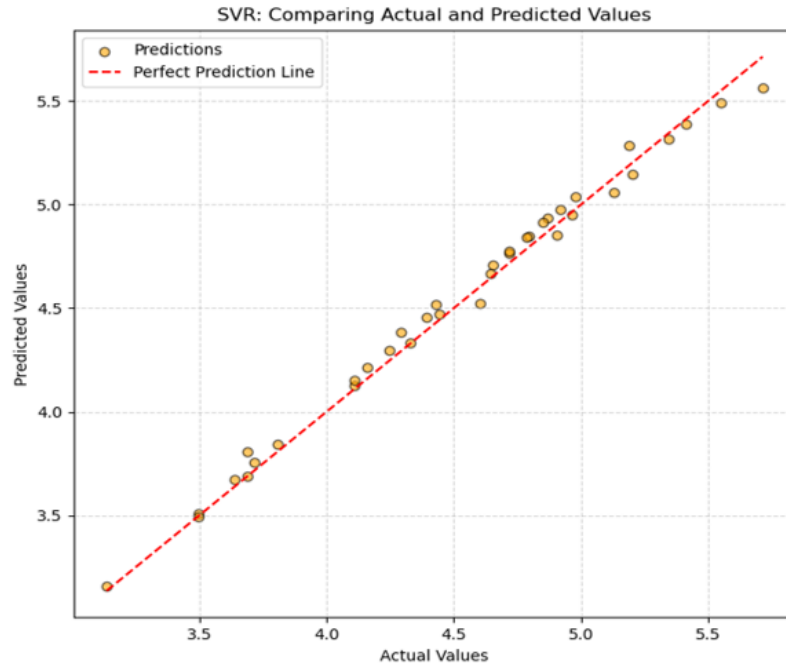


**Figure 9.** Support Vector Regression scatter graph

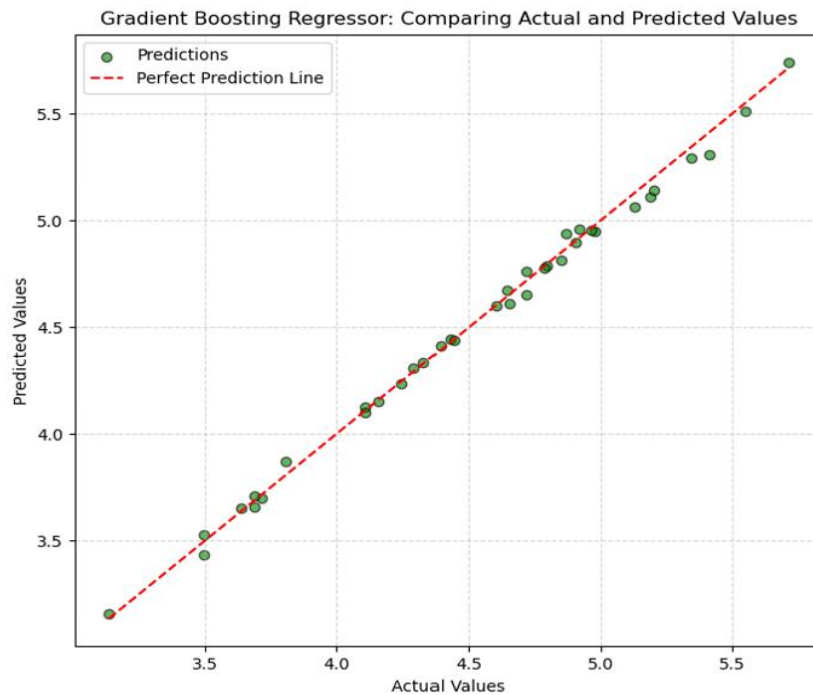


**Figure 10.** Gradient boosting regression distribution graph

#### 4. Conclusions

Since there was a linear relationship between the variables, a linear regression model was initially applied. Subsequently, Ridge and Lasso regression models were employed to prevent multicollinearity and overfitting problems. Random Forest, Support Vector Regression, and Gradient Boosting models, which are commonly used in regression analyses and aim to create a robust prediction model and minimize error, were also preferred. When the results of these applied models were examined, Linear Regression exhibited the best

performance by achieving the lowest error metrics with RMSE = 0.0181, MAE = 0.0136, and MSE = 0.0003. When comparing the results of Ridge and Lasso, Ridge outperformed Lasso, likely due to its ability to manage multicollinearity without eliminating variables. This is because Ridge regression works better when there is high correlation between variables, as it shrinks the coefficients but does not eliminate them. Lasso regression can reduce some variable coefficients to zero, effectively removing them from the model. Since all variables in the dataset contribute to the model, it can be inferred that Ridge Regression is a more suitable method. While Gradient Boosting performed well, it was outperformed by simpler models in this case. These results imply that while advanced models are capable of capturing complex relationships, simpler models may still offer optimal solutions for certain datasets.

Changes in model performance can be examined using larger or different datasets. The developed prediction models can be applied in various real-world field applications where WSNs operate. For instance, they can be preferred for securing border regions in military areas. By optimizing the number of barriers to be placed in these regions, security costs can be minimized. In the healthcare sector, they can be used to determine the number of sensors needed for monitoring patient movements in hospitals and for rapid response in emergencies. They can also be utilized in monitoring air pollution levels, detecting forest fires, predicting productivity in agricultural fields, and in industrial applications.

## **5. Discussion**

This study evaluates the performance of six different regression models to estimate the number of barriers required for security in wireless sensor networks. The findings reveal that Linear Regression and Ridge Regression models outperformed others by achieving the lowest error metrics compared to more complex models. The superior performance of these linear models can be attributed to the nature of the dataset, where the relationships between input variables and the target variable exhibit strong linearity. Models designed to capture intricate relationships, including Gradient Boosting Regression, Support Vector Regression, and Random Forest, exhibited higher error rates than simpler models. This indicates that conventional regression techniques are more efficient when dealing with straightforward relationships.

Since the dataset was synthetically generated via Monte Carlo simulations, real-world validation with empirical data is necessary. Additionally, environmental factors such as sensor failures, network congestion, and dynamic changes in attack patterns were not considered in the dataset. Future studies can conduct analysis including these factors. This study contributes to the optimization of WSN security infrastructure by determining the most effective regression model for barrier estimation.

## **6. Acknowledgment**

This study has been produced from the master thesis of Nisanur ÇAKAN.

## **7. Contributions of the Authors**

Both authors contributed equally to the research and manuscript preparation.

## **8. Statement of Research and Publication Ethics**

The study is complied with research and publication ethics. There is no conflict of interest between the authors.

## **9. Ethical Statement Regarding the Use of Artificial Intelligence**

During the writing process of this study, the artificial intelligence tool "ChatGPT" developed by "OpenAI" was used only for limited purposes for linguistic editing. The scientific content, analysis and results belong entirely to the authors.



## 10. References

- [1] J. Yick, B. Mukherjee, and D. Ghosal, "Wireless sensor network survey," *Comput. Netw.*, vol. 52, no. 12, pp. 2292–2330, Aug. 2008.
- [2] C. Okur, "Kablosuz sensör ağlarda ağ katmanında meydana gelen dos saldırılarının derin öğrenme yöntemleriyle tespit edilmesi," M.S. thesis, Gazi Univ., Inst. Sci., Dept. Inf. Security Eng., Ankara, Türkiye, Jun. 2022.
- [3] A. Alaybeyoğlu, A. Kantarcı, and K. Erciyes, "Telsiz duyurga ağlarında hedef izleme senaryoları," in *Proc. Akademik Bilişim'09*, Şanlıurfa, Türkiye, Feb. 2009, pp. 1–6.
- [4] B. Altun, "Kablosuz sensör ağları ve uygulama alanları," B.Sc. thesis, Karabük Univ., Fac. Eng., Dept. Mechatron. Eng., Karabük, Türkiye, 2016.
- [5] A. Singh, J. Amutha, J. Nagar, S. Sharma, and C. C. Lee, "LT-FS-ID: Log-transformed feature learning and feature-scaling-based machine learning algorithms to predict the k-barriers for intrusion detection using wireless sensor network," *Sensors*, vol. 22, no. 3, p. 1070, Jan. 2022.
- [6] H. Elbahadır and E. Erdem, "Kablosuz algılayıcı ağlarda hibrit saldırı tespit sistemi geliştirme," *Bilgi Bilim Derg.*, no. Special, pp. 162–174, Oct. 2021.
- [7] M. Çakiroğlu and A. T. Özcerit, "Kablosuz algılayıcı ağlarda hizmet engelleme saldırılarına dayanıklı ortam erişim protokolü tasarımı," *Gazi Univ. J. Sci. Eng.*, vol. 22, no. 4, pp. 697–707, 2007.
- [8] S. Salehian, F. Masoumian, and N. I. Udzir, "Energy-efficient intrusion detection in wireless sensor network," in *Proc. 2012 Int. Conf. Cyber Secur. Cyber Warf. Digit. Forensic (CyberSec)*, pp. 207–212, 2012.
- [9] S. Kumar, T. H. Lai, and A. Arora, "Barrier coverage with wireless sensors," in *Proc. ACM MOBICOM*, 2005, pp. 284–298.
- [10] A. Singh, J. Amutha, J. Nagar, and S. Sharma, "A deep learning approach to predict the number of k-barriers for intrusion detection over a circular region using wireless sensor networks," *Expert Syst. Appl.*, vol. 211, Jan. 2023.
- [11] Z. Wang, "Barrier Coverage in Wireless Sensor Networks," Ph.D. dissertation, Univ. of Tennessee, Knoxville, USA, 2014.
- [12] T. Sood et al., "Intrusion detection system in wireless sensor network using conditional generative adversarial network," *Wirel. Pers. Commun.*, vol. 126, no. 1, pp. 911–931, Sep. 2022.
- [13] S. Özdemir, "Wireless sensor network security: A comprehensive overview," *Politeknik Derg.*, vol. 11, no. 3, 2008.
- [14] R. Ahmad, R. Wazirali, and T. Abu-Ain, "Machine learning for wireless sensor networks security: An overview of challenges and issues," *Sensors*, vol. 22, no. 13, 2022.
- [15] T. Benahmed and K. Benahmed, "Optimal barrier coverage for critical area surveillance using wireless sensor networks," *Int. J. Commun. Syst.*, vol. 32, no. 10, Jul. 2019.
- [16] D. E. Boubiche et al., "Cybersecurity issues in wireless sensor networks: Current challenges and solutions," *Wirel. Pers. Commun.*, vol. 117, no. 1, pp. 177–213, Mar. 2021.
- [17] K. Sharma, M. Ghose, and D. Kumar, "A comparative study of various security approaches used in wireless sensor networks," *Int. J. Adv. Sci. Technol.*, vol. 17, 2010.
- [18] S. Yavuz, "Regresyon analizinde doğrusala dönüştürme yöntemleri ve bir uygulama," *İktisadi İdari Bilimler Derg.*, vol. 23, no. 1, Jan. 2009.
- [19] B. Arslan and İ. Ertuğrul, "Çoklu regresyon, ARIMA ve yapay sinir ağı yöntemleri ile Türkiye elektrik piyasasında fiyat tahmin ve analizi," *Yönetim Ekon. Araştırmaları Derg.*, vol. 20, no. 1, 2022.
- [20] B. Arseven and S. M. Çınar, "Dünya dışı ışınlımlarla iyileştirilmiş ARIMA, Ridge regresyon ve Lasso regresyon yöntemlerinin saatlik ısıtım tahmininde kullanılması," *Ömer Halisdemir Univ. Müh. Bilim. Derg.*, 2023.
- [21] R. Kantarcı and H. Çelik, "Transformer mimarisinde dropout oranlarının performans üzerindeki etkisi," in *Proc. 1st Int. Transylvania Sci. Res. Innov. Congr.*, Romania, Dec. 2024.
- [22] K. Kaysal, E. Akarslan, and F. O. Hocaoglu, "Türkiye kısa dönem elektrik yük talep tahmininde makine öğrenmesi yöntemlerinin karşılaştırılması," *Bilecik Şeyh Edebali Univ. Fen Bilim. Derg.*, vol. 9, no. 2, 2022.
- [23] S. Göksu, B. Sezen, and Y. S. Balcioğlu, "Makine öğrenmesi ile üretim performansı tahminlemesi,"

- Kahramanmaraş Sütçü İmam Univ. Müh. Bilim. Derg., vol. 28, no. 1, pp. 65–79, Mar. 2025.
- [24] K. Büyükanber, "Farklı katı yakıt türlerinin üst ısı değerlerinin çoklu lineer regresyon, karar ağacı, random forest ve yapay sinir ağları yöntemleriyle belirlenmesi," M.S. thesis, İstanbul Tech. Univ., Dec. 2022.
- [25] Ö. Karal, "Compression of ECG data by support vector regression method," J. Fac. Eng. Archit. Gazi Univ., vol. 33, no. 2, pp. 743–755, 2018.
- [26] A. Han and M. Güngör, "Ridge-Robust-Boosting topluluk regresyon yaklaşımı," J. Statisticians Stat. Actuarial Sci. IDIA 17, vol. 2, pp. 30–45, 2024.
- [27] S. Çelik and D. Özdemir, "Rastgele orman regresyon algoritması ile bitcoin fiyat tahmini," J. Sci. Rep.-B, no. 8, Dec. 2023.
- [28] N. Z. Abidin, A. R. Ismail, and N. A. Emran, "Performance analysis of machine learning algorithms for missing value imputation," Int. J. Adv. Comput. Sci. Appl., vol. 9, no. 6, pp. 442–447, 2018.
- [29] F. Ateş and R. Şenol, "Hava araçlarında buzlanma risk derecesinin yapay zeka ile tahmin edilmesi," Int. J. 3D Print. Technol. Digit. Ind., vol. 5, no. 3, pp. 457–468, Dec. 2021.



## Batman'daki Biyogaz Potansiyelinin Değerlendirilmesi ve Alternatif Enerji Kaynakları ile Ekonomik Karşılaştırması

Süleyman ATILGAN<sup>1\*</sup>, Umut ERCAN<sup>2</sup>, Muzaffer ALIM<sup>3</sup>

<sup>1</sup>Enerji Sistemleri Mühendisliği, Fen Bilimleri Enstitüsü, Fırat Üniversitesi, Elazığ, Türkiye.

<sup>2</sup>Makine ve Metal Teknolojileri, Beşiri OSB Meslek Yüksekokulu, Batman Üniversitesi, Batman, Türkiye.

<sup>3</sup>Tekstil, Giyim, Ayakkabı ve Deri, Beşiri OSB Meslek Yüksekokulu, Batman Üniversitesi, Batman, Türkiye.

<sup>1</sup>suleyman@batman.edu.tr, <sup>2</sup>umut.ercan@batman.edu.tr, <sup>3</sup>muzaffer.alim@batman.edu.tr

Geliş Tarihi: 31.12.2024

Kabul Tarihi: 15.04.2025

Düzeltilme Tarihi: 17.02.2025

doi: <https://doi.org/10.62520/fujece.1610687>

Araştırma Makalesi

Alıntı: S. Atılgan, U. Ercan ve M. Alım, "Batman'daki biyogaz potansiyelinin değerlendirilmesi ve alternatif enerji kaynakları ile ekonomik karşılaştırması", Fırat Üni. Deny. ve Hes. Müh. Derg., vol. 4, no 2, pp. 337-350, Haziran 2025.

### Öz

Küresel enerji talebi artmaya devam ettikçe, yenilenebilir enerji kaynaklarının sürdürülebilirliği sağlamadaki rolü giderek daha önemli hale gelmiştir. Ancak bu enerji türlerinin birçoğunun mevsimsel veya coğrafi koşullara bağlı olması nedeniyle tek başına enerji talebini karşılama yeteneği sınırlıdır. Bu zorluk, özellikle ithal enerji kaynaklarına bağımlı ülkelerde, yerel enerji kaynaklarından yararlanma ihtiyacını ortaya çıkarmaktadır. Çeşitli ve yerel enerji kaynaklarının kullanılması, yalnızca ithal kaynaklara olan bağımlılığı azaltmak için değil, aynı zamanda enerji çeşitlendirmesini teşvik etmek için de kritik öneme sahiptir. Bu bakış açısından, biyogaz en erişilebilir enerji üretim teknolojilerinden biri olarak tanımlanabilir. Bu çalışma, artan enerji talebini karşılamak için biyogaz enerjisi, jeotermal enerji, dizel yakıtı, fueloil ve asfaltit yatırımları için Net Bugünkü Değer (NBD) ve Seviyelendirilmiş Enerji Maliyeti (LCOE) analizlerini incelemektedir. Batman ilindeki atık potansiyelinden yararlanan bir biyogaz tesisinin ekonomik değerlendirmesine odaklanarak, bölgesel alternatifler arasında en uygun enerji kaynağının belirlenmesi amaçlanmaktadır. Biyogaz enerji kaynağı için birim enerji maliyeti %6 faiz oranıyla 75,73\$/MWh, %8 faiz oranıyla 80,65, %10 faiz oranıyla 85,89 ve %12 faiz oranıyla 91,41 olarak hesaplanmıştır. Biyogaz tesisinin 10 yıllık bir geri ödeme süresi olduğu tespit edilmiş ve 10 yıldan sonra yatırım kârlı hale gelmektedir. 20 yıllık ekonomik ömrü boyunca biyogaz yatırımının Net Bugünkü Değerinin yaklaşık 1,3 milyon dolara ulaşması öngörülmektedir.

**Anahtar kelimeler:** Biyogaz, Enerji ekonomisi, Net bugünkü değer analizi, Biyogaz potansiyeli

\*Yazışılan yazar

İntihal Kontrol: Evet – Turnitin

Şikayet: [fujece@firat.edu.tr](mailto:fujece@firat.edu.tr)

Telif Hakkı ve Lisans: Dergide yayın yapan yazarlar, CC BY-NC 4.0 kapsamında lisanslanan çalışmalarının telif hakkını saklı tutar.



## Assessment of Biogas Potential in Batman and Its Economic Comparison with Alternative Energy Sources

Süleyman ATILGAN<sup>1\*</sup> , Umut ERCAN<sup>2</sup> , Muzaffer ALIM<sup>3</sup> 

<sup>1</sup>Energy Systems Engineering, Institute of Science, Firat University, Elazığ, Türkiye.

<sup>2</sup>Machinery and Metal Technologies, Beşiri Organized Industrial Zone Vocational School, Batman University, Batman, Türkiye.

<sup>3</sup>Textiles, Clothing, Shoes and Leather, Beşiri Organized Industrial Zone Vocational School, Batman University, Batman, Türkiye.

<sup>1</sup>suleyman@batman.edu.tr, <sup>2</sup>umut.ercan@batman.edu.tr, <sup>3</sup>muzaffer.alim@batman.edu.tr

Received: 31.12.2024

Accepted: 15.04.2025

Revision: 17.02.2025

doi: <https://doi.org/10.62520/fujece.1610687>

Research Article

Citation: S. Atilgan, U. Ercan and M. Alim, "Assessment of biogas potential in batman and its economic comparison with alternative energy sources", *Firat Univ. Jour. of Exper. and Comp. Eng.*, vol. 4, no 2, pp. 337-350, June 2025.

### Abstract

The role of renewable energy sources in ensuring sustainability has become increasingly important as global energy demand continues to rise. However, many of these energy types have limited ability to meet energy demand alone due to their dependence on seasonal or geographic conditions. This challenge highlights the need for leveraging local energy resources, particularly in countries dependent on imported energy sources. Utilizing diverse and local energy sources is critical not only to reduce reliance on imported resources but also to promote energy diversification. From this perspective, biogas can be defined as one of the most accessible energy production technologies. This study conducts Net Present Value (NPV) and Levelized Cost of Electricity (LCOE) analyses for investments in biogas energy, geothermal energy, diesel fuel, fuel oil, and asphalted to help meet the growing energy demand. The research focuses on the economic evaluation of a biogas plant by utilizing organic waste potential in Batman province, aiming to identify the most suitable energy source among regional alternatives. For the biogas energy source, unit costs are calculated as 75.73 \$/MWh at a 6% interest rate, 80.65 at 8%, 85.89 at 10%, and 91.41 at 12%. The biogas plant has a payback period of 10 years; after which it becomes profitable. Over its 20-year lifespan, the NPV is projected to reach approximately \$1.3 million.

**Keywords:** Biogas, Energy economics, Net present value analysis, Biogas potential

\*Corresponding author

## **1. Introduction**

Energy is essential for improving quality of life and supporting all aspects of a country's economy. With technological advancements, increasing industrialization has led to a rapid rise in energy demand. The wide use of energy resources has caused the depletion of fossil fuels such as oil, coal, and natural gas at an alarming rate. Recent studies indicate that oil reserves may be depleted by 2047, while natural gas could run out by 2068. Additionally, coal reserves are expected to last until 2140. In addition to the environmental destruction caused in the areas where fossil fuel plants are established, these fuels also have adverse effects that threaten the entire planet with global warming. The inevitable depletion of fossil fuels and their negative impacts on human life have made the sustainability of energy resources one of the most critical global issues. Due to these negative effects, countries have turned to renewable energy sources that are clean and sustainable.

Renewable energy refers to naturally replenished sources like wind, solar and biomass. Renewable energy sources play a crucial role in addressing the depletion of fossil fuels and combating adverse effects such as global warming and climate change. The use of fossil fuels leads to significant environmental pollution through carbon dioxide and greenhouse gas emissions. In contrast, renewable energy sources are clean, environmentally friendly, and economical. Research on renewable energy has seen a notable increase in recent years. Renewable energy sources include solar energy, wind energy, hydroelectric energy, geothermal energy, wave energy, hydrogen energy, and biomass energy.

One of the most important methods for sustainable energy production and waste management is anaerobic digestion. Anaerobic digestion refers to a series of biological processes in which a microbial consortium breaks down organic matter in an oxygen-depleted environment. This process not only provides an alternative energy source but also offers a viable option for diverting organic waste from landfills and reducing greenhouse gas emissions. Consequently, it is a technology that can be effectively utilized by local governments and authorities to achieve waste management and sustainable environmental goals.

Biogas is a renewable energy source that can be used in various applications, including fuel for vehicles, heat, and electricity generation. A wide range of organic waste materials, such as animal waste/manure, food waste, organic municipal solid waste, industrial waste, sewage sludge, and agricultural residues, can potentially be utilized for biogas production. Among the different types of alternative and sustainable renewable energy sources, biogas is preferred due to its ease of production and its direct applicability as fuel for various devices, including generators, electrical and internal combustion engines, turbines, and fuel cells.

This study examines the economic analysis of biogas plant investments aimed at generating energy by determining the volume of potential waste that could be used as a biogas source in the province of Batman. The waste quantities are calculated based on the number of livestock in Batman, serving as the input for a biogas facility. An economic analysis of a potential biogas plant investment is conducted using the Net Present Value (NPV) approach under different financial scenarios. Additionally, a unit cost comparison is made through the Levelized Cost of Energy (LCOE) for energy produced from biogas and certain fossil-based fuels. Fluctuations in the raw material prices of energy sources like diesel and LPG have a positive impact on the economic sustainability of energy types like biogas, which are independent of external dependencies. This study bridges a critical gap in the field by combining biogas energy potential assessment with an in-depth economic analysis of various alternatives in terms of financial viability.

## **2. Literature Review**

There is an extensive literature on the existence of biogas production plants and the amount of energy they generate. Studies identify biogas as an important renewable energy source for addressing both energy and waste management issues. Kılıç [1] explores the general state of biogas and its position in Turkey. The study emphasizes the importance of utilizing waste for energy production to address the country's energy needs and resolve energy-related challenges. Chowdhury et al. [2] aim to evaluate biogas production from livestock waste in Bangladesh in 2016 and provide potential biological applications for converting and processing waste into biogas. The study presents the appropriate conversion technologies for calculating total biogas

production and includes mathematical equations related to biogas production mechanisms from animal waste. It demonstrates that approximately 229 million tons of animal waste are produced in 2016, with a total biogas production potential of  $16.68 \times 10^7$  MWh, equivalent to 16,988.97 million m<sup>3</sup> of biogas. From an environmental perspective, the study indicates that net CO<sub>2</sub> emissions could be reduced by producing 4.42 million tons of diesel energy and 29 million tons of bio fertilizer.

Şenol et al. [3] investigate the availability of key resources for biogas production in Turkey. The study states that the country has an abundance of organic materials suitable for biogas production, most of which are in waste form. They highlight the importance of evaluating these waste materials for energy production. Yılmaz et al. [4] analyzed biogas production in Turkey and mentioned that there are 73 active biogas plants in the country, generating a total of 385 MW of power. The study highlights that animal, agricultural, and municipal waste are important resources for biogas production in Turkey. In 2019, Yılmaz [5] explores the biogas production and energy generation capacity of licensed renewable waste energy plants in Turkey. The study reveals that there are 122 licensed plants with a combined production capacity of 634.2 MW. Durmuş et al. [6] report that the annual animal waste in Batman province amounts to 797,871.32 tons, with an energy value of 4,333.64 TEP and a total energy equivalent of 69,618.95 TEB. Işıkyürek [7] designs a biogas plant to meet the energy needs of the Mediterranean University's central campus. The study determines the total energy demand over three years and assesses the waste potential in the area, leading to the design and sizing of the biogas facility. It concludes that the plant will address both the waste problem and the electricity consumption costs.

Studies identify significant potential for biogas production from organic waste in residential areas, including animal, plant, industrial, and municipal waste. Arıcı et al. [8] investigate the biogas energy potential derived from livestock (cattle, sheep, goats) and poultry waste in Turkey's Eastern Anatolia region. Their study identifies the annual biogas potential in several provinces, with Ağrı contributing 95,511.586 m<sup>3</sup>/year, Ardahan 37,711.934 m<sup>3</sup>/year, Bingöl 36,056.08 m<sup>3</sup>/year, and Bitlis 35,834.288 m<sup>3</sup>/year. Other provinces include Elazığ with 44,578.567 m<sup>3</sup>/year, Erzincan 30,250.968 m<sup>3</sup>/year, Erzurum 108,746.365 m<sup>3</sup>/year, and Hakkari 38,114.012 m<sup>3</sup>/year. Additionally, Iğdır contributes 49,812.987 m<sup>3</sup>/year, Kars 76,560.456 m<sup>3</sup>/year, Malatya 32,547.220 m<sup>3</sup>/year, Muş 75,253.808 m<sup>3</sup>/year, Şırnak 29,026.576 m<sup>3</sup>/year, Tunceli 20,701.560 m<sup>3</sup>/year, and Van 130,354.586 m<sup>3</sup>/year. Aybek et al. [9] research the potential for biogas production from agricultural and animal waste in Kahramanmaraş province. Their study concludes that biogas production from agricultural waste (100 TJ/year) and animal manure (2077 TJ/year) would provide economic, social, and environmental benefits. Abdeshahian et al. [10] evaluate the biogas potential from organic waste derived from farm animals and slaughterhouses in Malaysia, showing an annual biogas production potential of 4589.49 million m<sup>3</sup>, which could generate  $8.27 \times 10^9$  kWh of electricity in 2012. Taşova [11] assesses the biogas potential from poultry waste in Tokat province, concluding that the biogas produced could meet the annual electricity needs of 3,654 households. Karaca [12] examines the potential for biogas production from animal manure in Hatay province, estimating that 15 million m<sup>3</sup> of biogas could be produced, equivalent to 8,000 tons of petroleum. Kocabey [13] analyzes biogas potential from animal waste in Balıkesir, finding a 112 MW biogas energy potential in the province. Atılğan and Yılmaz [14] examine the biogas potential from animal manure in Mardin, estimating that the biogas production could meet the energy needs of 51,852 people. Khalil et al. [15] provide technological suggestions for utilizing waste, particularly animal waste, for energy production in Indonesia. They estimate that Indonesia's animal waste amounts to approximately 9597.4 million m<sup>3</sup> annually, with the potential to produce  $1.7 \times 10^6$  kWh of electricity. Wine has also been identified as a high potential source for biogas production. The production of biogas from wine presents both economic and environmental benefits. Wine vinegar has a low carbon-to-nitrogen ratio, meaning that complementary materials, such as animal manure, industrial organic waste, and lime fertilizers, should be added to enhance biogas yield. Globally, 22.4 giga liters of wine are produced, with the potential to generate 407.68 giga liters of biogas, making it a significant renewable energy source. Parsaee et al. [16] summarize the properties of wine and its potential for biogas production, investigating the optimal conditions for biogas production and the advantages of biogas from wine.

Anaerobic digestion of organic waste offers several benefits, including reduced odor emissions, pathogen reduction, and low requirements for organic sludge. Additionally, the processed organic waste can be used as a mineral fertilizer for arable land or as an organic substrate for greenhouse cultivation. Nasir et al. [17]



evaluate the anaerobic treatment performance of cow manure and palm oil mill wastewater in terms of biogas production and volatile solid reduction. The study indicates that increasing the inoculum ratio has a significant impact on the biogas production rate. The results indicate that the average biogas yield is 0.346 m<sup>3</sup>/kg volatile solids when palm oil mill wastewater is used as the inoculum. Abraham et al. [18] research the inclusion of a pre-treatment step in anaerobic digestion processes, showing that it increases the digestibility of lignocellulosic biomass and promotes the removal of lignin and complex biomass structures, thus improving biogas yield. The study also demonstrates that when ionic liquids are used as a pre-treatment strategy for anaerobic digestion, biogas production improves by 1200%. Dehhaghi et al. [19] review recent technologies related to the application of nanomaterials in enhancing biogas production, investigating the effects of nanomaterials on both the quantity and quality of biogas produced. They state that nano-sized iron particles can increase biogas production rates.

Economic analyses of biogas energy in the literature consistently demonstrate its viability as a renewable energy source. Studies across different contexts, including composite material digesters Obileke et al. [20] cow manure processing Muharia et al. [21] and sugar factories Ogrodowczyk et al. [22] all report positive economic indicators. The economic performance of biogas projects varies regionally and depends on the type of waste utilized. For instance, Ogrodowczyk et al. [22] report an Internal Rate of Return (IRR) of 12.48% for a biogas investment, while [20] estimate this figure at 8.5%. Interestingly, some studies show IRR values as high as 249.8% Muharia et al. [21]. Similarly, payback periods for investments range from 8 years Ogrodowczyk et al. [22] to 6 years Al- Wahaibi et al. [23] and as low as 2 years Obileke et al. [20].

From the literature review, it is seen that most studies focus on estimating the biogas production potential in specific regions or analyzing its technical feasibility. However, a significant gap exists in the economic evaluation of biogas plants relative to other energy sources, particularly in terms of their comparative financial sustainability. Variation in economic outcomes of the biogas in the literature underscore the need for region specific analyses of biogas energy investments. To address this, the present study focuses on Batman province, aiming to evaluate the economic feasibility of biogas energy in this particular region, utilizing detailed NPV and LCOE calculations. By doing so, it provides a practical framework for assessing the viability of renewable energy investments in regions with high biogas potential. The analysis compares the economic viability of biogas against energy sources such as diesel, geothermal, fuel oil, and asphalted. The economic parameters used in these analyses are based on data provided by Kat [24], which is detailed in the following section.

### **3. Material and Method**

#### **3.1. Biogas**

Biogas is a colorless and odorless gas that is produced through the anaerobic (oxygen-free) fermentation of organic waste materials, such as animal, plant, industrial, and municipal waste. It is lighter than air due to its density of 1.2 kg/m<sup>3</sup>. When burned, biogas produces a bright blue flame. The components of biogas include methane (CH<sub>4</sub>), carbon dioxide (CO<sub>2</sub>), water vapor (H<sub>2</sub>O), nitrogen (N<sub>2</sub>), oxygen (O<sub>2</sub>), hydrogen (H<sub>2</sub>), ammonia (NH<sub>3</sub>), and hydrogen sulfide (H<sub>2</sub>S). The methane (CH<sub>4</sub>) content typically ranges between 40-75%, the carbon dioxide (CO<sub>2</sub>) content ranges from 15-60%, and the water vapor (H<sub>2</sub>O) content varies from 1-5% [25]. Table 1 summarize the volume of basic components of biogas.

**Table 1.** Basic Components of Biogas

Component	Volume
Methane (CH <sub>4</sub> )	40-75 %
Carbon Dioxide (CO <sub>2</sub> )	15-60 %
Water Vapoe (H <sub>2</sub> O)	1-5 %
Nitrogen (N <sub>2</sub> )	0-5 %
Oxygen (O <sub>2</sub> )	<2 %
Hydrogen (H <sub>2</sub> )	<1 %
Ammonia (NH <sub>3</sub> )	0-500 ppm
Hydrogen Sulfide (H <sub>2</sub> S)	0-5000 ppm

One cubic meter of biogas is equivalent to 4.7 kWh of electricity, 0.62 liters of gas, 0.66 liters of diesel, 0.43 kg of butane, 0.25 meters of propane, 1.46 kg of coal, and 3.47 kg of wood [26]. Figure 1 illustrates the energy content of 1 cubic meter (1 m<sup>3</sup>) of biogas compared to various conventional energy sources. The bar chart demonstrates that 1 m<sup>3</sup> of biogas is equivalent to approximately 4.7 kilowatt-hours (kWh) of electricity, highlighting its relatively high energy density. In comparison, equivalent energy values for gasoline, diesel, butane, propane, coal, and wood are significantly lower, indicating that biogas offers a more concentrated energy source. This underscores the potential of biogas as a valuable and versatile energy carrier, capable of substituting for a range of traditional fuels.

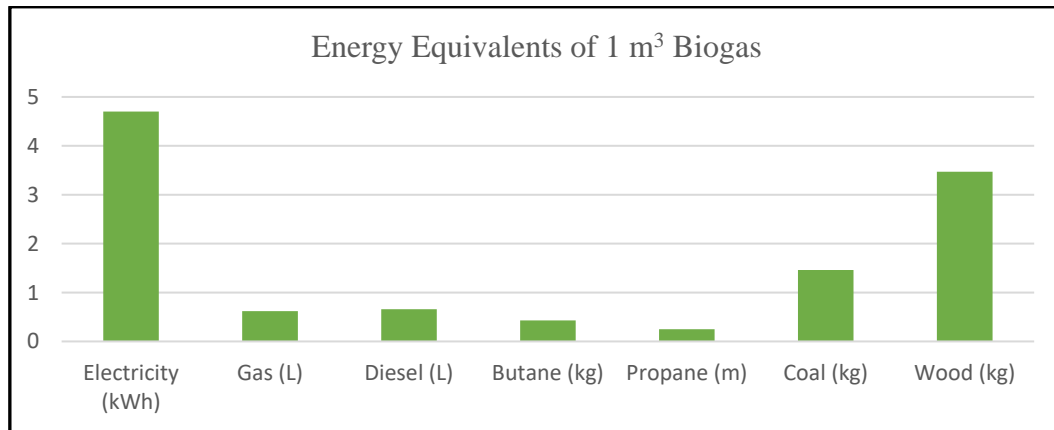


**Figure 1.** Energy Equivalents of 1 m<sup>3</sup> of Biogas

The size of a biogas plant varies depending on the purpose of usage. These plants are classified into four categories based on their capacity: family, farm, village, and industrial types as presented in Table 2 [27].

**Table 2.** Types of Biogas Production Plants

Plant Type	Production Capacity (m <sup>3</sup> )
Family-Type Biogas Plant	6 - 12
Farm-Type Biogas Plant	50 - 100 - 150
Village-Type Biogas Plant	100 - 200
Industrial-Type Biogas Plant	1000 - 10000

### **3.2. Main organic wastes used in biogas production**

In Turkey, organic waste constitutes approximately two-thirds of the total waste. The significant share of organic waste in the total waste is a great advantage for the country. However, leaving the waste to decompose or discarding it in the environment also presents disadvantages. The conscious utilization of organic waste materials is of great importance both in terms of energy production and environmental pollution. Various organic wastes are used in biogas production [27].

#### **3.2.1. Animal organic wastes**

Animal organic wastes are typically derived from cattle, sheep, goats, or poultry. The amount of manure generated by these animals varies depending on their feeding methods. On average, one cattle produces 3.6 tons of manure per year, one sheep or goat produces 0.7 tons per year, and one poultry animal produces 0.022 tons per year. These animal wastes represent a significant potential for biogas production, with 33 m<sup>3</sup> of biogas obtained from 1 ton of cattle manure, 58 m<sup>3</sup> from 1 ton of sheep or goat manure, and 78 m<sup>3</sup> from 1 ton of poultry manure [28].

#### **3.2.2. Plant organic wastes**

Plant organic wastes play a significant role in biogas production. In Turkey, 65 million tons of agricultural waste are produced annually from crops such as cotton, tobacco, barley, wheat, rice, etc. These wastes contribute significantly to environmental pollution. However, biogas production from these wastes is crucial both for environmental benefits and energy production [3]. The methane (CH<sub>4</sub>) content of biogas produced from corn stalks and residues is 59%, while the methane content in biogas produced from wheat and barley straw is 60%. Approximately 185 m<sup>3</sup> of biogas can be obtained from 1 ton of corn silage [29].

#### **3.2.3. Industrial and urban wastes**

Industrial development, urbanization, and rapid population growth have led to the production of various wastes (such as sewage, leather, paper, food, and textile industry wastes), which are utilized in biogas production. Two methods are used to produce biogas from urban and industrial wastes: the biomethanization method and anaerobic fermentation. The biomethanization method involves separating the organic components of industrial and urban wastes and producing biogas through anaerobic fermentation. The use of the biomethanization method in biogas production increases the efficiency of gas production. The anaerobic fermentation method directly produces biogas from the waste [30].

### **3.3. Biogas potential of Batman province**

In Batman Province, there are 121,631 cattle, 859,003 sheep and goats, and 76,440 poultry animals. A total of 11,250 families engages in animal husbandry in the province [31]. The annual manure production from cattle in Batman Province is 437,871.6 tons, from sheep and goats is 601,302.1 tons, and from poultry is 1,681.68 tons. If the manure produced by these animals is converted into biogas, 14,449,762.8 m<sup>3</sup> of biogas can be obtained from cattle, 34,875,521.8 m<sup>3</sup> from sheep and goats, and 131,171.04 m<sup>3</sup> from poultry. When the produced biogas is converted into electrical energy, it would yield 67,913,885.16 kWh from cattle, 163,914,952.5 kWh from sheep and goats, and 616,503.888 kWh from poultry, totaling 232,445,341.5 kWh of electrical energy. Table 3 shows the overall biogas potential in Batman. It has been determined that, with efficient and conscious use of the animal manure in Batman Province, significant energy could be generated.

**Table 3.** Biogas Potential of Batman

Animal Type	Animal Quantity (head)	Waste Quantity (tons)	Biogas Production Potential (m <sup>3</sup> )	Electricity Production Potential (kWh)
Cattle	121,631	437,871.6	14,449,762.8	67,913,885.16
Sheep and Goats	859,003	601,302.1	34,875,521.8	163,914,952.5
Poultry	76,440	1,681.68	131,171.04	616,503.888
<b>Total</b>	<b>1,057,074</b>	<b>1,040,855.38</b>	<b>49,256,455.64</b>	<b>232,445,341.5</b>

### 3.4. Method

Energy investments are typically long-term investments, and thus, the financial efficiency of such projects needs to be calculated based on varying economic conditions. The most commonly used method for the economic evaluation of energy projects is the Net Present Value (NPV) approach. The economic analysis is performed by calculating the present value of the planned project's current cost and the future cash flows, taking into account the interest rate. A positive NPV indicates that the project is profitable and that the investment is viable. The NPV value can be calculated as follows:

$$NPV = \sum_{t=1}^N \frac{R_t}{(1+r)^t} - I_0 \quad (1)$$

The parameters in Equation (1) are defined as follows;

- $R_t$  : Net cash flow of the project in year t (revenue - cost)
- $r$  : Interest rate of the cost of capital
- $N$  : Economic life of the project
- $I_0$  : Initial installation cost of the project

When calculating the net cash flow of the project, it is determined by subtracting the total operating costs, maintenance and repair costs, fuel costs, and other cost items from the revenue generated from the sale of produced electricity. In NPV calculation, the selection of a suitable discount rate is essential. This rate reflects the cost of capital or the required rate of return, accurately representing the project's risk profile and the opportunity cost of capital. NPV is highly sensitive to the discount rate; a higher rate reduces the present value of future cash flows, potentially rendering a project with a positive NPV at a lower rate unprofitable. Therefore, a thorough sensitivity analysis, varying the discount rate, is essential.

Another widely used method in the economic evaluation of energy investments is the Levelized Cost of Energy (LCOE), which is defined as the cost per unit of energy produced over the economic life of an energy source. This value is obtained by dividing the total present value of the project's cash flows by the amount of energy produced, as shown in Equation (2).

$$LCOE = \frac{\text{Total cost over economic life (NPV)}}{\text{Present value of electricity produced over economic life}}$$

$$LCOE = \frac{NPV}{\sum_{t=1}^N \frac{E_t}{(1+r)^t}} \quad (2)$$

In Equation (2),  $E_t$  represents the amount of electricity produced in year t when calculating the unit energy cost. When calculating LCOE, a detailed breakdown of all cost components is crucial, including capital expenditures, fixed and variable operating costs, fuel costs (if applicable), and decommissioning costs. Accurate estimation of energy output over the project's lifetime is also required, considering factors like capacity factors, resource availability, and technology performance. When comparing LCOE values across

different projects, it is vital to use a consistent discount rate to ensure a fair comparison. It is important to note that while NPV assesses profitability of the total investment, LCOE focuses on per-unit energy cost.

#### 4. Numerical Results

This section presents the economic evaluation of a biogas plant, assessing waste potential in Batman province. The Net Present Value (NPV) and Levelized Cost of Energy (LCOE) methods, as detailed in Section 3.4, are applied. To provide a comprehensive comparison, energy sources prevalent in the Batman region—diesel, geothermal, fuel oil, and asphaltite—are also economically evaluated. Economic parameters, derived from [20] and detailed in Table 4, form the basis of these analyses.

**Table 4.** Economic Parameters of Energy Production Technologies

Type (By Source)	Lifetime (Years)	Efficiency Factor	Initial Cost (\$/MW)	Fixed Cost (\$/MW)	Variable Cost (\$/MWh)	Fuel Cost (\$/MWh)	Annual Electricity Production (MWh/Yıl)
Biogas	20	0.4	2500000	90000	1	13.75	7446
Geothermal	30	0.0001	3750000	40000	10	-	7446
Diesel	30	0.54	900000	11600	2.66	91.75	7446
Fuel Oil	30	0.54	900000	11600	2.66	54.05	7446
Asphaltite	30	0.45	1200000	40000	4	6.89	7446

The biogas plant, with a 20-year lifespan and 0.4 efficiency factor, is evaluated with an initial cost of \$2,500,000/MW, fixed costs of \$90,000/MW, variable costs of \$1/MWh, fuel costs of \$13.75/MWh, and an annual electricity production of 7,446 MWh. An NPV analysis, assuming an electricity sale price of \$100/MWh and an 8% interest rate, is presented in Figure 2.

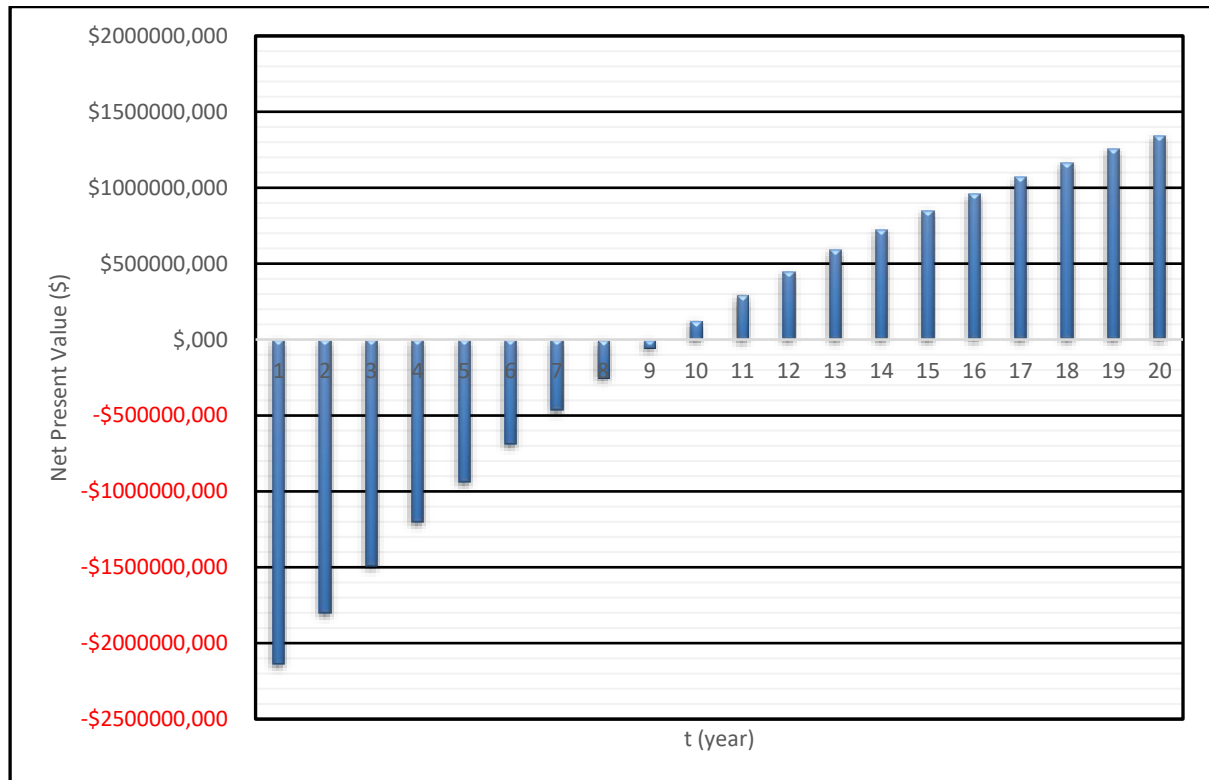


**Figure 2.** NPV Change of the 1 MW Biogas Plant Over the Years

The project's initial investment of \$2.5 million is recouped after approximately 10 years, with the NPV turning positive. The project reaches an NPV of approximately \$1.3 million by the end of its 20-year lifespan. The Internal Rate of Return (IRR) is calculated to be 14.6%, indicating the project's financial viability at interest rates below this threshold.

In such analyses, the interest rate plays a significant role, significantly affecting the investment viability and profitability of the project. One of the key economic indicators in this area is the IRR which is the interest rate that makes the NPV equal to zero. This rate is the interest rate that balances the initial cost when discounting the future cash flows to their present values. When the interest rate is equal to the IRR, the investment yields neither profit nor loss. For the investment to be considered profitable, the interest rate must be lower than the IRR value. According to the cash flow shown in Figure 2, the IRR is calculated to be 14.6%. This means that if the interest rate exceeds 14.6%, the project is not financially viable under the given economic conditions.

A comparison of biogas with other generation technologies reveals their relative costs based on the Levelized Cost of Energy (LCOE), which indicates the per-unit production cost of energy over the economic lifespan of a power plant and serves as a critical benchmark for investment decisions. Figure 3 illustrates the LCOE values for biogas, asphaltite, diesel, geothermal energy, and fuel oil, calculated at different interest rates, providing a clear comparison of which technologies are cheaper or more expensive under varying financial conditions.

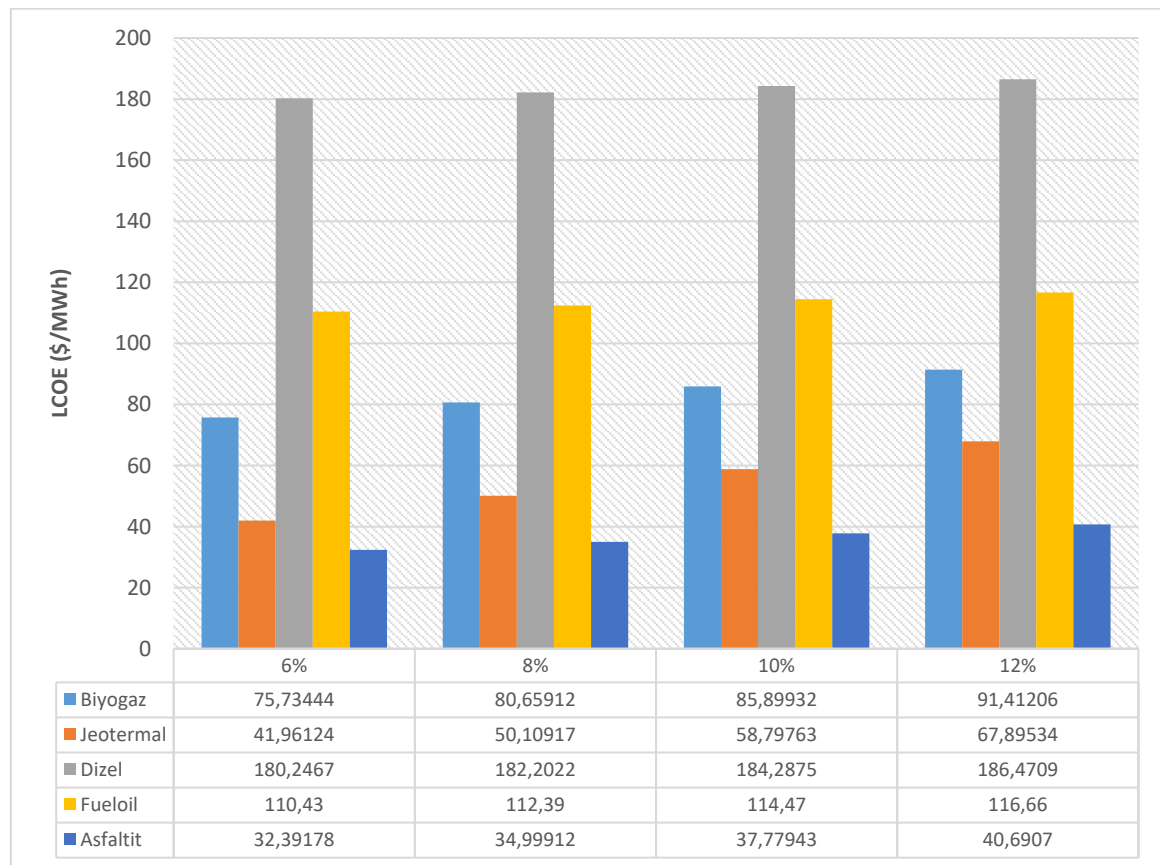


**Figure 3.** LCOE values for different energy production types at varying interest rates (\$/MWh)

In Figure 3, we present a clustered bar chart comparing the LCOE in dollars per megawatt-hour (\$/MWh) for five different energy sources: biogas, geothermal, diesel, fuel oil, and asphaltite. The X-axis represents varying interest rates, specifically 6%, 8%, 10%, and 12%, while the Y-axis displays the LCOE values. Each energy source is represented by a distinct color, with the corresponding LCOE value for each interest rate displayed within the respective bar. It effectively illustrates the impact of changing interest rates on the LCOE



of these energy sources, revealing that as interest rates increase, the LCOE rises across all sources as expected. Notably, geothermal and asphaltite consistently exhibit the lowest LCOE values, indicating their economic competitiveness, while diesel maintains the highest LCOE, suggesting it is the most expensive option. Biogas and fuel oil fall within the middle range, with biogas showing a more moderate increase in LCOE as interest rates rise compared to fuel oil.

Our economic analysis of a biogas plant in Batman province aligns with the broader literature demonstrating the viability of biogas energy. Our estimated IRR of 14.6% and payback period of 10 years fall within the range of values reported in studies on biogas production from various feedstocks, such as composite materials [20], cow manure [21], and sugar factory waste [22]. While our IRR is higher than some reported values [20], it is lower than the exceptionally high returns found in other studies [21], likely due to regional variations in factors such as feedstock costs, energy prices, and policy incentives. Our LCOE analysis further reinforces the cost-competitiveness of biogas, particularly compared to traditional liquid fuels. These findings underscore the potential of biogas to contribute to a more sustainable and secure energy future by utilizing waste streams, reducing reliance on fossil fuels, and mitigating climate change. Future research should explore strategies to optimize biogas production and further enhance its economic viability in diverse regional contexts.

When comparing the cost values calculated for biogas with other alternative energy sources, it is observed that biogas has higher costs than geothermal energy and asphalt, but lower costs compared to liquid fuels such as diesel and fuel oil. The findings in Figure 3 reveal that the highest unit cost is 50.11 \$/MWh for diesel. The most cost-effective option is geothermal energy. Geothermal energy stands out not only due to its cleaner and renewable nature but also because of its favorable cost. The cost differences between biogas and geothermal/asphaltite can be attributed to several factors. Geothermal energy's lower LCOE stems from its inherent resource availability and lower fuel costs, as it leverages the earth's natural heat. Asphaltite, a locally sourced solid fuel, benefits from lower fuel acquisition and processing costs compared to biogas, which involves more complex biological processes and feedstock management. These findings underscore the importance of tailored energy policies that consider regional resource availability and economic factors. For Batman province, while biogas presents a viable alternative to liquid fuels, incentives and technological advancements are needed to enhance its cost-competitiveness. Policies regarding biogas should focus on supporting the development of geothermal resources, given their cost effectiveness and sustainability.

## **5. Conclusion**

This study evaluates the economic potential of a biogas plant for assessing waste potential in Batman province. Net Present Value (NPV) and Levelized Cost of Electricity (LCOE) methods are used for the calculations. The economic comparison of biogas, along with other energy sources such as diesel, geothermal, fuel oil, and asphaltite, is made. The economic parameters used in these analyses are selected based on the data presented by [24].

For the local energy source, biogas, in Batman province, an initial investment cost of \$2.5 million corresponds to an annual net cash flow of \$362,220. The payback period of the plant is 10 years; after which it starts generating profit. Over the following years, the project continues to generate profit, and by the end of the 20th year, the NPV reaches approximately \$1.3 million.

In the coming years, the potential implementation of a carbon tax further reduces the costs of clean energy types. However, it should be noted that geothermal and many other renewable energy sources may not always provide electricity on demand due to seasonal conditions or other constraints. Therefore, ensuring energy diversity is essential for uninterrupted energy access. According to the results of this study, biogas is more cost-advantageous compared to diesel and fuel oil. Moreover, the import of liquid fuels in Turkey results in a significant current account deficit. Biogas, on the other hand, can be entirely considered within a circular economy, as it generates electricity while disposing of waste without the need for imports. These findings suggest that biogas may help reduce dependence on foreign energy sources.

Future research should explore the integration of hybrid energy systems, combining biogas with other renewable sources like solar or wind, to enhance reliability and reduce costs. Detailed lifecycle assessments, including environmental and social impacts, are also crucial.

## **6. Acknowledgments**

We would like to thank Firat University and anonymous reviewers for the contribution to our paper and publication.

## **7. Author Contribution Statement**

Süleyman Atilgan is responsible for the design of the study, conducting the literature review, and preparing the sections related to biogas. Umut Ercan contributes the introduction, the design of the study, writing and editing of the manuscript. Muzaffer Alim conducts the economic analysis, presents the numerical results, and proofreading the paper.

## **8. Ethics Committee Approval and Conflict of Interest**

It is not necessary to obtain approval from any ethics committee for the article being prepared. There are no conflicts of interest with any individual or institutions in relation to the content of the article.

## **9. Ethical Statement Regarding the Use of Artificial Intelligence**

No artificial intelligence-based tools or applications were used in the preparation of this study. The entire content of the study was produced by the author in accordance with scientific research methods and academic ethical principles.

## 10. References

- [1] F. Ç. Kiliç, "Biyogaz, önemi, genel durumu ve Türkiye'deki yeri," *Renew. Energy World*, vol. 8, no. 6, 2007. [Online]. Available: [http://www.normenerji.com.tr/menus/Biyogaz-onemi-durumu-yeri\\_04022012044242476508931.pdf](http://www.normenerji.com.tr/menus/Biyogaz-onemi-durumu-yeri_04022012044242476508931.pdf) (Visited on Jan. 15, 2024).
- [2] T. Chowdhury et al., "Latest advancements on livestock waste management and biogas production: Bangladesh's perspective," *J. Clean. Prod.*, vol. 272, p. 122818, 2020.
- [3] H. Şenol, E. A. Elibol, Ü. Açikel, and M. Şenol, "Türkiye'de biyogaz üretimi için başlıca biyokütle kaynakları," *Bitlis Eren Üniversitesi Fen Bilim. Derg.*, vol. 6, no. 2, pp. 81–92, 2017.
- [4] A. Yılmaz, S. Ünvar, T. Koca, and A. Koçer, "Türkiye'de biyogaz üretimi ve biyogaz üretimi istatistik bilgileri," *Technol. Appl. Sci.*, vol. 12, no. 4, pp. 218–232, 2017.
- [5] A. Yılmaz, "Türkiye'de biyogaz üretimi ve kurulu santrallerin ürettiği elektrik enerjisi," *Ecol. Life Sci.*, vol. 14, no. 1, pp. 12–28, 2019.
- [6] A. Durmuş, U. Ercan, A. S. Avcı, M. A. Kallioğlu, and H. Karakaya, "Batman İli Enerji Profiline Araştırılması," *Batman Üniversitesi Yaşam Bilim. Derg.*, vol. 7, no. 2/2, pp. 161–167, 2017.
- [7] Ç. Işıkyürek, "Akdeniz Üniversitesi Merkez Kampüsünün Enerji İhtiyacını Karşılamaya Yönelik Biyogaz Tesisinin Tasarımı ve Tekno-Ekonomik Analizleri," Ph. D. thesis, Akdeniz University, 2019.
- [8] F. Arıcı, Z. Karakuzulu, and M. Dumansızoğlu, "Doğu Anadolu Bölgesinin Biyogaz Enerji Potansiyeli," *The Journal of Academic Social Science*, 2024.
- [9] A. Aybek, S. Üçok, M. E. Bilgili, and M. A. İspir, "Kahramanmaraş ilinde bazı tarımsal atıkların biyogaz enerji potansiyelinin belirlenerek sayısal haritalarının oluşturulması," *Uludağ Üniversitesi Ziraat Fakültesi Derg.*, vol. 29, no. 2, 2015.
- [10] P. Abdesshahian, J. S. Lim, W. S. Ho, H. Hashim, and C. T. Lee, "Potential of biogas production from farm animal waste in Malaysia," *Renew. Sustain. Energy Rev.*, vol. 60, pp. 714–723, 2016.
- [11] M. Taşova, "Kümes Hayvanları Atıklarının Biyogaz Üretim Potansiyelinin Belirlenmesi: Tokat İli Örneği," *Kafkas Üniversitesi Fen Bilim. Enstitüsü Derg.*, vol. 10, no. 2, pp. 296–303, 2017.
- [12] C. Karaca, "Hatay ilinin hayvansal gübre kaynağından üretilebilir biyogaz potansiyelinin belirlenmesi," *Mustafa Kemal Üniversitesi Ziraat Fakültesi Derg.*, vol. 22, no. 1, pp. 34–39, 2017.
- [13] S. Kocabey, "Balıkesir İli İçin Hayvansal Atık Kaynaklı Biyogaz Potansiyelinin Belirlenmesi," *Eur. J. Sci. Technol.*, pp. 234–243, Dec. 2019, doi: 10.31590/ejosat.619058.
- [14] S. Atılğan and A. Yılmaz, "Mardin İlinin Hayvansal Gübre Kaynaklı Biyogaz Potansiyelinin Belirlenmesi," *Mühendis ve Makina*, vol. 62, no. 704, pp. 429–445, 2021.
- [15] M. Khalil, M. A. Berawi, R. Heryanto, and A. Rizalie, "Waste to energy technology: The potential of sustainable biogas production from animal waste in Indonesia," *Renew. Sustain. Energy Rev.*, vol. 105, pp. 323–331, 2019.
- [16] M. Parsaee, M. K. D. Kiani, and K. Karimi, "A review of biogas production from sugarcane vinasse," *Biomass Bioenergy*, vol. 122, pp. 117–125, 2019.
- [17] I. M. Nasir, T. I. M. Ghazi, R. Omar, and A. Idris, "Anaerobic digestion of cattle manure: Influence of inoculums concentration," *Int. J. Eng. Technol.*, vol. 10, no. 1, pp. 22–26, 2013.
- [18] A. Abraham et al., "Pretreatment strategies for enhanced biogas production from lignocellulosic biomass," *Bioresour. Technol.*, vol. 301, p. 122725, 2020.
- [19] M. Dehghani, M. Tabatabaei, M. Aghbashlo, H. K. S. Panahi, and A.-S. Nizami, "A state-of-the-art review on the application of nanomaterials for enhancing biogas production," *J. Environ. Manage.*, vol. 251, p. 109597, 2019.
- [20] K. Obileke, K. Makaka, G. Nwokolo, N. Meyer, E. L. Mukumpa, and P. Kat, "Economic analysis of biogas production via biogas digester made from composite material," *ChemEngineering*, vol. 6, no. 5, p. 67, 2022.
- [21] M. Muharia, M. Khotimal, D. R. Fitria, P. Andika, K. A. Isnani, and A. Badril, "Techno-Economic Analysis of biogas production from cow manure," *Jurnal Teknik Kimia dan Lingkungan*, vol. 8, no. 1, pp. 1–13, 2024.
- [22] D. Ogrodowczyk, T. Olejnik, M. Kaźmierczak, S. Brzeziński, and A. Baryga, "Economic analysis for biogas plant working at sugar factory," *Biotechnology and Food Science*, vol. 80, no. 2, pp. 129–136, 2016.

- [23] A. Al-Wahaibi, A. I. Osman, A. A. H. Al-Muhtaseb, O. Algaisi, M. Baawain, S. Fawzy, and D. W. Rooney, “Techno-economic evaluation of biogas production from food waste via anaerobic digestion,” *Scientific Reports*, vol. 10, no. 1, p. 15719, 2020.
- [24] B. Kat, “Clean energy transition in the Turkish power sector: A techno-economic analysis with a high-resolution power expansion model,” *Util. Policy*, vol. 82, p. 101538, 2023.
- [25] B. Bharathiraja, T. Sudharsana, J. Jayamuthunagai, R. Praveenkumar, S. Chozhavendhan, and J. Iyyappan, “Biogas production—A review on composition, fuel properties, feed stock and principles of anaerobic digestion,” *Renew. Sustain. Energy Rev.*, vol. 90, April, pp. 570–582, 2018.
- [26] T.C. Enerji ve Tabii Kaynaklar Bakanlığı, URL: <https://www.enerji.gov.tr/> (Visited on Mar. 15, 2024).
- [27] İ. Akova, *Yenilenebilir enerji kaynakları*. Nobel Yayın Dağıtım, 2008.
- [28] N. N. Koçer, C. Öner, and İ. Sugözü, “Türkiye’de hayvancılık potansiyeli ve biyogaz üretimi,” *Fırat Üniversitesi Doğu Araştırmaları Derg.*, vol. 4, no. 2, pp. 17–20, 2006.
- [29] S. O. Dahunsi, S. Oranusi, and V. E. Efevbokhan, “Optimization of pretreatment, process performance, mass and energy balance in the anaerobic digestion of *Arachis hypogaea* (Peanut) hull,” *Energy Convers. Manag.*, vol. 139, pp. 260–275, May 2017.
- [30] P. K. Mahla, P. C. Vithalani, and N. S. Bhatt, “Biomethanation: Advancements for Upgrading Biomethane Using Biogas Technologies,” in *Industrial Microbiology and Biotechnology*, P. Verma, Ed., Singapore: Springer Singapore, 2022.
- [31] Batman İl Tarım ve Orman Müdürlüğü, URL: <https://batman.tarimorman.gov.tr/> (Visited on Mar. 15, 2024).



## Transformer Tabanlı Yöntemlerin Restoran Yorumlarının Analizi Üzerindeki Başarımı

Mucahit KARADUMAN<sup>1</sup> , Muhammed Bedir BAYDEMİR<sup>2</sup> , Muhammed YILDIRIM<sup>3\*</sup> 

<sup>1</sup>Yazılım Mühendisliği, Mühendislik ve Doğa Bilimleri Fakültesi, Malatya Turgut Özal Üniversitesi, Malatya, Türkiye.

<sup>2</sup>Arapgir Meslek Yüksek Okulu, Malatya Turgut Özal Üniversitesi, Malatya, Türkiye.

<sup>3</sup>Bilgisayar Mühendisliği, Mühendislik ve Doğa Bilimleri Fakültesi, Malatya Turgut Özal Üniversitesi, Malatya, Türkiye.

<sup>1</sup>[mucahit.karaduman@ozal.edu.tr](mailto:mucahit.karaduman@ozal.edu.tr), <sup>2</sup>[muhammed.baydemir@ozal.edu.tr](mailto:muhammed.baydemir@ozal.edu.tr), <sup>3</sup>[muhammed.yildirim@ozal.edu.tr](mailto:muhammed.yildirim@ozal.edu.tr)

Geliş Tarihi: 3.02.2025

Kabul Tarihi: 24.03.2025

Düzeltilme Tarihi: 20.02.2025

doi: <https://doi.org/10.62520/fujece.1632266>

Araştırma Makalesi

Alıntı: M. Karaduman, M. B. Baydemir ve M. Yıldırım, “Transformer tabanlı yöntemlerin restoran yorumlarının analizi üzerindeki başarımı”, Fırat Üni. Deny. ve Hes. Müh. Derg., vol. 4, no 2, pp. 351-362, Haziran 2025.

### Öz

Duygu analizi, metinlerdeki duygusal tonları belirleyerek, müşteri geri bildirimlerinden sosyal medya paylaşımlarına kadar geniş bir alanda önemli veriler sağlar. Bu çalışmada, restoran yorumları kullanılarak duygu analizi gerçekleştirilmiştir. Çalışmada, duygu analizi için transformatör tabanlı bir model kullanılmıştır. Bu modellerin temelinde yer alan dikkat mekanizması, metin içindeki kelimelerin bağlamsal ilişkilerini dinamik olarak öğrenerek dilin anlamını daha iyi yakalar. Model, geniş bir bilgi kaynağına sahip bir veri seti ile eğitilmiş ve test edilmiştir. Öncelikle veri setinin tokenleştirme ve dolgu işlemleri gerçekleştirilmiş; daha sonra model eğitilmiş ve test sonuçları elde edilmiştir. Modelin eğitim doğruluğu %90,81, test doğruluğu ise %85,79 olarak hesaplanmıştır. Diğer performans metrikleri de göz önünde bulundurulduğunda, negatif ve pozitif sınıflar için yüksek başarı elde eden model, nötr sınıf için daha düşük bir başarı göstermiştir. Genel değerlendirme açısından modelin doğruluk oranı göz önüne alındığında, iyi bir performans sergilediği görülmektedir. Bu durum, transformatör tabanlı yaklaşımların doğal dil işleme için uygun olduğunu ve bu alandaki kullanılabilirliğini göstermektedir.

**Anahtar kelimeler:** Duygu analizi, Transformatör, NLP, Metin sınıflandırma

\*Yazılan Yazar

İntihal Kontrol: Evet – Turnitin

Şikayet: [fujece@firat.edu.tr](mailto:fujece@firat.edu.tr)

Telif Hakkı ve Lisans: Dergide yayın yapan yazarlar, CC BY-NC 4.0 kapsamında lisanslanan çalışmalarının telif hakkını saklı tutar.



## Performance of Transformer-Based Methods on Restaurant Reviews Analysis

Mucahit KARADUMAN<sup>1</sup> , Muhammed Bedir BAYDEMİR<sup>2</sup> , Muhammed YILDIRIM<sup>3\*</sup> 

<sup>1</sup>Software Engineering, Faculty of Engineering and Natural Sciences, Malatya Turgut Ozal University, Malatya, Türkiye.

<sup>2</sup>Arapgir Vocational School, Malatya Turgut Ozal University, Malatya, Türkiye.

<sup>3</sup>Computer Engineering, Faculty of Engineering and Natural Sciences, Malatya Turgut Ozal University, Malatya, Türkiye.

<sup>1</sup>[mucahit.karaduman@ozal.edu.tr](mailto:mucahit.karaduman@ozal.edu.tr), <sup>2</sup>[muhammed.baydemir@ozal.edu.tr](mailto:muhammed.baydemir@ozal.edu.tr), <sup>3</sup>[muhammed.yildirim@ozal.edu.tr](mailto:muhammed.yildirim@ozal.edu.tr)

Received: 3.02.2025

Accepted: 24.03.2025

Revision: 20.02.2025

doi: <https://doi.org/10.62520/fujece.1632266>

Research Article

Citation: M. Karaduman, M. B. Baydemir and M. Yıldırım, "Performance of transformer-based methods on restaurant reviews analysis", *Firat Univ. Jour. of Exper. and Comp. Eng.*, vol. 4, no 2, pp. 351-362, June 2025.

### Abstract

Sentiment analysis provides important data in various areas, from customer feedback to social media posts, by determining the text's emotional tones. In this study, sentiment analysis was performed using restaurant reviews with a transformer-based model. The attention mechanism underlying these models dynamically learns the contextual relationships of words in the text and better captures the meaning of the language. The model was trained and tested using a dataset from a vast information source. First, tokenization and padding operations of the dataset were performed; then, the model was trained, and test results were obtained. The training accuracy of the model was calculated as 90.81% and the test accuracy as 85.79%. When other performance metrics were also considered, the model, which achieved high success for negative and positive classes, showed lower success for the neutral class. In terms of general evaluation, it is seen that the model exhibited good performance when the accuracy rate was taken into account. This shows that transformer-based approaches are suitable for natural language processing and usability in this area.

**Keywords:** Sentiment analysis, Transformer, NLP, Text classification

---

\*Corresponding author



## 1. Introduction

In today's digitalized lifestyle, comments on online platforms are effective in decision-making processes in many areas, and consumers decide whether to take action based on these comments. In particular, elements in the natural flow of life, such as shopping, holiday planning, and reservations, have found their place on digital platforms. Digital platforms provide convenience in decision-making by saving time and providing a wide range of opportunities to analyze user comments. These services, which are an indispensable part of modern life, offer healthy progress to improve process efficiency and reliability by providing solutions and suggestions to users, especially regarding user experiences. Transactions that can be performed on the Internet are listed in general in Figure 1. These processes include determining the emotional tone of texts with sentiment analysis, categorizing content with text classification, and automatic translation between different languages with language translation. In addition, long content can be shortened with text summarization algorithms, and user interactions can be automated with chatbots and virtual assistants. Search and information extraction processes enable meaningful information to be extracted from large data sets, while speech recognition technologies convert voice input into text. Automatic text completion and language modeling techniques speed up the writing process and improve the user experience. News and spam filtering prevent unnecessary content, providing a safe internet environment, while recommendation systems help provide personalized content presentation. Finally, social media analysis provides data-driven insights into user tendencies, trends, and social events.

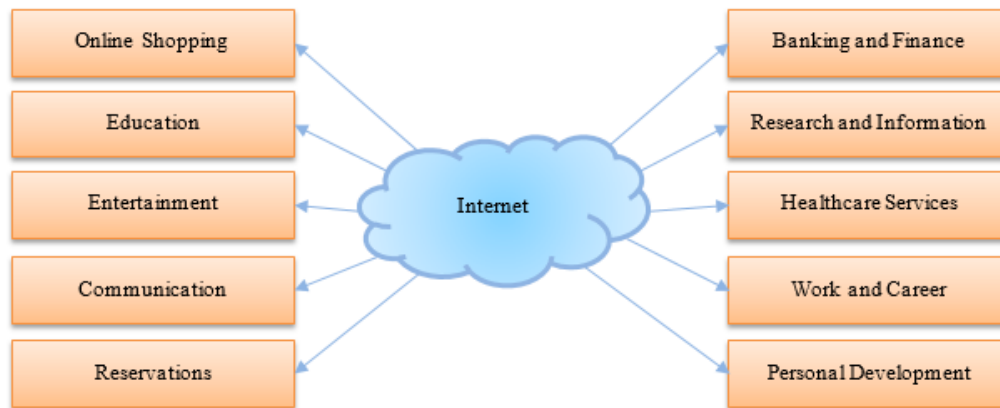


**Figure 1.** General list of transactions that can be done via the Internet

The Internet can be used for reservations, vacations, and restaurant dining. Customer experiences in the restaurant and service sector help companies to see their shortcomings and improve them, as well as to have prior knowledge about what kind of service they will receive. Restaurant reviews, also the subject of this study, are presented as a source of information regarding food quality, service, and general satisfaction. These reviews, which are on different platforms and are irregular, can make it difficult for users and company owners to access and analyze the correct information. These difficulties can cause mistakes when making the right decision. The development of artificial intelligence models, especially in natural language processing (NLP), offers significant benefits in interpreting and analyzing texts. Classifying complex texts by analyzing them and extracting meaningful information are among the essential tasks of NLP systems. Thanks to these systems, studies such as sentiment and subject-based analysis can be carried out from texts. Measuring the satisfaction levels of restaurant reviews, detecting sentiments in the text, and determining trends and changes are essential in improving service quality and providing correct analysis opportunities to customers and business owners. The operations performed with natural language processing are shown in Figure 2 [1–8]. Remarkably, the classification of texts is within the scope of this study.

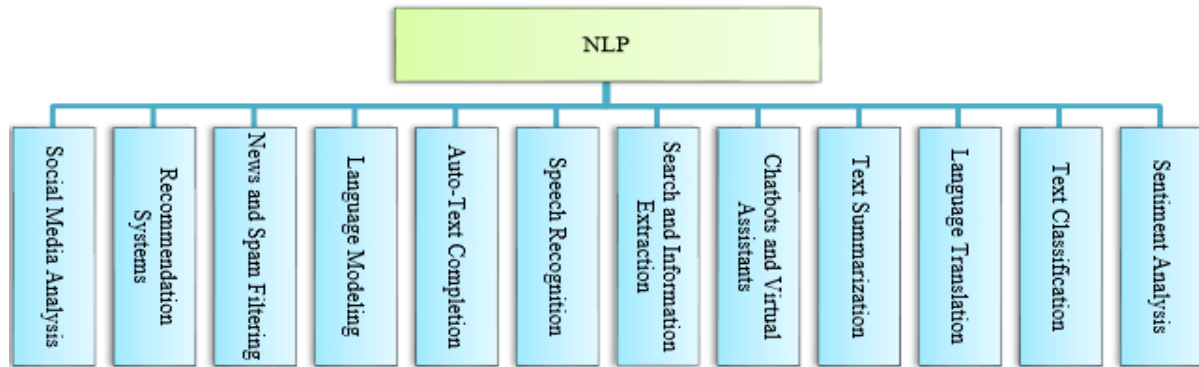


**Figure 2.** Applications made with NLP

This article is about analyzing restaurant reviews. When the studies in the literature are examined, there are many studies in the field of NLP. NLP offers a wide range of applications in the processing, analyzing, and interpreting text and speech data. Studies in this field focus on basic tasks such as Sentiment Analysis [9], Text Classification [10], Language Translation [11], and Text Summarization [12]. In addition, significant progress has been made in areas such as Chatbots and Virtual Assistants [13], Search and Information Extraction [14], Speech Recognition [15], Auto-Text Completion [16] and Language Modeling [17]. Applications such as News and Spam Filtering [18,19] Recommendation Systems [20], and Question-Answering task [21] increase the impact of natural language processing technologies in daily life and offer a wide range of usage scenarios. Studies in these areas enable NLP to provide more effective and efficient solutions in various sectors.

The literature contains studies on the subject. Luo et al. compared deep learning-based models to analyze restaurant reviews. The study stated that the most successful results were obtained from LSTM networks when sentiment analysis from restaurant reviews was performed. In this study also inferred that the most negative comments were in April, during the epidemic. In the study, researchers achieved an accuracy of 91.1% [22]. In this study, Asani et al. made different inferences to perform sentiment analysis on restaurant reviews. After sentiment analysis, they developed a recommendation system that considered user comments. The study evaluated restaurants using different performance measurement metrics. It obtained a precision value of 92.8% [23]. Punetha et al. present an unsupervised mathematical optimization framework for sentiment analysis in restaurant reviews. They developed this method because many studies in the literature have a complex and lengthy training process. The study was tested on two different data sets. Precision values of 89% and 90% were obtained in these datasets [24]. Patil et al. used deep and machine learning methods to classify restaurant reviews. This study concluded that Naive Bayes and Logistic regression models were more successful than other machine learning methods. The parameters of these two models were optimized with the grid search algorithm. The accuracy values obtained in this step were 89.6% and 89.9%, respectively. CNNs, which are deep learning architectures, achieved an accuracy value of 89%, and Bi-LSTM networks, 90% [25]. Khan et al. stated that traditional methods could not produce successful results in such studies and proposed a new model. A bidirectional LSTM network was proposed in the proposed model. The proposed model was tested on three different data sets. As a result of the evaluations, the proposed model reached 78.96%, 79.10%, and 79.03% F1-Score in three data sets, respectively [26]. Mamatha et al. followed a different method in their study. This study used images instead of text to analyze restaurant reviews. They stated that the metrics obtained from image classification were more successful than those obtained by Naive Bayes. Researchers used CNN networks in the image classification process [27]. Zahoor et al. focused on analyzing restaurant reviews in a specific region in their study. In the study, researchers made a two-way inference. The first was emotion detection, while the second was related to automatic feedback. The study compared the results obtained using different machine learning methods. It was stated that the best results were achieved in the Random Forest method [28]. Branco et al. used transfer learning and transformer methods in their study to analyze restaurant reviews. Recently, transformer-based

methods have been frequently preferred, especially in natural language processing. In this proposed model, they achieved an accuracy value of 84% in a 3-class emotion analysis detection [29].

This article analyzes restaurant reviews using natural language processing methods and classifies the reviews using the transformer-based method. The aim is to classify the reviews correctly, divide them into three groups, and understand the restaurant reviews, which are very complex and challenging to analyze and determine trends. This study gives information about the proposed model's general structure and the dataset used in section 2. In section 3, experimental results and performance metrics of the model applied to the dataset are included. The last section includes evaluation, interpretation, and recommendations for the results obtained.

## 2. System Theory

### 2.1. Dataset

The restaurant reviews dataset is a good source for analyzing restaurants, consisting of customer feedback [30]. The dataset, which consists of approximately 513,000 rows in general, consists of a two-column structure. While customer reviews are given with the title “text” in the dataset, the column that determines the emotional states is called “label.” Customer reviews are collected in three classes. These classes are numbered negative, neutral, and positive. The comments, which consist of a large amount of text in the dataset, provide a good source for NLP models.

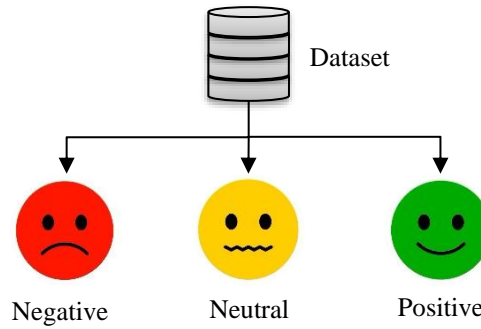


**Figure 3.** Dataset visualization by face icon

The simulation representation of the dataset is given in Figure 3. In Figure 3, negative, neutral, and positive classes are shown with facial expressions. A sad face expression was selected for negative, an expressionless face was selected for neutral and a smiling face was selected for positive.

### 2.2. Transformer based model

Transformer-based models are becoming popular due to successful image processing and text analysis results. It is seen that using the Transformer architecture provides high success results with NLP from complex texts. In the Deep Learning architecture used in this study, the Transformer block is used, and thus, the model is aimed to have high classification success. The general structure of the proposed system is given in Figure 4. First, data is taken from the ready restaurant review dataset, and tokenization and padding operations are performed during the pre-processing step.

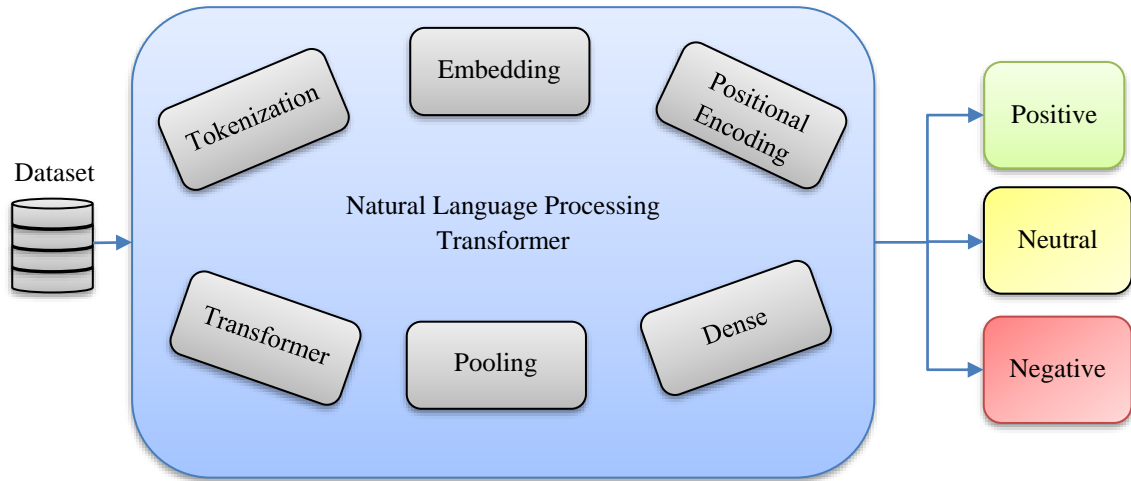


**Figure 4.** General structure of the Transformer method

The tokenization process is given in Figure 5. Sentences are analyzed one by one, and tokens are created. The tokenization process separates texts into subunits, such as words, and allows them to be represented with numerical indexes. For this purpose, the tokenizer class of the Keras library is used to convert the most used 20 thousand words into a word dictionary. The texts in the created word dictionary are converted into numerical sequences and converted into a usable format in the model.

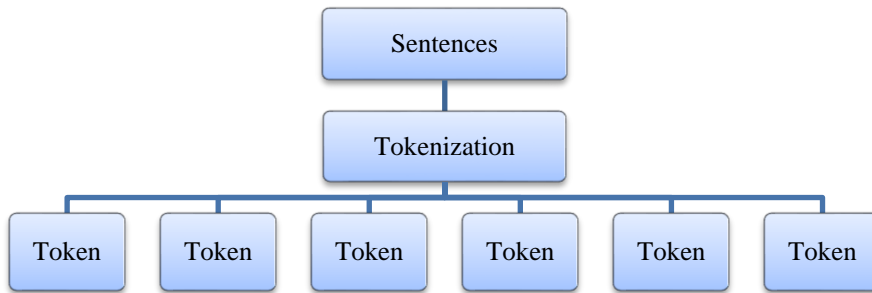


**Figure 5.** Tokenization processes

After the tokenization process, the padding step is started. In this step, the lengths of the sequences obtained after the tokenization process are equalized. The maximum length is determined as 200, and all sequences' length is adjusted according to this value. Zero values are added to the short sequences at this stage, and the long sequences are limited to 200 tokens. This standardization allows the data to be input into the model with a fixed length. At this stage, the training and testing processes of the model will begin.

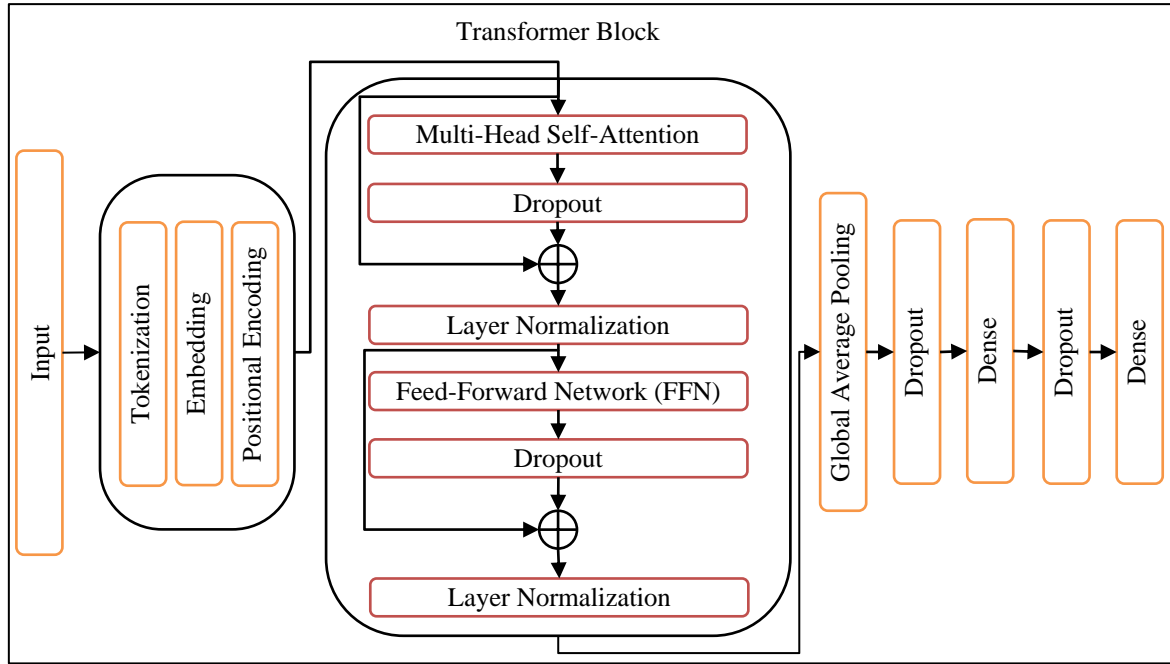


**Figure 6.** Transformer-based model structure

The structure of the transformer-based model is given in Figure 6 [31]. The model structure starts at the input layer and consists of token and position embedding layers, transformer block, global average pooling, dropout, dense, dropout, and dense layers. The model, which takes 200 parameters as input, is designed to have three classes at the output. The model's embedding size is 32, and the number of attention heads to focus on is determined as 2. The dropout value is entered as 0.2. 70% of the data used for the model is used for training and 30% for testing. The learning rate of the model is determined as 0.0001, and the batch size is entered as 32. The model was run for 20 epochs, and 11243 operations were performed in each epoch. Performance metrics were obtained with the values obtained by running the model, and comments were made about the model. Accuracy, F1 score, recall, and precision values were calculated as performance metrics [32]. The calculation formulas of these metrics are given in Table 1.

**Table 1.** Performance metrics

Performance Metric	Formula
<b>Accuracy</b>	$\frac{TP + TN}{TP + TN + FP + FN}$
	$\frac{TP}{TP + FP}$
<b>Precision</b>	$\frac{TP}{TP + FN}$
<b>Recall</b>	$\frac{TP}{TP + FN}$
<b>F1-Score</b>	$2 \cdot \frac{(\text{Precision} \cdot \text{Recall})}{(\text{Precision} + \text{Recall})}$

The accuracy rate measures the correct prediction rate of the model. Precision expresses the ratio of true positive predictions to all positive predictions. Recall value determines the correct classification rate of true positive examples. The F1 score also provides a measure of the balance of precision and recall values. The overall performance of the model is determined with these calculated metrics.

### 3. Experimental Result

The restaurant reviews dataset [30] is a text dataset consisting of approximately 513,000 rows and containing the classes negative, neutral, and positive, as shown in the graph in Figure 7.

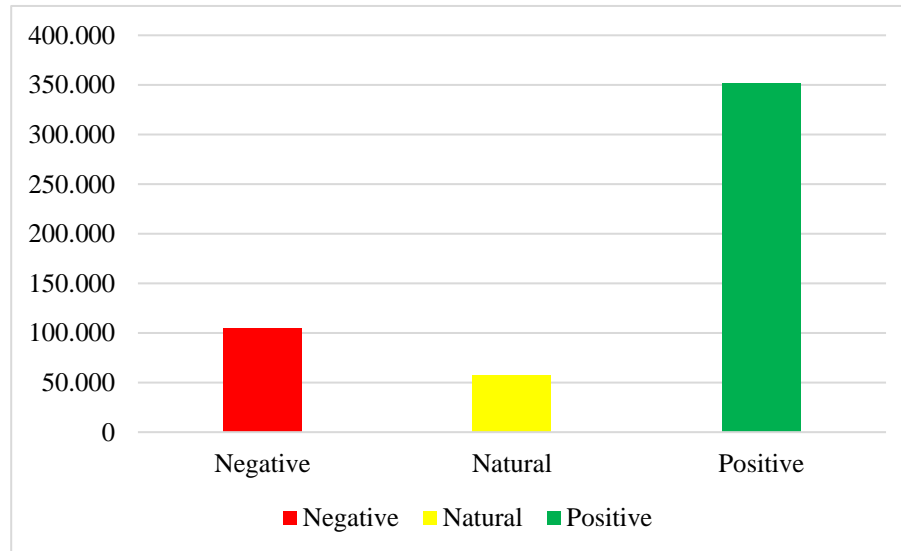


**Figure 7.** Restored comment dataset class data numbers

The tokenization step was carried out by considering the 20,000 most used words and tokens that were created. The maximum length of the tokens created was set to 200, and zeros were added to the short ones, while the long ones were limited to 200.

This prepared data was given as input to the model. The AdamW algorithm was used as an optimizer in the model and the learning rate was set to 0.0001. The batch size was set to 32 and the model was run for 20 epochs. The data was set as 70% training and 30% testing as input to the model, and the evaluation was made in this way. The graph showing the change in training and test accuracy according to epochs is given in Figure 8. When the graph is examined, it is observed that the accuracy of the model increases steadily in each epoch during the training period. The fact that the model's learning success in the training data reaches a high value of 90.81% shows that it has a strong ability in terms of generalization.

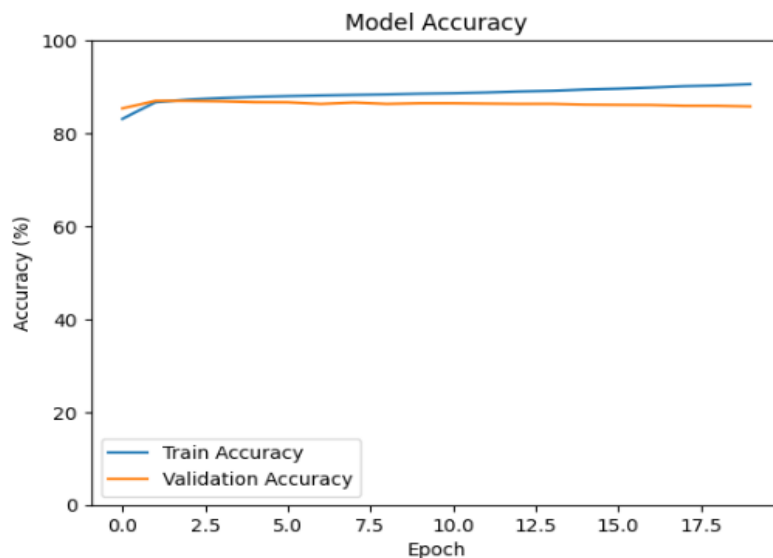


**Figure 8.** Model accuracy graph for train and test



The test accuracy rate was calculated as 85.79%. The difference in accuracy rate between test and training data shows that the model has a limited margin of error. This result shows that the model does not overfit and generalizes well for the data used for validation. Balancing the model's accuracy rates for training and test data shows that patterns are learned for both data sections, and a stable performance is achieved.

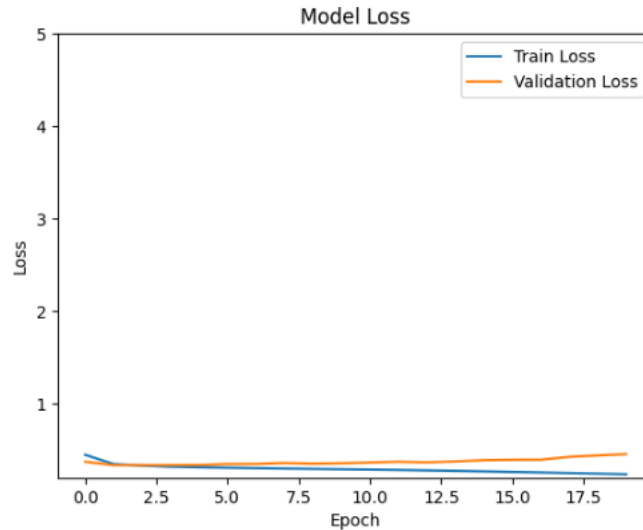


**Figure 9.** Model loss graphic for train and test

The graph showing the loss value of the model is given in Figure 9. During the training process, the loss value of the model decreases continuously and stabilizes after a certain point. The loss value on the training data was calculated as 0.2307. This value indicates that the training errors are minimized and the patterns are mostly recognized correctly. It indicates that the model is successfully optimized, and the relationship between the input and output is correctly established. The loss value calculated on the test data was determined as 0.4543. The difference between the training and test shows that the model has a certain margin of error. The low error margin indicates that the model generalizes on the test data and that there is no over-learning. The fact that the training and test losses are low and close to each other shows that the model exhibits a balanced performance. The confusion matrix created with the test data in line with the obtained results is given in Figure 10.

True Label	Negative	26649	2446	2441
	Neutral	4934	4734	7589
	Positive	2147	2358	100885
		Negative	Neutral	Positive
		Predicted Label		

**Figure 10.** Confusion matrix

Calculations were also made for other performance metrics; the results are shown in Table 2. The model performance seems to be successful for the class with negative comments. Precision 79%, Recall 85% and F1 Score 82% were calculated. It is seen that the generalization ability of the model for this class is good, and it has successful results. The performance values of the class with neutral comments were

determined as a Precision of 50%, Recall of 27%, and F1 Score of 35%. These values remained low, and it is understood that the generalization and accuracy of the prediction for this class are insufficient. This problem is caused by the data set being unbalanced. It is seen that the performance of the class with positive comments is good, and Precision 91%, Recall 96%, and F1 Score 93% were calculated. These results show that the model's generalization ability and correct prediction rate for this class are high, and it has achieved successful results.

**Table 2.** Model performance metrics results (%)

Class	Precision	Recall	F1 Score
Negative	79.00	85.00	82.00
Natural	50.00	27.00	35.00
Positive	91.00	96.00	93.00
<b>General Performance</b>	83.89	85.79	84.42

As seen in Table 2, a precision value of 83.89% was obtained in this study to analyze restaurant reviews. Eliminating the imbalance in the dataset or increasing the number of comments will increase the model's performance.

#### 4. Conclusion

In the study, a transform-based model was used to classify restaurant reviews using the NLP method. The model was trained with a comprehensive dataset of 3 classes, and tests were performed. The model's performance was evaluated using accuracy, precision, recall, and F1 score metrics. The test accuracy of the model was calculated as 85.79%. When the general results are examined, it is seen that the model achieves high performance in negative and positive classes. At the same time, it achieves limited success for the neutral class. The rates in the neutral class may be due to the uncertainty in the class or the imbalance in the dataset. In line with the calculated performance results, it is interpreted that the model is a successful approach for sentiment classification from restaurant reviews. This study shows that the transformer architecture provides effective results in NLP problems and contributes to the field of text classification. The imbalance of the dataset is the study's limitations. Testing the proposed model with a more comprehensive dataset is important to produce more realistic results.

#### 5. Author Contribution Statement

Authors 1, author 2, and author 3 prepared the study concept and design, performed the experiments, and analyzed and interpreted the data. Author contributions are equal.

#### 6. Ethics Committee Approval and Conflict of Interest

There is no need for an ethics committee approval in the prepared article. There is no conflict of interest with any person/institution in the prepared article.

#### 7. Ethical Statement Regarding the Use of Artificial Intelligence

No artificial intelligence-based tools or applications were used in the preparation of this study. The entire content of the study was produced by the author in accordance with scientific research methods and academic ethical principles

## 8. References

- [1] S. K. Mohapatra, P. K. Sarangi, P. K. Sarangi, P. Sahu, and B. K. Sahoo, "Text classification using NLP based machine learning approach," in *AIP Conf. Proc.*, 2022.
- [2] H. Liu, Q. Yin, and W. Y. Wang, "Towards explainable NLP: A generative explanation framework for text classification," *ArXiv Prepr. arXiv:1811.00196*, 2018.
- [3] V. Dogra *et al.*, "A Complete Process of Text Classification System Using State-of-the-Art NLP Models," *Comput. Intell. Neurosci.*, Art. no. 1883698, 2022.
- [4] Q. Zhao *et al.*, "Leveraging sensory knowledge into Text-to-Text Transfer Transformer for enhanced emotion analysis," *Inf. Process. Manag.*, vol. 62, Art. no. 103876, 2025.
- [5] M. Razno, "Machine learning text classification model with NLP approach," *Comput. Linguist. Intell. Syst.*, vol. 2, pp. 71–73, 2019.
- [6] Z. Li *et al.*, "A unified understanding of deep NLP models for text classification," *IEEE Trans. Vis. Comput. Graph.*, vol. 28, pp. 4980–4994, 2022.
- [7] J. Barbosa *et al.*, "Evaluating the noise tolerance of Cloud NLP services across Amazon, Microsoft, and Google," *Comput. Ind.*, vol. 164, Art. no. 104211, 2025.
- [8] S. Feuerriegel *et al.*, "Using natural language processing to analyse text data in behavioural science," *Nat. Rev. Psychol.*, pp. 1–16, 2025.
- [9] M. Arzu and M. Aydoğan, "Türkçe Duygu Sınıflandırma İçin Transformers Tabanlı Mimarilerin Karşılaştırılmalı Analizi," *Comput. Sci.*, pp. 1–6, 2023.
- [10] P. Guleria, "NLP-based clinical text classification and sentiment analyses of complex medical transcripts using transformer model and machine learning classifiers," *Neural Comput. Appl.*, pp. 1–26, 2024.
- [11] S. H. Ahammad *et al.*, "Improved neural machine translation using Natural Language Processing (NLP)," *Multimed. Tools Appl.*, vol. 83, pp. 39335–39348, 2024.
- [12] D. Van Veen *et al.*, "Adapted large language models can outperform medical experts in clinical text summarization," *Nat. Med.*, vol. 30, pp. 1134–1142, 2024.
- [13] A. Selvi *et al.*, "COLLEGEBOT: Virtual Assistant System for Enquiry Using Natural Language Processing," in *2nd Int. Conf. Intell. Data Commun. Technol. Internet Things*, pp. 1407–1414, 2024.
- [14] Z. Wang, "Information Extraction and Knowledge Map Construction based on Natural Language Processing," *Front. Comput. Intell. Syst.*, vol. 7, pp. 47–49, 2024.
- [15] M. Abdalla *et al.*, "An NLP-based system for modulating virtual experiences using speech instructions," *Expert Syst. Appl.*, vol. 249, Art. no. 123484, 2024.
- [16] D. Chen *et al.*, "Complex visual question answering based on uniform form and content," *Appl. Intell.*, vol. 54, pp. 4602–4620, 2024.
- [17] R. Patil *et al.*, "Next Word Prediction System Using NLP," in *IEEE Int. Conf. Smart Power Control Renew. Energy*, pp. 1–6, 2024.
- [18] M. Yıldırım, "Using and Comparing Machine Learning Techniques for Automatic Detection of Spam Website URLs," *NATURENGS*, vol. 3, pp. 33–41, 2022.
- [19] M. Asmitha and C. R. Kavitha, "Exploration of Automatic Spam/Ham Message Classifier Using NLP," in *IEEE 9th Int. Conf. Conver. Technol.*, pp. 1–7, 2024.
- [20] A. Mishra, S. K. Bisoy, and B. Naik, "Medication Recommendation System for Skin Diseases using NLP," in *Int. Conf. Adv. Smart, Secur. Intell. Comput.*, pp. 1–7, 2024.
- [21] M. Arzu and M. Aydoğan, "Comparison of Transformer-Based Turkish Models for Question-Answering Task," *Balk. J. Electr. Comput. Eng.*, vol. 12, pp. 387–393, 2025.
- [22] Y. Luo and X. Xu, "Comparative study of deep learning models for analyzing online restaurant reviews in the era of the COVID-19 pandemic," *Int. J. Hosp. Manag.*, vol. 94, Art. no. 102849, 2021.
- [23] E. Asani, H. Vahdat-Nejad, and J. Sadri, "Restaurant recommender system based on sentiment analysis," *Mach. Learn. Appl.*, vol. 6, Art. no. 100114, 2021.
- [24] N. Punetha and G. Jain, "Game theory and MCDM-based unsupervised sentiment analysis of restaurant reviews," *Appl. Intell.*, vol. 53, pp. 20152–20173, 2023.
- [25] R. N. Patil *et al.*, "Improving Sentiment Classification on Restaurant Reviews Using Deep Learning Models," *Procedia Comput. Sci.*, vol. 235, pp. 3246–3256, 2024.

- [26] M. U. Khan *et al.*, "A novel category detection of social media reviews in the restaurant industry," *Multimed. Syst.*, vol. 29, pp. 1825–1838, 2023.
- [27] M. Mamatha *et al.*, "Visual sentiment classification of restaurant review images using deep convolutional neural networks," in *IEEE Int. Conf. Electron. Comput. Commun. Technol.*, pp. 1–6, 2022.
- [28] K. Zahoor, N. Z. Bawany, and S. Hamid, "Sentiment analysis and classification of restaurant reviews using machine learning," in *21st Int. Arab Conf. Inf. Technol.*, pp. 1–6, 2020.
- [29] A. Branco *et al.*, "Sentiment analysis in portuguese restaurant reviews: Application of transformer models in edge computing," *Electronics*, vol. 13, Art. no. 589, 2024.
- [30] A. Nasef, "Restaurant Reviews," [Online]. Available: <https://www.kaggle.com/datasets/ahmedwaelnasef/restaurant-reviews>. [Accessed: Jan. 10, 2025].
- [31] A. Nandan, "Text classification with Transformer," [Online]. Available: [https://keras.io/examples/nlp/text\\_classification\\_with\\_transformer](https://keras.io/examples/nlp/text_classification_with_transformer). [Accessed: Jan. 23, 2025].
- [32] M. Yildirim and A. Cinar, "Classification with respect to colon adenocarcinoma and colon benign tissue of colon histopathological images with a new CNN model: MA\_ColonNET," *Int. J. Imaging Syst. Technol.*, vol. 32, pp. 155–162, 2022.



## Dalgacık Dönüşümü Tabanlı Özellikler Kullanarak Fırçasız DC Motor Seslerinin Makine Öğrenmesi Yöntemleri ile Analizi

Bilal TEKİN<sup>1</sup> , Turgay KAYA<sup>2\*</sup> 

<sup>1,2</sup>Elektrik-Elektronik Mühendisliği Bölümü, Mühendislik Fakültesi, Fırat Üniversitesi, Elazığ, Türkiye.

<sup>1</sup>bilaltekın4931@gmail.com, <sup>2</sup>tkaya@firat.edu.tr

Geliş Tarihi: 3.02.2025

Kabul Tarihi: 6.04.2025

Düzeltilme Tarihi: 21.03.2025

doi: <https://doi.org/10.62520/fujece.1632384>

Araştırma Makalesi

Alıntı: B. Tekin ve T. Kaya, “Dalgacık dönüşümü tabanlı özellikler kullanarak fırçasız dc motor seslerinin makine öğrenmesi yöntemleri ile analizi”, Fırat Üni. Deny. ve Hes. Müh. Derg., vol. 4, no 2, pp. 363-374, Haziran 2025.

### Öz

Fırçasız DA (BLDC) motorlar, yüksek verimlilikleri, güvenilirlikleri ve düşük bakım gereksinimleri nedeniyle çeşitli uygulamalarda yaygın olarak kullanılmaktadır. Bu motorlar, mekanik fırçaların bulunmaması nedeniyle daha az aşınma ve düşük bakım gereksinimi sağlar. Bu özellikleri, özellikle endüstriyel otomasyon, elektrikli araçlar, robotik sistemler gibi birçok alanda tercih edilmelerini sağlar. Makine öğrenimi (MÖ) ile BLDC motorlarının entegrasyonu, bu motorların verimliliğini, güvenilirliğini ve performansını önemli ölçüde artırabilir. ML algoritmaları, motorun performans verilerini analiz ederek arızaların önceden tespit edilmesine yardımcı olabilir. Motorun normal çalışma koşullarından sapmalarını izleyen ML algoritmaları, arızalı durumları hızlı bir şekilde tanımlayabilir. Makine öğrenimi, motorun çalışma koşullarına bağlı olarak en verimli çalışma noktalarını öğrenebilir ve buna göre motorun hızını veya diğer parametrelerini dinamik olarak optimize edebilir. Bu çalışmada ses analizi ile BLDC motorlarındaki mekanik arızaların tespit edilmesini sağlayan bir yöntem önerilmektedir. Ses analizi ile normal ve arızalı motorların ses kayıtlarından Ayrık Dalgacık Dönüşümü (ADD) tabanlı özellikler çıkarılmış ve elde edilen özellikler makine öğrenimi yöntemleriyle sınıflandırılmıştır. Burada, ADD ile veri boyutu azaltılmıştır, istenmeyen ve önemsiz katsayılar baskılanmıştır. Elde edilen yeni verilerle aşırı uyumdan kaçınacak Bagging trees kullanılmıştır. Bagging, birden fazla karar ağacını birleştirerek her ağacın aşırı uyum sağlama eğilimini dengelemeye çalışır ve modelin genelleme kapasitesi artar. Ayrıca, her model bağımsız olarak eğitildiği için paralel hesaplama imkân sağlar. Elde edilen model ile %89.205 doğruluk, 0.821 kappa değeri elde edilmiştir.

**Anahtar kelimeler:** Fırçasız doğru akım motoru, Ayrık dalgacık dönüşümü, Makine öğrenmesi, Arıza tespiti

\*Yazışılan Yazar

İntihal Kontrol:Evet– Turnitin

Şikayet: [fujece@firat.edu.tr](mailto:fujece@firat.edu.tr)

Telif Hakkı ve Lisans: Dergide yayın yapan yazarlar, CC BY-NC 4.0 kapsamında lisanslanan çalışmalarının telif hakkını saklı tutar



## Analysis of Brushless DC Motor Sounds with Machine Learning Methods Using Wavelet Transform Based Features

Bilal TEKİN<sup>1</sup> , Turgay KAYA<sup>2\*</sup>

<sup>1,2</sup>Electrical and Electronics Engineering Department , Faculty of Engineering, Firat University, Elazığ, Türkiye.

<sup>1</sup>bilaltekın4931@gmail.com, <sup>2</sup>tkaya@firat.edu.tr

Received: 3.02.2025

Accepted: 6.04.2025

Revision: 21.03.2025

doi: <https://doi.org/10.62520/fujece.1632384>  
Research Article

Citation: B. Tekin and T. Kaya, "Analysis of brushless dc motor sounds with machine learning methods using wavelet transform based features", Firat Univ. Jour. of Exper. and Comp. Eng., vol. 4, no 2, pp. 363-374, June 2025.

### Abstract

Brushless DC (BLDC) motors are widely used in various applications due to their high efficiency, reliability and low maintenance requirements. The absence of mechanical brushes reduces wear and minimizes maintenance. These features make them preferred in many areas, especially industrial automation, electric vehicles, and robotic systems. Integration of a BLDC motors with machine learning (ML) can significantly increase the efficiency, reliability and performance of these motors. ML algorithms can help detect faults in advance by analyzing the performance data of the motor. ML algorithms, which monitor deviations from the normal operating conditions of the motor, can quickly identify faulty situations. ML can learn the most efficient operating points depending on the operating conditions of the motor and dynamically optimize the speed or other parameters of the motor accordingly. In this study, a method is proposed that enables the detection of mechanical faults in a BLDC motors with sound analysis. With sound analysis, Discrete Wavelet Transform (DWT) based features were extracted from the sound recordings of normal and faulty motors and the obtained features were classified with machine learning methods. Here, the data size is reduced with DWT, unwanted and unimportant coefficients are suppressed. Bagging trees are used to avoid overfitting with extracted statistical features. Bagging tries to balance the overfitting tendency of each tree by combining multiple decision trees and the generalization capacity of the model increases. In addition, since each model is trained independently, it allows parallel calculation. With the obtained model, 89.205% accuracy and 0.821 kappa value were obtained.

**Keywords:** Brushless DC motors, Discrete wavelet transform, Machine learning, Fault detection

---

\*Corresponding author



## **1. Introduction**

Troubleshooting is critical to the continued and smooth operation of an industrial system. A brushless DC electric motor is a synchronous motor that uses direct current (DC). It is also known as a commutated motor. It started to become widespread in the 1960s [1]. A BLDC motor offers high power density, efficiency, and low noise levels. For this reason, they are used in industrial control systems, automotive, robots and white goods areas [2-4]. The presence of permanent magnets instead of windings in the rotor has reduced the weight and volume of the motor in addition to reducing losses [5]. In addition, BLDCs have complex control circuits and are expensive. They also need location information [6-8]. In these motors, where precise speed and position control can be made, it is important to detect the fault in advance so that any fault does not affect the sensitivity of the motor.

BLDC motor is frequently preferred in variable speed applications because it has high starting torque. It emits low acoustic noise due to the absence of brush friction [1,9]. A BLDC Motor is used in devices such as Electric vehicles, Hybrid vehicles, Industrial robots, Washing machines, Conveyors, Fans. Malfunctions occur in a BLDC Motor, just like other machines, and it is very important to follow these malfunctions in order to return them to normal operating conditions as soon as possible [10]. Intelligent techniques (AI) have been successfully used for fault diagnosis in machines.

In the study Ref. [11], NN classifies healthy and faulty conditions by analyzing the stator current and rotation speed of the motor. In [12], stator current and lateral vibration measurements were used to extract meaningful features by wavelet transform to identify bearing faults in BLDC under variable operating conditions. [13] presents a bearing failure analysis of BLDC motors. The vibration signal of both healthy and defective bearings was analyzed by identifying specific frequencies in the vibration spectrum. A recurrent neural network was then used to detect and classify the presence of bearing faults. Khan et al has contributed to the detection and classification of faults in electric vehicle interface connections by ML tools [14].

Sarman et al. presents a fault diagnosis method for brushless direct current motor drives using hybrid ML models, achieving 98.8% accuracy in detecting open circuit and short circuit faults [15].

In [16], SAC-DM technique was applied to diagnose malfunctions in electromechanical systems from audio signals through tests performed on a small BLDC motor. Wavelet Multiresolution Analysis (WMA) has been used to separate a chaotic signal component from the noise emitted by the engine. Similarly, 92% accuracy rate was achieved in the prediction of BLDC motors by using audio signal processing and ML models for preventive maintenance planning [17]. To estimate the remaining service life of BLDC motors, a prediction with 88% accuracy was made using the Random Forest algorithm [18].

In this proposed study, high and low frequency components in data will be separated by using DWT. Then, statistical features will be obtained, data size will be reduced and new features will be extracted. The new features obtained will be analyzed with ML methods, success metrics for the BLDC failure situation will be obtained and interpreted.

The workflow consists of the material and method part (dataset, used method steps) in section 2, the experimental results part in section 3 and finally the conclusions part.

## **2. Material and Method**

### **2.1. Dataset**

The dataset, used in this work, comprises of 43 .wav files and approximately 10 seconds each. In addition, sampling frequency is 16 kHz containing the sound of four A2212 BLDC motors [19]. Dataset comprises of healthy motors, propeller failure and bearing failure types. These categories number of file sizes are listed in Table 1 and samples are shown in Figure 1. The sound of an engine varies depending

on whether the various components are working properly. The sounds of normal, bearing faulty and propeller faulty engines are different as each type of fault affects the operating dynamics of the engine differently. The sound of a properly operating engine is constant and smooth (Figure 1a). The sound of a Propeller Faulty Engine is low, muffled, irregular and may have increased vibration (Figure 1b). The sound of a bearing faulty engine is high-pitched, humming and irregular (Figure 1c).

**Table 1.** Number of file sizes dataset

Sound Type	Number of File Sizes
Healthy Motor	20
Bearing Motor	7
Propeller Motor	16

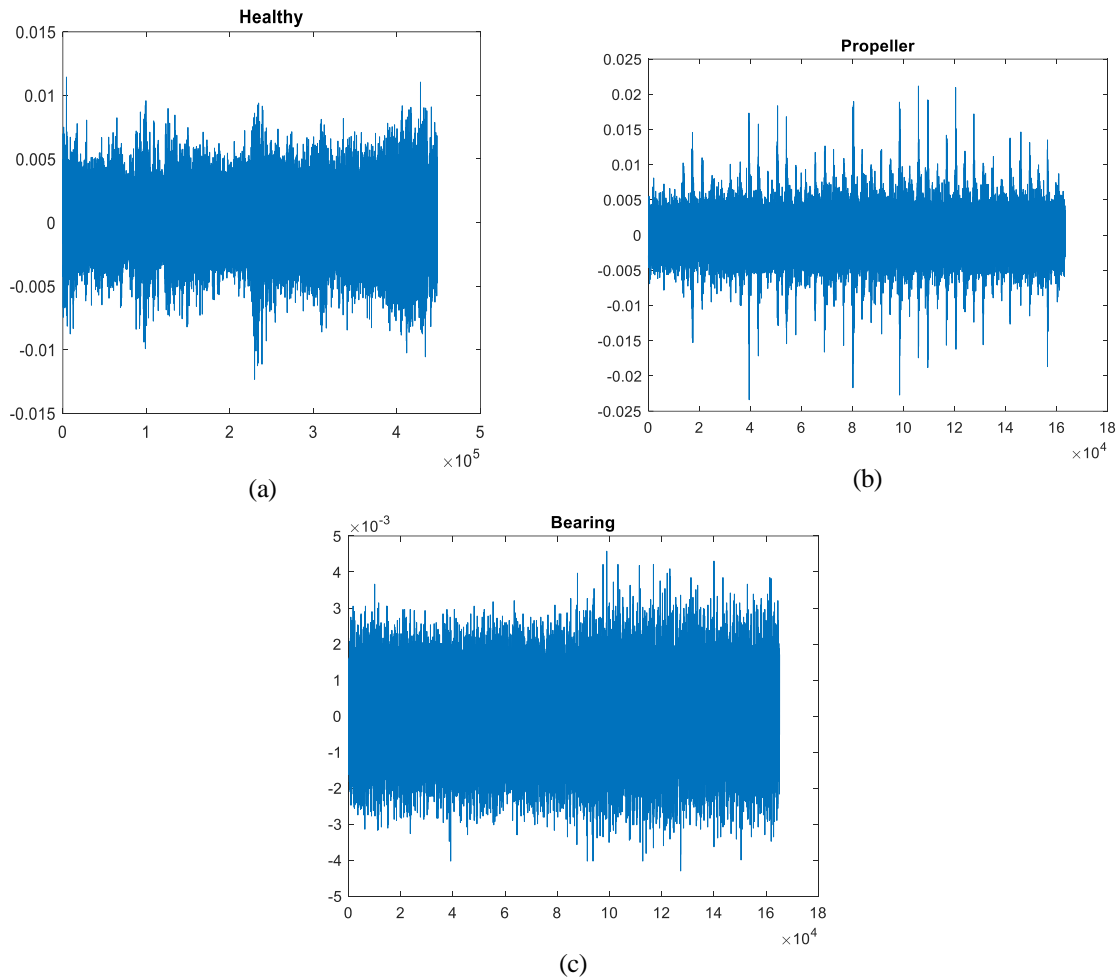


**Figure 1.** (a) Healthy, (b) propeller failure and (c) bearing failure motor sound samples

## 2.2. Application of flow chart

The dataset used in the study was taken as ready. In case of using a real-time system, external factors such as ambient noise will affect the analysis. Filtering techniques can be used to minimize these factors, increase the reliability of the system and reduce errors (low pass, Kalman filter, Wiener filter). To reduce electromagnetic noise, devices and sensors can be protected with special shields, the signal can be converted to the frequency domain and unwanted frequency components can be separated. Each approach can be customized according to the application area and the characteristics of the system.

As the dataset comprises audio signals, numerical conversion is required for feature extraction. Feature extraction is performed with DWT from signals belonging to different categories received from the

BLDC motor. After the signals are processed, the features obtained are classified with ML methods and engine error detection is made. Performance evaluation is made for new data entry with the model obtained by ML. The flow chart of the proposed model is given in Figure 2. WT is a signal processing method used in the analysis of stationary and non-stationary signals. While only frequency information is obtained with this analysis performed in Fourier Transform, frequency and time information of the signal can be obtained with WT [20-22]. Since optimum time-frequency resolution can be achieved in all frequency ranges of WT, it enables the analysis of systems with time-varying frequencies and temporal analyzes to be performed precisely. This allows analysis to be done quickly and easily [23]. DWT is an important tool in signal processing applications because it can efficiently capture local and global features of signals [24]. DWT separates the signal at each level into an approximation and detail component using wavelet functions. This provides the opportunity to discard the less informative part of the data for each level. If DWT is applied at more than one level, it gradually reduces the data size. Approximation coefficients at lower levels carry more information and detail coefficients at higher levels usually contain unnecessary details. It is possible to compress the data by resetting these details. The detail coefficients obtained after DWT can usually be noise or very low frequency details. These coefficients can be reduced to zero or low values. Coefficient thresholding serves to remove such low value coefficients and keep only the most significant components. After the unnecessary coefficients are zeroed out, the data is reconstructed using inverse DWT. The reconstructed data is reduced in size and compressed but retains important information.

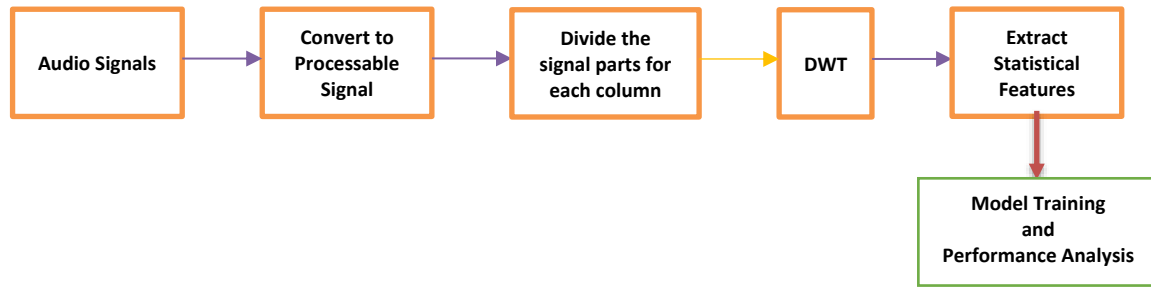


**Figure 2.** The flow chart of the proposed model

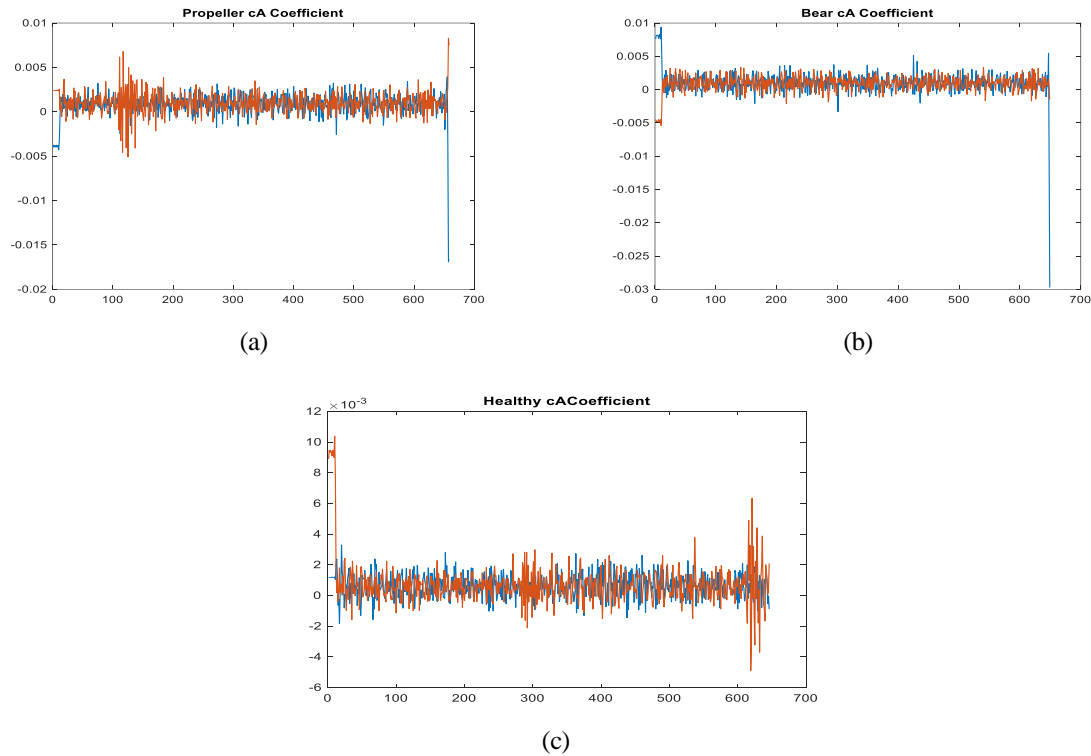


**Figure 3.** Wavelet coefficients of each data types ((a) propeller (b) bearing and (c) healthy)

In this work, to have a large number of features and to obtain efficient results with ML, each of the two-column data entries was divided into two segments for feature extraction. Wavelet transform was applied to four separate parts and their statistical properties were obtained. 7. Level Db7 is used. Wavelet coefficients of each data types are given in the Figure 3. Since there were different numbers of files for each species in the original data set, the data numbers were obtained as in the Table 2.

Statistical features refer to various measurements used to summarize and analyze a data set. After DWT, extracted statistical features which are mean, median, max, min, range, std, mad and norm as shown in Table 2. Mean is the value obtained by dividing the sum of all values in a data set by the number of observations. The mean indicates the central tendency of the data set. Median is the middle value when the values in a data set are ranked. The median determines the central tendency of the data set and is not affected by outliers. Mode is the most frequently occurring value in a data set. The mode is frequently used for categorical data. Standard Deviation measures how much the values in a data set spread around the mean. A higher standard deviation indicates that the values in the data set are more dispersed than the mean. Variance is the square of the standard deviation. It refers to the overall variability of the distribution of the data set. Minimum and Maximum Values are the smallest and largest values in the data set. The norm of a matrix is a scalar that gives some measure of the magnitude of the elements of the matrix. After statistical properties are obtained, normalization is performed to make the data uniform. Z-score was used as normalization. The normalized values are shown in Figure 4. The extracted features size is listed in Table 2, after DWT and extracted statistical features. Also, the related labels are given in Table 2.

**Table 2.** The extracted features size and used statistical features

Sound Type	Extracted Statistical Features Sizes	Label	Used Statistical Features	
Bearing Motor	28*11	0	Mean	Range
Healthy Motor	88*11	1	Median	Std
Propeller Motor	60*11	2	Maximum	Mad
Total	176*11		Minimum	Norm

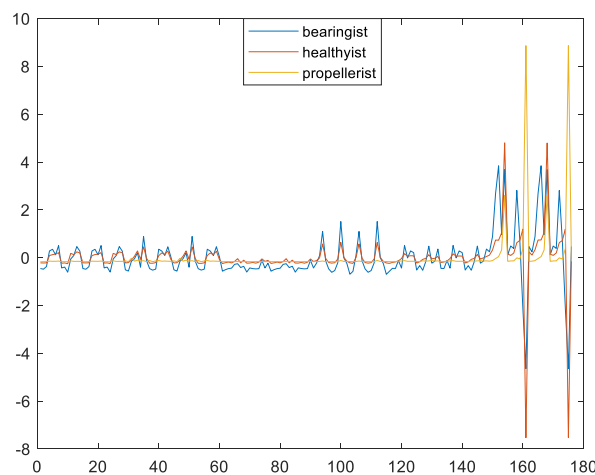


**Figure 4.** The normalized values for each data

ML is a field that enables AI to use data and different algorithms to mimic the human learning process and improve its accuracy. ML system; It consists of the steps of decision making, generating error function and updating weights. Classification, one of the ML applications, is a supervised ML process. With ML, a classification problem can be performed on used or unused data to accurately predict whether the data will fall into relevant categories. Classification algorithms refer to ML algorithms used to classify data into specific categories. Each of these algorithms may be more suitable for a specific data set and application. Logistic regression is a linear classification model and is usually used in binary classification problems [25]. Decision trees are a model that classifies data by dividing it into branches,

there is a risk of overfitting. Random forests are a method consisting of the combination of multiple decision trees [26]. Each tree is trained independently and the results are combined by majority voting. Support vector machines try to find the most appropriate hyperplane that separates data points into different classes. It can be used for two or multi-class problems [27]. Artificial neural networks process data with structures based on the working principle of the human brain. It performs very well with high accuracy and large data sets. LDA projects the data to a lower-dimensional space in order to distinguish classes [28]. It maximizes the differences between classes while minimizing the variance within the class, and is effective in working with high-dimensional data.

Bagged trees are an ensemble learning technique in ML and attempts to balance the tendency of each tree to overfit by combining multiple decision trees [29]. It allows creating multiple decision trees from different subsets of training data. It also combines predictions to improve model performance. Samples are taken from the original training dataset and several new training sets are created. Each of these examples is used to train a separate decision tree. A decision tree is trained on each of these datasets. Once all trees are trained it combines the predictions. Bagging helps reduce overfitting in decision trees because the average of more than one tree is taken [30]. In addition, it reduces variance, which in turn affects performance. Bagging makes the more stable output by reducing sensitivity to variations in the training data, as better generalization performance against different datasets. It also offers parallel computing since each model is trained independently. This is a significant advantage when working with large datasets.

### 3. Experimental Results

In this work, bagged trees is chosen over other algorithms (such as SVM, CNN and LSTM) because they reduce the risk of overfitting, can give good results with less data, can make fast calculations thanks to their simple structure and generally have high generalization ability. In the classification made after feature extraction and feature selection, the parameters obtained with the confusion matrix, ROC curve and kappa coefficient were interpreted. Confusion matrix is shown in Figure 5. Figure 6 shows True Positive Rates (TPR) - False Negative Rates (FNR), and it indicates the ability of the model to correctly classify each class. Figure 7 shows Positive Predictive Values (PPV) and False Discovery Rates (FDR) respectively. PPV and FDR are used to understand the model's performance on false positives and false negatives. If the PPV is high, most of the cases that the model predicts as positive are actually positive. A low FDR indicates that fewer of the positive predictions are actually incorrect. Using these metrics together helps evaluate the model's performance more comprehensively.

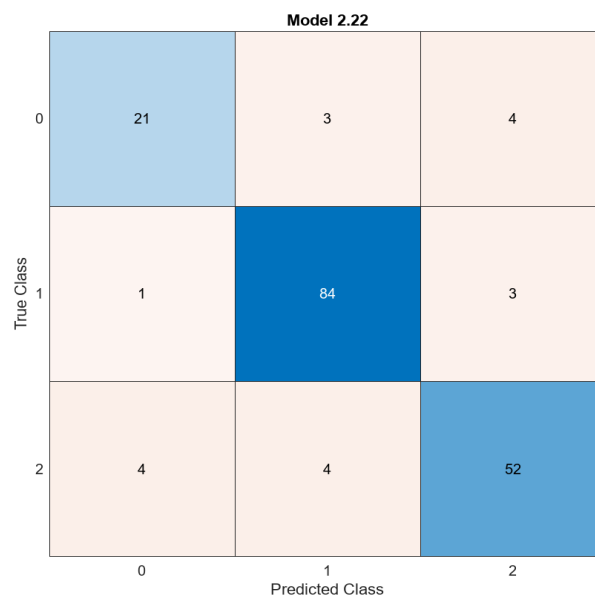
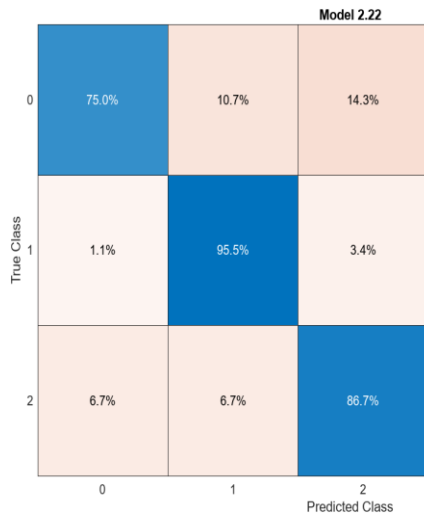
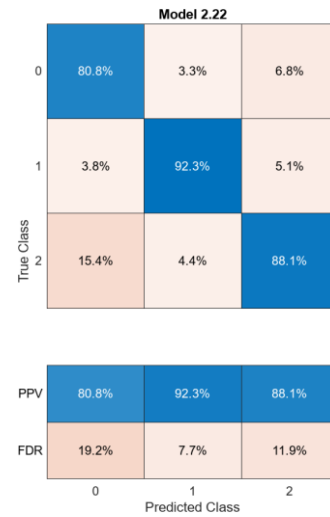
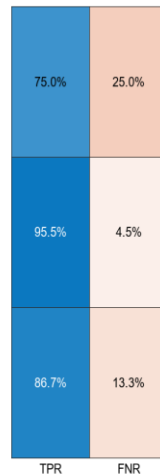


Figure 5. Confusion matrix of application



**Figure 6.** True Positive Rates (TPR) - False Negative Rates (FNR)



**Figure 7.** Positive Predictive Values (PPV) and False Discovery Rates (FDR)

Figure 8 and Figure 9 represent TPR-FNR and PPV-FDR bar graphs, respectively. These graphs allow the numerical visualization of the correct prediction performance of each class to be seen.

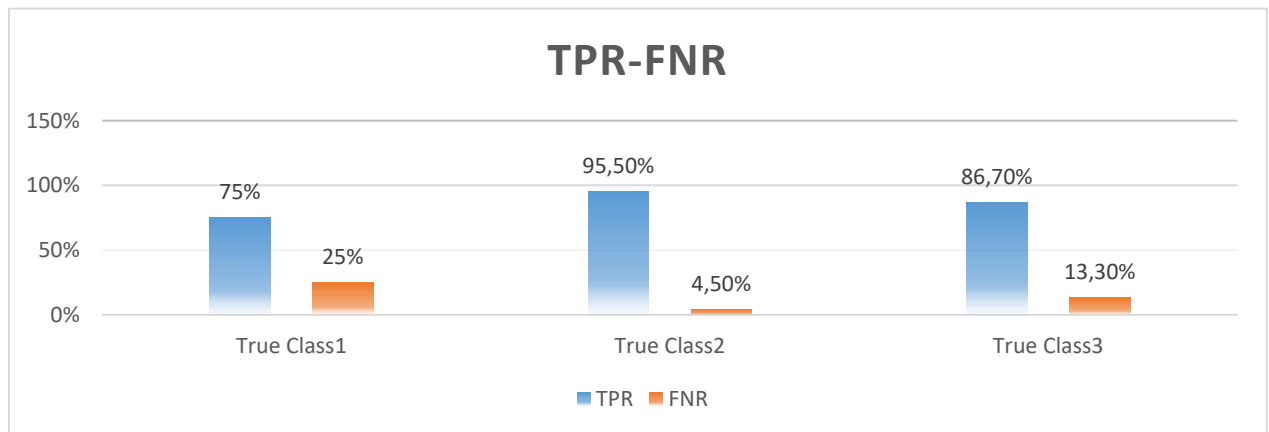


**Figure 8.** Numerical visualization of TPR-FNR values for each class

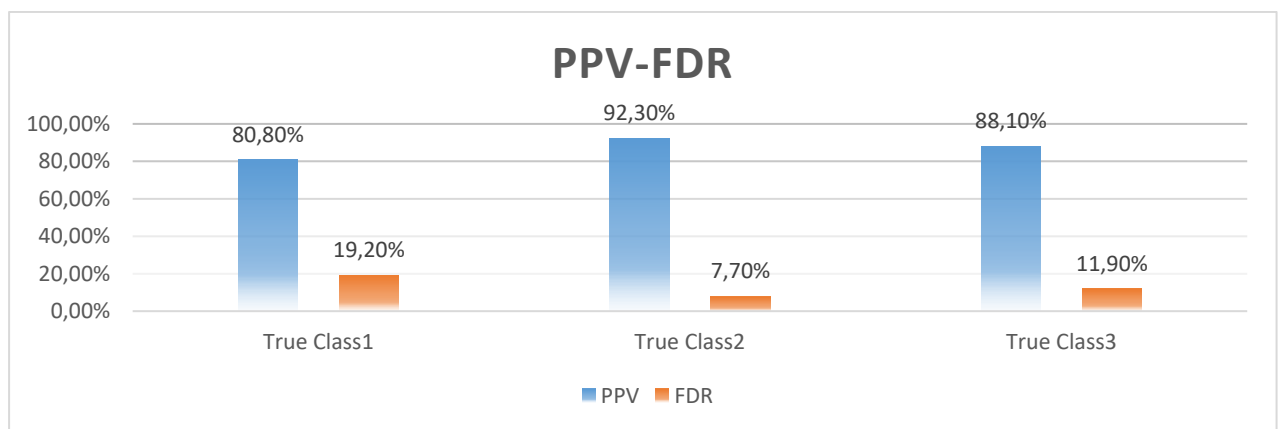


**Figure 9.** Numerical visualization of PPV-FDR values for each class



**Table 3.** Performance metrics

Truth Data						
Classifier Results		Class 1	Class 2	Class 3	Overall classification	Precision (%)
	Class 1	21	3	4	28	75
	Class 2	1	84	3	88	95.455
	Class3	4	4	52	60	86.667
	Truth Overall	26	91	59	176	
	Recall (%)	80.769	92.308	88.136		
Overall Accuracy	%89.205					
Kappa	0.821					

As shown in Table 3, performance metrics are listed for this work. While the overall accuracy is 89.205%, the Recall values for each class are %, 80.769, % 92.308, % 88.136 and Precision values are % 75, % 95.455, % 86.667. Additionally, the Kappa coefficient was found to be 0.821%. Kappa is used to evaluate the performance of classification models. It measures the agreement between observed and predicted classes in the classification model. The kappa value is between -1 and 1, and the closer it is to 1, the better the model performance. Figure 10 expresses ROC Curve and Area Under Curve (AUC). AUC is used to compare the performance of classification models, especially in unbalanced classification problems. Its value varies between 0-1. The closer a model's AUC value is to 1, the better the performance. If it closes to 0.5, the classification ability of the model consists of random guesses. The ROC curve shows the relationship between sensitivity and specificity at different cutoff points of the classification model.

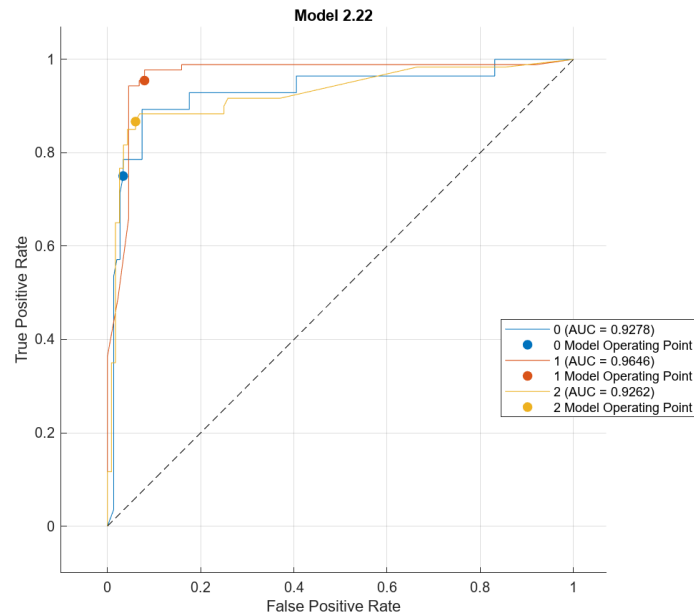


**Figure 10.** ROC Graphics

## 4. Conclusions

Classification of healthy and bad states in a BLDC motor and the use of data reduction methods provide practical benefits in many industries. Industrial robots using BLDC motors make precise and powerful movements. Motor failures can cause production errors and stoppages. Hence, continuous monitoring is essential to ensure early fault detection. Data reduction allows only critical data to be transmitted without affecting the processing speed of the robots and helps to detect motor failures more quickly.

Another area of use is in electric vehicles, where motor failures can negatively affect the performance of the vehicle and pose safety risks. In EVs, data reduction and healthy/bad classification techniques can be important in terms of battery consumption and processor load. Predictions of motor health allow users and maintenance teams to make timely interventions.

Three types of data were used in this study for a BLDC. Each data consists of 2 columns. Each column was divided into 2 parts and wavelet coefficients were determined with the db7 wavelet. Statistical features were extracted for 4 tracks. These features are mean, median, max, min, range, std, mad and norm. The obtained features were classified with the bagged trees algorithm. The probability of correct prediction of each class was examined with performance metrics. Recall, precision, accuracy, kappa, Roc Curve, AUC are used as the metric.

## **5. Discussion**

Although the dataset is relatively small, future studies could explore real-time deployments or augment data with sensor fusion.

## **6. Contributions of the Authors**

The authors' contributions to the paper are equal.

## **7. Statement of Research and Publication Ethics**

The study is complied with research and publication ethics. There is no conflict of interest between the authors.

## **8. Acknowledgment**

This study is produced from the first author's master's thesis titled "Analysis of Acoustic Data with Intelligent Computational Methods".

## **9. Ethical Statement Regarding the Use of Artificial Intelligence**

No artificial intelligence-based tools or applications were used in the preparation of this study. The entire content of the study was produced by the author in accordance with scientific research methods and academic ethical principles.

## 10. References

- [1] T. G. Wilson and P. H. Trickey, "D.C. Machine. With Solid State Commutation," AIEE Paper, no. CP62-1372, Oct. 7, 1962.
- [2] Y. Xu, H. B. Pan, S. Z. He, and L. Li, "Monolithic H-bridge brushless DC vibration motor driver with a highly sensitive Hall sensor in 0.18  $\mu\text{m}$  complementary metal-oxides semiconductor technology," IET Circuits, Devices & Systems, vol. 7, no. 4, pp. 204–210, 2013.
- [3] Y. Yaşa, "An Efficient Brushless DC Motor Design for Unmanned Aerial Vehicles," Eur. J. Sci. Technol., vol. 35, pp. 288–294, 2022.
- [4] B. Kaynak and A. Y. Arabul, "Sizing, Design and Analysis of Fixed Wing Unmanned Aerial Vehicle's Wing," in 6th Int. Mardin Artuklu Sci. Res. Conf., Mardin, Türkiye, pp. 74–81, Jun. 25–27, 2021.
- [5] M. R. Minaz, "Fırçasız DC Motorunun Eksen Kaçıklığı ve Kırık Mıknatıs Arızalarının Tespitinin Bilgisayar Benzetimi ile Yapılması," BEU J. Sci., vol. 9, no. 2, pp. 846–861, 2020.
- [6] F. Cira, M. Arkan, and B. Gümüş, "Detection of stator winding inter-turn short circuit faults in permanent magnet synchronous motors and automatic classification of fault severity via a pattern recognition system," J. Electr. Eng. Technol., vol. 11, no. 2, pp. 416–424, 2016.
- [7] F. Cira, "Sürekli Mıknatıslı Senkron Motorun Stator Kısa Devre Arızasının Tespiti ve Arıza Şiddetinin Otomatik Olarak Belirlenmesi," Ph.D. dissertation, İnönü Univ., Inst. Sci., Malatya, 2017.
- [8] Ö. Alaca, R. Selbaş, and M. Türkkalesi, "Fırçasız Motor Sürücülerin Enerji Verimliliği," Int. J. Sustain. Eng. Technol., vol. 6, no. 1, pp. 1–9, 2022.
- [9] B. Er, B. Demirsoya, and A. Fenercioğlu, "Analysis of the Effect of Switching Frequency on Acoustic Noise in External Rotor Brushless DC Motors," Balkan J. Electr. Comput. Eng., vol. 12, no. 1, 2024.
- [10] R. Kavin et al., "Fault Detection and Monitoring of BLDC Motor Using ANN," in Proc. 2023 Int. Conf. Netw. Commun. (ICNWC), Chennai, India, pp. 1–5, 2023.
- [11] W. Abed, S. Sharma, and R. Sutton, "Fault diagnosis of brushless DC motor for an aircraft actuator using a neural wavelet network," IET Conf. Proc., pp. 05–05, 2013.
- [12] W. Abed et al., "A Robust Bearing Fault Detection and Diagnosis Technique for Brushless DC Motors Under Non-stationary Operating Conditions," J. Control Autom. Electr. Syst., vol. 26, pp. 241–254, 2015.
- [13] K. Kudelina et al., "Bearing Fault Analysis of BLDC Motor for Electric Scooter Application," Designs, vol. 4, no. 4, Art. no. 42, 2020.
- [14] M. Khan et al., "Securing Electric Vehicle Performance: Machine Learning-Driven Fault Detection and Classification," IEEE Access, vol. 12, pp. 71566–71584, 2024.
- [15] K. Sarman, T. Madhu, and M. Prasad, "Fault Diagnosis in the Brushless Direct Current Drive Using Hybrid Machine Learning Models," ECTI Trans. Electr. Eng., Electron. Commun., 2022.
- [16] F. C. Veras et al., "Eccentricity Failure Detection of Brushless DC Motors From Sound Signals Based on Density of Maxima," IEEE Access, vol. 7, pp. 150318–150326, 2019.
- [17] R. Prieto, D. Montenegro, and C. Rengifo, "Machine hearing for predictive maintenance of BLDC motors," J. Qual. Maint. Eng., 2024.
- [18] R. Sree, S. Jayanthi, and E. Vigneshwaran, "Estimation of Remaining Useful Life (RUL) of BLDC Motor using Machine Learning Approaches," in Proc. 2022 7th Int. Conf. Commun. Electron. Syst. (ICCES), pp. 286–291, 2022.
- [19] P. Estacio and R. Stiward, "Brushless DC Motor sound dataset for PdM," Mendeley Data, vol. 1, 2023.
- [20] S. Santoso, E. J. Powers, W. M. Grady, and P. Hofman, "Power Quality assessment via wavelet transform analysis," IEEE Energy Oper. Energy Convers. Manag., vol. 52, no. 4, pp. 1959–1967, 1996.
- [21] M. Uyar, S. Yıldırım, and M. T. Gençoğlu, "Güç Kalitesindeki Bozulma Türlerinin Sınıflandırılması için bir örüntü tanıma yaklaşımı," Gazi Univ. J. Sci. Eng., vol. 26, no. 1, pp. 14–56, 2011.

- [22] M. A. S. K. and M. A. K. Rahman, "Development and Implementation of a Novel Fault Diagnostic and Protection Technique for IPM Motor Drives," *IEEE Trans. Ind. Electron.*, vol. 56, no. 1, pp. 85–92, 2009.
- [23] S. Bayhan and D. Yılmaz, "Güç Sistemlerinde meydana gelen dalga şekli bozukluklarının dalgacık dönüşümü yardımıyla tespiti," *Technol. Appl. Sci.*, vol. 4, no. 2, pp. 151–162, 2009.
- [24] I. Daubechies, "The wavelet transform time frequency localization and signal analysis," *IEEE Trans. Inf. Theory*, vol. 36, no. 5, pp. 961–1005, 1990.
- [25] J. Lever, M. Krzywinski, and N. Altman, "Points of Significance: Logistic regression," *Nat. Methods*, vol. 13, pp. 541–542, 2016.
- [26] M. Schonlau and R. Zou, "The random forest algorithm for statistical learning," *Stata J.*, vol. 20, no. 29, Art. no. 3, 2020.
- [27] R. Hu, X. Zhu, Y. Zhu, and J. Gan, "Robust SVM with adaptive graph learning," *World Wide Web*, vol. 23, pp. 1945–1968, 2019.
- [28] G. Singh, Y. Pal, and A. Dahiya, "Classification of Power Quality Disturbances using Linear Discriminant Analysis," *Appl. Soft Comput.*, vol. 138, Art. no. 110181, 2023.
- [29] G. Ngo, R. Beard, and R. Chandra, "Evolutionary bagging for ensemble learning," *Neurocomputing*, vol. 510, pp. 1–14, 2022.
- [30] O. Yıldız, O. Irsoy, and E. Alpaydın, "Bagging Soft Decision Trees," pp. 25–36, 2016.



## Akım Gözlemi Olmayan Havzalarda Sentetik Birim Hidrograf Yöntemleri ve CBS Kullanılarak Taşkın Debilerinin Tahmini

Erdal KESGİN<sup>1\*</sup>

<sup>1</sup>İnşaat Mühendisliği Bölümü, İnşaat Fakültesi, İstanbul Teknik Üniversitesi, İstanbul, Türkiye.

<sup>1</sup>kesgine@itu.edu.tr

Geliş Tarihi: 24.02.2025  
Kabul Tarihi: 22.04.2025

Düzeltilme Tarihi: 26.03.2025

doi: <https://doi.org/10.62520/fujece.1645774>  
Araştırma Makalesi

Alıntı: E. Kesgin, "Akım gözlemi olmayan havzalarda sentetik birim hidrograf yöntemleri ve cbs kullanılarak taşkın debilerinin tahmini", Fırat Üni. Deny. ve Hes. Müh. Derg., vol. 4, no 2, pp. 375-392, Haziran 2025.

### Öz

Taşkın, bir akarsuyun çeşitli nedenlerle yatağından taşarak çevresindeki arazi, yerleşim alanları, altyapı tesisleri ve ekosistem üzerinde oluşturduğu olumsuz etkiler olarak tanımlanabilir. Havza ölçeğinde, özellikle akım gözlem istasyonlarının bulunmadığı durumlarda, taşkın analizleri için yağış-akış ilişkileri için hidrograflar oluşturulmalıdır. Bu çalışmada, İstanbul, Sarıyer ilçesinde yer alan ve büyük ölçüde ormanlık niteliğindeki bir alt havza için sentetik hidrografların oluşturulması, yağış-akış ilişkilerinin analiz edilmesi ve farklı tekerrür aralıkları için taşkın debilerinin hesaplanması amaçlanmıştır. Ekstrem yağış analizleri kapsamında, Normal, Log-Normal, Log-Pearson Tip III ve Gumbel olasılık dağılım fonksiyonları kullanılarak çeşitli tekerrür aralıkları ( $T = 2, 5, 10, 25, 50, 100$  yıl) için 24 saatlik maksimum yağış değerleri hesaplanmıştır. Log-Pearson Tip III yöntemiyle elde edilen yağış değerlerinin daha yüksek olduğu belirlenmiş ve taşkınların ekstrem doğası göz önüne alındığında, debi hesaplamalarında bu yöntemin kullanılması tercih edilmiştir. Çalışmanın ikinci aşamasında, havzanın fiziksel özellikleri ve boyutsuz birim hidrograf koordinatları kullanılarak, DSI, Mockus ve Snyder birim hidrograf yöntemleri aracılığıyla çeşitli tekerrür aralıkları için havzaya özgü taşkın hidrografları üretilmiştir. Sonuçlar, DSI ve Mockus yöntemlerinin birbirine yakın ve yüksek pik debi değerleri ürettiğini ( $T = 100$  yıl için  $Q_{\max}$  sırasıyla 67,44 ve 63,76 m<sup>3</sup>/s), buna karşın Snyder yönteminin daha düşük pik debi değerleri ( $T = 100$  yıl için  $Q_{\max} = 32,17$  m<sup>3</sup>/s) ancak daha uzun süreli bir hidrograf oluşturduğunu ortaya koymuştur. Genel olarak, DSI ve Mockus yöntemlerinin, ormanlık ve nispeten küçük havzalarda ( $\approx 10$  km<sup>2</sup>) taşkın analizlerinde kullanılacak hidrografın oluşturulması açısından daha uygun olduğu sonucuna varılmıştır. Bu çalışma, İstanbul'un kentleşen bir bölgesinde, ormanlık alanların hâkim olduğu ölçüm istasyonu bulunmayan bir havza için özel olarak uyarlanmış üç yaygın sentetik birim hidrograf yönteminin karşılaştırmalı bir değerlendirmesini sunarak, veri yetersizliği yaşanan bölgelerde hidrolojik modelleme konusunda literatüre katkı sağlamaktadır.

**Anahtar kelimeler:** Coğrafi bilgi sistemleri (CBS), Sentetik birim hidrograf, Taşkın, Mockus, Snyder

\*Yazışılan Yazar

İntihal Kontrol: Evet – Turnitin

Şikayet: [fujece@firat.edu.tr](mailto:fujece@firat.edu.tr)

Telif Hakkı ve Lisans: Dergide yayın yapan yazarlar, CC BY-NC 4.0 kapsamında lisanslanan çalışmalarının telif hakkını saklı tutar



## Flood Discharge Estimation in Ungauged Basins Using Synthetic Unit Hydrographs and GIS

Erdal KESGİN<sup>1\*</sup>  

<sup>1</sup>Civil Engineering Department, Faculty of Civil Engineering, Istanbul Technical University, Istanbul, Türkiye.  
[kessine@itu.edu.tr](mailto:kessine@itu.edu.tr)

Received: 24.02.2025  
Accepted: 22.04.2025

Revision: 26.03.2025

doi: <https://doi.org/10.62520/fujece.1645774>  
Research Article

Citation: E. Kesgin, "Flood discharge estimation in ungauged basins using synthetic unit hydrographs and gis", Firat Univ. Jour. of Exper. and Comp. Eng., vol. 4, no 2, pp. 375-392, June 2025.

### Abstract

Flooding refers to the adverse effects caused by rivers overflowing their banks due to various reasons, affecting surrounding land, residential areas, and infrastructure. At the watershed scale, particularly in cases where flow monitoring stations are absent, hydrographs must be generated to analyze rainfall-runoff relationships for flood assessments. This study aims to generate synthetic hydrographs, analyze rainfall-runoff relationships, and estimate flood discharges for different return periods in a predominantly forested sub-watershed located in the Sarıyer district of Istanbul. The study analyzed extreme rainfall by calculating 24-hour maximum values for return periods of 2 to 100 years using four common probability distribution functions: Normal, Log-Normal, Log-Pearson Type III, and Gumbel. Among these methods, Log-Pearson Type III yielded higher rainfall values, and given the extreme nature of floods, it was preferred for discharge calculations. In the second stage of the study, flood hydrographs specific to the watershed were generated for different return periods using the DSI, Mockus, and Snyder unit hydrograph methods, incorporating watershed physical characteristics and dimensionless unit hydrograph coordinates. The results indicated that the DSI and Mockus methods produced similar and higher peak discharge values ( $Q_{\max} = 67.44$  and  $63.76 \text{ m}^3/\text{s}$ ,  $T=100$  years), whereas the Snyder method resulted in lower peak discharge ( $Q_{\max} = 32.17 \text{ m}^3/\text{s}$  for  $T = 100$  years) but a longer hydrograph duration. Overall, it was concluded that the DSI and Mockus methods are more suitable for flood analysis in forested and relatively small watersheds ( $\approx 10 \text{ km}^2$ ) due to their effectiveness in generating hydrographs for flood assessments. This study contributes to the literature by offering a comparative evaluation of three widely used synthetic unit hydrograph methods, specifically tailored for a forest-dominated ungauged basin in an urbanizing region of Istanbul, providing actionable insights for flood estimation in data-scarce, forested urban catchments.

**Keywords:** Geographical information systems (GIS), Synthetic unit hydrograph, Flood, Mockus, Snyder

\*Corresponding author

Plagiarism Checks: Yes – Turnitin  
Complaints: [fujece@firat.edu.tr](mailto:fujece@firat.edu.tr)

Copyright & License: Authors publishing with the journal retain the copyright to their work licensed under the CC BY-NC 4.0



## 1. Introduction

Flooding is a natural phenomenon in which a river overflows its banks due to various factors, causing damage to surrounding land, settlements, infrastructure, and living organisms while disrupting the economic and social life of the affected region [1]. Factors such as climate change, unplanned urbanization, unauthorized interventions in riverbeds, degradation of river basins, improper use of floodplains, and inadequate infrastructure for water flow in road and railway crossings further exacerbate the impacts of floods. Human influence plays a significant role in flood occurrence. In the absence of natural meteorological and geological conditions, flooding is unlikely to occur without natural or anthropogenic triggers. However, human interventions are a decisive factor in transforming floods into disasters. For instance, uncontrolled construction in floodplains, unauthorized urbanization in upstream areas, deforestation, vegetation loss, and improper land use are among the key contributing factors. Floods—frequently observed in Türkiye—rank second after earthquakes in terms of economic losses caused by natural disasters [2]. Compared to earthquakes, predicting the potential impacts of floods is relatively easier. However, it is not possible to determine the exact extent of the damage they may cause. Estimating flood discharges enables the modeling of flood scenarios and helps identify appropriate mitigation strategies. Therefore, the magnitude of floods can be scientifically calculated through statistical analyses based on available hydrometeorological data, allowing the development of flood scenarios with different return periods.

A river basin is defined as a system that transforms incoming rainfall into runoff. Therefore, for a given river basin, rainfall serves as the input parameter, while runoff is considered the output dependent on this rainfall. When there is a lack of flow measurements over a certain period or an absence of any flow observations within a river basin, estimating runoff values based on rainfall becomes a fundamental motivation for analyzing the basin as a system. However, due to the complex nature of the rainfall-runoff relationship in river basins, the system is often simplified through certain assumptions, leading to the development of a mathematical model [3]. During the planning of hydraulic structures or the construction of river engineering projects, it is essential to determine flood peaks that may occur at various return periods (e.g.,  $T = 10, 100, 500$  years). The most commonly used methods for estimating flood peaks include: (i) Statistical approaches based on streamflow observations to calculate flood peak and duration, and (ii) Methods utilizing rainfall data and unit hydrographs to estimate flood peaks and their durations. If a sufficient number of streamflow measurements are available for the watershed, statistical methods can yield reliable results for flood discharge estimation. However, in many rainfall-dominated regions, rainfall-runoff data are often unavailable. Consequently, synthetic unit hydrographs have been developed to address this limitation.

Sönmez et al., (2012) [4] applied the Snyder, Kirpich, Mockus, and Soil Conservation Service (SCS) methods to estimate flood discharge for eight streams in Istanbul. They reported that the Snyder method yielded higher discharge values; however, they also noted that this method is directly related to watershed area and geometric shape. Consequently, an increase in flood discharge was observed as the watershed area increased. Kumanlıoğlu and Ersoy (2018) [5] estimated flood discharges for various return periods in the Kızıldere stream, a tributary of the Gediz River, using the SCS and Mockus methods. They emphasized the necessity of determining these flood hydrographs to minimize potential loss of life and property, particularly in watersheds with high agricultural productivity. Bantchina and Gündoğdu (2021) [6] analyzed flood discharges and watershed characteristics for the Nilüfer Dam Basin (Türkiye) using Geographic Information Systems (GIS) and various synthetic unit hydrograph methods, including the DSI, Mockus, and the Snyder methods. Their results indicated that the highest peak discharge value was obtained using the DSI method ( $Q_p=4.40 \text{ m}^3/\text{s}/\text{mm}$ ), while the lowest was derived from the Mockus method ( $Q_p=3.75 \text{ m}^3/\text{s}/\text{mm}$ ). They highlighted the necessity of employing synthetic unit hydrograph methods in stations lacking direct flow measurements.

In the presented study, flood hydrographs corresponding to different return periods were determined for a sub-basin in Sarıyer, Istanbul, where no streamflow measurement data are available. These hydrographs were generated using synthetic unit hydrographs, including the DSI Synthetic Method, Mockus Method, and Snyder Method. As part of the analysis, a frequency analysis was conducted using the highest value among the annual maximum daily (24-hour) precipitation records, and the best-fitting probability distribution function was identified to derive daily maximum precipitation values for different return periods. These

precipitation values were then used as the primary input data for constructing synthetic unit hydrographs. Unlike many prior studies centered on rural or agricultural areas, this research examines a forested sub-basin in a rapidly urbanizing region. This setting offers a unique opportunity to evaluate the reliability of synthetic hydrograph methods in the complete absence of flow measurements. Furthermore, the study integrates high-resolution GIS data and evaluates method performance across a full range of return periods, which enhances its practical relevance for urban flood risk planning.

The main objective of the present study is to estimate flood discharges in a small, ungauged, forest-dominated sub-catchment in Istanbul's Sariyer district using three widely applied synthetic unit hydrograph methods DSI, Mockus, and Snyder. Even though synthetic methods have been used in many basins of Türkiye, comparative assessments for forested urban basins are limited in the literature. This study closes that gap by evaluating the performance of each method under different return periods, giving insight into their dependability in hydrologically similar basins. The results enhance not only knowledge on rainfall-runoff modeling in data-poor areas but also inform real-world practice among hydrologists and engineers designing drainage and flood control systems for rapidly urbanizing, topographically heterogeneous watersheds

## **2. Materials and Methods**

### **2.1. Study area and dataset**

The study area encompasses a sub-basin located within the boundaries of Sariyer district on the European side of Istanbul. This region, which covers an area of approximately 10 km<sup>2</sup>, is a mostly forested area located to the west of the Sariyer district center, south of the Zekeriyaköy district and west of the Bahçeköy district. A map generated using a 5-meter resolution Digital Elevation Model (DEM) provides a detailed representation of the study area and is presented in Figure 1. The elevation of the basin ranges from 2 to 234 meters, with an average elevation of 109.5 meters. While higher altitude values are observed in the northern parts, the altitude decreases towards the south. To analyze the land use and land cover (LULC) of the study area, Landsat-8 satellite images from 2023 were downloaded at a 10×10 m resolution using the Sentinel-2 Land Cover Explorer. According to the findings, approximately 80% of the basin area is forested and the remaining part is built area (Figure 1.). An analysis of the climatic characteristics of the study area, based on maps prepared by the Republic of Turkey Ministry of Environment, Urbanization, and Climate Change, reveals that the region falls within a humid to semi-humid climate zone according to various classification methods, including those of Aydeniz, Erinc, and Thornthwaite. This indicates that the area experiences mild winters and hot summers, exhibiting characteristics similar to the Mediterranean climate. In the calculation of flood discharges, the curve number (CN) of the basin was determined to be 55 by considering the basin's vegetation cover and geological structure together.

In this study, annual maximum rainfall data from the Turkish State Meteorological Service, specifically from the Sariyer station, were obtained (Figure 2.). Using the daily maximum rainfall data, extreme rainfall values were calculated using probability distribution functions commonly employed in the literature, such as Normal, Log-Normal, Log-Pearson Type III, and Gumbel. The calculated extreme rainfall values were used as input parameters for generating synthetic unit hydrographs across various return periods.

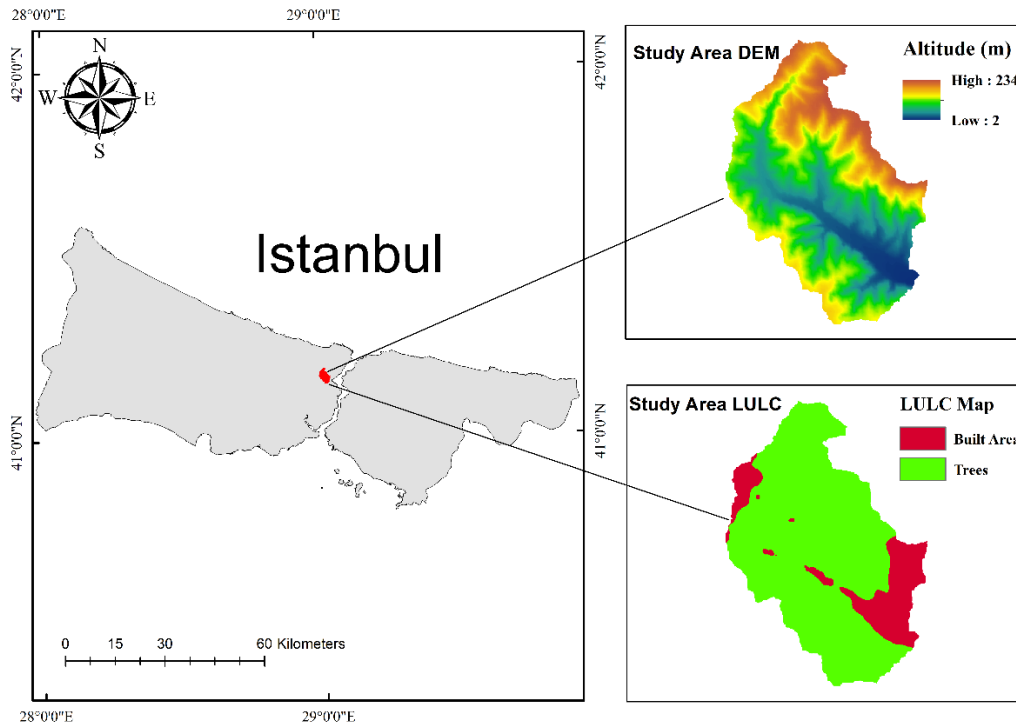


**Figure 1.** Study area DEM and land use land cover map (LULC)

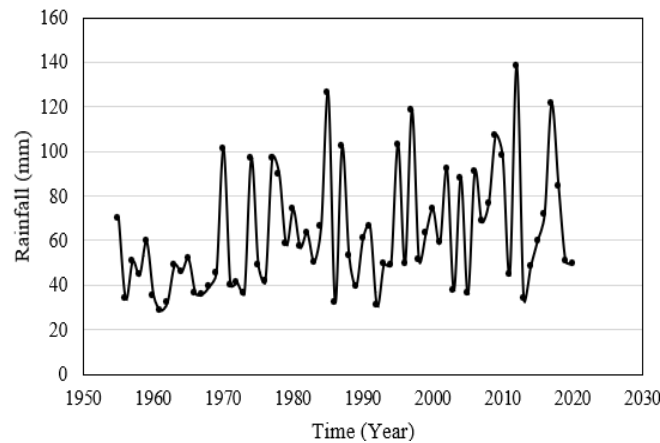


**Figure 2.** Annual maximum 24-hour observed precipitation at Sariyer Meteorological station

## 2.2. Probability density functions

The irregularity of rainfall leads to many hydrological variables exhibiting the characteristics of random variables. Due to the availability of long-term rainfall records, statistical methods have been employed in the calculation of extreme rainfall values. In this study, extreme rainfall values were calculated using probability distribution functions that are frequently used in the literature, including Normal, Log-Normal, Log-Pearson Type III, and Gumbel. The probability distribution functions and their parameters used for extreme rainfall analysis in this study are summarized in Table 1.

For the Normal distribution, the possible rainfall values for specific return periods ( $T$ ) are expressed in Equation 4 in Table 1. The three key parameters are the arithmetic mean ( $\mu_x$ ), standard deviation ( $\sigma_x$ ), and frequency factor ( $K_T$ ). While the mean and standard deviation are obtained from the dataset, the frequency

factor is calculated using Equation 3. The "w" parameter in Equation 3 is calculated based on the exceedance probability of the return period ( $p = 1/T$ ), as presented in Equation 2.

The Log-Normal distribution is expressed as the distribution of a random variable whose logarithm follows a normal distribution. The necessary operations to calculate the likely extreme rainfall for a given return period are equivalent to those of the Normal distribution. However, it is important to note that in this case, the "x" values must be processed as "logx."

The Gumbel distribution is widely used in hydrological studies due to its success in modeling extreme data [7-8]. It estimates rainfall values based on the mean, standard deviation, and a modified frequency factor ( $K_T$ ) defined specifically for extreme value distributions [9-10].

The Log-Pearson Type III distribution is frequently utilized in estimating floods for different return periods. Several studies have emphasized that this distribution is recommended for flood estimation because it accounts for the skewness in rainfall data [9-10]. The frequency factor (k) for the Log-Pearson Type III distribution is used as shown in Equation 14 and is read from various tables depending on the return periods and  $C_s$  value [11].

**Table 1.** Probability Density Functions and calculation formulas

PDF	Equations
Normal	$f(x) = \frac{1}{\sqrt{2\pi}\sigma_x} \exp\left[-\frac{1}{2}\left(\frac{x - \mu_x}{\sigma_x}\right)^2\right] \quad (1)$
	$w = \sqrt{\ln\left(\frac{1}{p^2}\right)} \quad (2)$
	$K_T = w - \frac{[2.515517 + (0.802853 \times w) + (0.010328 \times w^2)]}{[1 + (1.432788 \times w) + (0.189269 \times w^2) + (0.001308 \times w^3)]} \quad (3)$
	$X_T = \mu_x + (K_T \times \sigma_x) \quad (4)$
Log Normal	$f(x) = \frac{1}{x\sigma_y\sqrt{2\pi}} \exp\left[-\frac{(y - \mu_y)^2}{2\sigma_y^2}\right] \quad (5)$
Gumbel	$f(x) = \frac{1}{a} \exp\left[-\frac{(x - u)^2}{a} - \exp\left(-\frac{x - u}{a}\right)\right] \quad (6)$
	$a = \frac{\sqrt{6}S_x}{\pi} \quad (7)$
	$u = \bar{x} - 0.5772a \quad (8)$
	$K_T = -\frac{\sqrt{6}}{\pi} \left\{ 0.5772 + \ln\left[\ln\left(\frac{T}{T-1}\right)\right] \right\} \quad (9)$
	$X_T = \mu_x + (K_T \times \sigma_x) \quad (10)$

**Table 1.** (Continue) Probability Density Functions and calculation formulas

Log-Pearson Tip III	$\log \bar{x} = \frac{\sum \log x}{N}$		(11)
	$\sigma_{\log x} = \sqrt{\frac{\sum (\log x - \log \bar{x})^2}{N-1}}$		(12)
	$C_s = \left[ \frac{N \times \sum (\log x - \log \bar{x})^3}{(N-1) \times (N-2) \times (\sigma_{\log x})^3} \right]$		(13)
	$\log x = \log \bar{x} + k \times \sigma_{\log x}$		(14)

### 2.3. Synthetic unit hydrographs

Flood calculations are performed using synthetic unit hydrograph methods. For this purpose, various synthetic methods such as the DSI Synthetic Unit Hydrograph, the Mockus Synthetic Unit Hydrograph Method, and the Snyder Synthetic Unit Hydrograph Method can be utilized. In this study, the physical characteristics of the study area were first determined using maps created in a GIS environment. The calculation process consists of three main steps. In the first step, precipitation values representing the studied watershed were calculated for various return periods. In the second step, a watershed-specific unit hydrograph was created using the physical characteristics of the watershed and dimensionless unit hydrograph coordinates. Finally, based on these data, flood peak values were calculated. The dimensionless unit hydrograph coordinates used in creating the hydrographs are presented in Table 2, and the details of these calculation steps are explained in the following sections.

**Table 2.** Dimensionless unit hydrograph coordinates

T / T <sub>p</sub>	Q / Q <sub>p</sub>	T / T <sub>p</sub>	Q / Q <sub>p</sub>	T / T <sub>p</sub>	Q / Q <sub>p</sub>
0.0	0.000	1.0	1.000	2.4	0.180
0.1	0.015	1.1	0.980	2.6	0.130
0.2	0.075	1.2	0.920	2.8	0.098
0.3	0.160	1.3	0.840	3.0	0.075
0.4	0.280	1.4	0.750	3.5	0.036
0.5	0.430	1.5	0.660	4.0	0.018
0.6	0.600	1.6	0.560	4.5	0.009
0.7	0.770	1.8	0.420	5.0	0.000
0.8	0.890	2.0	0.320		
0.9	0.970	2.2	0.240		

#### 2.3.1. DSI synthetic unit hydrograph method

The DSI synthetic unit hydrograph Method is used for drainage areas up to 1000 km<sup>2</sup>. For larger drainage areas, these areas are divided into smaller units, each less than 1000 km<sup>2</sup>, to generate unit hydrographs [12]. Additionally, although the DSI synthetic unit hydrograph Method is recommended for application when T<sub>p</sub> > 2 hours, it is not applied for areas smaller than 1 km<sup>2</sup>. The catchment area (A) is determined using

topographic maps. Then, the longest branch of the river is measured from the map ( $L$ ), and the distance between the projection of the drainage area center onto the longest river branch and the project section is determined ( $L_c$ ).

Firstly, the harmonic slope calculation of the land is required. For this purpose, starting from the river source and following the project section, elevations and distances are recorded. The entire length is segmented into ten equal parts, and the harmonic slope is determined accordingly. Basin harmonic gradient,

$$S = \left( \frac{10}{\sum \frac{1}{\sqrt{s}}} \right)^2 \quad (15)$$

Basin parameter,

$$E = \frac{L \times L_c}{\sqrt{S}} \quad (16)$$

Once the catchment area and basin parameters are determined, the Rain productivity ( $q_p$ ) is calculated using Equation 17:

$$q_p = \frac{414}{A^{0.225} \times E^{0.16}} \quad (17)$$

$q_p$  represents the discharge per unit  $\text{km}^2$  of the rainfall area at the peak of the flood hydrograph, generated by a two-hour rainfall event that produces 1 mm of runoff over the basin.

The unit hydrograph peak discharge,  $Q_p$  ( $\text{m}^3/\text{s}/\text{mm}$ ):

$$Q_p = A \times q_p \times 10^{-3} \quad (18)$$

Unit hydrograph volume,  $V_b$  ( $\text{m}^3$ ):

$$V_b = A \times h_a \times 10^3 \quad (19)$$

The hydrograph duration ( $T$ , hours) and the hydrograph rise time ( $T_p$ , hours) are given in Equations 20 and 21, respectively.

$$T = 3.65 \frac{V}{Q} \quad (20)$$

$$T_p = \frac{T}{5} \quad (21)$$

After following the aforementioned procedure, the 24-hour rainfall-duration-return periods are multiplied by the number of pluviographs and the maximization factor (1.13). The adjusted rainfall values obtained are then used to determine the excess rainfall coefficients ( $h$ ). The runoff coefficient is calculated using Equation 22.

$$h = \frac{(P - 0.2S)^2}{(P + 0.8S)} \quad (22)$$



Finally, the flood discharges are calculated by multiplying the peak discharge by the runoff coefficients determined separately for each return period (Equation 23).

$$Q = h \times Q_p \quad (23)$$

The  $Q_p$  and  $T_p$  values of the unit hydrograph are scaled using the dimensionless unit hydrograph coordinates to obtain the DSI synthetic unit hydrograph coordinates specific to the basin. The dimensionless unit hydrograph coordinates are provided in Table 2.

### 2.3.2. Mockus unit hydrograph method

In the Mockus method, hydrographs are triangular in shape, making them preferable due to their computational and graphical simplicity [13]. This method can be applied in regions where no streamflow gauging station is available or where long-term recorded data are lacking. The Mockus method is suitable for drainage basins with a collecting time ( $T_c$ ) of less than 30 hours. The necessary parameters and procedural steps for generating a unit hydrograph using the Mockus method are presented below.

$$T_c = 0.00032 \times \frac{L^{0.77}}{S^{0.385}} \quad (24)$$

where  $T_c$  = Collecting Time (hours),  $L$  = Stream length (m),  $S$  = Harmonic slope

After determining the collecting time ( $T_c$ ) based on stream length and harmonic slope, Precipitation time ( $D$ ) is calculated using Equation 25:

$$D = 2\sqrt{T_c} \quad (25)$$

Then, the rise time of the hydrograph ( $T_p$ ) is calculated according to Equation 26:

$$T_p = (0.5 \times D) + (0.6 \times T_c) \quad (26)$$

Hydrograph descent time ( $T_r$ ) is calculated according to Equation 27:

$$T_r = 1.67 \times T_p \quad (27)$$

Flood time ( $T_b$ ) is expressed as the sum of the rise time of the hydrograph and hydrograph descent time:

$$T_b = T_p + T_r \quad (28)$$

The discharge,  $Q_p$ , generated by a 1 mm rainfall, can be calculated using the following relation:

$$Q_p = \frac{K \times A \times h_a}{T_p} \quad (29)$$

Here,  $K$  is the catchment coefficient. Istanbuluoglu et al., [14] investigated the  $K$  value for various basins of Türkiye and showed that it varies between 0.10-0.40.

After following the aforementioned procedure, the 24-hour rainfall-duration-return periods are multiplied by the number of pluviographs and the maximization factor (1.13). The adjusted rainfall values obtained are then used to determine the excess rainfall coefficients ( $h$ ). The runoff coefficient is calculated using Equation 22. Finally, the flood discharges are calculated by multiplying the peak discharge by the runoff coefficients determined separately for each return period, as given in Equation 23. The  $Q_p$  and  $T_p$  values of the unit

hydrograph are scaled using the dimensionless unit hydrograph coordinates to obtain the coordinates of the Mockus Synthetic Unit Hydrograph specific to the basin.

### 2.3.3. Snyder unit hydrograph method

This method was proposed by Snyder [15] and in this method, Snyder studied unit hydrographs of basins located in the high regions of the Appalachian Mountains in the United States, defining a standard unit hydrograph. By examining unit hydrographs of various basins in the U.S., Snyder developed the following formulas for the  $T_p$  rise time and  $Q_p$  peak discharge of the unit hydrograph:

$$T_p = 0.75 \times C_t \times (L \times L_c)^{0.3} \quad (30)$$

Here,  $T_p$  is the rise time,  $L$  is the stream length,  $L_c$  is the distance from the centroid of the catchment area to the catchment outlet, and  $C_t$  is a coefficient related to the watershed surface.

The relationship between the effective rainfall duration,  $T_r$ , and the shower time,  $T_p$ , is given in Equation 31:

$$T_r = \frac{T_p}{5.5} \quad (31)$$

The unit discharge at the peak point of the hydrograph ( $q_p$ ) ( $L/s/km^2/cm$ ) is calculated using the equation.

$$q_p = \frac{276 \times C_p}{T_p} \quad (32)$$

Here,  $C_p$  is a coefficient dependent on the characteristics of the catchment area. To determine the unit hydrograph for the catchment, the catchment parameters ( $C_p$  and  $C_t$ ) mentioned above must be known. Table 3 shows the values of the relevant parameters used in the literature.

**Table 3.** Coefficient values related to the surface for the Snyder method [16]

Soil Type	$C_t$	$C_p$
Sandly	1.65	0.56
Bog	1.50	0.63
Clayey or rocky	1.35	0.69

Finally, the unit hydrograph peak discharge ( $m^3/s/cm$ ):

$$Q_p = A \times q_p \times 10^{-3} \quad (33)$$

The unit hydrograph peak discharge ( $m^3/s/cm$ ) is calculated from the formula. The obtained values represent the discharge corresponding to a 1 cm flow height. After following the aforementioned procedure, the 24-hour rainfall-duration-return periods are multiplied by the number of pluviographs and the maximization factor (1.13). The adjusted rainfall values obtained are then used to determine the excess rainfall coefficients (h). The runoff coefficient is calculated using Equation 23. Finally, the flood discharges are calculated by multiplying the peak discharge by the runoff coefficients determined separately for each return period, as given in Equation 24.

The  $Q_p$  and  $T_p$  values of the unit hydrograph are multiplied by the dimensionless unit hydrograph coordinates of the synthetic method to obtain the coordinates of the Snyder Synthetic Unit Hydrograph specific to the basin.

### 3. Result and Discussion

In this study, frequency analysis was performed using the largest daily (24-hour) rainfall values of the current year from the Sarıyer meteorological station (Figure 2), and the distribution function that best fits the sample distribution was selected. Daily maximum rainfall values for various return periods ( $T = 2, 5, 10, 25, 50, 100$ ) were calculated. The extreme rainfall values for all probability functions at different return periods are summarized in Table 4 and presented in Figure 3. For short return intervals ( $T = 2, 5$  years), the Normal distribution provides the highest extreme rainfall values, while for relatively long return intervals ( $T = 10, 25, 50, 100$  years), the Log-Pearson Type III distribution generates the highest rainfall values.

**Table 4.** Extreme distribution of daily maximum precipitation

PDF	Return Periods (year)					
	2	5	10	25	50	100
Normal	62.80	85.24	96.95	109.48	117.56	124.80
Log-Normal	57.58	81.12	96.75	116.82	131.93	147.13
Gumbel	58.44	82	97.63	117.34	131.96	146.50
Log-Pearson Tip III	56.73	80.45	97.82	121.17	140.57	160.49

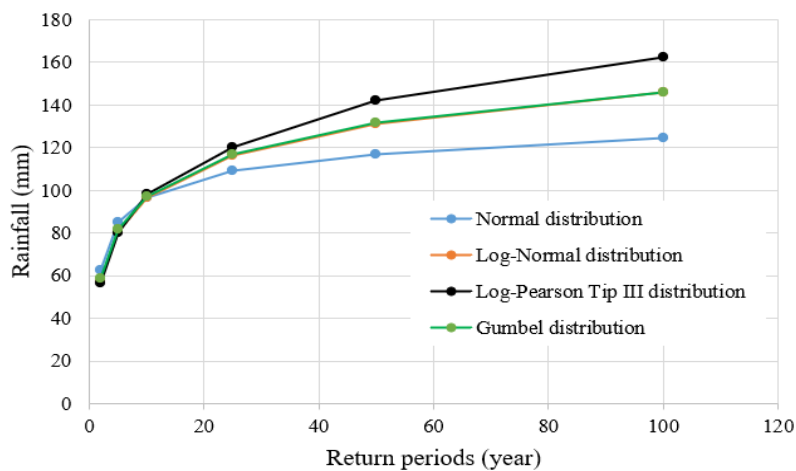


**Figure 3.** Extreme distribution of daily maximum precipitation

Many scientific studies in the literature have emphasized that the Log-Pearson Type III distribution should be used in flood discharge calculations [17-18]. Additionally, when compared to other probability distribution functions, the rainfall values obtained with the Log-Pearson Type III distribution are higher, and since floods are extreme events, the extreme rainfall values derived from this method have been used in discharge calculations.

As mentioned above, the basin unit hydrograph was obtained with the help of the basin's physical characteristics and the dimensionless unit hydrograph coordinates. Below, the physical characteristics of the basin that were initially identified, along with the magnitudes calculated using these characteristics, are presented (Table 5).

**Table 5.** Numerical values of study basin

Watershed Characteristics	Result
Watershed Area (km <sup>2</sup> )	A= 10
Watershed minimum height (m)	2
Watershed maximum height (m)	234
Watershed mean height (m)	109.5
Watershed Direction	South, Southeast
Watershed longest flow path (m)	L= 6515
Centroidal longest flow path (m)	L <sub>c</sub> = 2230

After the physical characteristics of the basin were determined in the ArcGIS 10.8 environment, the parameters required for the DSI synthetic unit hydrograph method were calculated as provided in Section 2.3.1 and are presented in Table 6.

**Table 6.** DSI synthetic method calculation table

Parameters	Calculation	Value
Harmonic slope	$\sqrt{S} = 10 / \sum (1/S)$	0.0197
Basin parameter	$E = L * L_c / \sqrt{S}$	103.43
Rain productivity	$q_p = 414 / (A^{0.225} * E^{0.16})$	117.39
Peak discharge	$Q_p = A * q_p * 10^{-3}$	1.174
Unit volume	$V_b = A * h_a * 10^3$	10000
Hydrograph duration	$T = (3.65 V_b / Q_p) / 3600$	8.64
Hydrograph rise time	$T_p$	1.728

After determining the physical characteristics of the basin and the parameters for the DSI synthetic method, the 24-hour rainfall repetitions, pluviograph factor, precipitation area adjustment coefficient, and maximization value were adjusted. For this process, the final multiplication factor of 1.13 was applied to the current rainfall values to obtain the 24-hour adjusted rainfall values (Table 7). Then, using the 24-hour adjusted rainfall values, the excess rainfall coefficients (h) was calculated as given in Equation 22. Flood discharge values were obtained by multiplying the runoff coefficients with the peak discharge values for different return periods (Table 7).

**Table 7.** DSI method flood discharge calculation

	Return Periods (year)					
	2	5	10	25	50	100
Log-Pearson Tip III Rainfall Value	56.73	80.46	97.82	121.17	140.57	160.49
Final multiplication factor (1.13)	64.10	90.92	110.54	136.92	158.84	181.35
Excess rainfall coefficients (h)	2.21	9.47	17.19	29.99	42.31	56.22
Flood discharge (m <sup>3</sup> /s)	2.498	11.083	20.340	34.546	51.002	67.443

The final obtained values of  $Q_p$ : 1.174 m<sup>3</sup>/s/mm and  $T_p$ : 1.728 hours were multiplied by the dimensionless unit hydrograph coordinates (Table 2) to derive the unit hydrograph for the stream (Figure 4a).

$T_c$  is calculated by substituting the values of  $L$  (Watershed longest flow path) and  $S$  (harmonic slope) into the Equation 24 according to the Mockus method.

$$T_c = 0.00032 * (6515^{0.77} / 0.0197^{0.385}) = 1.254 \text{ hour}$$

The value of  $D$  is calculated by substituting  $T_c$  into the Equation 25:

$$D = 2 * 1.254^{0.5} = 2.24 \text{ hour}$$

$T_p$  is calculated by substituting the values of  $D$  and  $T_c$  into the Equation 26:

$$T_p = 0.5 * 2.24 + 0.6 * 1.254 = 1.872 \text{ hour}$$

The values of  $T_r$  and  $T_b$  are calculated by substituting  $H$  (1.67 constant) and  $T_p$  into the Equation 27 to obtain  $T_r$ , and then substituting  $T_p$  and  $T_r$  into the Equation 28 to calculate  $T_b$ .

$$T_r = 1.67 * 1.872 = 3.126 \text{ hour}$$

$$T_b = 1.872 + 3.126 = 4.998 \text{ hour}$$

The value of  $Q_p$  is calculated by substituting the values of  $K$ ,  $A$  and  $h$  into the Equation 29:

$$Q_p = (0.208 * 10 * 1) / 1.872 = 1.111 \text{ m}^3/\text{s}$$

After determining the peak discharge, the 24-hour maximum rainfall values for different return periods and the excess rainfall coefficients were calculated (Table 8). As given in Equation 23, the peak discharge of the unit hydrograph multiplied by the flow coefficient resulted in the calculation of flood discharge values for different return periods, which are presented in Table 8.

**Table 8.** Mockus method flood discharge calculation

	Return Periods (year)					
	2	5	10	25	50	100
Log-Pearson Tip III Rainfall Value	56.73	80.46	97.82	121.17	140.57	160.49
Final multiplication factor (1.13)	64.10	90.92	110.54	136.92	158.84	181.35
Excess rainfall coefficients (h)	2.21	9.47	17.19	29.99	42.31	56.22
Flood discharge (m <sup>3</sup> /s)	2.362	10.479	19.231	32.662	48.221	63.766

The final obtained values of  $Q_p$ : 1.111 m<sup>3</sup>/s/mm and  $T_p$ : 1.872 hours were multiplied by the dimensionless unit hydrograph coordinates (Table 2) to derive the unit hydrograph for the stream (Figure 4b).

For the Snyder method, as given in Equation 30,  $T_p$  (time to peak) is calculated as the rise time.

$$T_p = 0.75 * 1.65 * (6.51 * 2.23)^{0.3} = 2.76 \text{ hour}$$

Using Equation 31,  $T_r$  is calculated:

$$T_r = 2.76 / 5.5 = 0.55 \text{ hour}$$

According to Equation 32, the peak discharge per unit area of the standard unit hydrograph is calculated in units of (l/sec/km<sup>2</sup>/mm):

$$q_p = 276 * 0.56 / 2.76 = 56 \text{ l/sec/km}^2/\text{mm}$$

Then, the discharge value at the flood peak is calculated using Equation 33:

$$Q_p = 10 * 56 * 10^{-3} = 0.560 \text{ m}^3/\text{s}/\text{mm}$$

The final obtained values of  $Q_p$ :  $0.560 \text{ m}^3/\text{s}/\text{mm}$  and  $T_p$ : 2.76 hours were multiplied by the dimensionless unit hydrograph coordinates (Table 2) to derive the unit hydrograph for the stream (Figure 4c).

**Table 9.** Snyder method flood discharge calculation

	Return Periods (year)					
	2	5	10	25	50	100
Log-Pearson Tip III Rainfall Value	56.73	80.46	97.82	121.17	140.57	160.49
Final multiplication factor (1.13)	64.10	90.92	110.54	136.92	158.84	181.35
Excess rainfall coefficients (h)	2.21	9.47	17.19	29.99	42.31	56.22
Flood discharge ( $\text{m}^3/\text{s}$ )	1.191	5.286	9.702	16.478	24.328	32.170

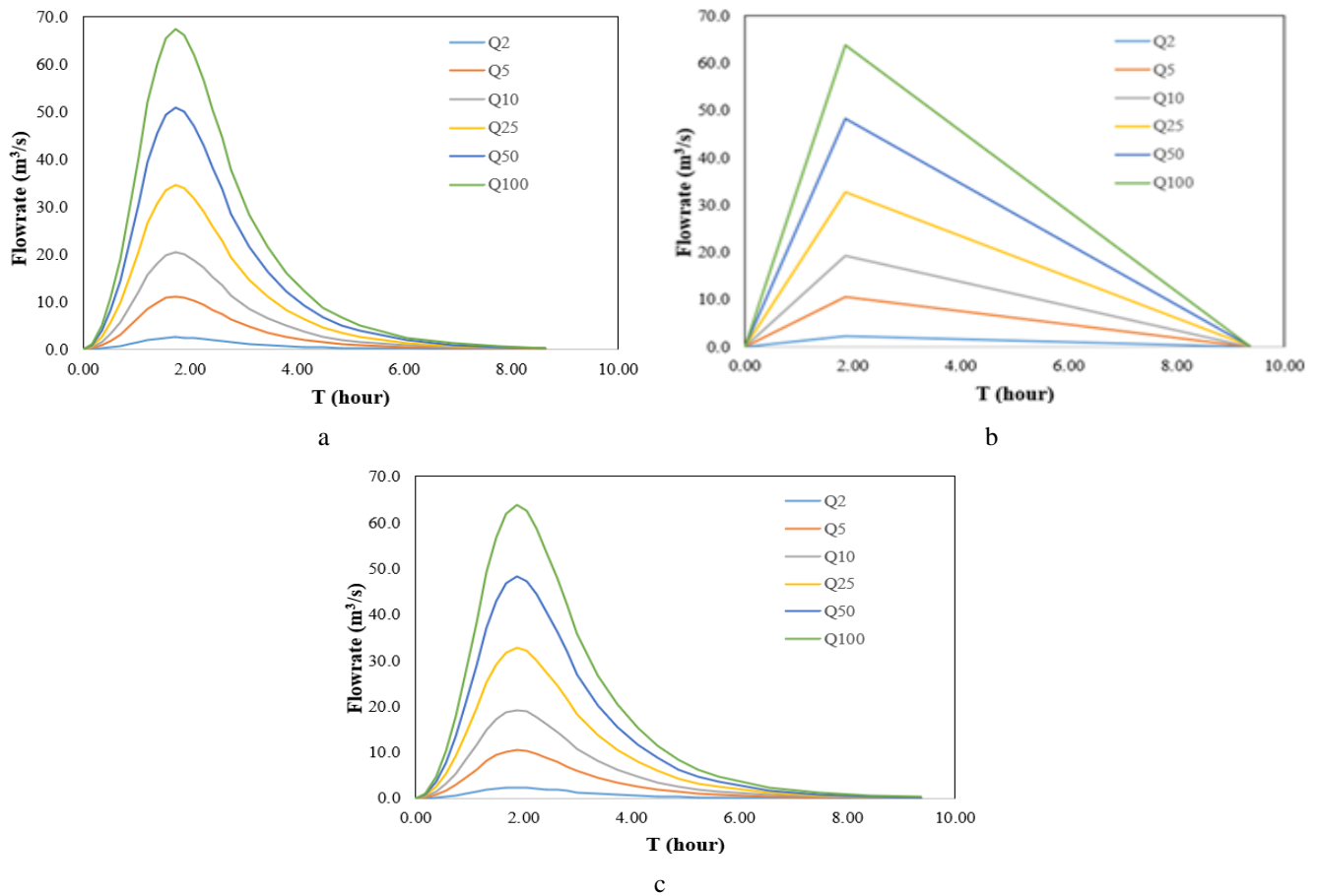
After determining the peak discharge, the 24-hour maximum rainfall values for different return periods and the flow coefficients were calculated (Table 9). As given in Equation 23, the peak discharge of the unit hydrograph multiplied by the excess rainfall coefficients resulted in the calculation of flood discharge values for different return periods, which are presented in Table 9.

Table 10 presents the flood discharge values calculated using different methods for various return periods. Additionally, Figure 4 illustrates the flood hydrographs computed for different methods and return periods. Furthermore, Figure 5 presents the flow values for different return periods obtained using different unit hydrograph methods and a representation of the maximum flood discharges observed for the 100-year recurring rainfall.

**Table 10.** Calculated flood discharge for different return periods

Methods	Return Periods (year)					
	2	5	10	25	50	100
DSI	2.498	11.083	20.340	34.546	51.002	67.443
Mockus	2.362	10.479	19.231	32.662	48.221	63.766
Snyder	1.191	5.286	9.702	16.478	24.328	32.170

When examining Figure 4 and Table 10, compared to the Snyder method, both the DSI and Mockus methods produced consistently higher peak discharges across all return periods. This similarity suggests not only comparable hydrograph shapes but also reinforces their reliability for small, forested catchments. In addition to the closeness of discharge values, these two methods also yield hydrographs with similar durations. In contrast to DSI and Mockus, the Snyder method generated substantially lower peak discharges and exhibited a more prolonged hydrograph response, likely due to its sensitivity to basin shape and longer time-to-peak assumptions. Furthermore, these discharges align with expectations for a small forest-dominated watershed of approximately  $10 \text{ km}^2$ . The highest peak discharge obtained ( $Q_{\max} = 67.44 \text{ m}^3/\text{s}$  for the DSI method at a 100-year return period) corresponds to an average unit discharge of  $\sim 6.74 \text{ m}^3/\text{s}/\text{km}^2$ . This value is within the range reported in the literature for similar basins in Türkiye, especially those located in humid to semi-humid climates [5, 6]. Furthermore, the lower discharges produced by the Snyder method can be attributed to its sensitivity to shape parameters and its assumption of a longer time to peak. The close agreement between the DSI and Mockus results strengthens their applicability in small, forested catchments and confirms the hydrological plausibility of the computed discharges within the adopted methodological framework.



**Figure 4.** Various synthetic unit hydrograph methods and flood hydrographs for return periods: a) DSI Method, b) Mockus Method, c) Snyder Method (The DSI and Mockus methods show higher peak discharges and shorter durations compared to the Snyder method)

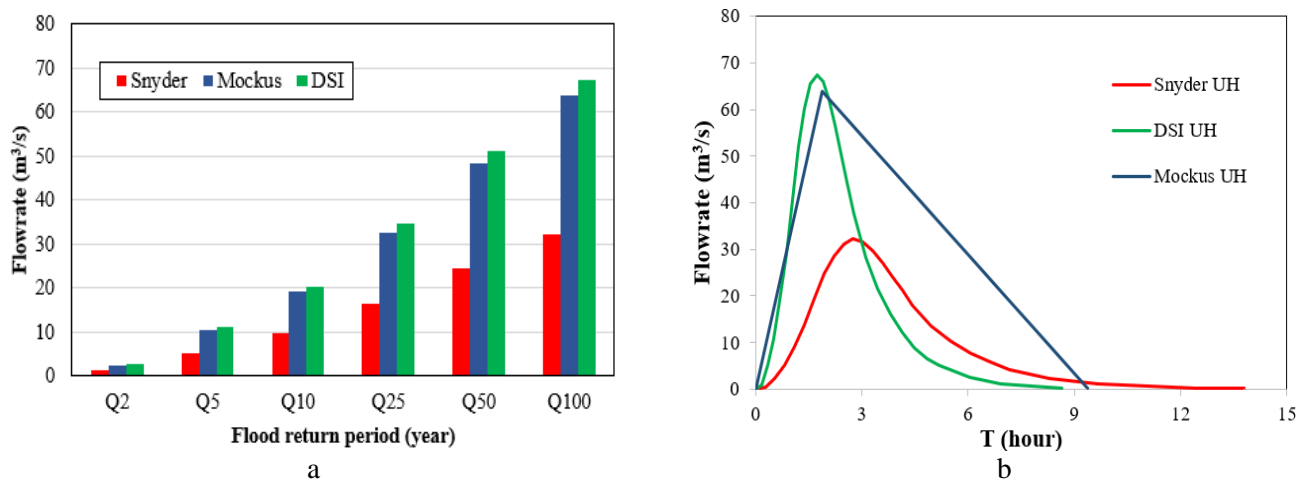


**Figure 5.** Comparison of flood discharges: a) DSI, Mockus, and Snyder methods for various return periods (The DSI method consistently produces the highest discharges across all return periods) b) Synthetic unit hydrographs for a 100-year return period (Snyder method results in a longer hydrograph duration and lower peak compared to DSI and Mockus methods)

In summary, the findings of the presented study are consistent with recent research highlighting the importance of method selection based on basin characteristics. Mukherjee et al. (2024) showed that deterministic methods are effective for small, forested headwater catchments, while other approaches perform better in larger basins [22]. Aziz et al. (2025) [23] emphasized statistical methods for urban



flood planning, and Saplıoğlu (2025) [24] demonstrated that optimization techniques can enhance model accuracy. These studies support the conclusion that the DSI and Mockus methods are particularly reliable for flood estimation in small, ungauged, forested basins, such as the one examined in this study.

Given the destructive nature of floods as extreme hydrological events, it is essential to utilize the most severe hydrograph obtained in flood modeling studies. Accurately generated precipitation data and hydrographs with high-resolution values play a critical role in areas such as flood risk management, drainage design, infiltration assessment, and the long-term sustainability of urban infrastructure systems [19-21]. Accordingly, this study developed hydrographs that effectively represent watershed-scale rainfall-runoff relationships, which are fundamental inputs for the creation of flood inundation and water depth maps.

On the other hand, there are many uncertainties in hydrological modeling of ungauged basins. The main ones are potential errors in rainfall data—specifically for the application of one station—statistical uncertainty of extreme rainfall distributions that were fitted, and errors in land use classification due to satellite resolution or seasonality. In addition, empirical coefficients used for synthetic unit hydrograph methods, which are occasionally borrowed from other basins, may not be representative of local conditions. While these uncertainties are not precisely quantified in this study, they need to be considered when evaluating the results and planning future research.

#### **4. Conclusion**

This study evaluated three synthetic unit hydrograph methods—DSI, Mockus, and Snyder—for estimating flood discharges in a small, forest-dominated ungauged sub-basin in Istanbul. Among these, the DSI and Mockus methods yielded consistently higher and more conservative discharge values, aligning closely with each other and demonstrating suitability for hydrological applications in similar catchments. Their reliance on physically-based parameters rather than empirical coefficients enhance their practical utility, particularly in data-scarce environments.

While the selected methods performed robustly, attention must be paid to uncertainties such as limitations in rainfall measurement, classification errors in land use data, and assumptions inherent to empirical coefficients. These factors, although not explicitly quantified in this study, underscore the importance of further calibration and sensitivity analyses in future research.

The outcomes of this work offer a strategic foundation for advancing flood risk assessment and infrastructure planning in other ungauged, forested urban basins—especially those facing intensified challenges from rapid urbanization and climate variability.

#### **5. Author Contribution Statement**

Author 1 contributed to the idea, design and literature review, evaluation of the results, could be reworded as of the manuscript, and reviewed the manuscript for language accuracy and overall coherence.

#### **6. Ethics Committee Approval and Conflict of Interest**

There is no need to obtain ethics committee permission for the prepared article. There is no conflict of interest with any person/institution in the prepared article.

#### **7. Ethical Statement Regarding the Use of Artificial Intelligence**

No artificial intelligence-based tools or applications were used in the preparation of this study. The entire content of the study was produced by the authors in accordance with scientific research methods and academic ethical principles.

## 8. References

- [1] F. Binici and T. Aksoy, "Şehirleşmenin Taşkın Üzerindeki Etkisi," *GSI J. Serie C: Advancements Inf. Sci. Technol.*, vol. 5, no. 1, pp. 64–76, 2022.
- [2] T. Akkuş, "Doğal Afetlerin Toplumsal Tarihe Etkileri Üzerine Yerel Bir Örnek: 1931–1941 Döneminde Edirne ve Çevresindeki Taşkınlar ve Sonuçları," *Uludağ Univ. J. Soc. Sci.*, vol. 24, no. 44, pp. 69–96, 2023.
- [3] Z. P. McEachran, J. Kietzmann, and M. Johnston, "Parsimonious streamflow forecasting system based on a dynamical systems approach," *J. Hydrol.*, vol. 641, 2024.
- [4] O. Sönmez, M. Öztürk, and E. Doğan, "İstanbul derelerinin taşkın debilerinin tahmini," *Sakarya Univ. J. Sci.*, vol. 16, no. 2, pp. 130–135, 2012.
- [5] A. A. Kumanlioğlu and S. B. Ersoy, "Akım gözlemi olmayan havzalarda taşkın akımlarının belirlenmesi: Kızıldere Havzası," *DEU Eng. Sci. J.*, vol. 20, no. 60, pp. 890–904, 2018.
- [6] B. B. Bantchina and K. S. Gündoğdu, "Watershed Characteristics and Synthetic Unit Hydrographs Determination using Geographical Information Systems," *J. Biol. Environ. Sci.*, vol. 15, no. 45, pp. 27–34, 2021.
- [7] P. Dutta and S. Deka, "Reckoning flood frequency and susceptibility area in the lower Brahmaputra floodplain using geospatial and hydrological approach," *River*, vol. 2, no. 3, pp. 384–401, 2023.
- [8] U. Ahad, U. Ali, M. Inayatullah, and A. R. Shah, "Flood Frequency Analysis: A Case Study of Pohru River Catchment, Kashmir Himalayas, India," *J. Geol. Soc. India*, vol. 98, no. 12, pp. 1754–1760, 2022.
- [9] A. I. Shah and N. D. Pan, "Evaluation of probability distribution methods for flood frequency analysis in the Jhelum Basin of North-Western Himalayas, India," *Cleaner Water*, vol. 2, 2024.
- [10] S. Malik and S. C. Pal, "Potential flood frequency analysis and susceptibility mapping using CMIP5 of MIROC5 and HEC-RAS model: A case study of lower Dwarkeswar River, Eastern India," *SN Appl. Sci.*, vol. 3, no. 1, 2021.
- [11] N. Usul, *Engineering Hydrology*, Ankara: ODTÜ Basımevi, 2001.
- [12] I. Gevrek and A. Irvem, "Antakya'da taşkına neden olan yan derelerde hidrograf analizi ile taşkın tahmini," *Mustafa Kemal Univ. J. Agric. Sci.*, vol. 26, no. 3, pp. 533–542, 2016.
- [13] Y. Koca, "Rize iyidere alt havzası ikizdere kesiti için birim hidrografın belirlenmesi," Uzmanlık Tezi, T.C. Orman ve Su İşleri Bakanlığı, Ankara, 2014.
- [14] A. Istanbuluoğlu, F. Konukcu, and I. Kocaman, "Precise determination of Turkish spillway sizes from synthetic unit hydrographs to prevent flood damage," *Acta Agric. Scand., Sect. B - Soil Plant Sci.*, vol. 54, no. 3, pp. 114–120, 2004.
- [15] F. F. Snyder, "Synthetic unit hydrographs," *Trans. Am. Geophys. Union*, vol. 19, pp. 447–454, 1938.
- [16] H. Çelik, "Sel Kontrolünde Hidroloji," *ÇEM Sel Kontrolü Semineri*, Afyonkarahisar, 2012.
- [17] O. Sönmez, T. Hırca, and F. Demir, "Akım Ölçümü Olmayan Nehirlerde Farklı Yağış Akış Modelleri ile Tekerrürlü Taşkın Debisi Hesabı: Mudurnu Çayı Örneği," in *Proc. 5th Int. Symp. Innov. Technol. Eng. Sci.*, Baku, Azerbaijan, pp. 2017, Sep. 29–30.
- [18] M. E. Yurdakul, "Güney Sapanca Havzası taşkın yayılım haritalarının modellenmesi: Keçi Deresi örneği," M.S. thesis, Sakarya Univ., Inst. Nat. Sci., Sakarya, 2019.
- [19] K. Gezici, E. Kesgin, and H. Agaccioglu, "Hydrological assessment of experimental behaviors for different drainage methods in sports fields," *J. Irrig. Drain. Eng.*, vol. 147, no. 9, 2021.
- [20] K. Gezici and S. Şengül, "Estimation and analysis of missing temperature data in high altitude and snow-dominated regions using various machine learning methods," *Environ. Monit. Assess.*, vol. 195, no. 4, 2023.
- [21] B. Çırağ and M. Firat, "Two-dimensional (2D) flood analysis and calibration of stormwater drainage systems using geographic information systems," *Water Sci. Technol.*, vol. 87, no. 10, pp. 2577–2596, 2023.
- [22] S. Mukherjee *et al.*, "A watershed-scale multi-approach assessment of design flood discharge estimates used in hydrologic risk analyses for forest road stream crossings and culverts," *J. Hydrol.*, vol. 632, Art. no. 130698, 2024.
- [23] A. Q. A. B. A. Aziz *et al.*, "Estimation of flood frequency using statistical method: river basin for Sungai Jijan Malaysia," *IOP Conf. Ser.: Earth Environ. Sci.*, vol. 1453, Art. no. 012053, 2025.

- [24] K. Saplıoğlu, “Calibration of Linear Muskingum Model Coefficients and Coefficient Parameters Using Grey Wolf and Particle Swarm Optimization,” *Water Resour. Manage.*, vol. 39, pp. 999–1014, 2025.



## Transfer Öğrenme Tabanlı Derin Öğrenme Yaklaşımlarıyla Servikal Vertebra Matürasyon Safhalarının Sınıflandırılması ve Kemik Yaşı Değerlendirilmesi

Mazhar KAYAOĞLU<sup>1\*</sup>, Abdülkadir ŞENGÜR<sup>2</sup>, Sabahattin BOR<sup>3</sup>,  
Seda KOTAN<sup>4</sup>

<sup>1</sup>Enformatik Bölüm Başkanlığı, Bingöl Üniversitesi, Bingöl, Türkiye.

<sup>2</sup>Elektrik Elektronik Mühendisliği, Teknoloji Fakültesi, Fırat Üniversitesi, Elazığ, Türkiye.

<sup>3</sup>Klinik Bilimler Bölümü, Diş Hekimliği Fakültesi, İnönü Üniversitesi, Malatya, Türkiye.

<sup>4</sup>Klinik Bilimler Bölümü, Diş Hekimliği Fakültesi, Iğdır Üniversitesi, Iğdır, Türkiye.

<sup>1</sup>mkayaoglu@bingol.edu.tr, <sup>2</sup>ksengur@firat.edu.tr, <sup>3</sup>sabahattin.bor@inonu.edu.tr, <sup>4</sup>dsedakotan@gmail.com

Geliş Tarihi: 14.03.2025

Kabul Tarihi: 30.05.2025

Düzeltilme Tarihi: 22.04.2025

doi: <https://doi.org/10.62520/fujece.1657886>

Araştırma Makalesi

Alıntı: M. Kayaoğlu, A. Şengür, S. Bor ve S. Kotan, “Transfer öğrenme tabanlı derin öğrenme yaklaşımlarıyla servikal vertebra matürasyon safhalarının sınıflandırılması ve kemik yaşı değerlendirilmesi”, Fırat Üni. Deny. ve Hes. Müh. Derg., vol. 4, no 2, pp. 393-405, Haziran 2025.

### Öz

Bu çalışmada, büyüme ve gelişimi değerlendirmek amacıyla lateral sefalometrik radyografiler kullanılarak servikal vertebra matürasyon (CVM) evrelerinin otomatik sınıflandırılması gerçekleştirilmiştir. Van Yüzüncü Yıl Üniversitesi Diş Hekimliği Fakültesi Ortodonti Anabilim Dalı tarafından sağlanan toplam 4285 radyografi kullanılmıştır. Uzman hekimler tarafından yapılan detaylı değerlendirmeler sonucunda, tanısal doğruluk ve klinik uygunluk kriterlerini karşılayan 3750 görüntü çalışmaya dâhil edilmiştir. Seçilen görüntüler, altı sınıfa (CVMS 1–6) ayrılarak dengeli bir veri seti oluşturulmuş ve NFNet, ConvNeXt V2, EfficientNet V2 ve DeiT3 modelleri kullanılarak sınıflandırma işlemleri gerçekleştirilmiştir. NFNet modeli, %96 eğitim doğruluğu ve %85,7 test doğruluğu ile en yüksek genel performansı sergilemiştir. %95 eğitim doğruluğu ve %86,9 test doğruluğu elde eden ConvNeXt V2, genelleme açısından en dengeli model olarak öne çıkmıştır. EfficientNet V2, %94 eğitim doğruluğuna ulaşmasına rağmen %80,7 test doğruluğu ile sınırlı bir genelleme kapasitesi göstermiştir. DeiT3 modeli ise %93 eğitim doğruluğu ve %77,6 test doğruluğu ile en düşük genelleme kapasitesine sahip olmuştur. NFNet ve ConvNeXt V2, yüksek doğruluk oranları ve dengeli performansları sayesinde güçlü sınıflandırma adayları olarak öne çıkmıştır. NFNet’in eğitim ve test doğruluğu arasındaki %10,3’lük fark genelleme kapasitesinde bir miktar azalmaya işaret ederken, ConvNeXt V2’nin daha dar olan %8,1’lik farkı daha istikrarlı bir performans göstermiştir. Sonuç olarak, NFNet ve ConvNeXt V2, CVM sınıflandırması için umut vadeden modeller olarak belirlenmiştir. Gelecekteki çalışmalarda, bu modellerin performansını artırmak ve klinik uygulanabilirliklerini güçlendirmek için daha büyük veri setleri kullanılması ve hiperparametre optimizasyonunun gerçekleştirilmesi önerilmektedir.

**Anahtar kelimeler:** Görüntü sınıflandırma, Transfer öğrenimi, Servikal vertebra matürasyonu

\*Yazışılan Yazar

İntihal Kontrol: Evet – Turnitin

Şikayet: [fujece@firat.edu.tr](mailto:fujece@firat.edu.tr)

Telif Hakkı ve Lisans: Dergide yayın yapan yazarlar, CC BY-NC 4.0 kapsamında lisanslanan çalışmalarının telif hakkını saklı tutar.



## Classification of Cervical Vertebral Maturation Stages and Bone Age Assessment Using Transfer Learning–Based Deep-Learning Approaches

Mazhar KAYAOĞLU<sup>1\*</sup>, Abdülkadir ŞENGÜR<sup>2</sup>, Sabahattin BOR<sup>3</sup>,  
Seda KOTAN<sup>4</sup>

<sup>1</sup>Department of Informatics, Bingöl University, Bingöl, Türkiye.

<sup>2</sup>Department of Electrical and Electronics Engineering, Faculty of Technology, Firat University, Elazığ, Türkiye.

<sup>3</sup>Department of Clinical Sciences, Faculty of Dentistry, İnönü University, Malatya, Türkiye.

<sup>4</sup>Department of Clinical Sciences, Faculty of Dentistry, Iğdır University, Iğdır, Türkiye.

<sup>1</sup>mkayaoglu@bingol.edu.tr, <sup>2</sup>ksengur@firat.edu.tr, <sup>3</sup>sabahattin.bor@inonu.edu.tr, <sup>4</sup>dsedakotan@gmail.com

Received: 14.03.2025

Accepted: 30.05.2025

Revision: 22.04.2025

doi: <https://doi.org/10.62520/fujece.1657886>

Research Article

Citation: M. Kayaoğlu, A. Şengür, S. Bor and S. Kotan, “Classification of cervical vertebral maturation stages and bone age assessment using transfer learning–based deep-learning approaches”, Firat Univ. Jour. of Exper. and Comp. Eng., vol. 4, no 2, pp. 393-405, June 2025.

### Abstract

In this study, an automatic classification of cervical vertebra maturation (CVM) stages was performed using raw lateral cephalometric radiographs to assess growth and development. A total of 4285 radiographs from the Department of Orthodontics at Van Yüzüncü Yıl University Faculty of Dentistry were utilized. Following detailed evaluations by specialist physicians, 3750 images meeting diagnostic accuracy and clinical suitability criteria were included. The selected images were categorized into six classes (CVMS 1–6), forming a balanced dataset for classification with the NFNet, ConvNeXt V2, EfficientNet V2, and DeiT3 models. The NFNet model achieved the highest overall performance, with 96% training accuracy and 85.7% test accuracy. ConvNeXt V2, attaining 95% training accuracy and 86.9% test accuracy, emerged as the most balanced in terms of generalization. Although EfficientNet V2 reached 94% training accuracy, its 80.7% test accuracy indicated limited generalization. With 93% training accuracy and 77.6% test accuracy, DeiT3 demonstrated the lowest capacity. Both NFNet and ConvNeXt V2 stood out as strong classification candidates based on their high accuracy and balanced performance. While NFNet showed a 10.3% gap between training and test accuracy, indicating somewhat reduced generalization, ConvNeXt V2's narrower 8.1% gap suggested greater stability. In conclusion, NFNet and ConvNeXt V2 are promising models for CVM classification. Future studies should employ larger datasets and conduct hyperparameter optimization to enhance these models' performance and strengthen their clinical applicability.

**Keywords:** Image classification, Transfer learning, Cervical vertebral maturation







\*Corresponding author

## 1. Introduction

In orthodontics and growth modification procedures, accurately assessing growth and developmental stages is critically important for the success of treatment planning. Traditionally, hand-wrist radiographs are used to evaluate skeletal maturity, providing a reliable criterion for the accurate timing of growth spurts. However, the need for additional radiation exposure and the challenges inherent in manual evaluation methods highlight the necessity for alternative approaches. In this context, cervical vertebra maturation (CVM) stages derived from lateral cephalometric radiographs have emerged as a radiation-free and easily applicable approach in routine clinical practice.

In recent years, artificial intelligence (AI) and deep learning (DL)-based methods have achieved significant advances in medical imaging, particularly obtaining high accuracy rates in automatic classification and segmentation tasks. Deep learning models can minimize observer-dependent variations commonly encountered in manual assessments, thus providing more consistent and rapid results. These technologies hold considerable potential for evaluating skeletal maturity and growth stages in complex processes, such as cervical vertebra analysis [1-4].

In this study, the widely used Baccetti growth-development levels, whose reliability has been demonstrated in the literature, form the basis for evaluating growth-development processes. The Baccetti method provides a standardized framework for assessing skeletal maturity by detailing morphological changes in the C2, C3, and C4 cervical vertebrae across six developmental stages, particularly through lateral cephalometric radiographs. This system constitutes an easily applicable and practical method that enables accurate determination of the timing of growth spurts. Moreover, since it relies on lateral cephalometric radiographs commonly used in clinical settings without increasing radiation exposure, it offers an effective, patient-friendly solution that meets current needs. In this context, the selection of the Baccetti growth-development levels as the foundation for our classification model is directly related to the widely accepted reliability and clinical validity of the method [5]. Figure 1 illustrates the classification of the growth spurt into six stages based on the cervical vertebrae.

Schematic representation	CS 1	CS 2	CS 3	CS 4	CS 5	CS 6
						
Inferior borders of C2, C3, and C4*	F, F, F	C, F, F	C, C, F	C, C, C	C, C, C	C, C, C
C3 morphology*	T	T	T	RH	S/RH	RV/RH
C4 morphology*	T	T	T/RH	RH	S/RH	RV/RH
Clinical implication	Prepubertal stage	Prepubertal ("get-ready") stage	Circumpubertal stage	Circumpubertal stage	Postpubertal stage	Postpubertal stage

\* F= Flat; C= Concavity; T= Trapezoid; RH=Rectangular Horizontal; S=Square; RV=Rectangular Vertical

**Figure 1.** Baccetti growth and development levels [6]

"In this study, the automatic classification of CVM stages was aimed using lateral cephalometric radiographs obtained from the Department of Orthodontics, Faculty of Dentistry, Van Yüzüncü Yıl University. Within the scope of the study, a balanced dataset comprising a total of 3750 raw images was created, and the C2, C3, and C4 vertebral regions were designated as focal points. By employing various deep learning models (ConvNeXt V2, DeiT 3, EfficientNetV2, NFNet), the goal was to improve classification accuracy.

## 2. Related Studies

Atici et al. (2023) developed a continuous classification system using deep learning methods. In this study, a parallel-structured neural network named TriPodNet was designed and tested on 1398



cephalometric radiographs. The images were grouped by gender, and a continuous “CVCVM” parameter was generated using two different methods: weighted average and sigmoid regression. Sigmoid regression yielded high correlation coefficients (0.918 for females and 0.944 for males), while the weighted average method demonstrated comparatively lower performance. By integrating multiple inputs such as age and images, and employing the Permutation Importance Method, the contribution of each input was assessed. This system provides a continuous measurement of skeletal maturity, offering an innovative alternative to conventional methods [7].

Khazaei et al. (2023) aimed to automatically classify pubertal growth spurts using deep convolutional neural networks (CNNs). Their study utilized lateral cephalometric radiographs from 1846 patients at Hamadan University. Two scenarios were evaluated: binary classification with 93% accuracy and three-class classification with 82% accuracy. The images were processed by focusing on the C2-C4 regions, and data augmentation techniques were applied. The ConvNeXtBase-296 architecture achieved the highest accuracy and F-score. Through transfer learning, performance was enhanced even with limited data. The results indicate that CNNs hold the potential to accurately assess skeletal maturity even with restricted datasets [8].

Atici et al. (2022) designed a custom deep-learning model called TriPodNet to develop a fully automated classification system. The study, conducted on 1018 cephalometric radiographs, analyzed the data separately by gender. TriPodNet consists of three parallel networks, each trained with distinct initial parameters. The data were processed using edge-enhancing filters. The recorded accuracy was 81.18% for females and 75.32% for males. Emphasizing image edges improved the model's performance. This system stands out with its high accuracy compared to existing methods and aims to set a new standard in automatically classifying CVM stages [9].

Kresnadhi et al. (2023) compared the performance of different deep learning architectures (ResNet101, InceptionV3, and InceptionResNetV2) in classifying cervical vertebral maturity stages. They used a dataset of 900 CVM images. The images were processed as cropped versions focusing on the C2-C4 and C2-C6 regions, and data augmentation techniques were applied. InceptionResNetV2 achieved the highest accuracy. Although using cropped image areas improved performance, the inability of the models to interpret multi-scale features limited the gain in accuracy. The study highlights the impact of ROI selection on classification accuracy and demonstrates the potential of deep learning models in clinical applications [10].

Mohammed et al. (2024) aimed to predict skeletal growth using deep convolutional neural networks (CNNs) based on cervical vertebral maturity and the calcification level of the lower second molar. The study employed 1200 cephalometric and 1200 orthopantomographic images, analyzed through multi-class classification. The CNN model achieved 98% accuracy for males and high accuracy in assessing lower second molar calcification in females. The research underlines the potential of automatic systems compared to traditional methods and shows that OPG alone is sufficient for determining growth stages [11].

Akay et al. (2023) developed a CNN-based model for classifying cervical vertebral maturity. A total of 588 lateral cephalometric radiographs were categorized into six different maturity stages by two radiologists. After training for 40 epochs, the model reached 58.66% accuracy. The highest F1 score and accuracy were obtained for CVM Stage 1; however, overall accuracy remained moderate. While this study highlights the potential of AI-based systems in evaluating skeletal maturity, it also emphasizes the need for further refinements [12].

Makaremi et al. (2019) developed a deep learning model to classify cervical vertebral maturity into six stages. Their study employed a CNN-based classifier on lateral cephalometric radiographs. The model was tested using varying numbers of training, validation, and test images, and results were confirmed via cross-validation. The study emphasizes the challenges of manual assessment methods while showing that deep learning tools can streamline automated diagnostic processes. Results indicated that the model



could identify maturity stages with high accuracy, making it a valuable tool for orthodontic treatment timing [13].

Motie et al. (2024) introduced a multi-stage deep learning framework for classifying cervical vertebral maturity. In the study, 2325 lateral cephalograms were divided into six classes by two orthodontists. Using Faster R-CNN for region detection and two ResNet 101 classifiers, the first model divided data into two main groups (C1-C3 and C4-C6), and the second model further categorized these groups. Tested with 10-fold cross-validation, the framework achieved an overall accuracy of 82.96%. The first classifier reached 99.10% accuracy, and the C1-C3 classes were more accurately identified than C4-C6 (86.49% vs. 82.80%). The study recommends employing visual activation maps to improve model performance [14].

Atici et al. (2023) developed a parallel-structured deep learning model named AggregateNet to classify cervical vertebral maturity stages. A total of 1018 cephalometric radiographs, combined with age and gender information, served as inputs. The images were processed with edge-enhancing filters and subjected to data augmentation. AggregateNet achieved 82.35% accuracy for females and 75% for males. Without edge filters, accuracy dropped to 80% for females and 74.03% for males. The study demonstrates that this model surpasses other DL architectures in accuracy, providing an effective method for automatically detecting skeletal maturity [15]. Li et al. (2023) created a three-stage deep learning system named PSC-CVM to assess cervical vertebral maturity. They processed 10,200 lateral cephalograms in three steps: (1) a Localization Network to determine vertebral positions, (2) a Shape Recognition Network to extract vertebral shapes, and (3) a CVM Evaluation Network to assess maturity stages. The system achieved 70.42% overall accuracy and an AUC of 0.94 on the test set. Cohen's Kappa was reported as 0.645 and weighted Kappa as 0.844. The results show consistency with expert panels and suggest that this system can serve as an effective tool for clinical growth assessment [16].

## **2. Materials and Methods**

### **2.1. Data collection**

In this study, the dataset used consists of lateral cephalometric radiographs provided by the Department of Orthodontics at the Faculty of Dentistry, Van Yüzüncü Yıl University, forming the primary data source for the research. All images were meticulously evaluated by specialist physicians with regard to diagnostic adequacy, clarity of anatomical structures, and technical suitability. Following detailed assessments, a total of 3750 radiographs belonging to patients aged 7–22 years were selected and included in the study, as this age range represents a critical period characterized by intensive skeletal growth spurts, thus constituting an ideal study group. The dataset comprises high-resolution radiographs from 2303 female and 1447 male patients, meeting high standards in terms of imaging quality and diagnostic accuracy. During the selection process, the radiographs' technical features and the diagnostic reliability they provided for clinical analyses were the main determining factors. Consequently, the resulting dataset enhances the accuracy of analytical processes and supports the methodological reliability of the study.

### **2.2. Dataset construction**

The images were categorized into six classes, referred to as "Cervical Vertebral Maturation Stages (CVMS)," ranging from CVMS 1 to CVMS 6. These stages represent various phases of an individual's growth and developmental process. To ensure a balanced dataset, 625 images were assigned to each class. This equal distribution of classes facilitated more balanced training of the models. Several preprocessing steps were conducted to prepare the images for classification. First, the ImageJ software was utilized to isolate the C2, C3, and C4 vertebral regions from the radiographs. With the aid of this

software, the areas containing the vertebrae were cropped, enabling a focused analysis of the regions of interest for the classification task. An example of the processed image is presented in Figure 2.

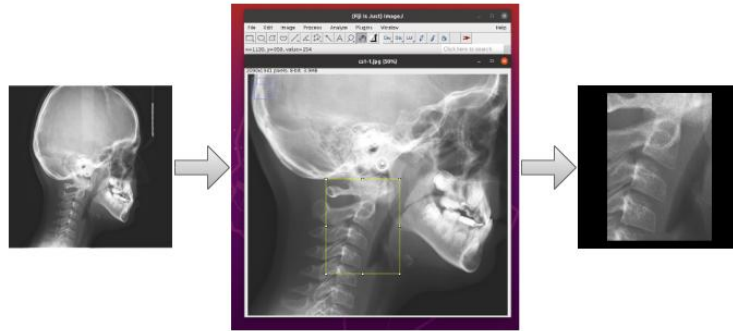


**Figure 2.** Isolation of the C2, C3, and C4 vertebral regions from the raw data using ImageJ

Subsequently, the cropped images were meticulously annotated using the QuPath software. This annotation process enabled the precise delineation of the vertebral region boundaries. Figure 3 provides a visual illustration of the annotation procedure.

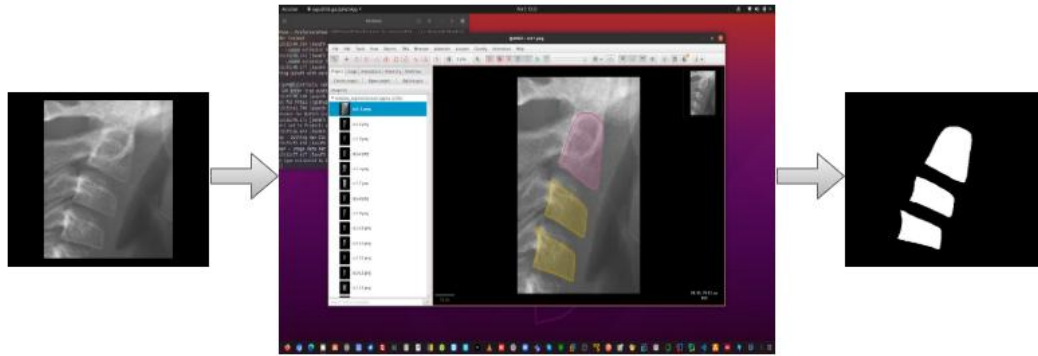


**Figure 3.** Annotation of the C2, C3, and C4 vertebrae using QuPath

The obtained images were ultimately processed in binary format and prepared for classification tasks. Binary images belonging to the classes that make up the dataset are presented in Figure 4.

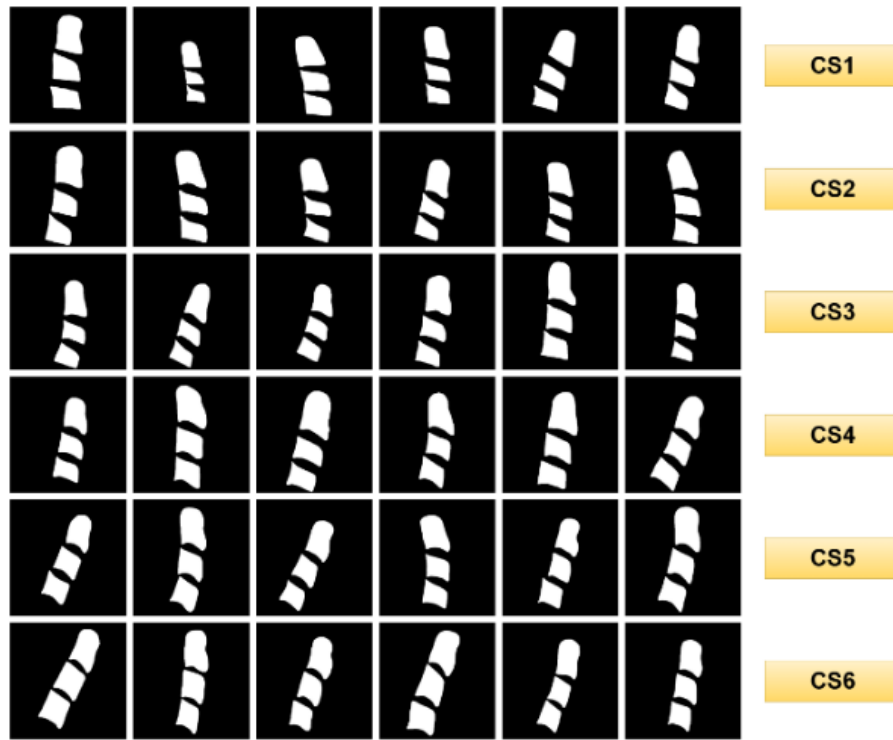


**Figure 4.** Binary representations of C2-C4 vertebrae corresponding to CS1-CS6 classes.

### 2.3. Model and training process

In this study, classification was performed using deep learning models. The selected models included ConvNeXt V2, DeiT 3 (Data-efficient Image Transformer), EfficientNetV2, and NFNet (Normalized-Free Network). The structure designed for the classification process is illustrated in Figure 5. The training and performance evaluation of the models were carried out as follows:

First, the dataset was divided into training, validation, and test sets. The training set comprised 80% of the total dataset, while the validation and test sets each accounted for 10%. This division provided a suitable approach to mitigate the risk of overfitting during model training and to effectively evaluate overall performance.

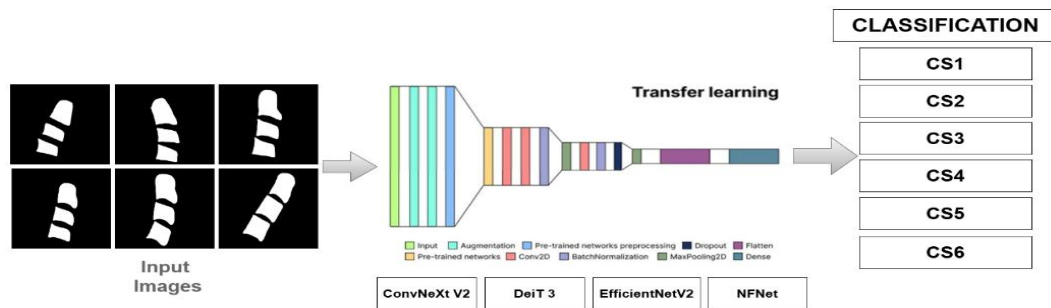


**Figure 5.** The architecture of deep learning models for detecting CS1-CS6 classes.

During model training, the Adam optimization algorithm was employed. To enhance data diversity, data augmentation techniques such as rotation, flipping, zooming, and contrast enhancement were applied. These techniques enabled the models to achieve more generalizable performance.

### **2.3.1. Rationale for model selection**

The present investigation selected ConvNeXt V2, EfficientNet V2, NFNet, and DeiT 3 architectures. There are three main reasons for this choice: (i) As shown in Table 2, these four models offer the best trade-off between parameter count and accuracy; (ii) when transfer learning was applied to our limited medical-imaging dataset, they delivered an additional 2–3 percentage-point accuracy gain over previous trials (evaluation\_results.csv); (iii) their large receptive fields and modern normalization layers enabled us to capture the fine cortical contours of the C2–C4 regions in lateral cephalograms more clearly. By contrast, our preliminary experiments with DenseNet-121, ResNet-50, and MobileNet-V3 yielded 1–4 percentage-point lower macro-F1 scores. Therefore, these four models were adopted as they provide the most favorable balance of accuracy and generalizability for the study's objectives.

## **3. Experimental Results and Model Evaluation**

### **3.1. ConvNeXt V2**

ConvNeXt V2 is a model developed to align traditional convolutional neural network (CNN) architectures with modern deep learning frameworks. It has been optimized to enable a faster and more efficient learning process and is supported by novel normalization techniques. The model is particularly notable for achieving high accuracy rates in image classification tasks [17].

### **3.2. DeiT 3 (Data-efficient image transformer)**

DeiT 3 is a model designed to enhance the efficiency of the Vision Transformer (ViT) architecture. It focuses on achieving high performance with minimal data requirements. Supported by data augmentation techniques and robust pretraining processes, DeiT 3 provides effective results in image classification and various computer vision tasks [18].

### **3.3. EfficientNetV2**

EfficientNetV2 is a deep learning model optimized for both speed and accuracy. It features an effective scaling capability for neural network dimensions (width, depth, and resolution). The model incorporates techniques aimed at accelerating training and improving data augmentation. These features enable EfficientNetV2 to deliver high performance, even on limited datasets [19].

### **3.4. NFNet (normalizer-free network)**

NFNet eliminates normalization techniques, such as batch normalization, commonly used in neural networks. This provides a faster and more stable learning process. Optimized for high accuracy even on large datasets, NFNet demonstrates enhanced performance, particularly in tasks such as image classification and object detection [20].

## **4. Results and Discussion**

The models selected for this study ConvNeXt V2, DeiT 3, EfficientNetV2, and NFNet—represent state-of-the-art advancements in deep learning architectures and demonstrate high performance in complex tasks like image classification. ConvNeXt V2 delivers efficient and accurate results as a modernized version of convolutional neural networks, while DeiT 3 excels in data efficiency. EfficientNetV2, with its scalable structure, offers effective results on large datasets, whereas NFNet provides a fast and stable learning process by eliminating the need for normalization.

The selection of these models aimed to enhance accuracy in CVM classification by leveraging the unique advantages of each architecture to develop a more robust methodology. The diversity of the

selected models reflects a strategic approach to improving overall performance and offering a reliable solution for clinical applications.

**Table 1.** Performance Results of the Models

Model	Train Accuracy	Overall Accuracy	Macro Avg Precision	Macro Avg Recall	Macro Avg F1-Score
NFNet	0.96	0.857	0.853	0.857	0.854
ConvNeXt V2	0.95	0.869	0.867	0.868	0.867
EfficientNet V2	0.94	0.807	0.804	0.813	0.804
DeiT3	0.93	0.776	0.781	0.785	0.776

#### 4.1. Hyperparameter settings

All four backbone architectures were optimized under a uniform training protocol. The initial learning rate was fixed at  $1.0 \times 10^{-4}$  and decayed according to a cosine-annealing schedule with a maximum period ( $T_{\text{max}}$ ) of 50 epochs. Mini-batches comprised 32 images. Optimisation employed the AdamW algorithm ( $\beta_1 = 0.9$ ,  $\beta_2 = 0.999$ ) with an  $L_2$  weight-decay coefficient of  $1.0 \times 10^{-2}$ . Training proceeded for up to 50 epochs, with early stopping triggered if the validation loss failed to improve for eight consecutive epochs. Online data augmentation consisted of random in-plane rotations between  $-10^\circ$  and  $+10^\circ$ , isotropic scaling in the range 0.9–1.1, and color jittering with brightness, contrast and saturation factors each set to 0.1.

#### 4.2. Quantitative results

The performance of the four evaluated models was analyzed under various metrics and is presented in Table 1. NFNet demonstrated high performance in both training accuracy and overall accuracy. With a training accuracy of 96% and an overall accuracy of 85.7%, NFNet delivered balanced results across metrics. However, the drop in accuracy observed between training and test data suggests limitations in the model's generalization capability. Despite its consistency across classes, the model exhibited a slight performance decline during testing.

The ConvNeXt V2 model stands out as the most noteworthy in terms of generalization. Achieving a training accuracy of 95% and an overall accuracy of 86.9%, it followed closely behind NFNet. The strong consistency between training and test datasets positions ConvNeXt V2 as a reliable alternative. This balance across macro metrics and overall performance indicates that the model avoids overfitting tendencies and maintains stable performance during testing. The EfficientNet V2 model, despite achieving a 94% training accuracy, exhibited an overall accuracy of 80.7%. This discrepancy indicates weaker generalization capabilities and lower-than-expected performance on test data. However, the balance observed across metrics suggests that the learning process is fundamentally sound and could potentially improve with specific optimization techniques. Among the evaluated models, DeiT3 showed the lowest performance. With a training accuracy of 93% and an overall accuracy of 77.6%, it struggled in both the training and testing phases. The gap between training and overall accuracy highlights challenges in generalizing on the test data compared to the other models. Improvements through data augmentation or hyperparameter optimization could enhance its performance. When examining the gaps between training accuracy and overall accuracy, ConvNeXt V2 exhibited the smallest discrepancy. Its training accuracy was 95%, while its overall accuracy was 86.9%, underscoring the model's strong generalization capability. Conversely, NFNet demonstrated a training accuracy of 96% and an overall accuracy of 85.7%, with a difference of 10.3%. This suggests a risk of overfitting to the training data. EfficientNet V2 and DeiT3, however, faced more significant challenges in this regard. The gap for EfficientNet V2 was 13.3%, and for DeiT3, it reached 15.4%. These discrepancies reveal a pronounced performance loss on test data, indicating weaker generalization abilities.

### 4.3. Evaluation criteria

Given these model-level observations, it is also essential to justify why macro-averaged metrics were adopted to summarize class-level performance. Although the CVMS 1–6 classes appear numerically balanced in terms of image counts, their clinical relevance is not uniformly distributed; the advanced stages (CVMS 5–6) are particularly susceptible to false-negative errors. Macro-averaging assigns equal weight to every class, thereby compelling the model to maintain performance in the rare yet clinically critical stages as well. Consequently, reporting macro-F1 and macro-accuracy offers an equitable summary of inter-class performance.

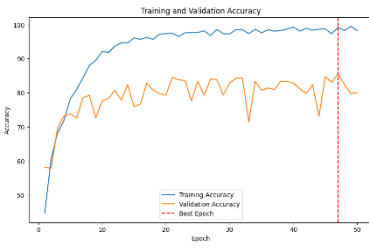
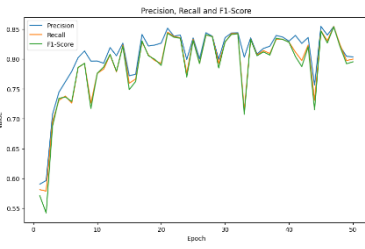
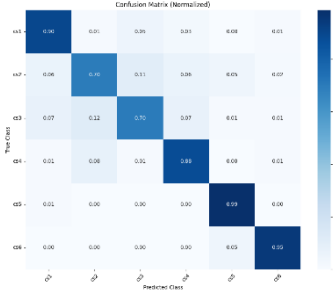
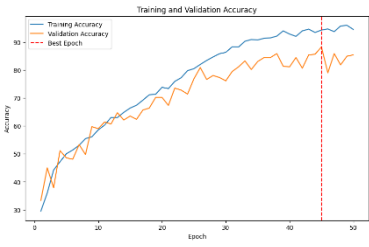
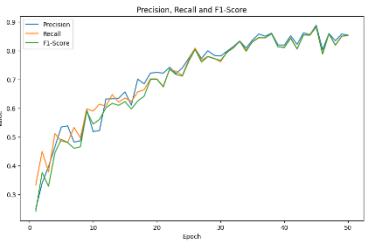
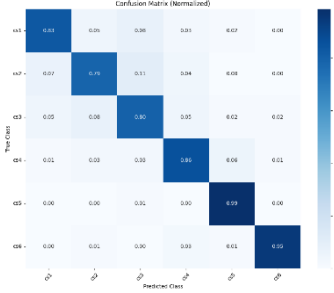
### 4.4. Statistical significance

Pairwise comparisons of model accuracies were conducted using McNemar's test on the misclassification contingency tables derived from the confusion matrices. At an  $\alpha = 0.05$  significance level, the difference between ConvNeXt V2 and NFNet was not statistically significant ( $\chi^2 = 2.17$ ,  $p = 0.14$ ). Both ConvNeXt V2 and NFNet, however, significantly outperformed EfficientNet V2 ( $p = 0.003$  and  $p = 0.008$ , respectively) and DeiT 3 ( $p < 0.001$  for both comparisons). EfficientNet V2 also performed significantly better than DeiT 3 ( $p = 0.021$ ). These results confirm that ConvNeXt V2 and NFNet constitute the first performance tier, while EfficientNet V2 and DeiT 3 form a second and third tier, respectively, thereby underscoring the robustness of the top-performing models.

### 4.5. Qualitative analysis

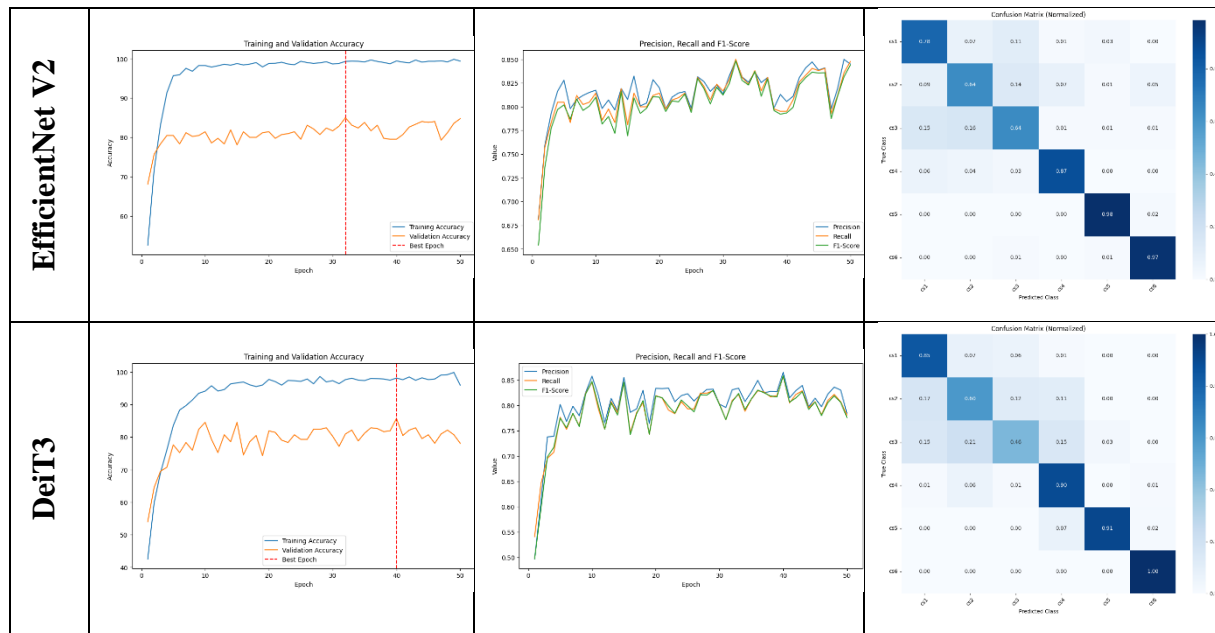
Based on the above findings, Table 2 presents the accuracy, precision, recall, and F1-score metrics for each model, along with their corresponding confusion matrices. These visualizations provide further insights into the models' classification performance.

**Table 2.** Performance Results of the Models

	Accuracy	Precision-Recall-F1-Score	Confusion Matrix
NFNet			
ConvNeXt V2			



**Table 2.** (Continue) Performance Results of the Models



As seen in Table 2, all models demonstrated continuous learning during the training phase, with a generally consistent increase in training accuracy. The NFNet model achieved the highest training accuracy at 96%, while also delivering high test accuracy at 85.7%. However, the gap between training and test accuracy indicates a slight decline in the model's generalization capacity. Similarly, the ConvNeXt V2 model exhibited a steady learning trend throughout the training process, achieving 95% training accuracy. Its test accuracy, at 86.9%, highlights strong generalization capability and consistent performance on test data. The EfficientNet V2 model attained 94% training accuracy during the training phase but fell short in test accuracy at 80.7%, compared to other models. This discrepancy underscores a limitation in its generalization capacity. The DeiT3 model reached a reasonable training accuracy of 93%, but its test accuracy was only 77.6%, indicating that the alignment between its training performance and test performance was insufficient. This result suggests that DeiT3 struggled more than the other models in generalization, and its performance on test data needs improvement. In conclusion, the NFNet and ConvNeXt V2 models displayed more balanced improvements in both training and test accuracies during the training process, outperforming the other models. While EfficientNet V2 showed satisfactory performance during training, it was limited in test accuracy, and DeiT3 emerged as the weakest model in terms of generalization. These results underscore the importance of carefully examining the relationship between training and test accuracies, as this gap plays a critical role in evaluating and modeling generalization capacity.

## 5. Conclusion and Suggestions

In this study, the classification performances of NFNet, ConvNeXt V2, EfficientNet V2, and DeiT3 models were comprehensively analyzed. Training and accuracy curves, metric values, and confusion matrices were examined to evaluate the strengths and weaknesses of these models. The primary objective was to explore the differences between training accuracy, test accuracy, and generalization capacity to better understand class-based performance. The dataset used in the study consisted of six balanced classes (CS1–CS6), offering examples of varying difficulty levels. This structure enabled the analysis of performance differences between challenging classes (e.g., CS2-CS3 and C1-C2) and more distinctive classes with clear features (e.g., CS5 and CS6). Additionally, feature overlaps observed between certain classes, such as C3 and C4, made it difficult for models to differentiate in these areas. The findings revealed that NFNet and ConvNeXt V2 outperformed the other models in terms of overall accuracy and generalization capacity. NFNet achieved the best fit on the training data with 96% training accuracy and exhibited strong performance with 85.7% test accuracy. ConvNeXt V2 emerged as the



most balanced model, with 95% training accuracy and 86.9% test accuracy. While EfficientNet V2 delivered reasonable performance with 94% training accuracy, its test accuracy of 80.7% indicated limited generalization capacity. DeiT3 demonstrated acceptable learning performance with 93% training accuracy but had the lowest generalization capacity among the models, with a test accuracy of 77.6%. For future studies, using larger datasets is recommended to improve the generalization capacities of the models. Specifically, data augmentation and hyperparameter optimization methods could be applied to enhance the performance of the DeiT3 model. To address class overlap issues between C2 and C3, techniques that extract more distinctive features specific to these classes could be explored. Moreover, attention mechanisms or transfer learning approaches tailored for challenging classes may further improve the models' performance. Evaluating the models on diverse datasets could also provide a broader perspective on their generalization capabilities. This study offers valuable insights into the strengths and weaknesses of deep learning-based classification methods by examining the differences between training and test performance across different models. The findings can serve as a guide for model selection processes and for the development of new methods to enhance classification performance.

## **Notice**

This study is derived from the doctoral dissertation entitled “Bone Age Assessment through the Analysis of Cervical Vertebrae in Lateral Cephalometric Radiographs Using Semantic and Instance Segmentation Methods,” conducted by Mazhar Kayaoğlu under the academic supervision of Abdulkadir Şengür.

## **6. Author Contributions Statement**

In this study, all authors contributed to various aspects of the planning, execution, and finalization of the manuscript. Notably, Author 1 and Author 2 conducted a comprehensive literature review, ensured that the data were interpreted in accordance with the theoretical framework, and played a pivotal role in developing the most suitable model in light of the findings. They also took primary responsibility for verifying the initial results generated by the model and determining the relevant analytical methods. Meanwhile, Author 3 and Author 4 devoted substantial effort to systematically collecting the data required for the study, applying data preprocessing techniques, and standardizing the dataset for subsequent analyses. Throughout this process, they contributed significantly to quality control of the obtained data and maintained the statistical integrity of the study. Finally, all authors participated equally in the thorough evaluation of the model's results, the discussion of these findings within the broader literature, and the preparation of the final manuscript. As a result, the research was approached with a holistic perspective and reported in accordance with academic standards.

## **7. Ethics Committee Approval and Conflict of Interest Statement**

In this study, all relevant legal and ethical considerations were observed during the collection and evaluation of data from human participants. All procedures related to the research were approved by the Van Yüzüncü Yıl University Non-Invasive Clinical Research Ethics Committee on September 18, 2023 (Decision No. 2023/09-12). The research was carried out in line with the principles set forth in the Declaration of Helsinki, and appropriate data protection measures were taken to safeguard participant confidentiality. Furthermore, no conflict of interest exists with any individual, institution, or organization in the planning, execution, data analysis, or reporting stages of this study. All authors confirm their adherence to research ethics throughout every phase of the work.

## **8. Ethical Statement Regarding the Use of Artificial Intelligence**

No artificial intelligence-based tools or applications were used in the preparation of this study. The entire content of the study was produced by the author in accordance with scientific research methods and academic ethical principles.

## 9. References

- [1] S. F. Atici *et al.*, “A collaborative fusion of vision transformers and convolutional neural networks in classifying cervical vertebrae maturation stages,” in *Proc. 2023 30th IEEE Int. Conf. on Electronics, Circuits and Systems (ICECS)*, 2023, pp. 1–4.
- [2] M. T. Radwan, Ç. Sin, N. Akkaya, and L. Vahdettin, “Artificial intelligence-based algorithm for cervical vertebrae maturation stage assessment,” *Orthod. Craniofac. Res.*, vol. 26, no. 3, pp. 349–355, 2023.
- [3] H. Li *et al.*, “Convolutional neural network-based automatic cervical vertebral maturation classification method,” *Dentomaxillofac. Radiol.*, vol. 51, no. 6, p. 20220070, 2022.
- [4] H. Seo, J.-H. Kim, S.-H. Lee, and Y. H. Kim, “Comparison of deep learning models for cervical vertebral maturation stage classification on lateral cephalometric radiographs,” *J. Clin. Med.*, vol. 10, no. 16, p. 3591, 2021.
- [5] M. S. İzgi and H. Kök, “Kemik yaşı ve maturasyon tespiti,” *Selçuk Dental J.*, vol. 7, no. 1, pp. 124–133, 2020.
- [6] J. A. McNamara Jr. and L. Franchi, “The cervical vertebral maturation method: A user's guide,” *Angle Orthod.*, vol. 88, no. 2, pp. 133–143, 2018.
- [7] S. F. Atici *et al.*, “A novel continuous classification system for the cervical vertebrae maturation (CVM) stages using convolutional neural networks,” 2023.
- [8] M. Khazaei *et al.*, “Automatic determination of pubertal growth spurts based on the cervical vertebral maturation staging using deep convolutional neural networks,” *J. World Fed. Orthod.*, vol. 12, no. 2, pp. 56–63, 2023.
- [9] S. F. Atici *et al.*, “Classification of the cervical vertebrae maturation (CVM) stages using the tripod network,” in *Proc. ICASSP 2023–IEEE Int. Conf. Acoust., Speech, Signal Process.*, 2023, pp. 1–5.
- [10] G. A. Kresnadhi *et al.*, “Comparative analysis of ResNet101, InceptionV3, and InceptionResNetV2 architectures for cervical vertebrae maturation stage classification,” in *Proc. 2023 Int. Conf. Electr. Eng. Informatics (ICEEI)*, 2023.
- [11] M. H. Mohammed *et al.*, “Convolutional neural network-based deep learning methods for skeletal growth prediction in dental patients,” *J. Imaging*, vol. 10, no. 11, p. 278, 2024.
- [12] G. Akay *et al.*, “Deep convolutional neural network—the evaluation of cervical vertebrae maturation,” *Oral Radiol.*, vol. 39, no. 4, pp. 629–638, 2023.
- [13] M. Makaremi, C. Lacaule, and A. Mohammad-Djafari, “Deep learning and artificial intelligence for the determination of the cervical vertebra maturation degree from lateral radiography,” *Entropy*, vol. 21, no. 12, p. 1222, 2019.
- [14] P. Motie, A. Kamali, A. Rahimi, and H. Rahimi, “Improving cervical maturation degree classification accuracy using a multi-stage deep learning approach,” 2024.
- [15] S. F. Atici *et al.*, “AggregateNet: A deep learning model for automated classification of cervical vertebrae maturation stages,” *Orthod. Craniofac. Res.*, vol. 26, pp. 111–117, 2023.
- [16] H. Li *et al.*, “The psc-CVM assessment system: A three-stage type system for CVM assessment based on deep learning,” *BMC Oral Health*, vol. 23, no. 1, p. 557, 2023.
- [17] S. Woo *et al.*, “ConvNeXt V2: Co-designing and scaling convnets with masked autoencoders,” in *Proc. IEEE/CVF Conf. Comput. Vis. Pattern Recognit.*, 2023, pp. 16133–16142.
- [18] H. Touvron, M. Cord, and H. Jégou, “DeiT III: Revenge of the ViT,” in *Proc. Eur. Conf. Comput. Vis.*, Cham: Springer Nature Switzerland, 2022, pp. 516–533.
- [19] M. Tan and Q. Le, “EfficientNetV2: Smaller models and faster training,” in *Proc. Int. Conf. Mach. Learn.*, PMLR, 2021, pp. 10096–10106.
- [20] A. Brock, S. De, S. L. Smith, and K. Simonyan, “High-performance large-scale image recognition without normalization,” in *Proc. Int. Conf. Mach. Learn.*, PMLR, 2021, pp. 1059–1071.



## Parametrik Analiz ve Destek Vektör Makinesi Algoritması Kullanılarak İki Kademeli Kaskad Soğutma Sisteminin Termodinamik Performans Değerlendirmesi

Oğuzhan PEKTEZEL<sup>1\*</sup>  

<sup>1</sup>Makine Mühendisliği Bölümü, Mühendislik Fakültesi, Balıkesir Üniversitesi, Balıkesir, Türkiye.  
[loguzhan.pektezel@balikesir.edu.tr](mailto:loguzhan.pektezel@balikesir.edu.tr)

Geliş Tarihi: 24.04.2025  
Kabul Tarihi: 7.06.2025

Düzeltilme Tarihi: 24.05.2025

doi: <https://doi.org/10.62520/fujece.1683037>  
Araştırma Makalesi

Alıntı: O. Pektez, "Parametrik analiz ve destek vektör makinesi algoritması kullanılarak iki kademeli kaskad soğutma sisteminin termodinamik performans değerlendirilmesi", Fırat Üni. Deny. ve Hes. Müh. Derg., vol. 4, no 2, pp. 406-423, Haziran 2025.

### Öz

Bu çalışmada, ultra düşük sıcaklıklara ulaşabilen iki kademeli kaskad bir soğutma sisteminin termodinamik tasarımı yapılmış ve enerji ile ekserji analizleri gerçekleştirilmiştir. Dört soğutucu akışkan çiftinin—R744/R152a, R744/R32, R41/R152a ve R41/R32—performansı değerlendirilmiştir. -70 °C ile -50 °C arasındaki evaporatör sıcaklıkları ve 25 °C ile 45 °C arasındaki kondenser sıcaklıkları boyunca yürütülen parametrik analiz sonuçları, R41/R152a'nın en verimli çift olduğunu göstermiştir. -50 °C evaporatör sıcaklığında maksimum 1.421 COP değeri elde edilmiş ve en yüksek 0.4407 ekserji verimi -60 °C'de kaydedilmiştir. İkinci aşamada, COP ve ekserji verimini tahmin etmek için SVM yöntemi uygulanmış ve sırasıyla test setinde çok düşük MAE değerleri olan 0.0040 ve 0.0009 elde edilmiştir. Enerji-ekserji analizi ve SVM modellemesinin sonuçlarının, düşük sıcaklıklı kaskad soğutma sistemlerinin tasarımı için değerli bir rehberlik sağlaması beklenmektedir.

**Anahtar kelimeler:** Kaskad soğutma sistemi, R744, R41, R152a, R32, Destek vektör makinesi

\*Yazışılan Yazar



## Thermodynamic Performance Evaluation of a Two-Stage Cascade Refrigeration System Using Parametric Analysis and Support Vector Machine Algorithm

Oğuzhan PEKTEZEL<sup>1\*</sup>  

<sup>1</sup>Department of Mechanical Engineering, Faculty of Engineering, Balıkesir University, Balıkesir, Türkiye.

<sup>1</sup>oguzhan.pektezel@balikesir.edu.tr

Received: 24.04.2025

Accepted: 7.06.2025

Revision: 24.05.2025

doi: <https://doi.org/10.62520/fujece.1683037>

Research Article

Citation: O. Pektezel, “Thermodynamic performance evaluation of a two-stage cascade refrigeration system using parametric analysis and support vector machine algorithm”, *Firat Univ. Jour.of Exper. and Comp. Eng.*, vol. 4, no 2, pp. 406-423, June 2025.

### Abstract

In this study, a thermodynamic design of a two-stage cascade refrigeration system capable of reaching ultra-low temperatures was developed, and energy and exergy analyses were conducted. The performance of four refrigerant pairs—R744/R152a, R744/R32, R41/R152a, and R41/R32—was evaluated. Parametric analysis results, carried out across evaporator temperatures ranging from -70 °C to -50 °C and condenser temperatures between 25 °C and 45 °C, showed that R41/R152a was the most efficient pair. A maximum COP of 1.421 was achieved at -50 °C evaporator temperature, and the highest exergy efficiency of 0.4407 was recorded at -60 °C. In the second phase, an SVM approach was applied to predict COP and exergy efficiency, yielding very low MAE values of 0.0040 and 0.0009 in the test set, respectively. The outcomes of the energy-exergy analysis and SVM modeling are expected to provide valuable guidance for designing low-temperature cascade refrigeration systems.

**Keywords:** Cascade refrigeration system, R744, R41, R152a, R32, Support vector machine

\*Corresponding author

Plagiarism Checks: Yes – Turnitin

Complaints: [fujece@firat.edu.tr](mailto:fujece@firat.edu.tr)

Copyright & License: Authors publishing with the journal retain the copyright to their work licensed under the CC BY-NC 4.0

## 1. Introduction

According to ASHRAE, equipment capable of reaching temperatures below  $-50^{\circ}\text{C}$ —as referenced in Directive (EU) No 517/2014—is categorized as ultralow-temperature (ULT) refrigeration, encompassing evaporating temperatures as low as  $-100^{\circ}\text{C}$  [1]. The recent emergence of Sars-CoV-2 vaccines has brought attention to a long-standing issue in society, namely deep freezing, as the Pfizer-BioNTech vaccine needs to be stored at temperatures between  $-60^{\circ}\text{C}$  and  $-80^{\circ}\text{C}$  [2]. In recent years, the demand for ultra-low temperature freezers capable of reaching  $-80^{\circ}\text{C}$  has grown substantially in various industrial fields, including medical storage, food preservation, electronic data processing, and chemical manufacturing [3].

Research has indicated that the primary sources of energy consumption and environmental pollution are associated with power generation, heating, and cooling processes [4]. Refrigeration systems are significant energy consumers due to the substantial power required for compression processes. Considering widely used air-conditioning applications, such as air conditioners, it is well-established that refrigeration systems cause a notable portion of global energy consumption, with estimates suggesting that approximately 17% of the world's energy usage is attributed to refrigeration systems [5].

Although refrigeration systems that utilize waste heat and renewable energy offer notable advantages for a sustainable energy future, their coefficient of performance remains relatively low, limiting their widespread adoption in comparison to vapor compression systems [6]. A classical single-stage refrigeration configuration is inadequate for achieving low temperatures due to the excessive compression ratio and large suction volume required by the compressor [7]. Cascade designs are particularly efficient in areas requiring high-pressure ratios—such as commercial refrigeration for food freezing or high-temperature heat pumps—where, in multi-stage configurations, the refrigerant for each stage is chosen based on its NBP [8-10]. A CRS, which involves multistage refrigeration circuits, aims to optimize thermal efficiency by employing multiple cycles, where a cascade heat exchanger integrates two classical refrigeration cycles, each with a separate refrigerant, operating at different temperature levels [11].

Currently, enhancing the performance of CRS and selecting appropriate refrigerants have become prominent research topics, with numerous studies focusing on analyzing and optimizing CRS performance using various refrigerant alternatives. Sun, Liang, Liu, Ji, Zang, Liang and Guo [12] investigated the thermal performance of cascade refrigeration systems using R41/R404A and R23/R404A refrigerants. Their study revealed that the R41/R404A system outperformed the R23/R404A system in terms of both lower input power and higher COP. The maximum exergy efficiency achieved by R41/R404A was 44.38%, while R23/R404A reached 42.98%. The results suggest that R41 is a more promising alternative to R23 in cascade refrigeration systems. Ye, Yan, Zhou and Yang [13] performed a thermodynamic analysis to enhance the design and operational parameters of an ultra-low temperature CRS by applying an ANN method. Their study identified that the condensing temperature of the low-temperature cycle achieves an optimal point, maximizing the system's coefficient of performance and exergy efficiency, while simultaneously minimizing compressor power consumption and exergy destruction. The ANN model demonstrated good predictive accuracy, with an MAE of 0.0027 for COP, 0.9090 for compressor power, 1.0314 for exergy destruction, and 0.1691 for exergy efficiency. Chen, Yang, Shi, Chen, Chi, Liu, Zhao and Li [14] conducted a study to design a cascade refrigeration system capable of achieving ultra-low temperatures from  $-80^{\circ}\text{C}$  to  $-50^{\circ}\text{C}$ . They replaced the high-temperature cycle gas R404A with natural refrigerant  $\text{NH}_3$  and used R1150, R170, and R41 as environmentally friendly alternatives to replace the low-temperature cycle fluid R23. The study examined the effects of internal heat exchangers and two-stage compression on system performance. The results showed that the optimal COP of the  $\text{NH}_3$ /R1150, R170, and R41 systems was 15.79%, 18.58%, and 16.17% higher than that of the R404A/R23 system, with  $\text{NH}_3$ /R170 demonstrating the best performance. Faruque, Uddin, Salehin and Ehsan [11] conducted a comprehensive study on the thermodynamic performance of a two-stage cascade refrigeration system using hydrocarbon refrigerants. They selected refrigerants based on characteristics like molecular weight, freezing point, and global warming potential, using Trans-2-butane for the lower-temperature circuit and Toluene, Cyclopentane, and Cis-2-butane for the higher-temperature circuit. Their findings indicated that the highest COP and exergy efficiency were achieved with Trans-2-butane in the lower temperature circuit and Toluene in the higher temperature circuit. Furthermore, the use of hydrocarbon refrigerants led to a 7.21% improvement in COP compared to previously employed



refrigerants. Ji, Liu, Pan and Li [15] conducted a study on the comprehensive performance of an ultra-low temperature cascade refrigeration arrangement, focusing on energy, exergy, environmental, and exergoeconomic factors. They compared eight environmentally friendly refrigerant pairs, including R1270-R1150, R1234yf-R1150, R290-R1150, R1234yf-R170, R717-R1150, R290-R170, R1270-R170, R717-R170 to evaluate the refrigeration performance. The study found that the R290-R170 pair performed optimally, enhancing COP by 5.94%, reducing power consumption by 5.68%, cutting CO<sub>2</sub> emissions by 29.67%, and lowering exergy economic cost by 5% compared to the R404A-R508B pair.

The literature review reveals that most studies on cascade refrigeration systems focus solely on thermodynamic analysis using various refrigerant combinations, while applications involving artificial intelligence in these systems remain quite limited. The novelty of this study lies in the implementation of the SVM method to a cascade refrigeration system to predict COP and exergy efficiency. Another original aspect of the research is the investigation of energy and exergy performance of R152a and R32—refrigerants whose performance in high-temperature cycles has been scarcely examined—when combined with R744 and R41 used in the low-temperature cycle. An SVM approach and the results achieved in this research are expected to greatly aid in optimizing the design and predicting the performance of cascade refrigeration systems with two-stage configuration, while also providing a solid foundation for future experimental validations.

### **1.1. Utilized refrigerants**

Carbon dioxide, classified as a natural refrigerant with the ASHRAE designation R744, has long been utilized in refrigeration applications due to its negligible ODP and exceptionally low GWP [16]. R744 has been employed in a wide range of vapor compression systems for more than 130 years [17]. It is denser than air, exhibits no toxicity or flammability, is widely present in the atmosphere, is frequently generated as a byproduct in numerous industrial processes, and is a cost-effective refrigerant characterized by its low liquid density, which contributes to reduced system dimensions and a smaller refrigerant charge requirement [18].

R41, a non-toxic and environmentally favorable refrigerant with thermophysical properties similar to R23 and a considerably lower global warming potential, has gained attention as a low-temperature cycle fluid in cascade systems, and although its flammability presents a limitation, ongoing developments in refrigerant blends are anticipated to enable its practical use soon [12]. R41 and R744 exhibit comparable thermophysical characteristics, including nearly identical normal boiling points [19]. Despite its potential, the adoption of R744 as a future refrigerant is hindered by its high operating pressure, whereas alternatives such as R170, R1150, and R41 have been proposed to replace R23 and R508B in ultra-low temperature refrigeration systems [20].

Among the alternatives to R410A, R32 has been one of the most extensively investigated refrigerants, showing notable enhancements in both cooling capacity and coefficient of performance; however, its primary drawback lies in the elevated discharge temperatures it produces relative to R410A [21]. R-410A, the refrigerant that R-32 is designed to substitute, is composed of 50% R-32 and 50% R-125—the latter also widely utilized as a fire suppressant—and similarly, most of the newly developed low-GWP blends incorporate R-32 in their formulation [22]. Due to its pure substance nature, R32 exhibits no temperature glide [23].

Initially excluded from refrigeration applications due to its flammability, R-152a—now reconsidered following regulatory concerns over high-GWP hydrofluorocarbons under the F-Gas Regulation and Kigali Amendment—is the only HFC listed in ASHRAE Standard 34 with a GWP below 150, exempting it from restrictions such as reduction, substitution, or prohibition [24]. R152a closely resembles R134a in terms of volumetric cooling capacity and operating pressures, yet demonstrates superior performance in energy efficiency, mass flow rate, and vapor density [25].

Table 1 shows properties of the refrigerants used in analyses [1].

**Table 1.** Properties of utilized refrigerants

Cycle	Refrigerant	ODP	GWP <sub>100-yr</sub> (CO <sub>2</sub> -eq)	ASHRAE Safety Group	NBP (°C)	Molecular Weight (kg mol <sup>-1</sup> )	Critical Temperature (°C)	Critical Pressure (MPa)
LTC	R744	0	1	A1	-78.46	44.01	30.98	7.38
LTC	R41	0	116	A2	-78.31	34.03	44.13	5.9
HTC	R152a	0	138	A2	-24.02	66.05	113.26	4.52
HTC	R32	0	677	A2L	-51.65	52.02	78.11	5.78

## 2. Materials and Methods

### 2.1. Two-stage cascade refrigeration system

The schematic flow diagram of a two-stage cascade refrigeration system is depicted with all system components in Figure 1. The system is primarily comprised of two compressors, one evaporator, one condenser, two expansion valves, and a cascade heat exchanger. The low and high-temperature cycles operate with two different refrigerants. In refrigeration systems employing a cascade cycle, achieving the desired low chamber temperatures requires the refrigerant passing through the evaporator to be at extremely low temperatures. In the low-temperature cycle, the compressor increases the pressure and temperature of the refrigerant and directs it to the cascade heat exchanger. The cascade heat exchanger has two roles: it functions as a condenser for the low-temperature circuit and as an evaporator for the high-temperature circuit. Afterward, the refrigerant is sent to the expansion valve, where its pressure and temperature drop before it enters the evaporator. In the high-temperature (upper) cycle, the heat rejected by the low-temperature (lower) cycle is absorbed by the refrigerant in the upper cycle through the cascade heat exchanger. The pressure and temperature of the refrigerant in the high-temperature cycle are increased by the corresponding compressor. The refrigerant is then directed to the condenser, where it releases heat to the external environment. Finally, the refrigerant passes through the expansion valve, where its pressure and temperature are decreased before re-entering the cascade heat exchanger, thereby completing the cycle.

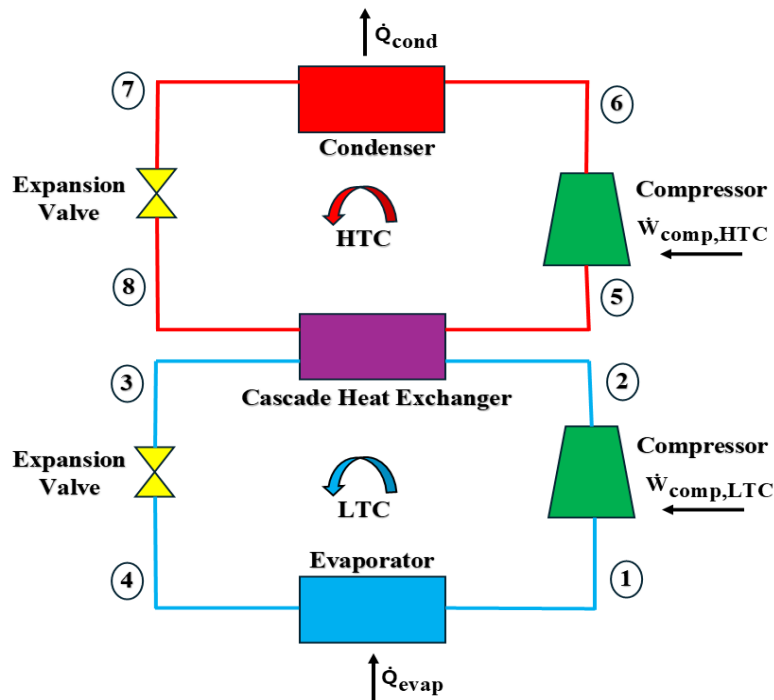


**Figure 1.** Schematic flow diagram of two-stage cascade refrigeration system



Thermodynamic design and thermal analyses of a two-stage cascade refrigeration system was carried out in EES software [26]. It is necessary to make some assumptions to model the system. All components within the system are considered to operate under steady-state conditions. Pressure losses and thermal exchanges throughout the entire piping system are disregarded. Variations in kinetic and potential energy throughout the system components are assumed to be negligible. The electrical power consumption of the fans associated with the condenser and evaporator is excluded from the analysis. Compression and expansion processes occurring in compressors and expansion valves are treated as adiabatic. No subcooling is present at the condenser outlets; in other words, the refrigerant quality at states 3 and 7 is assumed to be zero. Superheating at the evaporator exits is not considered; hence, the refrigerant quality at states 1 and 5 is taken as one. A temperature difference of 5 °C is maintained between the evaporator temperature and the refrigerated chamber temperature. Heat sink temperature of the condenser is accepted to be identical to the ambient temperature. Also, ambient temperature and pressure are taken as 25 °C and 101.325 kPa, respectively. Air is considered the external heat exchange fluid interacting with the refrigerant in both the condenser and the evaporator.

COP of the system can be calculated using Equation 1.

$$\text{COP} = \frac{\dot{Q}_{\text{evap}}}{\dot{W}_{\text{comp,total}}} \quad (1)$$

Total compressor power consumption can be detected with the following equation.

$$\dot{W}_{\text{comp,total}} = \dot{W}_{\text{comp,LTC}} + \dot{W}_{\text{comp,HTC}} \quad (2)$$

Cooling capacity is defined with Equation 3.

$$\dot{Q}_{\text{evap}} = \dot{m}_{\text{LTC}}(h_1 - h_4) \quad (3)$$

Exergy of all points in the system can be calculated with Equation 4.

$$e_i = (h_i - h_0) - T_0(s_i - s_0) \quad (4)$$

Flow exergy is determined with multiplication of exergy and mass flow rate.

$$\dot{E}_i = \dot{m}_i e_i \quad (5)$$

Total exergy destruction of cascade refrigeration system is determined with the Equation 6.

$$\dot{E}_{\text{dest,total}} = \dot{E}_{\text{dest,evap}} + \dot{E}_{\text{dest,comp,LTC}} + \dot{E}_{\text{dest,CHX}} + \dot{E}_{\text{dest,valve,LTC}} + \dot{E}_{\text{dest,comp,HTC}} + \dot{E}_{\text{dest,cond}} + \dot{E}_{\text{dest,valve,HTC}} \quad (6)$$

Exergy efficiency can be determined with Equation 7.

$$\eta_{\text{ex}} = 1 - \left( \frac{\dot{E}_{\text{dest,total}}}{\dot{W}_{\text{comp,total}}} \right) \quad (7)$$

Table 2 shows the design parameters required to model the system. The primary consideration in selecting the design parameters of the cascade refrigeration system, as presented in Table 2, was ensuring that the chosen analysis parameters are consistent with those used in similar studies in the literature. A cooling capacity of 10 kW has been commonly used as a design parameter in many cascade refrigeration studies in the literature [11, 12, 27]. Additionally, the selected evaporator temperatures are similar to the range applied in studies on two-stage cascade refrigeration systems in the literature [14, 28].

**Table 2.** Design parameters of the model

<i>Operational Parameter</i>	<i>Input Value</i>	<i>Interval</i>
$\dot{Q}_{\text{evap}}$	10 kW	-
$\Delta T_{\text{CHX}}$	5 °C	-
$T_{\text{evap}}$	-60 °C	-70 °C to -50 °C
$T_{\text{cond}}$	35 °C	25 °C to 45 °C

## 2.2. SVM approach

Developed by Vapnik, the SVM is a classification algorithm renowned for its strong generalization capability, grounded in the structural risk minimization concept of statistical learning theory [29]. SVM is classified in the group of supervised machine learning approaches [30, 31]. In contrast to conventional neural network approaches, SVMs are capable of identifying a unique optimal solution, capturing nonlinear relationships effectively, and do not encounter dimensionality issues [32]. SVMs represent a robust and widely adopted approach in engineering, capable of handling complex problems with high efficiency [33]. Initially developed for constructing hyperplane-based decision boundaries, SVMs were later extended to handle nonlinear classification tasks through the use of the kernel trick [34]. The SVM algorithm starts by functioning within a space of lower dimensionality. Subsequently, the input data is transformed into a higher-dimensional feature space through the application of a kernel function. In this transformed space, the optimal separating hyperplane is then constructed. The SVM algorithm seeks to construct the most appropriate decision boundary, known as a hyperplane, that divides an n-dimensional space into definite classes, thereby making easier the accurate classification of new data points [35]. Support vectors refer to the data points that lie nearest to the decision boundary, while the margin denotes the distance between these points and the decision boundary itself [36].

For the optimization of the SVM, four different kernel functions were employed: normalized polynomial kernel, polynomial kernel, Pearson VII (PUK) kernel, and radial basis function kernel. Table 3 and Table 4 present the prediction errors for COP and exergy efficiency, respectively, obtained using the models built with these kernels. Upon examining the error values, it is evident that the Pearson VII (PUK) kernel function, represented in Model 3, resulted in the lowest prediction errors for both COP and exergy efficiency. Therefore, Model 3 was identified as the optimal model, and the Pearson VII (PUK) kernel function was used in the prediction phase. In studies conducted on thermal systems using the SVM algorithm, it has been found—consistent with the observations in this study—that the Pearson VII (PUK) kernel function results in lower prediction errors compared to other kernel functions [32, 37, 38].

**Table 3.** SVM models for COP

<i>No</i>	<i>Kernel Type</i>	<i>Training Set MAE &amp; RMSE for COP</i>	<i>Test Set MAE &amp; RMSE for COP</i>
1	Normalized Polynomial Kernel Function	0.0541 & 0.0792	0.0700 & 0.0926
2	Polynomial Kernel Function	0.0172 & 0.0266	0.0267 & 0.0335
3	Pearson VII (PUK) Kernel Function	0.0015 & 0.0033	0.0040 & 0.0064
4	Radial Basis Function Kernel Function	0.0963 & 0.1213	0.1155 & 0.1431

**Table 4.** SVM models for exergy efficiency

<i>No</i>	<i>Kernel Type</i>	<i>Training Set MAE &amp; RMSE for Exergy Efficiency</i>	<i>Test Set MAE &amp; RMSE for Exergy Efficiency</i>
1	Normalized Polynomial Kernel Function	0.0249 & 0.0320	0.0284 & 0.0370
2	Polynomial Kernel Function	0.0032 & 0.0043	0.0046 & 0.0057
3	Pearson VII (PUK) Kernel Function	0.0003 & 0.0004	0.0009 & 0.0015
4	Radial Basis Function Kernel Function	0.0306 & 0.0364	0.0339 & 0.0381

The formulation for a Pearson VII (PUK) kernel function is presented in equation 8. Here,  $x_i$  and  $x_j$  are used to express the vector arguments,  $\sigma$  is utilized to direct Pearson half-width, and a  $w$  term shows the tailing element of the peak.

$$K(x_i, x_j) = \frac{1}{\left[ 1 + \left( \frac{2 \left( \frac{\|x_i - x_j\|^2}{\sigma^2} \right)^{1/w} - 1}{2} \right)^w \right]} \quad (8)$$

To reduce prediction error, the hyperparameters  $C$  and  $\Sigma$  were systematically adjusted within defined intervals. In the first step,  $\Sigma$  was kept at its default value while the  $C$  parameter was varied between 1 and 7. It was found that setting  $C$  to 3.5 yielded the lowest error on both the training and testing datasets, making  $C = 3.5$  the optimal choice. In the next step, with  $C$  fixed at 3.5,  $\Sigma$  was varied between 1 and 4. The analysis revealed that the minimum error occurred when  $\Sigma$  was set to 3, indicating that  $\Sigma = 3$  is the optimal setting.

### 3. Results

#### 3.1. Parametric energy and exergy analysis results

Figure 2 shows the effect of evaporator temperature on COP. The increase in evaporator temperature from  $-70^\circ\text{C}$  to  $-50^\circ\text{C}$  led to a notable increase in COP across all working fluid pairs. A similar trend was observed in previous studies [12]. In the study conducted by Sun, Liang, Liu, Ji, Zang, Liang and Guo [12], when a  $20^\circ\text{C}$  increase in evaporator temperature was applied (from  $-60^\circ\text{C}$  to  $-40^\circ\text{C}$ ) using the R41/R404A pair, the COP increased from approximately 1.05 to 1.5, corresponding to a 42.9% improvement. Similarly, in the present study, a comparable increase in COP was observed for a  $20^\circ\text{C}$  rise in evaporator temperature. For R41/R152a, the COP rose from 1 to 1.421, marking a 42.1% increase. R744/R152a exhibited a COP rise from 0.9769 to 1.408, equivalent to a 44.13% improvement. COP of R744/R32 couple increased from 0.9611 to 1.38 which indicated a 43.59% rise. In addition, a COP of R41/R32 improved by 41.62%, from 0.9836 to 1.393. At  $-50^\circ\text{C}$ , all refrigerant couples exhibited the highest COP. Overall, R41/R152a provides the highest COP values, making it the most efficient in terms of energy performance under varying evaporator temperatures.

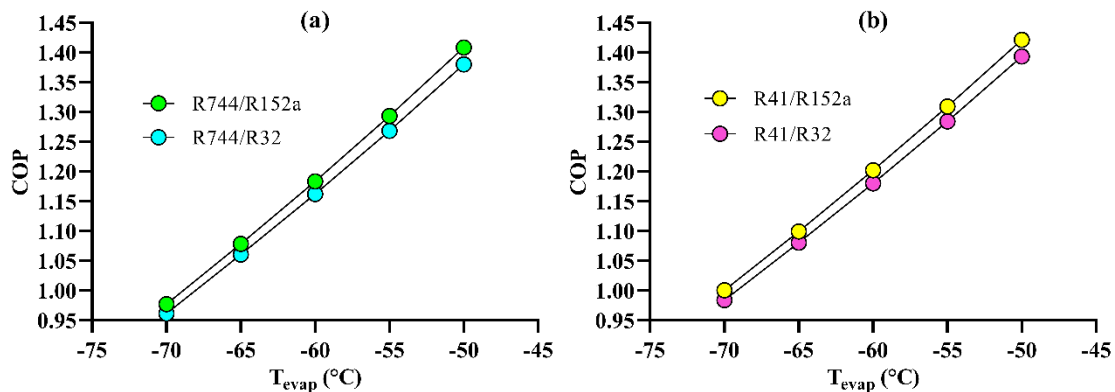


**Figure 2.** Evaporator temperature and COP relation

Figure 3 presents the influence of evaporation temperature on exergy efficiency. It can be stated that the exergy efficiency initially exhibits an increasing trend with the rising evaporator temperature; however, after reaching a peak point, it subsequently begins to decline. Similar observations were made in previous studies [28]. In the study conducted by Sun, Wang, Xie, Liu, Su and Cui [28], when the R41/R32 refrigerant pair was used, the exergy efficiency was approximately 0.39 at an evaporator temperature of  $-70^\circ\text{C}$ , reaching a peak value of around 0.42 at  $-50^\circ\text{C}$ , after which it began to decline. A similar trend was also observed in the

present study. For the R744/R152a refrigerant pair, the exergy efficiency is 0.4224 at  $-70^{\circ}\text{C}$ , increases to its peak value of 0.4345 at  $-55^{\circ}\text{C}$ , and subsequently decreases to 0.4319 at  $-50^{\circ}\text{C}$ . For the R744/R32 refrigerant pair, the exergy efficiency exhibits an increasing trend from  $-70^{\circ}\text{C}$  to  $-55^{\circ}\text{C}$ , after which it begins to decline, reaching a value of 0.4234 at  $-50^{\circ}\text{C}$ . For the R41/R152a refrigerant pair, the exergy efficiency shows an increasing trend from  $-70^{\circ}\text{C}$  to  $-60^{\circ}\text{C}$ , rising from 0.4324 to 0.4407; thereafter, it begins to decrease. For the R41/R32 refrigerant pair, the exergy efficiency is 0.4253 at  $-70^{\circ}\text{C}$ , reaches its peak value of 0.4328 at  $-60^{\circ}\text{C}$ , and finally decreases to 0.4273 at  $-50^{\circ}\text{C}$ . In general, R41/R152a stands out as the most exergy-efficient refrigerant pair under changing evaporator temperatures.

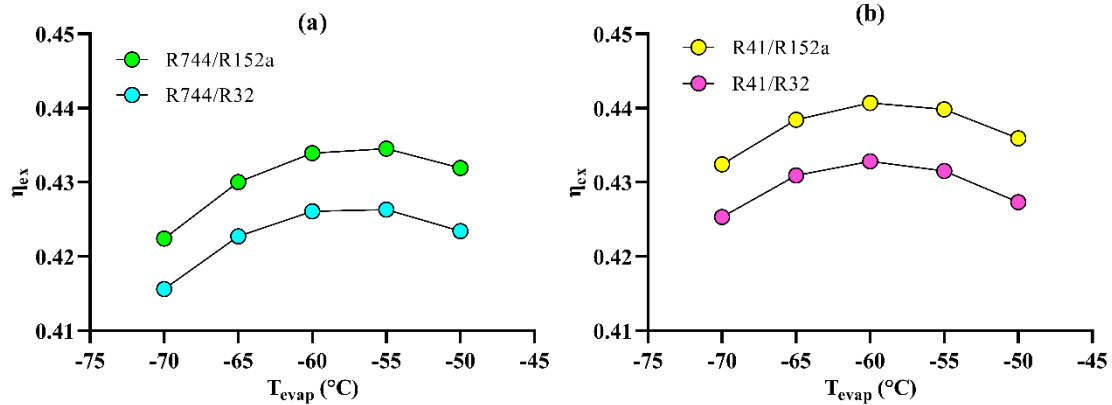


Figure 3. Evaporator temperature and exergy efficiency connection

Figure 4 depicts the impact of varying evaporator temperatures on total exergy destruction. Raising the evaporator temperature from  $-70^{\circ}\text{C}$  to  $-50^{\circ}\text{C}$  resulted in a decrease in total exergy destruction for all refrigerant couples. Previous studies revealed similar findings [11]. In the study conducted by Faruque, Uddin, Salehin and Ehsan [11], when the evaporator temperature was increased from  $-70^{\circ}\text{C}$  to  $-50^{\circ}\text{C}$  using the T2BUTENE/toluene refrigerant pair, the total exergy destruction decreased from approximately 4.75 kW to 3.38 kW, corresponding to a 28.8% reduction. Similarly, in the present study, a comparable reduction in total exergy destruction was observed when the evaporator temperature was varied within the same range. R41/R152a refrigerant couple showed a 30% reduction in total exergy destruction, from 5.676 kW to 3.971 kW. Total exergy destruction decreased by 29.6% for R41/R32, from 5.843 to 4.113 kW. In addition, a total exergy destruction of a R744/R152a pair dropped by 31.7%, from 5.912 to 4.036 kW. For R744/R32, total exergy destruction declined by 31.3%, from 6.081 to 4.178 kW. To sum up, R41/R152a exhibits the lowest total exergy destruction, making it the most thermodynamically favorable option in this respect.

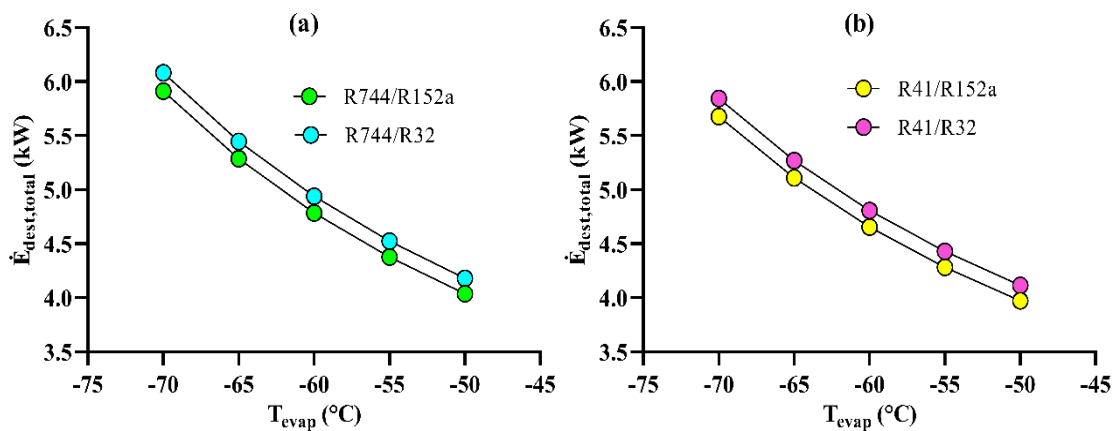
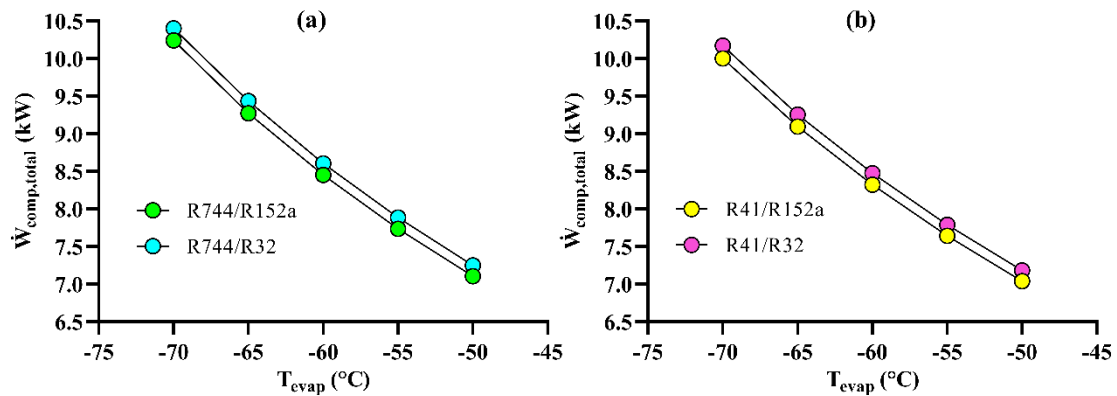


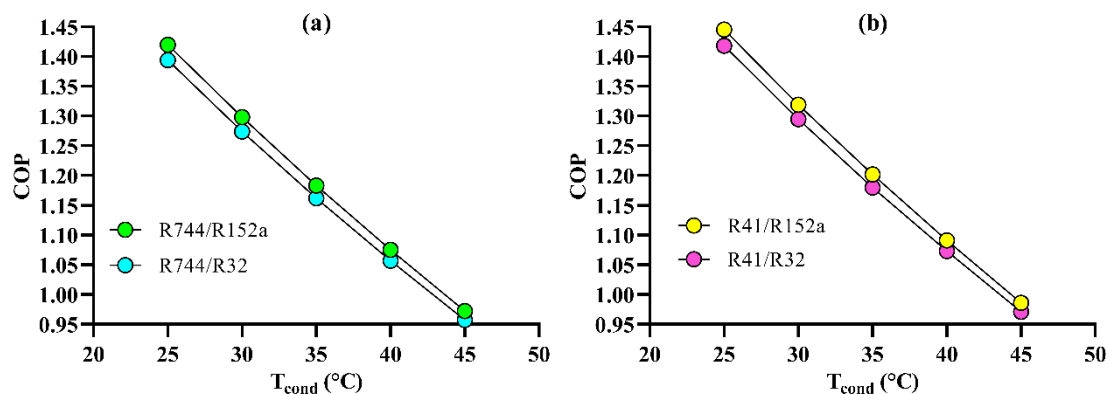
Figure 4. Evaporator temperature and total exergy destruction association

Figure 5 exhibits the influence of change in evaporator temperature on a total compressor power consumption of the system. As an evaporator temperature increased from  $-70^{\circ}\text{C}$  to  $-50^{\circ}\text{C}$ , total compressor power consumption decreased for all refrigerant couples. Previous studies demonstrated a similar behavior for compressor consumption [14]. A total compressor power consumption of a R41/R152a refrigerant pair declined from 10 to 7.039 kW, a 29.6% reduction. R41/R32 couple experienced a decrease in total compressor power consumption from 10.17 to 7.181 kW, a 29.4% drop. In addition, a total compressor consumption of R744/R152a dropped from 10.24 to 7.104 kW, representing a 30.6% reduction. For R744/R32, total compressor consumption fell by 30.3%, from 10.4 to 7.247 kW. Overall, R41/R152a demonstrates the lowest compressor power demand, indicating superior energy performance.



**Figure 5.** Change of total compressor consumption with evaporator temperature

Figure 6 illustrates the effect of condenser temperature on COP. Increasing condenser temperature from  $25^{\circ}\text{C}$  to  $45^{\circ}\text{C}$  caused a decline in COP for all refrigerant combinations. Similar findings regarding the decrease in COP values with increasing condenser temperature have also been reported in the literature [13]. COP of R41/R152a pair decreased from 1.445 to 0.9859, a 31.8% reduction. R41/R32 experienced a COP reduction of 31.5%, from 1.418 to 0.9709. COP of a R744/R32 refrigerant couple declined from 1.394 to 0.9574, a 31.3% decrease. In addition, increasing condenser temperature caused COP of R744/R152a to drop by 31.5%, from 1.42 to 0.9721. In general, R41/R152a delivers the highest COP under all condenser temperature levels, confirming its energy efficiency.



**Figure 6.** Change of COP under various condenser temperatures

Figure 7 shows the relationship between condenser temperature and exergy efficiency. Exergy efficiency decreased as condenser temperature increased from  $25^{\circ}\text{C}$  to  $45^{\circ}\text{C}$  for all refrigerant pairs. Similar results indicating that the exergy efficiency of the cascade refrigeration system decreases with increasing condenser temperature have been highlighted in the literature [6]. Exergy efficiency of a R41/R152a pair declined from 0.5298 to 0.3615, corresponding to a 31.8% decrease. Increasing condenser temperature caused exergy

efficiency of a R41/R32 to drop from 0.5199 to 0.356, a 31.5% reduction. R744/R32 experienced an exergy efficiency fall by 31.3%, from 0.5111 to 0.3511. Also, exergy efficiency of a R744/R152a refrigerant pair decreased by 31.5%, from 0.5207 to 0.3565. In conclusion, a R41/R152a consistently shows superior exergy efficiency in comparison with other refrigerant groups, especially under lower condenser temperatures.

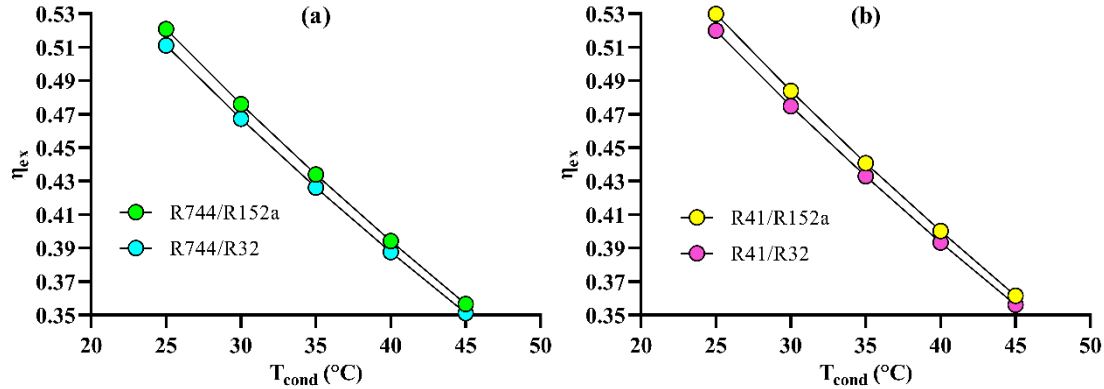


**Figure 7.** Effect of condenser temperature on exergy efficiency

Figure 8 represents the relationship between condenser temperature and total exergy destruction. A rise in condenser temperature from 25 °C to 45 °C led to higher total exergy destruction for all refrigerant groups. Similar findings indicating that the total exergy destruction of the cascade refrigeration system increases with increasing condenser temperature have been presented in the literature [3]. Total exergy destruction of a R41/R152a pair increased from 3.255 to 6.476 kW, a 98.9% rise. A R41/R32 pair experienced a total exergy destruction increase of 95.9%, from 3.386 to 6.633 kW. Increasing condenser temperature resulted with an increase total exergy destruction from 3.376 to 6.62 kW for R744/R152a, meaning a 96% increase. In addition, total exergy destruction of R744/R32 increased by 93.2%, from 3.508 to 6.778 kW. In general, R41/R152a exhibits the least exergy destruction, indicating better exergy performance under varying condenser temperatures.

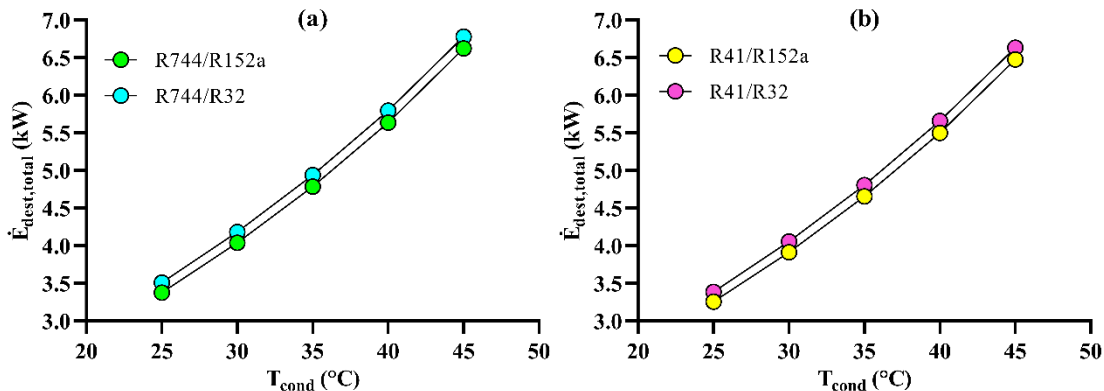


**Figure 8.** Impact of condenser temperature on total exergy destruction

Figure 9 presents the relationship between condenser temperature and total compressor power consumption. Compressor power consumption rose with an increase in condenser temperature from 25 °C to 45 °C. Similar results indicating that the total compressor power consumption of the cascade refrigeration system increases with an increase in condenser temperature have been reported in relevant studies in the literature [15]. Compressor power consumption of a R41/R152a pair increased from 6.922 to 10.14 kW, marking a 46.5% increase. Increasing condenser temperature caused an increase in compressor consumption by 46% for R41/R32 group, from 7.053 to 10.3 kW. For R744/R152a, 46.1% increase in total compressor power was recorded, from 7.043 to 10.29 kW. In addition, R744/R32 showed a 45.5% increase in total compressor



consumption, from 7.175 to 10.44 kW. To sum up, R41/R152a shows the lowest compressor power requirement, strengthening its position as the most energy-efficient pair.

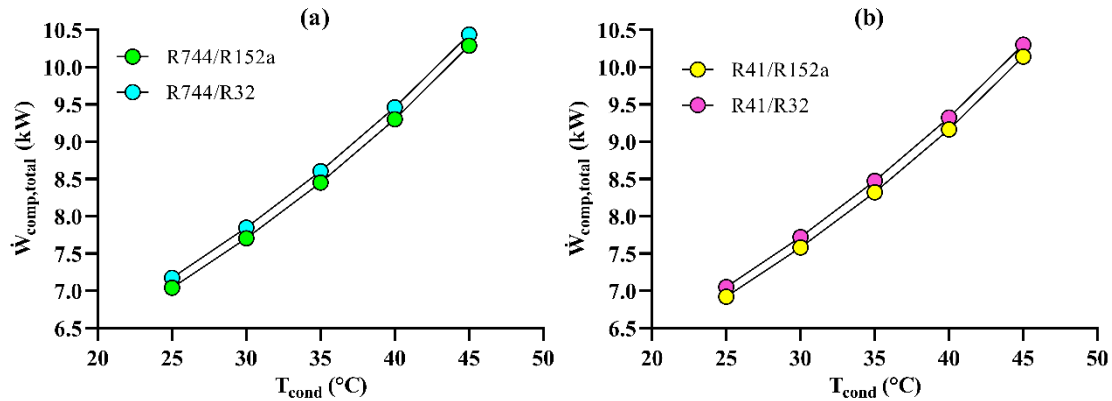


**Figure 9.** Condenser temperature and total compressor consumption relation

Table 5 summarizes the trends obtained from the parametric analysis.

**Table 5.** Effect of change of evaporator and condenser temperatures on thermodynamic parameters

Parameter	Performance Indicator	Effect
Evaporator Temperature Increase	COP	Increase
	Exergy Efficiency	First increase and then decrease after reaching a peak
	Total Exergy Destruction	Decrease
	Total Compressor Consumption	Decrease
Condenser Temperature Increase	COP	Decrease
	Exergy Efficiency	Decrease
	Total Exergy Destruction	Increase
	Total Compressor Consumption	Increase

### 3.2. Machine learning results with SVM approach

SVM algorithm was selected for this study due to its well-established ability to perform effectively with limited datasets, its robustness against overfitting, and its capacity to model nonlinear relationships through kernel functions. Given that the available dataset consists of a relatively small number of observations, and that the relationships between system parameters and target outputs such as COP and exergy efficiency are inherently nonlinear, SVM was deemed a suitable and efficient modeling approach. For these reasons, the present study focused on the application and performance evaluation of the SVM method.

To enable prediction using the SVM method, a dataset was constructed. In this dataset, evaporator and condenser temperatures were used as input parameters, while COP and exergy efficiency were selected as the output variables to be predicted. The dataset was generated using the data of the R41/R152a refrigerant pair, which was identified as the most efficient refrigerant combination based on the parametric analysis. During the dataset generation process, the evaporation temperature was varied between  $-70^{\circ}\text{C}$  and  $-50^{\circ}\text{C}$ , and the condenser temperature between  $25^{\circ}\text{C}$  to  $45^{\circ}\text{C}$ , both in increments of  $2.5^{\circ}\text{C}$ . All possible combinations of evaporation and condenser temperatures within these ranges were included in the dataset. For instance, when the evaporator temperature was  $-70^{\circ}\text{C}$ , the condenser temperature was varied across 25, 27.5, 30, 32.5, 35, 37.5, 40, 42.5, and  $45^{\circ}\text{C}$ . This process was then repeated for evaporator temperatures of  $-67.5$ ,  $-65$ ,  $-62.5$ ,  $-60$ ,  $-57.5$ ,  $-55$ ,  $-52.5$ , and  $-50^{\circ}\text{C}$ , with the condenser temperature adjusted accordingly as described. Seventy percent of the dataset was allocated for training, while the remaining thirty percent was used for testing. Each dataset created for the prediction of COP and exergy efficiency consists of 243 data points. The training set contains 168 data points, while the test set includes 75 data points. To ensure the

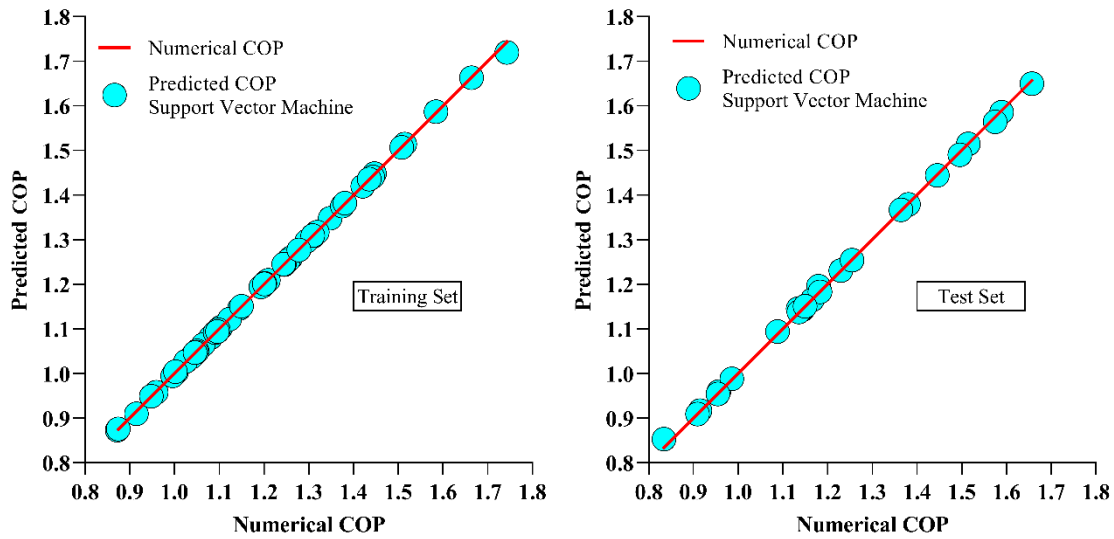
reliability of the predictions, care was taken to maintain a clear distinction between the data used in the training and test sets. The performance of the predictions was evaluated using statistical metrics, specifically the MAE and RMSE, the formulations of which are given below [39]. In these equations, the predicted value is denoted by  $y$ , the actual value by  $x$ , and the number of samples by  $n$ .

$$MAE = \frac{|y_1 - x_1| + \dots + |y_n - x_n|}{n} \quad (9)$$

$$RMSE = \sqrt{\frac{1}{n} \sum_{i=1}^n (y_i - x_i)^2} \quad (10)$$

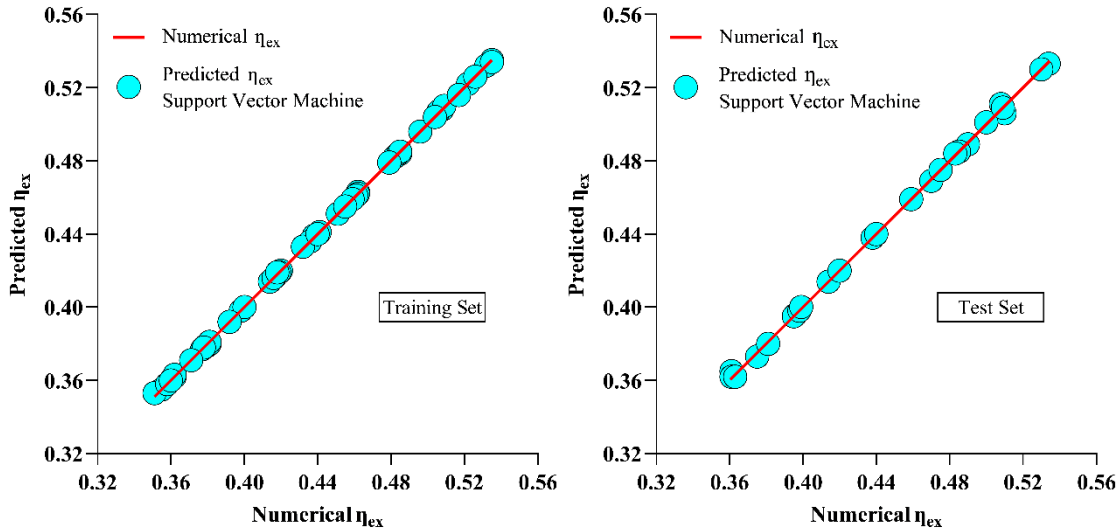
Figure 10 and Figure 11 present the prediction results for COP and exergy efficiency, covering both the training and test datasets. In Figure 10 and Figure 11, the predictions obtained using the SVM method are represented by light blue circles. The COP and exergy efficiency values obtained from numerical analysis are illustrated by the red  $y=x$  line. The proximity of the blue circles to the red  $y=x$  line indicates the prediction accuracy of the machine learning method used.

Figure 10 shows the COP prediction results obtained using the SVM method. As observed in Figure 10, the predicted COP values are very close to the actual COP values obtained from numerical analysis, which is evident from the near-perfect alignment of the light blue circles along the diagonal line. The results yielded an MAE of 0.0015 and an RMSE of 0.0033 for the training dataset. For the test set, the MAE and RMSE were 0.0040 and 0.0064, respectively.



**Figure 10.** COP prediction results

Figure 11 illustrates the exergy efficiency prediction results generated using the SVM algorithm. A close examination of Figure 11 reveals that the predicted exergy efficiency values align remarkably well with the actual values obtained from numerical analysis, as demonstrated by the tight clustering of the light blue circles along the diagonal reference line. For the training dataset, the model achieved a MAE of 0.0003 and an RMSE of 0.0004. In the testing dataset, the corresponding MAE and RMSE values were 0.0009 and 0.0015, respectively.



**Figure 11.** Exergy efficiency prediction results

Figure 12 and Figure 13 display the prediction errors of COP and exergy efficiency obtained using the SVM method. In Figure 12 and Figure 13, the error values shown on the y-axis represent the variation between the estimated values and the corresponding numerical data. The x-axis denotes the index of each data point within the complete dataset, which includes both the training and test samples. The prediction errors generated by the SVM model are illustrated by black lines. A value of zero on the y-axis indicates a perfect match between the predicted and numerical values. Significant deviations from zero imply poor prediction accuracy, reflecting a large discrepancy between predicted and actual values, whereas smaller deviations suggest better prediction performance.

An analysis of the COP prediction errors presented in Figure 12 reveals that the maximum error in the training dataset is 0.023. In the test dataset, the biggest COP prediction error was found to be 0.019. The relatively low prediction errors indicate that a successful model for COP prediction has been developed using the SVM method.

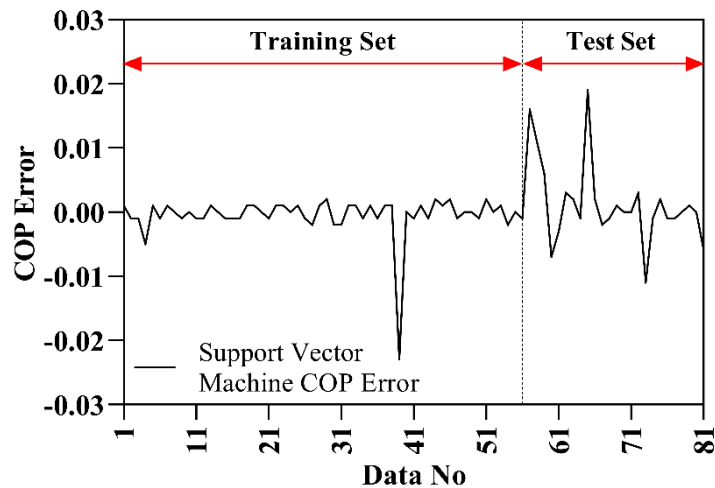


**Figure 12.** COP prediction errors

Upon examining the exergy efficiency prediction errors shown in Figure 13, it is observed that the highest error in the training set is 0.002. For the test set, the maximum exergy efficiency prediction error was 0.004.

The minimal prediction errors suggest that an effective model for exergy efficiency prediction has been established using the SVM method.

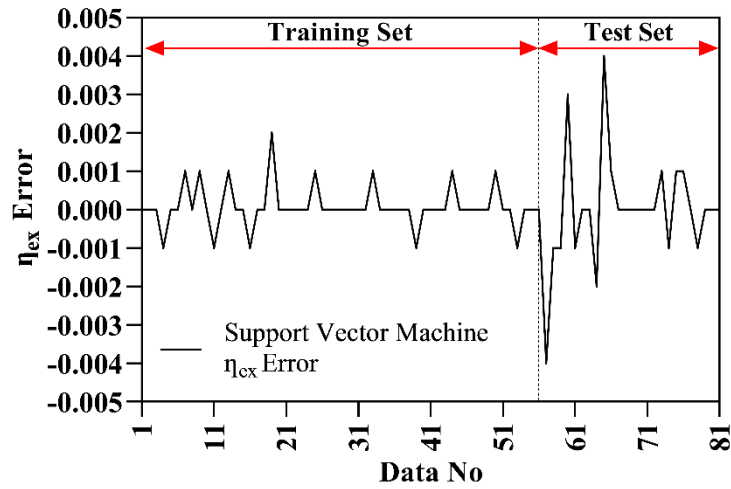


Figure 13. Exergy efficiency prediction errors

#### 4. Conclusions

In this study, a thermodynamic analysis was conducted for a two-stage cascade refrigeration cycle. The performance of four different refrigerant pairs was evaluated under varying evaporator and condenser temperatures. Through a series of parametric analyses, the most efficient refrigerant pair and the corresponding optimal operating parameters were identified. In the subsequent phase of the study, SVM was applied to the system data to predict the COP and exergy efficiency. The key findings of this work are summarized below:

1. Increasing the evaporator temperature from  $-70^{\circ}\text{C}$  to  $-50^{\circ}\text{C}$  led to an improvement in COP and a rise in exergy efficiency up to a certain point, after which a declining trend was observed. Additionally, both compressor power consumption and exergy destruction decreased with rising evaporator temperature. Conversely, increasing the condenser temperature from  $25^{\circ}\text{C}$  to  $45^{\circ}\text{C}$  resulted in reductions in both COP and exergy efficiency, along with increases in exergy destruction and compressor power demand, thus degrading overall system performance.
2. The thermodynamic analysis revealed that the most effective refrigerant pair was R41/R152a. For this combination, the system achieved a maximum COP of 1.421, a peak exergy efficiency of 0.4407, a minimum exergy destruction of 3.971 kW, and a minimum compressor power consumption of 7.039 kW under varying evaporator conditions.
3. Among the predictive models used, the SVM model with a PUK kernel yielded the most accurate estimates. It achieved an MAE of 0.0040 and an RMSE of 0.0064 for COP, and an MAE of 0.0009 and an RMSE of 0.0015 for exergy efficiency in the dataset prepared for testing the model.

The increasing demand for refrigeration systems operating at ultra-low temperatures has motivated the design of a two-stage cascade refrigeration system in this study. The findings are expected to provide valuable insights for researchers and industrial stakeholders involved in low-temperature refrigeration system development. Moreover, the successful performance carried out by the SVM approach in accurately modeling the performance parameters of the cascade system is a notable aspect of the research. This study enhances the existing body of knowledge by providing a comprehensive thermodynamic parametric analysis of a two-stage cascade refrigeration system and developing an accurate predictive model based on the SVM algorithm. The proposed approach offers a robust framework for the optimal design and performance forecasting of ultra-low temperature refrigeration systems. In summary, this research highlights that artificial intelligence techniques are valuable decision-making aids for forecasting, system configuration, and enhancing the performance of cascade refrigeration systems. Future studies are planned to develop an

experimental setup to investigate the performance of cascade refrigeration systems capable of operating at ultra-low temperatures.

## 5. Author Contribution Statement

In this study, all processes including the literature review on the analyzed cascade refrigeration system, thermal design, energy and exergy analyses, prediction using SVM, and analysis of the results were carried out by Author 1.

## 6. Ethics Committee Approval and Conflict of Interest Statement

Ethics committee approval was not required for the preparation of this article. The author declares no conflict of interest regarding this study.

## 7. Nomenclature and Subscripts

ANN	Artificial Neural Network
ASHRAE	American Society of Heating, Refrigerating and Air-Conditioning Engineers
COP	Coefficient of Performance
CRS	Cascade Refrigeration System
EES	Engineering Equation Solver
GWP	Global Warming Potential
MAE	Mean Absolute Error
NBP	Normal Boiling Point
ODP	Ozone Depletion Potential
RMSE	Root Mean Square Error
SVM	Support Vector Machine
$e$	Specific Exergy (kJ/kg)
$\dot{E}$	Flow Exergy (kW)
$h$	Enthalpy (kJ/kg)
$\dot{m}$	Mass Flow Rate (kg/s)
$\eta$	Efficiency
$\dot{Q}$	Heat Transfer Rate (kW)
$T$	Temperature (°C)
$\dot{W}$	Compressor Consumption (kW)
$\Delta T$	Temperature Difference (°C)
evap	Evaporator
CHX	Cascade Heat Exchanger
comp	Compressor
cond	Condenser
dest	Destruction
HTC	High-Temperature Circuit
$i$	Any Point in System
LTC	Low-Temperature Circuit
0	Dead-State

## 8. Ethical Statement Regarding the Use of Artificial Intelligence

No artificial intelligence-based tools or applications were used in the preparation of this study. The entire content of the study was produced by the author in accordance with scientific research methods and academic ethical principles.

## 9. References

- [1] A. Mota-Babiloni *et al.*, “Ultralow-temperature refrigeration systems: Configurations and refrigerants to reduce the environmental impact,” *Int. J. Refrig.*, vol. 111, pp. 147–158, 2020.
- [2] C. M. Udriou, A. Mota-Babiloni, and J. Navarro-Esbri, “Advanced two-stage cascade configurations for energy-efficient -80°C refrigeration,” *Energy Convers. Manag.*, vol. 267, 115907, Sep. 1, 2022.
- [3] W. Ye, F. Liu, Y. Yan, and Y. Liu, “Application of response surface methodology and desirability approach to optimize the performance of an ultra-low temperature cascade refrigeration system,” *Appl. Therm. Eng.*, vol. 239, 2024.
- [4] S. Khalilzadeh, A. H. Nezhad, and F. Sarhaddi, “Reducing the power consumption of cascade refrigeration cycle by a new integrated system using solar energy,” *Energy Convers. Manag.*, vol. 200, 112083, 2019.
- [5] O. Pektezeli, M. Das, and H. I. Acar, “Experimental analysis of different refrigerants’ thermal behavior and predicting their performance parameters,” *J. Thermophys. Heat Transf.*, vol. 37, no. 2, pp. 309–319, 2023.
- [6] A. Ustaoglu *et al.*, “Performance optimization and parametric evaluation of the cascade vapor compression refrigeration cycle using Taguchi and ANOVA methods,” *Appl. Therm. Eng.*, vol. 180, 2020.
- [7] S. Asgari, A. Noorpoor, and F. A. Boyaghchi, “Parametric assessment and multi-objective optimization of an internal auto-cascade refrigeration cycle based on advanced exergy and exergoeconomic concepts,” *Energy*, vol. 125, pp. 576–590, 2017.
- [8] R. Llopis *et al.*, “Energy and environmental comparison of two-stage solutions for commercial refrigeration at low temperature: Fluids and systems,” *Appl. Energy*, vol. 138, pp. 133–142, 2015.
- [9] A. Mota-Babiloni *et al.*, “Optimisation of high-temperature heat pump cascades with internal heat exchangers using refrigerants with low global warming potential,” *Energy*, vol. 165, pp. 1248–1258, 2018.
- [10] W. L. Luyben, “Estimating refrigeration costs at cryogenic temperatures,” *Comput. Chem. Eng.*, vol. 103, pp. 144–150, 2017.
- [11] M. W. Faruque *et al.*, “A Comprehensive Thermodynamic Assessment of Cascade Refrigeration System Utilizing Low GWP Hydrocarbon Refrigerants,” *Int. J. Thermofluids*, vol. 15, 2022.
- [12] Z. Sun *et al.*, “Comparative analysis of thermodynamic performance of a cascade refrigeration system for refrigerant couples R41/R404A and R23/R404A,” *Appl. Energy*, vol. 184, pp. 19–25, 2016.
- [13] W. Ye *et al.*, “Parametric analysis and performance prediction of an ultra-low temperature cascade refrigeration freezer based on an artificial neural network,” *Case Stud. Therm. Eng.*, vol. 55, 2024.
- [14] M. Chen *et al.*, “Performance comparison of ultra-low temperature cascade refrigeration cycles using R717/R170, R717/R41 and R717/R1150 to replace R404A/R23,” *Therm. Sci. Eng. Prog.*, vol. 44, 2023.
- [15] S. Ji *et al.*, “Energy, exergy, environmental and exergoeconomic (4E) analysis of an ultra-low temperature cascade refrigeration system with environmental-friendly refrigerants,” *Appl. Therm. Eng.*, vol. 248, 2024.
- [16] A. K. Vuppaladadiyam *et al.*, “Progress in the development and use of refrigerants and unintended environmental consequences,” *Sci. Total Environ.*, vol. 823, 153670, 2022.
- [17] K. Uddin and B. B. Saha, “An overview of environment-friendly refrigerants for domestic air conditioning applications,” *Energies*, vol. 15, no. 21, 8082, 2022.
- [18] N. Abas *et al.*, “Natural and synthetic refrigerants, global warming: A review,” *Renew. Sustain. Energy Rev.*, vol. 90, pp. 557–569, 2018.
- [19] A. Atmaca *et al.*, “Thermodynamic performance of the transcritical refrigeration cycle with ejector expansion for R744, R170, and R41,” *Isi Bilimi ve Tekniği Dergisi*, vol. 38, no. 2, pp. 111–127, 2018.
- [20] A. Usman *et al.*, “Viability of the Proposed Alternative Refrigerants as Future Refrigerants,” *Macromol. Symp.*, vol. 414, no. 1, 2025.
- [21] Y. Heredia-Aricapa *et al.*, “Overview of low GWP mixtures for the replacement of HFC refrigerants: R134a, R404A and R410A,” *Int. J. Refrig.*, vol. 111, pp. 113–123, 2020.



- [22] A. Mota-Babiloni *et al.*, “Refrigerant R32 as lower GWP working fluid in residential air conditioning systems in Europe and the USA,” *Renew. Sustain. Energy Rev.*, vol. 80, pp. 1031–1042, 2017.
- [23] V. H. Panato *et al.*, “Experimental evaluation of R32, R452B and R454B as alternative refrigerants for R410A in a refrigeration system,” *Int. J. Refrig.*, vol. 135, pp. 221–230, 2022.
- [24] A. Maiorino *et al.*, “R-152a as an alternative refrigerant to R-134a in domestic refrigerators: An experimental analysis,” *Int. J. Refrig.*, vol. 96, pp. 106–116, 2018.
- [25] B. Bolaji, “Experimental study of R152a and R32 to replace R134a in a domestic refrigerator,” *Energy*, vol. 35, no. 9, pp. 3793–3798, 2010.
- [26] S. A. Klein, “Engineering Equation Solver (EES),” Academic Professional Version, F-Chart Software: Middleton, 2013.
- [27] R. Roy and B. K. Mandal, “Energetic and exergetic performance comparison of cascade refrigeration system using R170-R161 and R41-R404A as refrigerant pairs,” *Heat Mass Transf.*, vol. 55, no. 3, pp. 723–731, 2018.
- [28] Z. Sun *et al.*, “Energy and exergy analysis of low GWP refrigerants in cascade refrigeration system,” *Energy*, vol. 170, pp. 1170–1180, 2019.
- [29] O. E. Akay and M. Das, “Modeling the total heat transfer coefficient of a nuclear research reactor cooling system by different methods,” *Case Stud. Therm. Eng.*, vol. 25, 100914, 2021.
- [30] M. Türk, C. Haydaroglu, and H. Kılıç, “Machine Learning-Based Detection of Non-Technical Losses in Power Distribution Networks,” *Firat Univ. J. Exp. Comput. Eng.*, vol. 4, no. 1, pp. 192–205, 2025.
- [31] A. B. Tatar, “Predicting Three-Dimensional (3D) Printing Product Quality with Machine Learning-Based Regression Methods,” *Firat Univ. J. Exp. Comput. Eng.*, vol. 4, no. 1, pp. 206–225, 2025.
- [32] O. Pektezel and H. I. Acar, “Experimental comparison of R290 and R600a and prediction of performance with machine learning algorithms,” *Sci. Technol. Built Environ.*, vol. 29, no. 5, pp. 508–522, 2023.
- [33] S. Salcedo-Sanz *et al.*, “Support vector machines in engineering: an overview,” *Data Min. Knowl. Discov.*, vol. 4, no. 3, pp. 234–267, 2014.
- [34] M. E. Cholette *et al.*, “Using support vector machines for the computationally efficient identification of acceptable design parameters in computer-aided engineering applications,” *Expert Syst. Appl.*, vol. 81, pp. 39–52, 2017.
- [35] M. Bansal, A. Goyal, and A. Choudhary, “A comparative analysis of K-nearest neighbor, genetic, support vector machine, decision tree, and long short term memory algorithms in machine learning,” *Decis. Anal. J.*, vol. 3, 100071, 2022.
- [36] N. Akgün, “Testing The Performance of Random Forest and Support Vector Machine Algorithms for Predicting Cyclist Casualty Severity,” *Firat Univ. J. Exp. Comput. Eng.*, vol. 2, no. 3, pp. 124–133, 2023.
- [37] M. Das, E. Alic, and E. K. Akpınar, “Detailed analysis of mass transfer in solar food dryer with different methods,” *Int. Commun. Heat Mass Transf.*, vol. 128, 105600, 2021.
- [38] Y. E. Güzelel *et al.*, “New multiple regression and machine learning models of rotary desiccant wheel for unbalanced flow conditions,” *Int. Commun. Heat Mass Transf.*, vol. 134, 106006, 2022.
- [39] O. Pektezel, M. Das, and H. I. Acar, “Experimental exergy analysis of low-GWP R290 refrigerant and derivation of exergetic performance equations with regression algorithms,” *Int. J. Exergy*, vol. 40, no. 4, pp. 467–482, 2023.



## İmar Mevzuatına Uygunluk Denetimi için Yapı Bilgi Modellemesi Tabanlı Otomatik Kural Kontrolü Uygulaması: Türkiye Örneği

Cengiz YILMAZ<sup>1\*</sup> , Hüseyin Atilla DIKBAŞ<sup>2</sup> 

<sup>1</sup>İnşaat Yönetimi ve Hukuku Doktora Programı, Fen Bilimleri Enstitüsü, İstanbul Medipol Üniversitesi, İstanbul, Türkiye.

<sup>2</sup>Güzel Sanatlar Tasarım ve Mimarlık Fakültesi, İstanbul Medipol Üniversitesi, İstanbul, Türkiye.

<sup>1</sup>cy@cengizyilmaz.com, <sup>2</sup>hadikbas@medipol.edu.tr

Geliş Tarihi: 4.05.2025

Kabul Tarihi: 7.06.2025

Düzeltilme Tarihi: 31.05.2025

doi: <https://doi.org/10.62520/fujece.1691523>

Araştırma Makalesi

Alıntı: C.Yılmaz ve H. A. Dikbaş, "İmar mevzuatına uygunluk denetimi için yapı bilgi modellemesi tabanlı otomatik kural kontrolü uygulaması: Türkiye örneği", Fırat Üni. Deny. ve Hes. Müh. Derg., vol. 4, no 2, pp. 424-445, Haziran 2025.

### Öz



Türkiye’de inşaat projelerinin tasarım ve onay aşamalarında, yapı bilgi modellemesi (YBM) ile oluşturulan proje verilerinin imar mevzuatına uygunluğunu hızlı, şeffaf ve verimli biçimde denetlemeye olanak tanıyan bir otomatik kural kontrolü uygulaması geliştirilmesi bu çalışmanın temel amacını oluşturmaktadır. Bu kapsamda, mevzuat metinlerinde yer alan kurallar önermeler mantığı esas alınarak yazılım diline uyarlanabilir bir yapıya dönüştürülmüş, karar yapıları oluşturulmuş ve YBM ortamına aktarılabilecek ayırt edici parametreler tanımlanmıştır. Model verileri, paylaşımına açık olan Endüstri Temel Sınıfları (Industry Foundation Classes, IFC) formatında dışa aktarılmış ve Python diliyle geliştirilen yazılım aracılığıyla dört farklı örnek proje üzerinde test edilerek otomatik denetim raporları elde edilmiştir. Elde edilen bulgular, mevzuat kurallarının mantıksal yapılara dönüştürülerek Endüstri Temel Sınıfları veri yapılarıyla karşılaştırılabileceğini ve böylece yapı projelerinin mevzuata uygunluğunun dijital ortamda denetlenebileceğini göstermektedir. Bu yaklaşım, kamu otoritelerinin tasarım ve onay süreçlerinde daha etkin ve şeffaf bir kontrol mekanizması geliştirmelerine katkı sağlayabilir. Çalışmanın özgün yönü, klasik mantık sisteminde yer alan ve karmaşık mantıksal operatörler içermeyen önermeler mantığının, yönetmeliklerdeki girift kurallara uygulanabilmiş olmasıdır. Ayrıca elde edilen doğru önermeler kümesi, yalnızca kural ihlalini göstermekle kalmayıp, ilgili kuralın kapsamlı bir analizini mümkün kılan tamamlayıcı bilgilerle birlikte sunulmaktadır.

**Anahtar kelimeler:** Otomatik kural kontrolü, Yapı bilgi modellemesi, Mantık tabanlı kural yorumlama, Model tabanlı kural denetimi, İmar mevzuatına uygunluk

\*Yazışılan Yazar



## A Building Information Modeling Based Automated Rule-Checking Application for Zoning Regulation Compliance: The Case of Türkiye

Cengiz YILMAZ<sup>1\*</sup> , Hüseyin Atilla DIKBAŞ<sup>2</sup> 

<sup>1</sup>Construction Management and Law PhD Program, Institute of Science, Istanbul Medipol University, Istanbul, Türkiye.

<sup>2</sup>Faculty of Fine Arts, Design and Architecture, Istanbul Medipol University, Istanbul, Türkiye.

<sup>1</sup>cy@cengizyilmaz.com, <sup>2</sup>hadikbas@medipol.edu.tr

Received: 4.05.2025

Accepted: 7.06.2025

Revision: 31.05.2025

doi: <https://doi.org/10.62520/fujece.1691523>

Research Article

Citation: C. Yılmaz ve H. A. Dikbaş, “A building information modeling based automated rule-checking application for zoning regulation compliance: the case of Türkiye”, *Firat Univ. Jour. of Exper. and Comp. Eng.*, vol. 4, no 2, pp. 424-445, June 2025.

### Abstract

The aim of this study is to develop an automated rule-checking application that enables the rapid, transparent, and efficient verification of building design data, created through Building Information Modeling (BIM), in compliance with zoning regulations during the design and approval phases of construction projects in Türkiye. In this context, rules expressed in regulatory texts were transformed into a format adaptable to software using propositional logic, and decision structures were created. Distinctive parameters based on the rules to be checked were assigned to the BIM environment. Model data were exported in the shareable Industry Foundation Classes (IFC) format, and a Python-based software was developed to test the automated rule-checking method on four different sample projects, generating result reports. The findings show that regulatory provisions can be converted into logical structures and compared with Industry Foundation Classes data, making it possible to digitally assess a project's compliance with regulations. This approach could contribute to enabling public authorities to implement a more effective and transparent control mechanism in the design and approval processes. The originality of the study lies in the successful application of classical propositional logic—despite its lack of complex logical operators—to complex regulatory rules. Moreover, the set of validated propositions not only defines the outcome of the rule check but also provides comprehensive contextual information related to the rule, allowing for a more in-depth evaluation of the results.

**Keywords:** Automated rule checking, Building information modeling, Logic-based rule interpretation, Model-based code checking, Zoning regulation compliance

\*Corresponding author

## **1. Introduction**

Digitalization has led to profound transformations in the production and service sectors since the Industrial Revolution. However, the construction sector has adapted to this transformation process more slowly compared to other industries. Studies show that the construction industry is still one of the sectors with the lowest level of digitalization [1]. This situation prevents the industry from fully achieving its potential productivity gains and sustainability goals.

Traditional construction projects are inherently complex systems due to their multi-stakeholder structures, variable conditions, and high coordination requirements. This complexity poses significant challenges to the integration of digital technologies and constitutes a major barrier to digital transformation [2]. Additionally, the prevailing traditional approach to construction and habits in the sector create a cultural barrier to technological adaptation when combined with resistance to innovation. Furthermore, firms in the sector often operate under intense competitive pressure, leading them to focus on short-term cost advantages. This results in delays in investments in digital infrastructure that offer long-term benefits. As a result, the integration of industrial innovations into the construction sector remains limited. Despite all these challenges, the construction sector needs new technologies supported by digital transformation for more efficient, safer, and sustainable projects to replace traditional methods.

One of the most prominent technologies in this transformation is Building Information Modeling (BIM). BIM offers an information-driven approach in the design, planning, construction, and maintenance phases, increasing integration among all stakeholders and ensuring transparency in project management [3]. BIM is considered one of the core elements of digital transformation in the construction industry. Researchers and BIM software developers define BIM not only as a design tool but also as a holistic information management process that encompasses information generation, management, and usage across all stages of the project lifecycle [4]. In this context, the impact of BIM is not limited to its technical dimension; it is also directly related to business processes, communication between stakeholders, and legal regulations.

Since the early 2000s, many countries, including the United States, European countries, Australia, and East Asia, have begun to promote the use of BIM at a strategic level [5]. Key factors accelerating the adoption of BIM in these countries include increasing project efficiency, reducing costs, lowering error rates, and enhancing stakeholder interaction [6]. Public institutions have taken various strategic steps to promote the widespread use of this technology. For example, in the United States, the General Services Administration (GSA) has encouraged the use of BIM in public projects, while the United Kingdom made BIM usage mandatory for all central government projects by 2016, paving the way for transformation in the sector. Similarly, countries like Singapore, Norway, and Finland have institutionalized BIM integration by creating guidelines, application manuals, and mandatory standards [5].

Although the implementation of Building Information Modeling (BIM) in Türkiye remains limited, it has started to be adopted in large-scale projects carried out through public–private partnerships, such as city hospitals, airports, and certain infrastructure developments [7]. However, these examples are exceptional, and BIM has yet to be widely adopted across the construction sector. The main barriers to the widespread use of BIM in Türkiye include the complexity of the industry, high investment costs, lack of knowledge and technical skills, as well as the absence of a well-established legal and institutional framework [8-10]. In particular, the lack of explicit provisions for BIM integration in current zoning and building inspection regulations, the absence of defined standards, and the lack of a legal basis for the structured digital exchange of project data have significantly hindered progress. Consequently, the full potential of BIM-enabled information management, automated rule checking, and data exchange has not yet been realized.

The primary objective of this research is to examine an application for integrating BIM practices with the existing legal framework in Türkiye. Specifically, it aims to test a system that enables the comparative analysis of data extracted from BIM models against legal regulations in areas such as building inspection, zoning compliance, and energy performance codes. The study employs classical logic-based propositional reasoning to enable the computational processing of construction regulations. Complex rules from regulatory texts are translated into simplified and inferable propositions, which are then structured into decision

frameworks and decision tables within the software. Although a software application has been developed within the scope of this research, the primary objective of the study is not the software itself, but rather the examination of how BIM data can be integrated with existing legal regulations. In this context, the scope of the research is primarily limited to building inspection processes and compliance checks with zoning regulations.

## **2. Literature Review**

In the construction industry, knowledge sharing and management are critically important in projects where various disciplines (architecture, civil engineering, electrical, mechanical, etc.) collaborate during the project management, planning, and design phases. In this context, common data environments (CDE) and model-based working methods, which are considered key components of digital transformation, have gained significant momentum in recent years [12].

In recent years, although there has been a noticeable increase in the digitalization of the construction industry, it remains one of the least digitized sectors [1, 13]. Compared to other industries, the construction sector has been slow to adopt and integrate digital technologies. Despite the potential benefits, the industry continues to face challenges in fully embracing digital transformation and incorporating digital tools into its operational processes. One of the major barriers in this regard is the inherent complexity of construction projects [2, 14]. Another significant factor is the sector's strong adherence to traditional construction practices, which contributes to resistance to change. Moreover, the lack of digital skills and knowledge among industry professionals further exacerbates the difficulties faced during the digitalization process [15].

Despite these challenges, there is a growing need in the construction sector to replace traditional methods with new technologies supported by digital transformation to ensure more efficient, safer, and more sustainable project delivery. These technologies have led stakeholders—particularly contractors, engineers, and designers—to increasingly adopt various digital tools to optimize construction processes and reduce costs. Among these tools, Building Information Modeling (BIM) stands out as the most widely adopted foundational technology [2].

Digitalization is regarded not only as a technological innovation but also as a strategic necessity for sustainability, efficiency, and competitive advantage. Rapid urbanization, climate change, and increasing global competitive pressures are among the main factors that make it inevitable for construction companies to use digital tools [13, 14]. Nonetheless, in the past decade, national Building Information Modeling (BIM) mandates and digital transformation policies introduced in many countries have facilitated the adoption of software-supported design approaches in the sector. The digitalization process not only simplifies information management but also contributes to preventing project errors by enabling real-time data sharing among stakeholders. For example, early detection of a design error in the design phase can prevent costly revisions on the construction site.

In this context, the analysis of the necessity of digital transformation and the current state of the industry stands out as a strategic factor that will directly affect the future competitiveness of the construction sector. Globally, efforts to digitalize the construction industry are accelerating through university-industry collaborations and public support, further supporting the structural transformation of the sector.

### **2.1. Application areas and concepts of building information modeling (BIM)**

Building Information Modeling (BIM) is at the center of the digital transformation of the construction industry and is regarded as a catalyst by governments and public suppliers to achieve productivity, cost, and quality policy goals in the sector [3]. Although BIM is defined in various ways, it is widely accepted as a form of collaboration that makes information about buildings and facilities digitally accessible and analyzable [16-18]. This approach surpasses the traditional two-dimensional design understanding by integrating multiple disciplines and not only going beyond three-dimensional models but also systematizing data sharing in the design, construction, and operation processes.



The scope of BIM has expanded over time, and this expansion has led to the emergence of the concept of BIM dimensions. Today, the term “nBIM” indicates that there is no limit to these dimensions, with 3D, 4D, 5D, 6D, and 7D being the most commonly used BIM dimensions [19].

3D BIM offers an enhanced visualization capability, but it is not limited to the three-dimensional digital representation of the structure. This application can include information for analysis tailored to the goals of stakeholders such as designers, contractors, employers, and project managers, and through dynamic use, it enables early detection of potential problems.

4D BIM integrates the construction schedule by adding the time dimension to the 3D model. This integration visualizes the flow of the work schedule, enabling more effective planning and time management.

5D BIM integrates cost data into the project, allowing cost estimation in the design process and evaluating the cost impacts of design decisions. During the construction process, it helps in conducting cost analysis.

6D BIM is focused on sustainability and contributes to improving the energy efficiency of buildings through energy calculations. Interventions such as optimizing the layout plans can reduce energy loss and waste.

7D BIM enables information management throughout the lifecycle of buildings. By integrating information such as technical specifications, maintenance schedules, inspection records, and warranty details, it creates an efficient operational process for project managers and owners.

The BIM dimensions are not limited to these. 8D addresses occupational health and safety issues, helping to reduce risks in projects, while 9D incorporates lean manufacturing principles and aims to improve the efficiency of production processes [20].

BIM is also an essential tool that supports management approaches such as Integrated Project Delivery (IPD). IPD is a management system aimed at increasing productivity and improving project delivery speed in construction projects. Emerging in the United States in the 1990s, this system requires widespread and comprehensive communication between teams, taking into account the complexity of projects, and the effective use of digital tools such as BIM in project decision-making processes [21, 22].

The Common Data Environment (CDE) is a critical component in the success of BIM applications. CDE allows all project-related data to be collected, managed, and shared on a centralized platform. This digital system enables project stakeholders (architects, engineers, contractors, consultants, etc.) to access the most up-to-date data they have created, making information exchange between the project team transparent, consistent, and effective [23].

The BIM implementation plan provides a strategic roadmap for how a project will use BIM technologies. This plan defines details such as which data will be collected in which processes and how this data will be managed and shared. As a result, it ensures that project processes are managed more transparently and efficiently. Furthermore, the implementation plan creates an effective collaboration environment among project stakeholders by minimizing potential inconsistencies and uncertainties [24]. Preparing the BIM implementation plan correctly is a crucial step that facilitates the achievement of project objectives.

The ISO 19650 standard defines the principles and requirements for information management and provides fundamental guidelines for implementing BIM applications. This standard provides detailed guidelines on issues such as information sharing, digital data management, production methods, and delivery processes. Additionally, it clarifies the roles and responsibilities of project stakeholders along with BIM Execution Plan (BEP) templates [25].

Eastman et al. (2011) emphasize that BIM reduces error rates in projects, lowers costs, and increases efficiency by preventing material waste [26]. Bryde et al. (2013) highlight the importance of BIM as a strong communication tool among project stakeholders [2]. Similarly, Becerik-Gerber and Rice (2010) state that BIM has systematized information management in the construction industry, optimized project processes, and allowed all stakeholders to meet on a common platform [4].



In conclusion, the use of BIM technology enables construction projects to be executed more effectively, efficiently, and sustainably. BIM allows significant gains in project processes and will continue to be an essential tool for the digitalization of the construction industry in the future.

## **2.2. IFC standard**

Industry Foundation Classes (IFC) is an open and international data standard that enables data exchange and interoperability between building information models (BIM). IFC provides an object-based data model that allows for the detailed definition of building elements, systems, and processes. Through this standard, data transfer and model integration between different BIM software can be performed seamlessly [27, 28]. IFC was approved by ISO in 2012 and standardized in 2013, becoming an open and international standard that can be used across hardware devices, software platforms, and interfaces for various use cases [29].

The IFC data model offers the possibility of sharing data used at every stage of the project process by encompassing the geometric and functional properties of building elements, their connections, material information, and other technical details [27]. The IFC model consists of four main layers. These layers ensure that information is organized hierarchically and shared in an orderly manner [30].

- **Main Layer:** The main layer contains asset definitions, including customizations for specific disciplines, products, processes, or resources.
- **Interoperability Layer:** This layer facilitates the sharing of structure, construction, and management information between the project team. It is particularly useful when different disciplines need to collaborate and make decisions together.
- **Core Layer:** The core layer contains the most general asset definitions for building components. Here, the properties of building elements, additional comments, and other detailed information can be found.
- **Resource Layer:** The resource layer includes all individual schemas containing resource definitions. These definitions generally do not include unique identifiers and should not be used without a definition provided at a higher layer. This layer stores the basic properties and simple information of building components, such as geometry, material, quantity, measurements, timing, and cost.

There are various challenges that arise during the model and data transfer, especially when using different software. To effectively address these challenges, a collaborative approach is adopted, and IFC is often preferred as a solution. IFC facilitates model conversion between different software, offering solutions to such issues.

## **2.3. Automatic rule checking**

Various automatic rule-checking methods have been developed to automatically verify legal requirements during the design and approval processes of construction projects. However, in some applications, written rules are directly interpreted and converted into computer code by the programmer without using a systematic method. This requires both expertise in interpreting regulations and proficiency in software development. Furthermore, the first studies on automatic rule processing date back to the 1960s. One of the pioneering studies in this field is the decision table approach developed by Fenves in 1966. However, due to its inadequacy in defining the relationships between rules and the overall organization, a four-layer theoretical structure was proposed in 1973 by AISC (American Institute of Steel Construction). This structure defines elements such as terms forming the rule, provisions, relationships between provisions, and rule organization in hierarchical layers [31].

Another important approach in this field is the rule-based method. In this method, rules are represented as condition-action pairs expressed in the "If-Then" format. In other words, the action to be performed when a specific condition is met is clearly defined [32]. Although this structure allows rules to be modeled systematically, it can be limited in expressing more complex situations.

The logic-based approach is similar to the rule-based method in that it uses the "If-Then" structure; however, it employs a more formal language expressed with logical predicates and propositions. This method allows for the complete and consistent definition of rules. Additionally, it enables inferences to be made in cases of missing information. However, the use of this method requires knowledge of logic, and it would involve user-defined predicates and logic operators [33].

In the object-based approach, rules are directly linked to the objects in the building model and organized through class-subclass relationships. For example, in a building model, objects such as "floor," "room," and "column" are defined by their properties (height, material type, etc.), and rule checks are performed based on these objects [34]. However, it may not always be easy to directly incorporate regulatory rules into an object-based model. In this regard, Yabuki and Law (1993) argue that engineering standards should be supported by logic rules alongside object models [35].

Recently, Natural Language Processing (NLP) techniques have emerged as an important tool for digitizing and interpreting regulatory texts. Regulatory texts are often long, complex, and written in natural language, making it difficult for machines to directly understand these documents [36]. Chalkidis et al. (2019) demonstrated with their system for the automatic analysis of legal documents that judicial decisions can be interpreted using machine learning and NLP methods [37]. Fuchs and Amor (2021) discuss the analysis of building regulations with NLP algorithms and their transformation into logic-based structures [38]. However, these studies highlight that complex sentence structures, exceptions, and ambiguous definitions limit the performance of NLP systems. Construction regulations are characterized by a formal, technical, and often complex linguistic structure. Since most regulatory texts are not explicitly written in a rule-based format, extracting logical rules from these documents is a highly intricate process. Representing rules using Natural Language Processing (NLP) techniques such as generating "if-then" structures requires advanced semantic analysis and contextual tracking. Moreover, NLP tools available for the Turkish language are not as developed as those for English. For these reasons, NLP was not utilized in the software developed within the scope of this study.

The primary motivation behind these historical developments has been to reduce human error that may occur during manual checking processes and to accelerate project approval procedures. At the same time, how to effectively integrate factors such as the continuous updating of regulations and regional variations into digital environments has emerged as a significant area of research. In particular, differences in language and terminology across countries are frequently cited as one of the main barriers to the widespread adoption of automated code compliance checking.

### **3. Method**

The framework proposed by Eastman et al. (2009) for systematically implementing rule-based control applications in Building Information Modeling (BIM) has formed the basis for many subsequent studies and is frequently referenced in the development of rule-checking applications [39]. As shown in Figure 1, this framework defines the overall process as the flow and interaction of four distinct steps.

In this study, the application examined will be structured according to the steps of rule interpretation, preparation of the building information model, execution of rule checking, and reporting of the results, as shown in Figure 2.

The first and most fundamental stage of BIM-based rule checking applications is the conversion of regulatory rules into machine-readable language. This process aims to digitize the contents of rules expressed in natural language as accurately as possible, meaning converting them into binary or logical codes. However, the diversity of syntactical structures and the content-related ambiguities in rule expressions make it quite difficult to standardize this process [40].

The regulatory compliance checking software to be developed in this study will be usable both by engineers and architects during the design process and by authorized institutions during official approval procedures. Therefore, the software will be developed as an independent structure that does not rely on design tools but

instead can receive and evaluate design data from external sources. In this context, the IFC (Industry Foundation Classes) open data standard, which is supported by many BIM software tools and offers an impartial data model, will be used for the sharing and processing of design data.

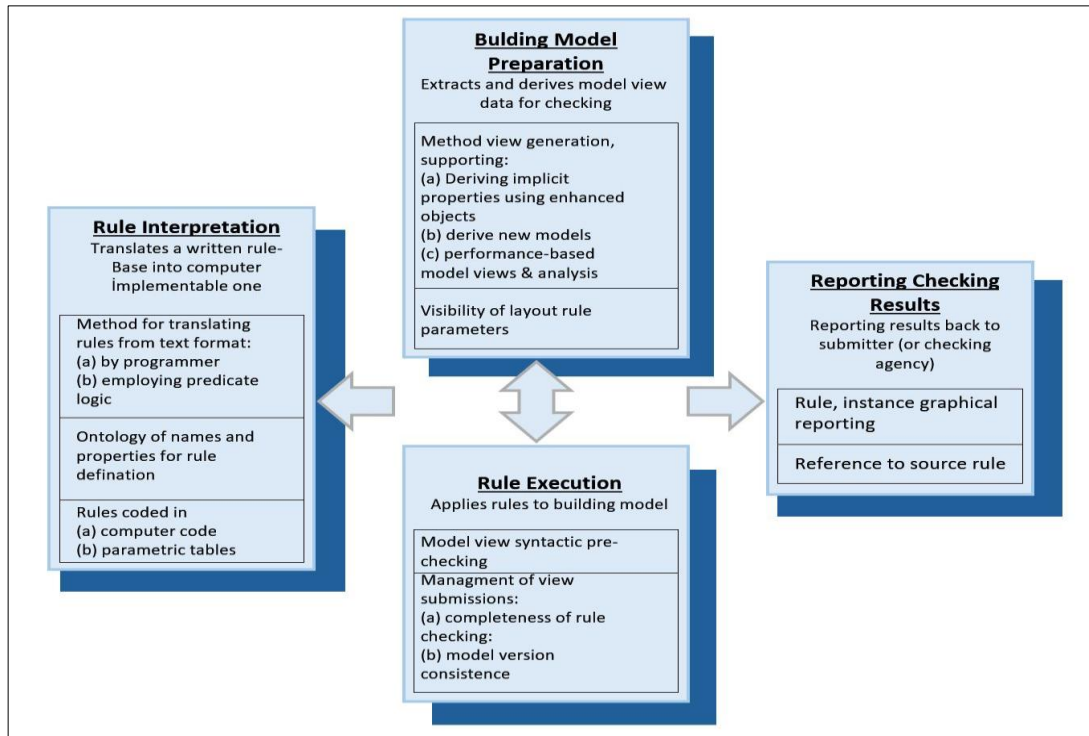


Figure 1: Framework for BIM-based rule checking [39]

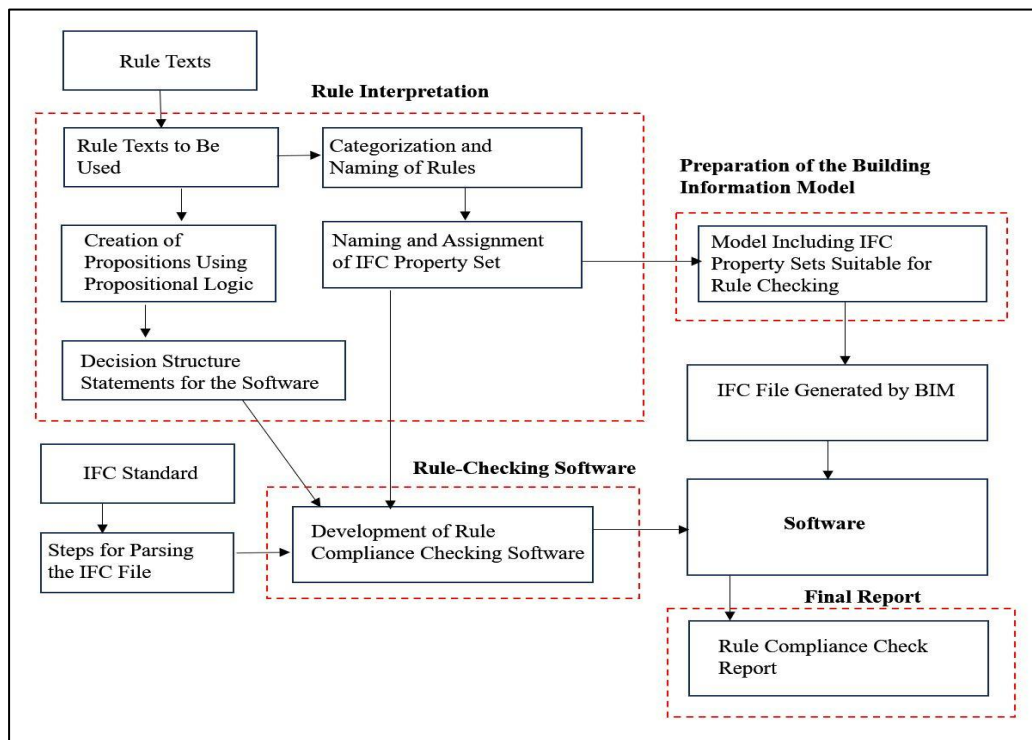


Figure 2: Connection diagram of the rule checking software

### 3.1. Rule interpretation

One of the primary legal instruments regulating construction processes in Türkiye is the Regulation on Planned Areas Construction, which defines the construction requirements for planned development zones. In addition to this national regulation, there are also locally issued zoning regulations specific to metropolitan municipalities such as Istanbul, Ankara, and Izmir. However, these local regulations are generally aligned in terms of core content and guiding principles. In this study, the Regulation on Planned Areas Construction (2017) is selected as the primary normative source for testing the developed automated rule-checking application [41].

To enable the application to assess architectural project compliance, two specific provisions, Articles 9 and 28, located under the section titled “Provisions Related to Construction” in Chapter 4 of the regulation have been selected as focal points.

- Article 9 outlines the relationship between road width and the permissible number of building floors.
- Article 28 establishes the maximum floor heights for various building usage types, including residential, commercial, and mixed-use developments.

Both articles contain multi-variable rule structures that are directly related to project data and serve as representative examples of automated rule-checking systems. For instance, when evaluating a project, the system must determine whether the number of floors and the building height are explicitly defined in the zoning plan. If not, the number of floors is inferred based on road width, and building height is subsequently calculated, considering the number of floors. Floor height, in turn, is determined based on both floor location and functional building usage. This process requires simultaneous consideration of multiple interdependent variables.

Such multi-variable logic exemplifies the complex rule inference structures often encountered in automated compliance systems.

In this study, a logic-based approach is adopted for the digital modeling and interpretation of regulatory provisions. Specifically, propositional logic (zero-order logic) is utilized, which enables formal reasoning based on the truth values of propositions. This logic framework is widely used in information systems for rule inference, knowledge representation, and automatic interpretation, and is also frequently applied in BIM-based compliance checking processes [42].

Within this framework, propositions are categorized into two types based on the source of their truth values:

- Direct Propositions, which are dependent on observable project variables.
- Inference Propositions, which are based on logical premise-consequence relationships.

Figure 3 schematically illustrates the structural relationship and logical sources of these propositions.

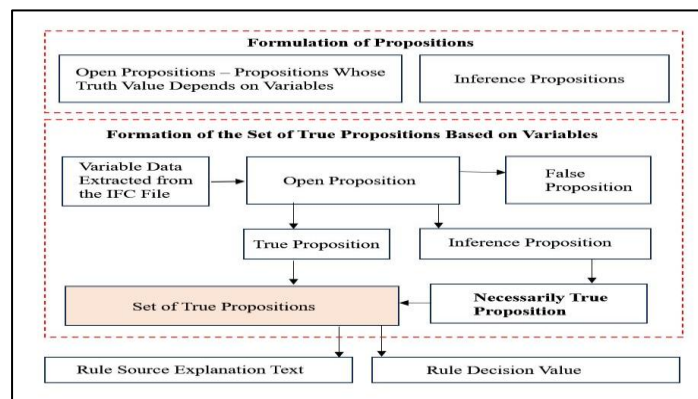
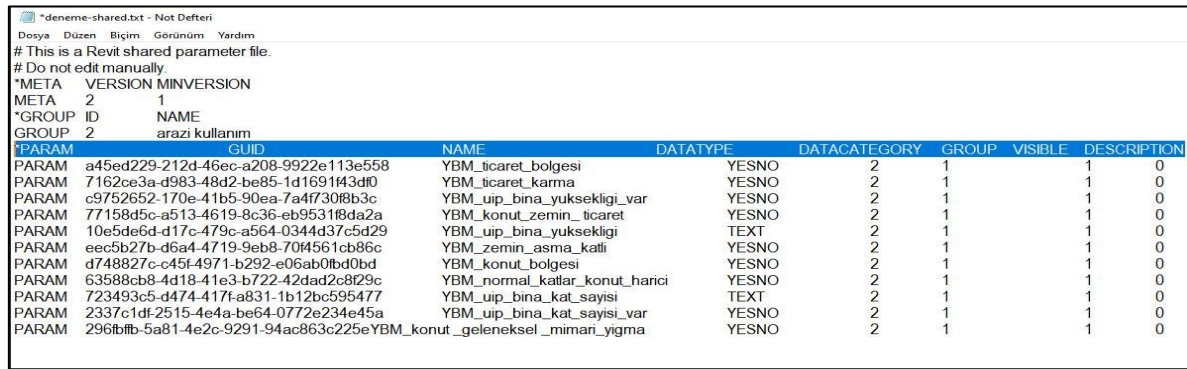


**Figure 3:** The truth source and formation of propositions

### 3.2. Preparation of the building information model

To enable the automatic digital control of regulatory rules, propositions validating the values to be compared have been predefined. In evaluating these propositions, the Building Information Modeling (BIM) model will be used as a second data source. For the joint processing of both data sources (i.e., the regulatory rules and the BIM model parameters), it is essential to distinctly define the parameters of the BIM objects. Therefore, concepts representing the regulatory rules will be assigned as parameter names to the relevant objects within the BIM model (Figure 4).

Since the model developed in this study is intended not only to be specific to a certain regulation but also adaptable to regulations across different disciplines, this naming system has been categorized and structured. The IFC (Industry Foundation Classes) format will be used for independent data sharing of the BIM model across software platforms. By using the IFCPROPERTYSET class, which represents object properties within the IFC structure, the defined naming conventions will be directly integrated into the model. After these definitions, the model file produced with the BIM software "Autodesk Revit" will be exported in IFC format, allowing the establishment of a digital environment that facilitates the automatic control of the rules [43, 44].



The image shows a screenshot of a Revit shared parameter file. At the top, there is a header section with the following text: "# This is a Revit shared parameter file. # Do not edit manually." Below this, there is a table with the following columns: PARAM, GUID, NAME, DATATYPE, DATACATEGORY, GROUP, VISIBLE, and DESCRIPTION. The table contains 10 rows of parameters, each with a unique GUID and a name starting with "YBM\_".

PARAM	GUID	NAME	DATATYPE	DATACATEGORY	GROUP	VISIBLE	DESCRIPTION
PARAM	a45ed229-212d-46ec-a208-9922e113e558	YBM_ticaret_bolgesi	YESNO	2	1	1	0
PARAM	7162ce3a-d983-48d2-be85-1d1691f43d0f	YBM_ticaret_karma	YESNO	2	1	1	0
PARAM	c9752652-170e-41b5-90ea-7a4f730f8b3c	YBM_uip_bina_yuksekligi_var	YESNO	2	1	1	0
PARAM	77158d5c-a513-4619-8c36-eb95318da2a	YBM_konut_zemin_ticaret	YESNO	2	1	1	0
PARAM	10e5de6d-d17c-479c-a564-0344d37c5d29	YBM_uip_bina_yuksekligi	TEXT	2	1	1	0
PARAM	eec5b27b-d6a4-4719-9eb8-70f4561cb86c	YBM_zemin_asma_katli	YESNO	2	1	1	0
PARAM	d748827c-c45f-4971-b292-e06ab01bd0bd	YBM_konut_bolgesi	YESNO	2	1	1	0
PARAM	63588cb8-4d18-41e3-b722-42dad2c8f29c	YBM_normal_katlar_konut_harici	YESNO	2	1	1	0
PARAM	723493c5-d474-417f-a831-1b12bc595477	YBM_uip_bina_kat_sayisi	TEXT	2	1	1	0
PARAM	2337c1df-2515-4e4a-be64-0772e234e45a	YBM_uip_bina_kat_sayisi_var	YESNO	2	1	1	0
PARAM	2961f1fb-5a81-4e2c-9291-94ac863c225e	YBM_konut_geleneksel_mimari_yigma	YESNO	2	1	1	0

Figure 4. Shareable parameter file

### 3.3. Rule control software

The rule control software has been developed using Python 3.9 version on the Windows operating system. The user interface of the software has been prepared in Turkish. This software processes the data of files created in the "Autodesk Revit" model and produced in the appropriate format (IFC) by parsing them. The features and workflow of the software can be summarized as follows:

**Loading and Parsing the IFC File:** The software analyzes the uploaded IFC file and performs a parsing operation for design project information, applicable rules, and project values.

**Creating the Data Set:** After parsing, the obtained data is converted into a data set. This set includes the design project information, comparison values for applicable rules, and project values. If there is not enough data to make a comparison, the process is stopped and the user is informed about the missing data.

**Comparison and Inspection:** If the necessary data is available, the project's compliance with regulations is determined using the comparison values and project values. At this stage, a comparison is made for each rule related to the project.

**Generating the Results Report:** In the final stage, a results report containing the user's information and the design project's data is prepared. The report includes the propositions in the correct propositions set, comparison values, and compliance statuses. This report is presented to the user in HTML format.

**User Interface:** The software's user interface is designed using Python's "tkinter" library. The software's workflow is shown in Figure 5 as a flow diagram.



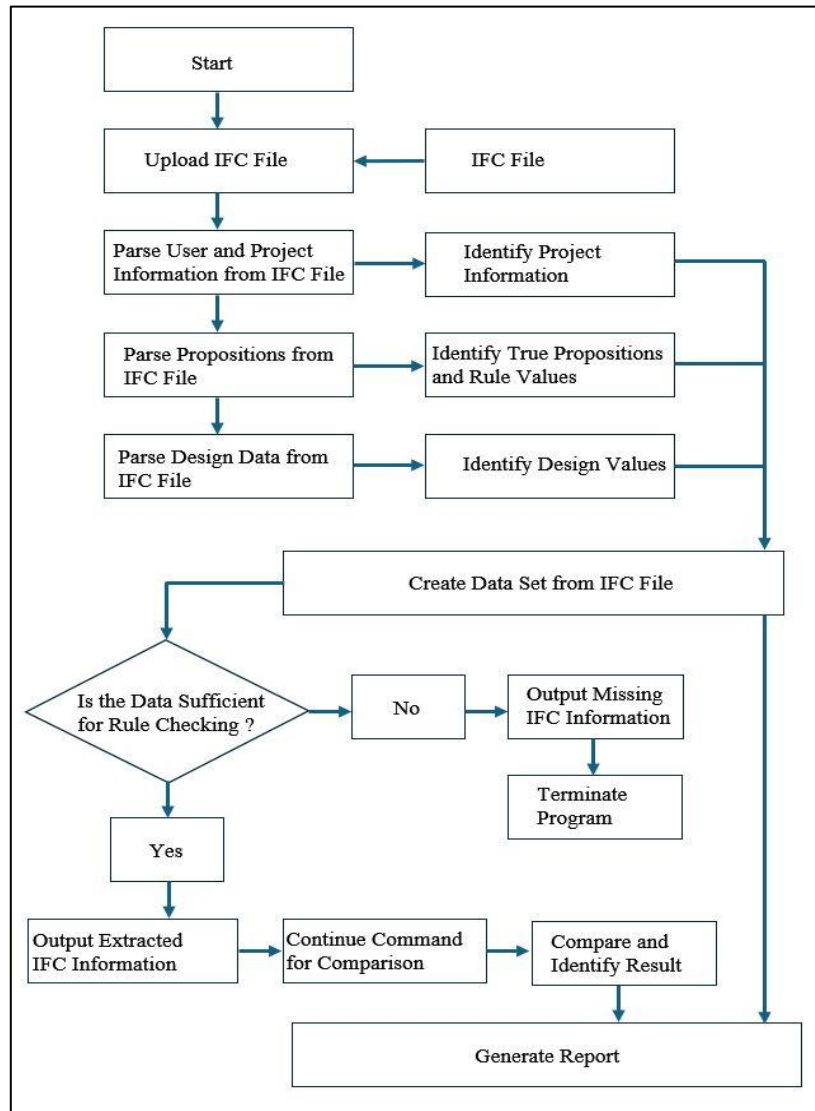


**Figure 5.** Rule-Checking Software Flowchart

### 3.4. Results report

The software generates a detailed document titled "Regulation Compliance Report", which systematically presents each stage of the rule-checking process to the user. This report is produced in HTML format, making it easily accessible across various operating systems and web browsers.

The report provides a comprehensive overview of all data related to the project that has undergone compliance validation. The content is organized into the following eight sections:

- Regulation Reference: The title and date of the applicable regulation, along with the specific articles and headings used in the compliance validation.
- Source File and User Information: The name of the IFC file from which the data was extracted and the username of the individual running the analysis.
- Construction Information refers to the construction-related project data that is retrieved from the IFC file.
- Project Identification: General project information identified from the IFC model.
- Correct Propositions: A list of validated logical propositions used for deriving comparison values.



- Comparison Values refer to the reference values derived from the correct propositions for compliance evaluation.
- Extracted Project Data refers to all relevant project data obtained from the IFC file.

This structured report format enables users to access detailed information regarding all data inputs and validation processes. As shown in Figure 6, the user interface for report presentation is currently available in Turkish. Furthermore, the software enhances the transparency and traceability of regulatory validation, thereby supporting stakeholders in making accurate and timely decisions.

Yönetmelik Uygunluk Raporu		Karşılaştırma Değerleri	
Planlı Alanlar İmar Yönetmeliği / 03.07.2017		imar planlarında kat adetleri belirtilmemiştir.	
Madde-9: Yol genişliklerine göre bina kat adetleri		yol genişliklerine göre bina kat adetleri belirlenecektir.	
Madde-28: Kat yüksekliği		imar planlarında bina yüksekliği belirtilmemiştir.	
		kat yükseklikleri ve kat sayısına göre belirlenecektir.	
		konut bölgesindedir.	
Dosya Adı : 240527-B1-al.ifc		En Çok Kat Adeti	: 4
Kullanıcı : aa		En Çok Bina Yüksekliği (cm)	: 1440
		En Çok Zemin Kat Yüksekliği (cm)	: 360
		En Çok Normal Kat Yüksekliği (cm)	: 360
<b>Proje Bilgileri</b>		<b>IFC Dosya Verileri</b>	
Yapılaşma Bilgileri		Yol Genişliği (cm) : 1200.0	
YBM konut bölgesi : Evet		Bina Kat Adeti : 4	
YBM konut geleneksel mimari yığma : Hayır		Bina Yüksekliği (cm) : 1164.0	
YBM konut zemin ticaret : Hayır		Zemin Kat Kat Yüksekliği (cm) : 291.0	
YBM normal katlar konut harici : Hayır		1. Normal Kat Kat Yüksekliği (cm) : 291.0	
YBM ticaret bölgesi : Hayır		2. Normal Kat Kat Yüksekliği (cm) : 291.0	
YBM ticaret karma : Hayır		3. Normal Kat Kat Yüksekliği (cm) : 291.0	
YBM uip bina kat sayısı : Veri Yok			
YBM uip bina kat sayısı var : Hayır			
YBM uip bina yüksekliği : Veri Yok			
YBM uip bina yüksekliği var : Hayır			
YBM zemin asma katlı : Hayır			
Kimlik Bilgileri		<b>Rapor Sonucu</b>	
Tasarlayan : mimar		Bina Kat Adeti En Çok Kat Adetine Eşittir ; Uygun	
Kurum Tanımı : kamu		Bina Yüksekliği En Çok Bina Yüksekliğinden Küçüktür ; Uygun	
Kurum Adı : AAA Belediyesi		Zemin Kat Yüksekliği Uygun	
Müşteri : müşteri adı		1. Normal Kat Yüksekliği Uygun	
İl/İlçe/Mah/Ada/Parsel : istanbul kartal		2. Normal Kat Yüksekliği Uygun	
Proje Yayın Tarihi : 23.02.2024		3. Normal Kat Yüksekliği Uygun	
Proje Adı : proje adı			
Proje Numarası : B1012			
Proje Durumu : Rev_1			

Figure 6. Regulation compliance report (interface in Turkish)

#### 4. Findings

Four different models were used to test the software, and the different results obtained from the IFC files of these four models clearly demonstrate the functionality of the software. As the first step, the software checked whether the necessary data for comparison was available. Additionally, it detected whether there were any contradictions within the data. In models with sufficient data and no contradictions, the software determined the comparison values for the model and the rule. As a result, the software generated a report containing the outcomes of the operations performed. The software's user interface consists of two main sections, both designed to facilitate intuitive and efficient user interaction.

When the software is launched, the user is presented with the initial interface, which includes five functional components. As illustrated in Figure 7, the interface is currently available in Turkish:

- Drag-and-Drop Area for the IFC File: Users can drag and drop a suitable IFC file into this area. The file name and path are automatically detected. The system verifies the file format, and if a format other than IFC is selected, a warning message is displayed.

- Username Entry: Users can enter their username for identification purposes. If this field is left blank, a warning message is triggered.
- Naming for IFC Objects: This section allows users to modify the default names assigned to objects within the IFC file.
- Start Data Validation: Users initiate the parsing process by clicking the "Validate IFC File Data" command button.
- Rules to Be Checked: At the bottom of the interface, the rule set to be applied during the validation process is displayed.
- Rules to Be Checked: At the bottom of the user interface, the rules that will be checked are displayed.

**Figure 7.** Software startup interface (interface in Turkish)

If the IFC file format is invalid or the username is not provided, the system alerts the user via a warning message (see Figure 8). Once the parsing process is initiated, the second user interface is automatically launched (see Figure 8). It comprises the following five components:

- Name of the Parsed IFC File and User Information: Displays the name of the selected IFC file along with the entered username.
- Project Information and Values: Presents extracted project data and construction parameters retrieved from the IFC file.
- Comparison Values: Displays the values used for rule-based comparisons against the model.
- Missing Information Status: If any required data is missing, a message listing the incomplete items is shown, along with a command button to restart the process.
- Create Rule Control Report: If no missing information is detected, the user is enabled to generate the rule control report.

Kural Kontrol Yazılımı

**Yüklenen dosya IFC değil !**

Dosya Adı : schema.log

Kullanıcı Adı :

**Kullanıcı Adı Giriniz !**

IFC Nesnesi İsimlendirme :

Yol Genişliği :

Zemin Kat :

Normal Kat :

Bina Yüksekliği :

**IFC Dosyası Verilerini Denetle**

**Kural Kontrolleri:**

Planlı Alanlar İmar Yönetmeliğine göre;

En Çok Kat Adeti

En Çok Kat Yükseklikleri

En Çok Bina Yüksekliği

Kural Kontrol Yazılımı

**Dosya Adı : 240527-B1-a1.ifc**

**Kullanıcı : cy**

**IFC Dosyasında Proje Bilgileri:**

YBM_konut_bolgesi:	Evet
YBM_konut_geleneksel_mimari_yigma:	Hayır
YBM_konut_zemin_ticaret:	Hayır
YBM_normal_katlar_konut_harici:	Hayır
YBM_ticaret_bolgesi:	Hayır
YBM_ticaret_karma:	Hayır
YBM_uip_bina_kat_sayisi:	Veri Yok
YBM_uip_bina_kat_sayisi_var:	Hayır
YBM_uip_bina_yuksekligi:	Veri Yok
YBM_uip_bina_yuksekligi_var:	Hayır
YBM_zemin_asma_katli:	Hayır

**IFC Model Verileri :**

Binada Toplam Kat Sayısı : 4

Zemin Kat Yüksekliği (cm): 291.0

3 Adet Normal Kat Toplam Yüksekliği (cm): 873.0

Bina Yüksekliği (cm): 1164.0

Yol Genişliği (cm): 1200.0

**Eksik Bilgi Tespit Edilmedi**

**Kural Kontrol Raporu Oluştur**

**Figure 8.** Error message on the software startup interface and user interface after IFC file validation (interface in Turkish)

In cases where missing information is found, a separate screen displays the incomplete fields, and report generation is disabled (see Figure 9). If all required data is present, the "Create Rule Control Report" tab becomes active, allowing the user to export the report in HTML format. Upon completion, the software automatically terminates.

With the sample model used, which contains 956 elements, a file size of 6.38 MB, and approximately 197,000 words, the rule control report is generated in approximately 3 seconds. This demonstrates the software's ability to perform efficiently, even when handling large-scale data.

Kural Kontrol Yazılımı

Dosya Adı : 240527-B1-a4.ifc

Kullanıcı : cy

**IFC Dosyasında Proje Bilgileri:**

YBM_konut_bolgesi:	Evet
YBM_konut_geleneksel_mimari_yigma:	Hayır
YBM_konut_zemin_ticaret:	Hayır
YBM_normal_katlar_konut_harici:	Hayır
YBM_ticaret_bolgesi:	Hayır
YBM_ticaret_karma:	Hayır
YBM_uip_bina_kat_sayisi:	Veri Yok
YBM_uip_bina_kat_sayisi_var:	Evet
YBM_uip_bina_yuksekligi:	Veri Yok
YBM_uip_bina_yuksekligi_var:	Evet
YBM_zemin_asma_katli:	Hayır

**IFC Model Verileri :**

Binada Toplam Kat Sayısı : 4

Zemin Kat Yüksekliği (cm): 291.0

3 Adet Normal Kat Toplam Yüksekliği (cm): 873.0

Bina Yüksekliği (cm): 1164.0

Yol Genişliği (cm): 1200.0

**Eksik Bilgiler:**

İmar planındaki bina yüksekliği geçerli olmasına rağmen,  
imar planı bina yüksekliği bilgisi eksiktir.

Yeniden Başla

**Figure 9.** Warning screen when missing information is detected in the IFC file (interface in Turkish)

The results of the software tests with four different models are shown in Table 1.

**Table 1.** Software testing with four different models and results

Model Name	Project Construction Information	Comparison Value	Road Width (cm)	Suitable Results	Unsuitable Results
240527-B1-a1	Number of floors and floor height not specified in the zoning plan	Building height to be determined according to regulations	1200	6	0
240527-B1-a2	Number of floors and floor height specified in the zoning plan	Building height: 950 cm and number of floors: 3 floors according to regulations	1200	4	2
240527-B1-a3	Number of floors and floor height not specified in the zoning plan	Building height to be determined according to regulations	900	4	2
240527-B1-a4	Number of floors and floor height specified in the zoning plan	Zoning plan missing building height information	-	-	-

For the model named "240527-B1-a1," the zoning plan does not specify the number of floors and floor height. The number of floors will be determined based on the road widths in the model, and the building height will be calculated according to the floor heights and the number of floors. The project is located in a residential area. The data for this model are shown in Table 2, and the comparison values are shown in Table 3. According to the result report, all 6 rules were found to be suitable for the "240527-B1-a1" model (Table 4).

**Table 2.** Model data for "240527-B1-a1" from the IFC file

Model Data	Value
Road Width (cm)	1200
Number of Floors	4
Building Height (cm)	1164
Ground Floor Height (cm)	291
1st Normal Floor Height (cm)	291
2nd Normal Floor Height (cm)	291
3rd Normal Floor Height (cm)	291

**Table 3.** Comparison values for the "240527-B1-a1" model

Comparison Name	Value
Max Number of Floors	4
Max Building Height (cm)	1440
Max Ground Floor Height (cm)	360
Max Normal Floor Height (cm)	360

**Table 4.** Rule compliance results for the "240527-B1-a1" model

Compliance Name	Status
The number of floors is equal to the maximum number of floors	Suitable
Building height complies with the maximum allowable height	Suitable
Ground floor height	Suitable
1st normal floor height	Suitable
2nd normal floor height	Suitable
3rd normal floor height	Suitable

For the model named "240527-B1-a2," the zoning plan specifies the number of floors, and the condition for the number of floors in the zoning plan is valid. The zoning plan also specifies the building height, which is valid. The project is located in a residential area. The data for this model are shown in Table 5, and the comparison values are shown in Table 6. According to the result report, 4 out of the 6 rules were suitable, and 2 were unsuitable for the "240527-B1-a2" model (Table 7).

**Table 5.** Model data for "240527-B1-a2" from the IFC file

Model Data	Value
Road Width (cm)	1200
Number of Floors	4
Building Height (cm)	1164
Ground Floor Height (cm)	291
1st Normal Floor Height (cm)	291
2nd Normal Floor Height (cm)	291
3rd Normal Floor Height (cm)	291

**Table 6.** Comparison values for "240527-B1-a2" model

Comparison Name	Value
Max Number of Floors	3
Max Building Height (cm)	950
Max Ground Floor Height (cm)	360
Max Normal Floor Height (cm)	360

**Table 7.** Rule compliance results for "240527-B1-a2" model

Compliance Name	Status
The number of floors is equal to the maximum number of floors	Not Suitable
Building height complies with the maximum allowable height	Not Suitable
Ground floor height	Suitable
1st normal floor height	Suitable
2nd normal floor height	Suitable
3rd normal floor height	Suitable

For the model named "240527-B1-a3," the zoning plan does not specify the number of floors. The number of floors will be determined based on road widths, and the building height is not specified in the zoning plan. The height and number of floors will be determined based on the floor heights and the number of floors, and the project is located in a residential area. The data for this model are shown in Table 8, and the comparison values are shown in Table 9. According to the result report, 4 out of the 6 rules were suitable, and 2 were unsuitable for the "240527-B1-a3" model (Table 10).

**Table 8.** Model data for "240527-B1-a3" from the IFC file

Model Data	Value
Road Width (cm)	900
Number of Floors	4
Building Height (cm)	1164
Ground Floor Height (cm)	291
1st Normal Floor Height (cm)	291
2nd Normal Floor Height (cm)	291
3rd Normal Floor Height (cm)	291



**Table 9.** Comparison values for "240527-B1-a3" model

Comparison Name	Value
Max Number of Floors	3
Max Building Height (cm)	1080
Max Ground Floor Height (cm)	360
Max Normal Floor Height (cm)	360

**Table 10.** Rule compliance results for "240527-B1-a3" model

Compliance Name	Status
The number of floors is equal to the maximum number of floors	Not Suitable
Building height complies with the maximum allowable height	Not Suitable
Ground floor height	Suitable
1st normal floor height	Suitable
2nd normal floor height	Suitable
3rd normal floor height	Suitable

For the model named "240527-B1-a4," the model was created with missing information, and therefore, no report was generated. The software detected that although the building height in the zoning plan was valid, the zoning plan was missing the building height information, and the user was informed via a warning message.

## 5. Discussion and Recommendations

This study provides an original contribution to the relatively underdeveloped field of BIM–regulation integration in Türkiye by proposing a software-based solution that enables automated compliance checking. However, some critical issues and development opportunities remain for wider implementation.

### 5.1. Discussion

- **Lack of Data Standardization:** The absence of standardized BIM practices and consistent IFC data structures in Türkiye results in data variation depending on the software used [8, 9]. This may limit the reliability and compatibility of the proposed rule-checking mechanism.
- **Ambiguity in Legal Texts:** Zoning regulations often include vague language, exceptions, and non-technical expressions. These characteristics can hinder the precise formalization of rules and reduce the software's ability to interpret them consistently [36].
- **Limits of Propositional Logic:** While propositional logic is effective for simple rule modeling [42], it lacks the capacity to handle more advanced relational inferences. First-order logic or ontology-based reasoning might be necessary for more complex rule hierarchies.
- **Institutional Readiness:** The success of such a system depends on whether public agencies are digitally prepared and whether their personnel can use these tools. In Türkiye, the level of digital maturity in public-sector approval workflows specifically related to construction projects remains limited [7].

### 5.2. Recommendations

- **Develop a National BIM–Regulation Integration Guide:** Similar to Singapore's "BIM Guide" and initiatives like CORENET [45], Türkiye should develop a national guideline that outlines how BIM data should be structured and linked with legal provisions.

- Adopt NLP and AI for Regulatory Modeling: Legal texts can be automatically translated into formal rules using NLP and machine learning techniques [37, 38], reducing the burden of manual rule definition.
- Pilot Implementation through Public–Private Collaboration: The developed software should be tested in municipalities, building inspection firms, and architecture offices to collect feedback and refine the model.
- Standardize BIM Parameters and Naming Conventions: BEP (BIM Execution Plan) documents should include standardized property naming, classification systems, and IFC usage protocols [24, 25].
- Develop an Open API for Integration: To facilitate interoperability with e-permit systems and other platforms, an open-source API should be created for wider institutional adoption.
- The prototype software developed for testing purposes can be further enhanced. It is possible to improve the system both by expanding data input capabilities and by enabling multi-user access, allowing multiple users to utilize the software collaboratively.

## 6. Conclusions

This study presents a comprehensive framework and a functional software application for the automatic digital verification of BIM-based design data in line with current zoning regulations in Türkiye. Specifically, Articles 9 and 28 of the Regulation on Planned Areas Construction were selected as the basis for developing and testing rule-checking mechanisms that involve multi-variable rule structures [41]. The developed software parses IFC-format BIM models to extract architectural parameters such as road width, number of floors, building height, and floor heights. These are then compared with reference values derived from the regulation. The system successfully functioned in both complete and inconsistent data scenarios, producing user-friendly reports and guiding the user in each step. Test results from four different models demonstrated the system's accuracy, speed, and operational stability. A significant methodological contribution of the study is the successful implementation of propositional logic for translating regulatory rules into machine-readable formats [42]. Unlike traditional systems that rely solely on fixed comparison values, the proposed approach allows for the dynamic evaluation of derived values based on multiple interrelated parameters using an "If–Then" logic structure.

The study offers both theoretical and practical contributions. Theoretically, it proposes a logic-based mechanism for integrating legal rules with BIM data; practically, it demonstrates how this mechanism can be converted into a functioning digital system. Unlike conventional control tools, the software provides scalable and adaptable logic-based validation, which enables broader use across different regulatory conditions. The findings emphasize that automatic rule-checking software can significantly improve efficiency, early error detection, and transparency in both design and public approval processes. For public authorities, such systems may help to accelerate permitting, streamline inspections, and strengthen accountability. For private sector professionals, it offers the opportunity to test compliance before submission, reducing the likelihood of legal obstacles.

In the future, the system can be extended beyond 3D modeling by incorporating 4D (schedule), 5D (cost), 6D (energy and sustainability), and 7D (operation and maintenance) dimensions [19, 20]. This would make it possible to evaluate regulatory compliance not only in terms of geometry but also across the entire project lifecycle. Moreover, the integration of AI and natural language processing (NLP) may allow complex, vague, and exception-based regulations to be interpreted automatically [36, 38]. This would eliminate the need for manual logic translation and broaden the applicability of the system in large-scale regulatory frameworks. In conclusion, this research introduces an original and applicable model for the automated, regulation-based control of BIM data in Türkiye. Both its software infrastructure and logical framework present a transformative potential for digitalization in the construction industry, offering benefits to both public institutions and private stakeholders.

## **7. Author Contribution Statement**

Author 1 contributed to the design, analysis of the data, interpretation of the results, spelling check and content. Author 2 contributed to the creation of the idea, interpretation of the results, and checking the paper in terms of content.

## **8. Ethics Committee Approval and Conflict of Interest**

There is no need to obtain ethics committee permission for the prepared article. There is no conflict of interest with any person/institution in the prepared article.

## **9. Ethical Statement Regarding the Use of Artificial Intelligence**

During the writing process of this study, the artificial intelligence tool "ChatGPT" developed by "OpenAI" was used only for limited purposes for linguistic editing. The scientific content, analysis and results belong entirely to the authors.

## 10. References

- [1] E. Bellini and K. Bang, "Digitalization in construction: An overview of trends and challenges," \*J. Constr. Innov.\*, vol. 1122, no. 1, pp. 1–10, 2022.
- [2] D. Bryde, M. Broquetas and J. M. Volm, "The project benefits of Building Information Modelling (BIM)," \*Int. J. Project Manag.\*, vol. 31, no. 7, pp. 971–980, 2013.
- [3] EU BIM Task Group, "Handbook selection - Turkish handbook." [Online]. Available: <http://www.eubim.eu/handbook-selection/turkish-handbook>. [Accessed: Apr. 30, 2025].
- [4] B. Becerik-Gerber and S. Rice, "The perceived value of building information modeling in the US building industry," \*J. Inf. Technol. Constr.\*, vol. 15, no. 15, pp. 185–201, 2010.
- [5] P. Smith, "BIM implementation—global strategies," \*Procedia Eng.\*, vol. 85, pp. 482–492, 2014.
- [6] O. Hany and D. Mohammed, "Solutions for effective diffusion of BIM for BIM late adopters: case study of UAE AEC industry," \*Int. J. Constr. Manag.\*, vol. 23, no. 9, pp. 1484–1493, 2023.
- [7] G. Şahinkaya, F. A. Sesli, K. Varol and Ö. F. Uzun, "Investigation of Application of Building Information Modeling for Turkey," \*Bilecik Şeyh Edebali Univ. J. Sci.\*, vol. 9, no. 1, pp. 555–563, 2022.
- [8] H. Aladağ, G. Demirdöğen and Z. Işık, "Building information modeling (BIM) use in Turkish construction industry," \*Procedia Eng.\*, vol. 161, pp. 174–179, 2016.
- [9] B. Özorhon, \*Yapı Bilgi Modellemesi IBB Anadolu Yakası Raylı Sistem Projeleri\*, Istanbul, Turkey: Abaküs Yayınları, 2018.
- [10] M. Z. Tel, "Legislation and Legal Framework BIM Implementation National Assessment," M.S. thesis, Inst. of Sci., Istanbul Medipol Univ., Istanbul, Turkey, 2021.
- [11] N. Yamak, S. Koçak and S. Samut, "The Short and Long-Run Dynamics of The Construction Sector In Turkey," \*J. Econ. Manag. Res.\*, vol. 7, no. 1, pp. 96–113, 2018.
- [12] T. Liebich, J. Wix, J. Forester and Z. Qi, "Speeding-up the Building Plan Approval – the Singapore E-Plan Checking Project Offers Automatic Plan Checking Based on IFC," in \*E-Work and E-Business in Architecture, Engineering and Construction\*, Portoroz, Rotterdam: Balkema, pp. 467–471, 2002.
- [13] T. F. Sing and Q. Zhong, "Construction and Real Estate Network (CoreNet)," \*Facilities\*, vol. 19, no. 11/12, pp. 419–428, 2001.
- [14] N. Nisbet, J. Wix and D. Conover, "The Future of Virtual Construction and Regulation Checking," in \*Virtual Futures for Design, Construction & Procurement\*, Oxford, UK: Blackwell Publ., pp. 241–250, 2009.
- [15] Y. Gholami, "Investigating Adoption of Digital Technologies in Construction Projects," Linköping Univ. Electron. Press, 2023. doi:10.3384/9789180750257
- [16] AIA American Institute of Architects California Council, "Integrated Project Delivery: A Guide," 2007. [Online]. Available: [https://www.aia.org/sites/default/files/2023-11/ipd\\_guide.pdf](https://www.aia.org/sites/default/files/2023-11/ipd_guide.pdf). [Accessed: Apr. 30, 2025].
- [17] JG China Construction Industry Standard, "JGT198-2007." [Online]. Available: <https://www.chinesestandard.net/PDF/English.aspx/JGT198-2007?Redirect>. [Accessed: Apr. 30, 2025].
- [18] NBIMS, "National Building Information Modeling Standard v3." [Online]. Available: <https://www.nibs.org/nbims/v3>. [Accessed: Apr. 30, 2025].
- [19] T. Akkoyunlu, "A BIM Execution Plan Proposal for Urban Transformation Projects," Ph.D. dissertation, Inst. of Sci., Istanbul Technical Univ., Istanbul, Turkey, 2015.
- [20] T. Sariçiçek, "BIM Implementation Roadmap for Architectural SMEs in Turkey," M.S. thesis, Inst. of Sci., Hasan Kalyoncu Univ., Gaziantep, Turkey, 2019.
- [21] M. S. Salim and A. M. R. Mahjoob, "Achieving the Benefits and Requirements of Integrated Project Delivery Method Using BIM," \*IOP Conf. Ser.: Mater. Sci. Eng.\*, vol. 901, no. 1, pp. 1–12, 2020.
- [22] C. J. Kibert, \*Sustainable Construction: Green Building Design and Delivery\*. Hoboken, NJ: John Wiley & Sons. [Online]. Available: <https://thuvienso.hoasen.edu.vn/bitstream/handle/123456789/9374/Contents.pdf?sequence=5>. [Accessed: Apr. 30, 2025].

- [23] J. Radl and J. Kaiser, "Benefits of Implementation of Common Data Environment (CDE) into Construction Projects," *\*IOP Conf. Ser.: Mater. Sci. Eng.\**, vol. 471, pp. 1–22, 2019.
- [24] E. Cekin and S. Seyis, "BIM Execution Plan based on BS EN ISO 19650-1 and BS EN ISO 19650-2 Standards," in *\*Proc. 6th Int. Project and Construction Management Conf.\**, pp. 67–74, 2020.
- [25] Penn State University, "Building Information Modeling (BIM) Project." [Online]. Available: <http://bim.psu.edu>. [Accessed: Apr. 30, 2025].
- [26] C. Eastman, P. Teicholz, R. Sacks and K. Liston, *\*BIM Handbook: A Guide to Building Information Modeling for Owner, Manager, Designer, Engineers and Contractors\**. Hoboken, NJ: John Wiley & Sons, 2011.
- [27] T. Froese, "Future directions for IFC-based interoperability," *\*J. Inf. Technol. Constr.\**, vol. 8, pp. 231–246, 2003.
- [28] M. Nour, "Manipulating IFC Sub-Models in Collaborative Teamwork Environments," in *\*Proc. 24th CIB W78 Conf. on Inf. Technol. Constr.\**, pp. 26–29, 2007.
- [29] Industry Foundation Classes, "IFC4 Add2 TC1 RV1.2." [Online]. Available: [https://standards.buildingsmart.org/MVD/RELEASE/IFC4/ADD2\\_TC1/RV1\\_2/HTML/](https://standards.buildingsmart.org/MVD/RELEASE/IFC4/ADD2_TC1/RV1_2/HTML/). [Accessed: Apr. 30, 2025].
- [30] buildingSMART, "Four-layer IFC structure." [Online]. Available: [https://standards.buildingsmart.org/IFC/DEV/IFC4\\_2/FINAL/HTML/link/introduction.htm](https://standards.buildingsmart.org/IFC/DEV/IFC4_2/FINAL/HTML/link/introduction.htm). [Accessed: Apr. 30, 2025].
- [31] S. Macit and H. M. Günaydın, "Building Code Representation: A New Model," *\*J. BAUN Inst. Sci. Technol.\**, vol. 17, no. 2, pp. 83–102, 2015.
- [32] S. Macit, "Computer Representation of Building Codes for Automated Compliance Checking," Ph.D. dissertation, Grad. School of Eng. and Sci., Izmir Inst. of Technol., Izmir, Turkey, 2014.
- [33] M. M. Hakim and J. H. Garrett, "A description logic approach for representing engineering design standards," *\*Eng. with Comput.\**, vol. 9, pp. 108–124, 1993.
- [34] H. Lee, J.-K. Lee, S. Park and I. Kim, "Translating building legislation into a computer-executable format for evaluating building permit requirements," *\*Autom. Constr.\**, vol. 71, pp. 49–61, 2016.
- [35] N. Yabuki and K. H. Law, "An Object-Logic Model for the Representation and Processing of Design Standards," *\*Eng. with Comput.\**, vol. 9, no. 3, pp. 133–159, 1993.
- [36] L. Ding, R. Drogemuller, M. Rosenman, D. Marchant and J. Gero, "Automating code checking for building designs Design Check," in *\*Clients Driving Innovation: Moving Ideas into Practice\**, pp. 1–16, 2006.
- [37] I. Chalkidis, I. Androutsopoulos and N. Aletras, "Neural Legal Judgment Prediction in English," arXiv preprint, arXiv:1906.02059, 2019.
- [38] S. Fuchs and R. Amor, "Natural Language Processing for Building Code Interpretation: A Systematic Literature Review," in *\*Proc. Conf. CIB W78\**, vol. 2021, pp. 11–15, 2021.
- [39] C. Eastman, J. M. Lee, Y. S. Jeong and J. K. Lee, "Automatic rule-based checking of building designs," *\*Autom. Constr.\**, vol. 18, no. 8, pp. 1011–1033, 2009.
- [40] C. Preidel and A. Borrmann, "Automated code compliance checking based on a visual language and building information modeling," in *\*Proc. Int. Symp. Autom. Robot. Constr. Min. (ISARC)\**, Oulu, Finland, 2015.
- [41] Türkiye Cumhuriyeti Resmî Gazete, "Planlı Alanlar İmar Yönetmeliği," no. 30113, Jul. 3, 2017, Ankara.
- [42] A. Kfoury, "Mathematical Logic in Computer Science," *\*arXiv\**, [Online]. Available: <https://doi.org/10.48550/arXiv.1802.03292>. [Accessed: Apr. 30, 2025].
- [43] buildingSMART, "Technical resources." [Online]. Available: <https://technical.buildingsmart.org/>. [Accessed: Apr. 30, 2025].
- [44] J. Garrett and S. J. Fenves, "A knowledge-based standards processor for structural component design," *\*Eng. with Comput.\**, vol. 2, pp. 219–238, 1987.
- [45] C. Lee, K. Yeo and S. Dritsas, "BIM-enabled regulatory design rule checking for building circulation," in *\*Proc. CAADRIA 2024\**, pp. 211–220, 2024.



## Medikal Veri İşlemede Makine Öğrenme Yaklaşımları: Felç için Akıllı Teşhis Sistemi Önerisi

Azra Şilan PERİ<sup>1</sup> , Nida KATI<sup>2</sup> , Ferhat UÇAR<sup>3\*</sup> 

<sup>1,3</sup>Yazılım Mühendisliği, Teknoloji Fakültesi, Fırat Üniversitesi, Elazığ, Türkiye.

<sup>2</sup>Metalurji ve Malzeme Mühendisliği, Teknoloji Fakültesi, Fırat Üniversitesi, Elazığ, Türkiye.

<sup>1</sup>azraperi497@gmail.com, <sup>2</sup>nkati@firat.edu.tr, <sup>3</sup>fucar@firat.edu.tr

Geliş Tarihi: 7.05.2025

Kabul Tarihi: 12.06.2025

Düzeltilme Tarihi: 10.06.2025

doi: <https://doi.org/10.62520/fujece.1694558>

Araştırma Makalesi

Alıntı: A. Ş. Peri, N. Katı, F. Uçar, “Medikal veri işlemede makine öğrenme yaklaşımları: felç için akıllı teşhis sistemi önerisi”, Fırat Üni. Deny. ve Hes. Müh. Derg., vol. 4, no 2, pp. 446-459, Haziran 2025.

### Öz

Bu çalışma, felç teşhisi için makine öğrenmesi ve derin öğrenme tabanlı bir akıllı teşhis sistemi önermektedir. Sağlık sektöründe yapay zekânın (AI) kullanımı, büyük veri analitiği ve dijitalleşme ile birlikte artmaktadır. Felç, dünya genelinde yaygın bir nörolojik hastalık olup erken teşhisle ölüm ve sakatlık oranları önemli ölçüde azaltılabilir. Çalışmada, Kaggle platformundaki 4909 bireyi kapsayan “Felç Tahmin Veri Seti” kullanılmıştır. Bu veri seti, yaş, cinsiyet, hipertansiyon, kalp hastalığı, yaşam tarzı gibi 12 giriş özelliği ve felç durumunu gösteren bir çıkış özelliği içermektedir. Veri ön işleme adımları olarak eksik verilerin ortalama ile doldurulması, kategorik verilerin One-Hot Encoding ile sayısallaştırılması, Min-Max Ölçeklendirme ve SMOTE ile sınıf dengesizliği çözülmüştür. Çalışmada, 15 farklı makine öğrenmesi ve derin öğrenme algoritması (Random Forest, Voting Classifier, Histogram Gradient Boosting, SVM, MLP vb.) değerlendirilmiş; performansları doğruluk, hassasiyet, geri çağırma, F1-skoru ve ROC-AUC metrikleriyle ölçülmüştür. Voting Classifier, %98,5 doğruluk ve 0,99 AUC ile en yüksek performansı göstermiştir. Random Forest ve Histogram Gradient Boosting gibi ağaç tabanlı modeller de yüksek doğruluk oranlarıyla dikkat çekmiştir. Hiperparametre optimizasyonu için GridSearchCV ve RandomizedSearchCV kullanılmış, aşırı öğrenmeyi önlemek için erken durdurma, düzenleme ve dropout teknikleri uygulanmıştır. Bulgular, topluluk öğrenme yöntemlerinin felç teşhisinde geleneksel yöntemlere üstünlük sağladığını göstermektedir. Çalışma, yapay zeka tabanlı klinik karar destek sistemlerinin sağlık sektörüne entegrasyonunun önemini vurgulamakta ve gelecekte daha büyük veri setleriyle model performansının artırılabilirliği önermektedir.

**Anahtar kelimeler:** Felç teşhisi, Makine öğrenmesi, Derin öğrenme, Topluluk öğrenmesi, Klinik karar destek sistemleri

\* Yazışılan yazar





## Machine Learning Approaches in Medical Data Processing: A Proposal for an Intelligent Stroke Diagnosis System

Azra Şilan PERİ<sup>1</sup> R, Nida KATI<sup>2</sup> R, Ferhat UCAR<sup>3\*</sup> R

<sup>1,3</sup>Software Engineering, Faculty of Technology, Firat University, Elazığ, Türkiye.

<sup>2</sup>Metallurgy and Materials Engineering, Faculty of Technology, Firat University, Elazığ, Türkiye.

<sup>1</sup>azraperi497@gmail.com, <sup>2</sup>nkati@firat.edu.tr, <sup>3</sup>fucar@firat.edu.tr

Received: 7.05.2025  
Accepted: 12.06.2025

Revision: 10.06.2025

doi: <https://doi.org/10.62520/fujece.1694558>  
Research Article

Citation: A. Ş. Peri, N. Kati, F. Uçar, "Machine learning approaches in medical data processing: a proposal for an intelligent stroke diagnosis system", Firat Univ. Jour. of Exper. and Comp. Eng., vol. 4, no 2, pp. 446-459, June 2025.

### Abstract

This study proposes an intelligent diagnostic system based on machine learning and deep learning for stroke detection. The use of artificial intelligence (AI) in healthcare is increasing alongside big data analytics and digitalization. Stroke, a prevalent neurological disease worldwide, can have its mortality and disability rates significantly reduced through early diagnosis. The study utilizes the "Stroke Prediction Dataset" from Kaggle, encompassing 4909 individuals. This dataset includes 12 input features such as age, gender, hypertension, heart disease, and lifestyle factors, along with one output feature indicating stroke status. Data preprocessing steps involved filling missing values with the mean, converting categorical data to numerical format using One-Hot Encoding, applying Min-Max Scaling, and addressing class imbalance with SMOTE. Fifteen different machine learning and deep learning algorithms (e.g., Random Forest, Voting Classifier, Histogram Gradient Boosting, SVM, MLP) were evaluated, with performance measured using accuracy, precision, recall, F1-score, and ROC-AUC metrics. The Voting Classifier achieved the highest performance with 98.5% accuracy and an AUC of 0.99. Tree-based models like Random Forest and Histogram Gradient Boosting also demonstrated high accuracy. Hyperparameter optimization was performed using GridSearchCV and RandomizedSearchCV, while early stopping, regularization, and dropout techniques were applied to prevent overfitting. The findings highlight the superiority of ensemble learning methods over traditional approaches in stroke diagnosis. The study underscores the importance of integrating AI-based clinical decision support systems into healthcare and suggests that model performance could be further enhanced with larger datasets in the future.

**Keywords:** Stroke diagnosis, Machine learning, Deep learning, Ensemble learning, Clinical decision support systems

\*Corresponding author

## 1. Introduction

Artificial intelligence (AI) enables computer systems to learn from examples, allowing them to mimic the learning process, one of the basic functions of the human brain. Deep learning, as a sub-branch of machine learning, stands out with its ability to analyze large datasets and identify complex patterns. Especially in healthcare, AI-based systems are widely used to speed up diagnostic processes, support treatment decisions and improve patient care [1-2]. Healthcare is becoming increasingly digitalized and the need for big data analytics is growing as patient data moves to electronic media. The Health 4.0 concept promotes the use of artificial intelligence in disease diagnosis, supporting personalized treatment approaches [3]. Artificial intelligence provides successful results in many fields such as medical imaging, analysis of patient records and evaluation of genetic data, and increases the diagnostic accuracy of physicians with clinical decision support systems [4].

Stroke is one of the most common neurological diseases worldwide, affecting approximately 13.7 million people and causing 5.5 million deaths each year [5]. Ischemic strokes account for 87% of total strokes and this proportion has been increasing over the years [6]. Stroke is a sudden health problem that can seriously affect the quality of life of patients and cause permanent disability. However, with early diagnosis and rapid intervention, stroke-related deaths and disability rates can be prevented by approximately 80%. [7].

Recent studies show that machine learning and deep learning algorithms offer significant advantages in stroke diagnosis [8-9]. Compared to traditional diagnostic methods, artificial intelligence models can make disease predictions over large datasets and help diagnose diseases faster. In particular, combining methods such as deep neural networks (DNN), convolutional neural networks (CNN) and recurrent neural networks (RNN) with medical image analysis significantly improves diagnostic accuracy [1], [10]. The use of machine learning (ML) and deep learning (DL) based models for stroke diagnosis has become an important area of research in recent years [11]. Performance comparisons of various algorithms have been made and the most accurate methods have been identified. Caliskan and Ates used common machine learning algorithms such as Logistic Regression (LR), Decision Tree (DT), Support Vector Machines (SVM) and k-Nearest Neighbors (KNN) for stroke risk assessment. According to the results obtained, the DT model showed the highest success with 91% accuracy rate. Other models were evaluated in terms of classification performance with 89% accuracy for SVM, 81% for KNN and 75% for LR. [12]. In a similar study, Oğuz et al. performed a comparative analysis using 13 different machine learning models for early diagnosis and risk classification of stroke. As a result of the experiments, the Random Forest Classifier (Random Forest) was found to be the most successful model with a 99.425% accuracy rate [13].

In addition to machine learning-based approaches, DL and ML techniques also provide effective results in medical image analysis and classification processes. Alhatemi et al. conducted a study on the analysis of brain MRI images using DNN. Popular deep learning models such as DenseNet121, ResNet50, Xception, MobileNet, VGG16 and EfficientNetB2 were used in the study. The highest accuracy rate of 98.8% was obtained with the EfficientNetB2 model. The model's sensitivity, precision and F1-score were also quite high, indicating that deep learning has great potential in stroke diagnosis [14]. Nancy et al. developed a stroke diagnosis model based on Deep Kernel Extreme Learning Machine (DKELM-AS) using electroencephalogram (EEG) data. The Fast Hartley Transform (FHT) was used to extract features from EEG signals and the DKELM-AS model achieved 95.2% accuracy. EEG-based diagnostic systems offer a faster and more cost-effective alternative to conventional imaging methods [15]. In another study focused on image analysis, UmaMaheswaran et al. developed a model for optimal feature selection in acute stroke diagnosis by analyzing computed tomography (CT) images. Feature extraction methods such as Local Binary Pattern (LBP), Gabor Filter and Discrete Wavelet Transform (DWT) were used. The XGBoost model achieved the best results with a 97% accuracy and a 0.015% false positive rate. The model showed a higher accuracy than traditional support vector machine (SVM), artificial neural network (ANN) and naive Bayes (NB) methods [16]. Ensemble machine learning techniques also offer significant advantages for stroke diagnosis. Srivinas et al. developed an ensemble learning-based diagnosis method by combining Random Forest, Extra Trees and Histogram Gradient Boosting (HGB) models. By combining the predictions from the individual classifiers, the model improved accuracy and enabled more reliable results in clinical practice. The study also suggested that the use of swarm intelligence-based optimization techniques in the future could further

improve model performance [17]. These studies emphasize the importance of artificial intelligence (AI) and big data analytics in stroke diagnosis. Artificial intelligence models can support clinicians in the early diagnosis process by analyzing individual patient data in detail. With the Health 4.0 concept, personalized healthcare services are becoming widespread and the integration of machine learning-based models into clinical decision support systems is becoming increasingly important [4].

In this study, unlike the literature, the performance of ensemble learning techniques and traditional machine learning models in stroke diagnosis is investigated in depth. In this context, we systematically evaluate the potential of ensemble methods such as Random Forest, Extreme Randomized Trees and Histogram-based Gradient Boosting to offer superior performance compared to individual classifiers. Furthermore, the practicality and generalizability of these models in clinical applications are tested on real-world data to provide a new perspective to the literature.

The datasets used in this study consist of a comprehensive pool of data including patient histories, biometric measurements and lifestyle factors [18]. During the modeling process, detailed analyses were performed on these data to evaluate the performance of AI-based diagnostic systems. By emphasizing the critical importance of early diagnosis, the study aims to demonstrate the integration of AI-based clinical decision support systems into the healthcare sector and their transformative impact on clinical applications.

In the rest of the paper, the study consists of Material and Method, Results and Discussion, and Conclusion sections. In the Materials and Method section, the datasets, algorithms and modeling processes used are explained in detail. In the Results and Discussion section, the performance of the proposed models is evaluated and comparative analysis with the literature is presented. The conclusion summarizes the findings of the study, discusses its contributions to clinical practice and provides recommendations for future research.

## 2. Material and Method

The use of artificial intelligence and machine learning algorithms in stroke diagnosis increases the importance of big data analysis in the healthcare industry. Machine learning (ML) has become an effective tool in pattern recognition and data classification processes in disease diagnosis. Deep learning (DL) offers the ability to learn from more complex datasets using neural network structures. In this study, various ML and deep learning algorithms are used to determine the model with the highest accuracy rate in stroke diagnosis.

### Dataset Description

In this study, the “Stroke Prediction Dataset” [18] on Kaggle, which covers 4909 individuals, is used. This dataset consists of 13 attributes in total, 12 different input attributes for classification and prediction about the risk of having a stroke and a single output attribute that provides information about the stroke status. Each attribute in the dataset represents various information about the health status and lifestyle of individuals and reveals important factors affecting the risk of stroke. Table 1 provides detailed descriptions of each attribute.

**Table 1.** Dataset descriptions

Attribute	Description
id	Identification Number
gender	Female/Male
age	age
hypertension	Available :1, Not Available :0
heart_disease	Available :1, Not Available:0
ever_married	Yes/No
work_type	Private Sector / State / Unemployed
residence_type	Rural/Urban
avg_glucose_level	Reference Value
bmi	Reference Value
smoking_status	Yes/No
stroke	Stroke:1, No stroke:0

Analyzing these variables together provides a better understanding of the relationships between individuals' health status and their risk of stroke. Stroke is a common health problem worldwide and such data plays an important role in formulating health policies and directing health services [4-5].

In the data analysis process, data cleaning, visualization and application of various machine learning algorithms were performed. In this process, the general structure of the dataset was examined by considering the missing data processing with appropriate methods. The distribution of the data was visualized using histograms and box plots for continuous variables and bar charts for categorical variables (Figure 1).

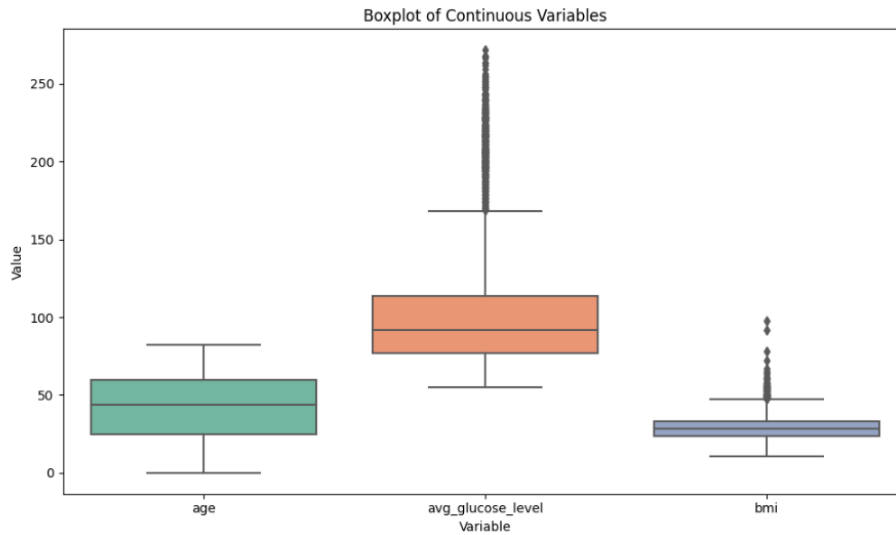


**Figure 1.** Boxplot presentation of age, bmi and avg\_glucose\_level features

In addition, correlation analyses were performed to evaluate the relationships between variables (Figure 2). The findings contributed to the development of medical decision support systems and enabled the analysis of determinants of health outcomes. These analyses provided important information for personalizing treatment plans, increasing the efficiency of healthcare services and improving clinical decision-making processes [3]. Data-driven approaches have the potential to help develop future health applications and optimize patient care processes.

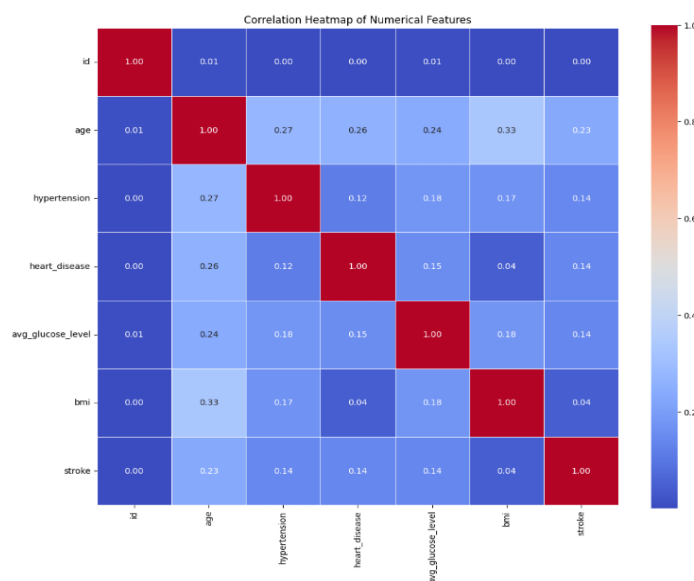


**Figure 2.** Heatmap of the Correlation Matrix for Numerical Variables

## Data Preprocessing Methods

In the data analysis process, it is often not possible to use the raw data directly. Therefore, a series of pre-processing steps were applied to improve the quality of the data and the performance of the machine learning models.

During the initial data quality analysis, it was observed that the dataset contained missing values. Upon inspection, these were found exclusively in the “Body Mass Index” (BMI) variable, with a total of 201 records lacking this information. To maintain the integrity of the dataset and prevent a negative impact on model performance, these missing entries were imputed using the mean of the BMI variable. This mean imputation method was chosen as it is a standard technique that preserves the central tendency of the variable without significantly distorting its overall distribution. This process ensured that the statistical properties of the dataset were maintained, providing a more reliable foundation for the modeling phase.

The categorical variables in the dataset (e.g. gender, marriage status, smoking) should be converted into the numerical format required by the machine learning models. For this purpose, the One-Hot Encoding method was applied. This method digitized categorical data by creating new binary (0/1) variables for each categorical variable.

Numerical features in the dataset (age, BMI, glucose level) may negatively affect the performance of machine learning models due to their different scales. To solve this problem, these variables are scaled between 0 and 1 using the Min-Max Scaling method. This method performs normalization by considering the minimum and maximum values of each feature. Scaling is especially critical for distance-based algorithms (e.g. K-Nearest Neighbor) and gradient-based methods, as it ensures that models give equal weight to all features.

Since the proportion of individuals who suffered a stroke in the dataset is quite low, the problem of class imbalance arises. This can lead to models not learning enough about the minority class (stroke survivors). SMOTE (Synthetic Minority Over-sampling Technique) was used to solve this problem. SMOTE is a technique that balances the class distribution by adding synthetic examples to the minority class. This method generates new samples by interpolating between data points in the minority class, thus allowing the model to better learn the minority class [19]. These pre-processing steps made the dataset suitable for machine learning models and contributed to improving model performance.

## Modeling Process and Algorithms Used

In this study, 15 different algorithms based on machine learning (ML) and deep learning (DL) were evaluated to optimize stroke diagnosis. The algorithms used in this study are grouped into three main categories according to their learning methods. These categories are 1) ensemble learning models, 2) support vector machines and neural networks, and 3) tree-based and statistical models. The aim of the study is to contribute to the analysis of health data by identifying the method with the highest accuracy as its overall schema visually described in Figure 3.

### Community Learning Models

Ensemble learning models aim to achieve higher accuracy by combining the predictions of multiple algorithms. The following algorithms are used in this category:

- **Random Forest (RF):** It is a model created by combining multiple decision trees. Trees trained with random subsets produce the final prediction by voting [20]. Each tree is trained on a different random subset of the data (a technique known as bootstrapping), and each split in the tree considers only a random subset of features. This methodology promotes diversity among the trees and significantly reduces the model’s risk of overfitting. It is known for its robustness against extreme learning in medical datasets.
- **Gradient Boosting (GB):** Minimizes the error rate by training decision trees sequentially [21]. Delivers strong performance on complex datasets [22].

- **Histogram Gradient Boosting (HGB):** It is an optimized version of Gradient Boosting and provides computational efficiency on large datasets [23].
- **AdaBoost (AB):** Strengthens weak learners by weighting examples with high error rates [24]. Advantageous in medical diagnostics.
- **Voting Classifier (VC):** Make decisions by combining the predictions of different models [25]. Accuracy is improved by majority or weighted voting [26].

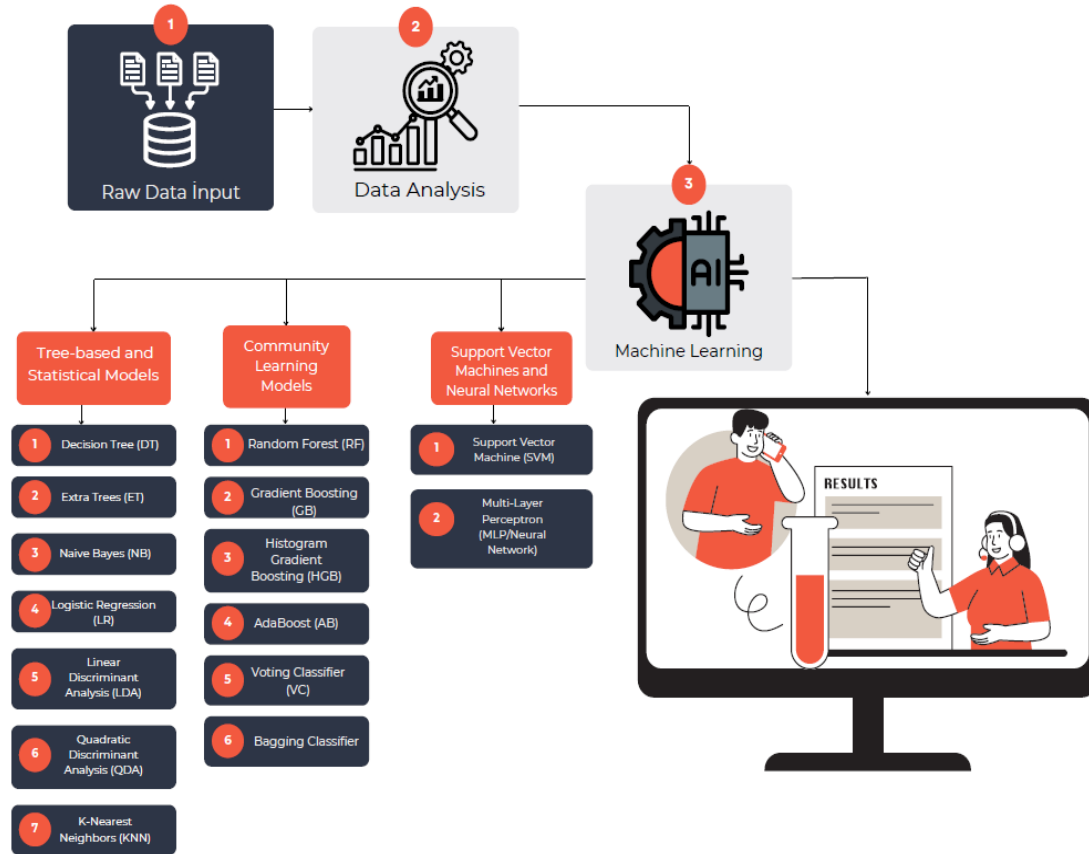


Figure 3. Preferred methodology of the overall framework

### Support Vector Machines and Neural Networks

These models perform effective classification on high-dimensional datasets:

- **Support Vector Machine (SVM):** Aims to find the best hyperplane separating data points [27]. For non-linearly separable data, SVM utilizes the kernel trick to map features into a higher-dimensional space where a linear separation becomes possible. The performance of the model is highly dependent on the choice of the kernel function and the regularization parameter. SVM is also effective on small and medium-sized datasets [28].
- **Multi-Layer Perceptron (MLP):** It is a feed-forward neural network and stands out for its ability to learn complex relationships [1].

### Tree-based and Statistical Models

These models classify data based on rules and produce explainable results:

- **Decision Tree (DT):** Makes predictions by branching the data [29] and provides fast results on small datasets [30].
- **Extra Trees (ET):** Similar to Random Forest, but with more randomness [31].



- **Naive Bayes (NB):** Based on the Bayes theorem, it is effective in areas such as text mining in the medical diagnostics [32].
- **Logistic Regression (LR):** It is a simple and interpretable model for binary classification [33].
- **Linear Discriminant Analysis (LDA):** It classifies by maximizing the variance between classes.
- **Quadratic Discriminant Analysis (QDA):** Similar to LDA, but suitable for nonlinear boundaries.
- **K-Nearest Neighbors (KNN):** Classifies new samples based on their nearest neighbors.
- **Bagging Classifier:** It trains multiple models with random subsets of samples and combines predictions.

## Performance Metrics

The performance of the models was evaluated based on the following metrics:

- **Accuracy:** The rate at which the model correctly performs all classifications.
- **Precision:** Accuracy rate of positive predictions.
- **Recall:** The ratio of true positives to all positives.
- **F1-Score:** Harmonic mean of precision and sensitivity.
- **ROC-AUC:** A metric that measures the classification ability of the model.

Criteria such as the robustness of the models to overlearning and computational costs were also compared [20-21, 26].

## Model Training and Hyperparameter Optimization

Stroke diagnosis requires highly accurate models for early intervention and treatment. In this study, a comprehensive process of model training and hyperparameter optimization is applied to maximize the performance of machine learning models. Hyperparameter optimization aims to increase the generalization capabilities of the models, resulting in more reliable results for datasets with class imbalance, such as stroke. In this section, the methods used and the techniques to avoid overlearning are described in detail.

### Hyperparameter Optimization Methods

In order to obtain the best performance of the models, hyperparameter optimization was performed with two different methods:

- **GridSearchCV:** It was used to systematically search for all possible hyperparameter combinations in small datasets. This method identifies the best parameters by evaluating model performance with 5-fold cross-validation. GridSearchCV is particularly effective when computational resources are limited.
- **RandomizedSearchCV:** It was preferred to provide faster optimization in large datasets. It reduces processing time by evaluating randomly selected hyperparameter combinations. This method provides an efficient search in large hyperparameter spaces.

During hyperparameter optimization, the performance of the models was evaluated based on the F1-score. The F1-score was chosen as an appropriate metric to measure the balance between precision and recall in class imbalanced datasets.

Overfitting is the problem that the model overfits the training data and loses its ability to generalize, especially in complex models. The following techniques were used to avoid this problem.

- **Early Stopping:** In neural network-based models (e.g. Multi-Layer Perceptron - MLP), training is automatically terminated when the validation loss stops improving. This technique prevents the model from overlearning and improves generalization performance.
- **Regularization:** L1 and L2 regularization techniques were used to reduce model complexity. Especially in Support Vector Machines (SVM) and Logistic Regression models, regularization parameters (e.g. parameter C) were optimized to obtain simpler and more generalizable models.

- **Dropout:** In the MLP model, the dependencies of the model are reduced by dropping out randomly selected neurons during training. The dropout rate was determined during hyperparameter optimization (e.g., between 20-50%).

### 3. Results and Discussion

In this study, the performance of 15 different machine learning models for stroke prediction was evaluated on the metrics of accuracy, precision, recall, F1-Score and area under the ROC curve (AUC). The comparative results of the models revealed that the Voting Classifier performed the best with an accuracy of 98.5% and an AUC of 0.99 (Table 2). By combining the predictions of different classification algorithms, this model offered high generalization ability and proved to be a reliable method for stroke prediction.

**Table 2.** Performance metrics of the overall models

Model	Accuracy (%)	Precision	Recall	F1-Score	AUC
Voting Classifier	98.5	0.98	0.97	0.975	0.99
Random Forest	98.0	0.97	0.96	0.965	0.99
Hist Gradient Boosting	98.1	0.97	0.96	0.966	0.99
Gradient Boosting	97.2	0.96	0.95	0.955	0.98
Bagging Classifier	97.5	0.96	0.95	0.955	0.98
MLP (Neural Network)	97.0	0.95	0.96	0.955	0.98
AdaBoost	96.0	0.94	0.93	0.935	0.97
Extra Trees	98.0	0.97	0.96	0.965	0.98
SVM	95.0	0.94	0.92	0.930	0.96
Decision Tree	93.0	0.91	0.89	0.900	0.93
LDA	90.0	0.88	0.86	0.870	0.91
QDA	89.0	0.87	0.85	0.860	0.90
KNN	94.0	0.92	0.90	0.910	0.94
Naive Bayes	88.0	0.86	0.84	0.850	0.89
Logistic Regression	92.0	0.90	0.88	0.890	0.92

Tree-based models, especially Random Forest, Histogram Gradient Boosting and Extra Trees, have attracted attention with their high performance. These models are characterized by their robustness and resistance to overlearning on complex medical datasets. Random Forest and Extra Trees are also frequently reported in the literature with high accuracy rates, and they were similarly effective in this study.

These results are in line with recent studies in the literature. For [instance](#), Wijaya et al. reported that ExtraTrees Classifier achieved 98.24% accuracy and 98% AUC, while Random Forest achieved 98.03% accuracy and 98% AUC [34]. Similarly, another study reported that four models, including the Voting Classifier, achieved over 96% accuracy after data imbalance was corrected with Random Over Sampling (ROS) [35]. Additionally, an ensemble voting model combining models such as Random Forest, XGBoost, and LightGBM achieved 96% accuracy for stroke prognosis [36]. These findings show that ensemble methods and tree-based models provide high accuracy and reliability for stroke prediction.

Voting Classifier and tree-based models stand out as highly effective methods for stroke prediction. This study confirms that ensemble methods provide high performance on medical datasets and also provide results competitive with the best practices in the literature. In future studies, it may be possible to further improve these results by using feature selection techniques and larger datasets.

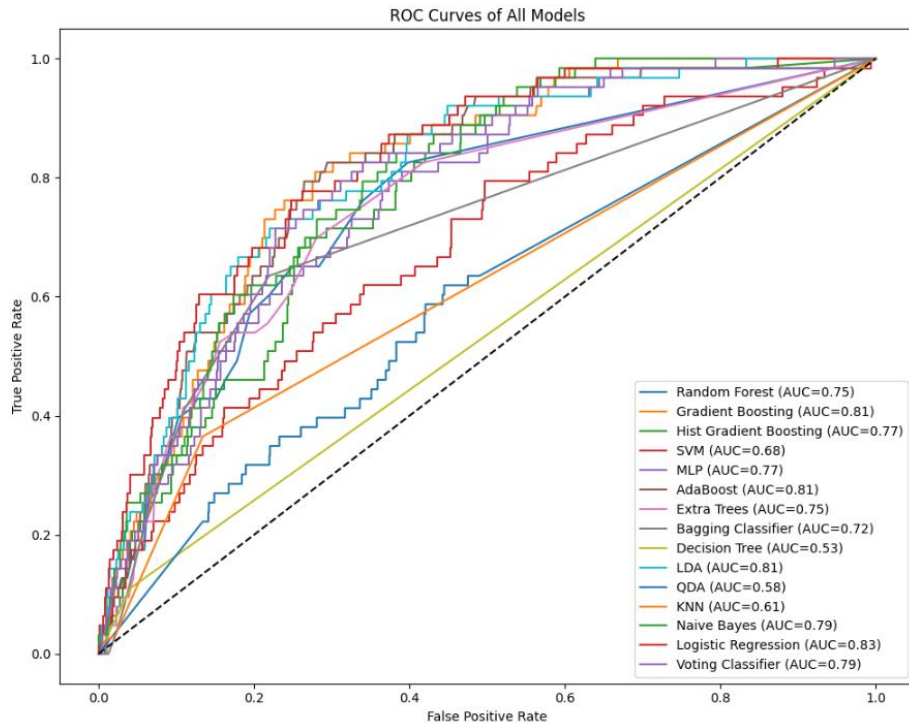


**Figure 4.** Model ROC curves comparison

Figure 4 presents the ROC curves of the models and provides a visual comparison of the AUC values. Again, it is observed that the Voting Classifier and Hist Gradient Boosting models have the highest AUC values.

According to the results obtained in the study, the Voting Classifier model stood out as the most successful model with an accuracy rate of 98.5% and an AUC value of 0.99 thanks to the principle of combining the outputs of different algorithms. This model exhibited high overall performance by combining the strengths of different classification methods. In addition, the Random Forest and Histogram Gradient Boosting models also achieved successful results with accuracy rates above 98%, which once again proved the effectiveness of tree-based models on large datasets. Models such as Support Vector Machines (SVM) and Multilayer Perceptron (MLP - Neural Network) have fallen behind tree-based methods in terms of accuracy, despite their ability to learn complex decision boundaries. In addition, linear models (LDA, QDA, Naive Bayes and Logistic Regression) have produced lower accuracy rates and limited performance compared to other models due to the complexity of the dataset.

In order to support these findings, the confusion matrix images of the first four models, Voting Classifier, Random Forest, Histogram Gradient Boosting and Gradient Boosting algorithms, are presented in Figure 5. These matrices provide a more comprehensive evaluation opportunity for the model selection process by detailing the prediction performance of each model on the basis of incorrect and correct classifications.

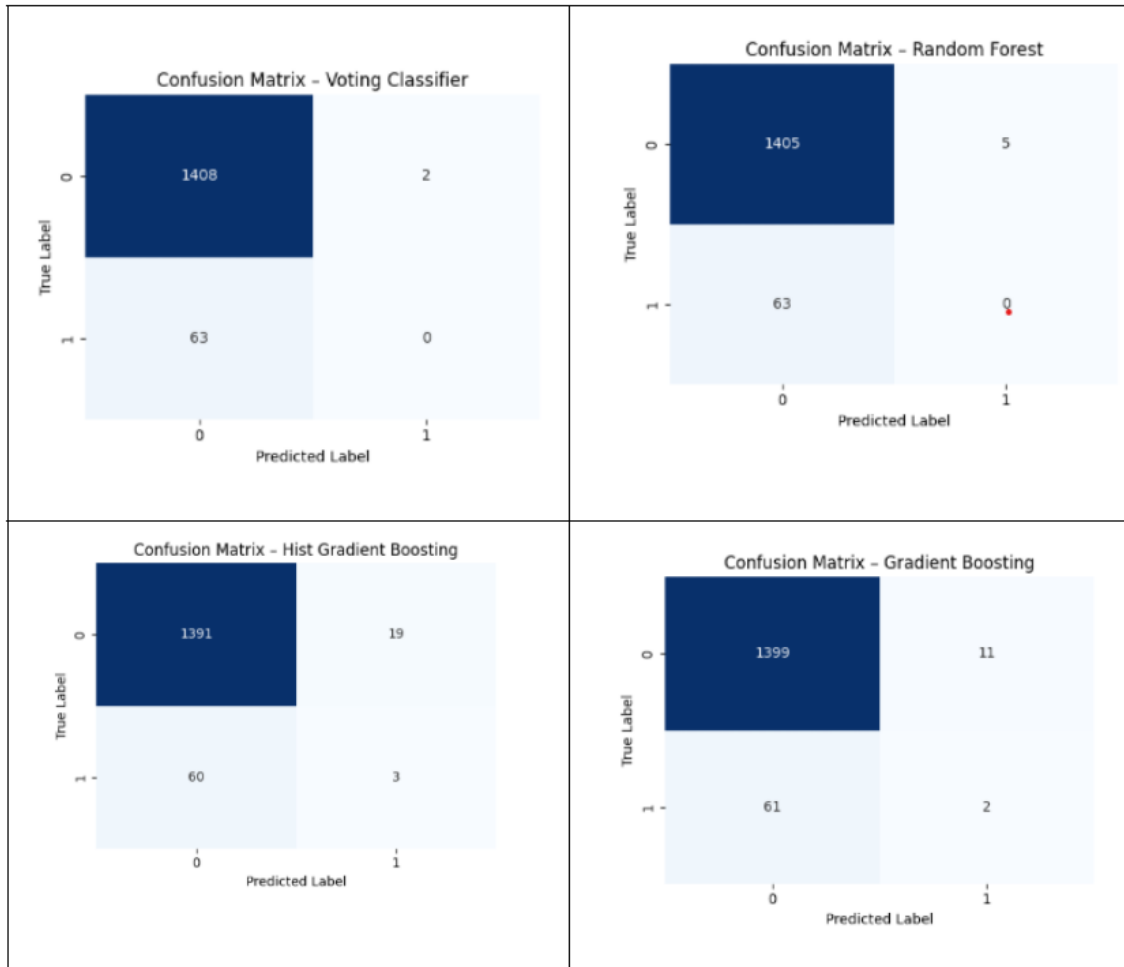


**Figure 5.** Confusion Matrix presentations

These findings show that ensemble learning methods and hybrid models offer significant advantages over traditional linear methods in high-variance health problems such as stroke risk prediction. In particular, tree-based and ensemble learning models were found to provide more reliable results on large datasets and multivariate health data. The findings also reveal that the application of machine learning models together with hyperparameter optimization is a critical factor that increases model performance. As a result, it was concluded that ensemble methods and tree-based algorithms should be primarily evaluated in selecting the optimal model for stroke risk prediction.

#### 4. Conclusion

In this study, the performance of 15 different machine learning and deep learning models for stroke prediction was evaluated based on accuracy, precision, recall, F1-score, and the area under the ROC curve (AUC) metrics. Comparative results revealed that the Voting Classifier achieved the highest performance with 98.5% accuracy and an AUC of 0.99. By combining predictions from various classification algorithms, this model demonstrated high generalization capability and proved to be a reliable method for stroke prediction. Tree-based models, particularly Random Forest, Histogram Gradient Boosting, and Extra Trees, exhibited high performance due to their robustness and resistance to overfitting on complex medical datasets. Random Forest and Extra Trees, frequently reported in the literature for their high accuracy, were similarly effective in this study. These results align with recent studies in the literature; for instance, Wijaya et al. reported that the Extra Trees Classifier achieved 98.24% accuracy and 98% AUC, while Random Forest attained 98.03% accuracy and 98% AUC. Additionally, after addressing data imbalance with Random Over Sampling (ROS), four models, including the Voting Classifier, achieved accuracy above 96%. The Results and Discussion section confirmed that ensemble learning methods and tree-based models are highly effective for stroke

prediction. It is suggested that future studies could further enhance these results by employing feature selection techniques and larger datasets.

## **5. Acknowledgement**

Our research was funded by the Scientific and Technological Research Council of Turkey (TÜBİTAK) under the 2209-A University Students Research Projects Support Program with project number 1919B012323732. This support provided a fundamental contribution to the execution of our project and is gratefully acknowledged.

## **6. Author Contribution Statement**

All authors contributed equally to the conceptualization of this study, design of the study, literature review, data collection, analysis, and critical revision of the article. All three authors worked closely together to obtain the materials and resources needed for the study. Each author contributed significantly to the writing and editing of the article, ensuring that the final version submitted for publication met all criteria for accuracy and integrity.

## **7. Ethics Committee Approval and Conflict of Interest**

There is no need for an ethics committee approval in the prepared article. Also, there is no conflict of interest with any person/institution in the proposed article.

## **8. Ethical Statement Regarding the Use of Artificial Intelligence**

In the writing process of this study, the artificial intelligence tool "Claude" developed by "Anthropic" was used only for limited purposes of linguistic editing. The scientific content, analysis and results belong entirely to the authors. The entire content of the study was produced by the authors in accordance with scientific research methods and academic ethical principles.

## 9. References

- [1] Y. LeCun, Y. Bengio, and G. Hinton, "Deep learning," *Nature*, vol. 521, no. 7553, pp. 436–444, May 2015.
- [2] A. Esteva *et al.*, "A guide to deep learning in healthcare," *Nat. Med.*, vol. 25, no. 1, pp. 24–29, Jan. 2019.
- [3] E. J. Topol, "High-performance medicine: the convergence of human and artificial intelligence," *Nat. Med.*, vol. 25, no. 1, pp. 44–56, Jan. 2019.
- [4] M. Elhaddad, S. Hamam, M. Elhaddad, and S. Hamam, "AI-Driven Clinical Decision Support Systems: An Ongoing Pursuit of Potential," *Cureus*, vol. 16, no. 4, Apr. 2024.
- [5] World Health Organization, *World Health Statistics 2023*, vol. 69, no. 9, 2023.
- [6] V. L. Feigin *et al.*, "Global, regional, and national burden of stroke and its risk factors, 1990–2019: A systematic analysis for the Global Burden of Disease Study 2019," *Lancet Neurol.*, vol. 20, no. 10, pp. 1–26, Oct. 2021.
- [7] E. J. Benjamin *et al.*, "Heart disease and stroke statistics – 2018 update: A report from the American Heart Association," *Circulation*, vol. 137, no. 12, pp. e67–e492, Mar. 2018.
- [8] G. Litjens *et al.*, "Deep learning as a tool for increased accuracy and efficiency of histopathological diagnosis," *Sci. Rep.*, vol. 6, May 2016.
- [9] M. Wang, G. Yang, K. Luo, Y. Li, and L. He, "Early stroke behavior detection based on improved video masked autoencoders for potential patients," *Complex Intell. Syst.*, vol. 11, no. 1, p. 30, 2025.
- [10] I. Goodfellow, Y. Bengio, and A. Courville, "Deep learning," *Genet. Program. Evolvable Mach.*, vol. 19, no. 1–2, pp. 305–307, 2018, [Online]. Available: [https://books.google.com/books/about/Deep\\_Learning.html?hl=tr&id=Np9SDQAAQBAJ](https://books.google.com/books/about/Deep_Learning.html?hl=tr&id=Np9SDQAAQBAJ)
- [11] G. Thakre, R. Raut, C. Puri, and P. Verma, "A Hybrid Deep Learning Approach for Improved Detection and Prediction of Brain Stroke," *Appl. Sci.*, vol. 15, no. 9, p. 4639, 2025.
- [12] H. A. Ateş, "Detection of Stroke (Cerebrovascular Accident) Using Machine Learning Methods," *Bitlis Eren Üniversitesi Fen Bilim. Derg.*, pp. 242–246, 2023.
- [13] Ö. Oğuz, "Makine Öğrenmesi Yöntemlerinin Felç Riskinin Belirlenmesinde Performansı: Karşılaştırmalı bir çalışma," pp. 274–287, 2021.
- [14] R. A. J. Alhatemi and S. Savaş, *Journal of Computer Science*, vol. 55, no. 35, pp. 1–100, 2010.
- [15] P. Nancy, M. Parameswari, and J. S. Priya, "ASO-DKELM: Alpine skiing optimization based deep kernel extreme learning machine for elderly stroke detection from EEG signal," *Biomed. Signal Process. Control*, vol. 88, no. PC, p. 105295, 2024.
- [16] S. K. UmaMaheswaran *et al.*, "Enhanced non-contrast computed tomography images for early acute stroke detection using machine learning approach," *Expert Syst. Appl.*, vol. 240, p. 122559, 2024.
- [17] A. Srinivas and J. P. Mosiganti, "A brain stroke detection model using soft voting based ensemble machine learning classifier," *Meas. Sensors*, vol. 29, p. 100871, 2023.
- [18] "Stroke Prediction Dataset." [Online]. Available: <https://www.kaggle.com/datasets/fedesoriano/stroke-prediction-dataset>
- [19] S. Uddin *et al.*, "Comparative performance analysis of K-nearest neighbour (KNN) algorithm and its different variants for disease prediction," *Sci. Rep.*, vol. 12, no. 1, pp. 1–11, Dec. 2022.
- [20] L. Breiman, "Random forests," *Int. J. Adv. Comput. Sci. Appl.*, vol. 7, no. 6, pp. 1–33, 2016.
- [21] J. H. Friedman, "Greedy function approximation: a gradient boosting machine," *Ann. Statist.*, vol. 29, no. 5, pp. 1189–1232, Oct. 2001.
- [22] A. Natekin and A. Knoll, "Gradient boosting machines, a tutorial," *Front. Neurobot.*, vol. 7, p. 63623, Dec. 2013.
- [23] G. Ke *et al.*, "LightGBM: A Highly Efficient Gradient Boosting Decision Tree," *Adv. Neural Inf. Process. Syst.*, vol. 30, 2017, [Online]. Available: <https://github.com/Microsoft/LightGBM>
- [24] Y. Freund and R. E. Schapire, "A Decision-Theoretic Generalization of On-Line Learning and an Application to Boosting," *J. Comput. Syst. Sci.*, vol. 55, no. 1, pp. 119–139, Aug. 1997.
- [25] L. I. Kuncheva, *Combining Pattern Classifiers*, Jul. 2004.
- [26] P. Rajpurkar *et al.*, "Deep learning for chest radiograph diagnosis: A retrospective comparison of the CheXNeXt algorithm to practicing radiologists," *PLOS Med.*, vol. 15, no. 11, p. e1002686, Nov. 2018.



- [27] C. Cortes, V. Vapnik, and L. Saitta, "Support-vector networks," *Mach. Learn.*, vol. 20, no. 3, pp. 273–297, Sep. 1995.
- [28] W. S. Noble, "What is a support vector machine?," *Nat. Biotechnol.*, vol. 24, no. 12, pp. 1565–1567, Dec. 2006.
- [29] J. R. Quinlan, "Induction of decision trees," *Mach. Learn.*, vol. 1, no. 1, pp. 81–106, Mar. 1986.
- [30] L. Rokach and O. Maimon, "Top-down induction of decision trees classifiers – a survey," *IEEE Trans. Syst. Man Cybern. C Appl. Rev.*, vol. 35, no. 4, pp. 476–487, Nov. 2005.
- [31] P. Geurts, D. Ernst, and L. Wehenkel, "Extremely randomized trees," *Mach. Learn.*, vol. 63, no. 1, pp. 3–42, Apr. 2006.
- [32] D. D. Lewis, "Naive (Bayes) at forty: The independence assumption in information retrieval," *Lect. Notes Comput. Sci.*, vol. 1398, pp. 4–15, 1998.
- [33] D. W. Hosmer, S. Lemeshow, and R. X. Sturdivant, *Applied Logistic Regression: Third Edition*, pp. 1–510, Aug. 2013.
- [34] R. Wijaya *et al.*, "An Ensemble Machine Learning and Data Mining Approach to Enhance Stroke Prediction," *Bioengineering*, vol. 11, no. 7, 2024.
- [35] N. Biswas, K. M. M. Uddin, S. T. Rikta, and S. K. Dey, "A comparative analysis of machine learning classifiers for stroke prediction: A predictive analytics approach," *Healthc. Anal.*, vol. 2, p. 100116, 2022.
- [36] M. Al Duhayyim *et al.*, "An Ensemble Machine Learning Technique for Stroke Prognosis," *Comput. Syst. Sci. Eng.*, vol. 47, no. 1, pp. 413–429, 2023.